

**Multiphase Flow and Icing
Predictions with Control-
Volume Based Finite-Element
Method and PIV Laser
Measurements**

by

Marko Milanez

A THESIS SUBMITTED TO
THE UNIVERSITY OF MANITOBA
IN PARTIAL FULFILLMENT OF THE
REQUIREMENTS FOR THE DEGREE OF
DOCTOR OF PHILOSOPHY
IN MECHANICAL ENGINEERING

DEPARTMENT OF MECHANICAL AND
MANUFACTURING ENGINEERING,
UNIVERSITY OF MANITOBA
WINNIPEG, MANITOBA, CANADA

July 2005

Copyright © 2005 by Marko Milanez

THE UNIVERSITY OF MANITOBA
FACULTY OF GRADUATE STUDIES

COPYRIGHT PERMISSION

**Multiphase Flow and Icing Predictions with Control-
Volume Based Finite-Element Method and PIV Laser
Measurements**

by

Marko Milanez

**A Thesis submitted to the Faculty of Graduate Studies of
The University of Manitoba in partial fulfillment of the requirement
of the degree**

of

DOCTOR OF PHILOSOPHY

Marko Milanez © 2005

Permission has been granted to the Library of the University of Manitoba to lend or sell copies of this thesis to the National Library of Canada to microfilm this thesis and to lend or sell copies to the film, and to University Microfilms Inc. to publish an abstract to this thesis.

This reproduction or copy of this thesis has been made available by authority of the copyright owner solely for the purpose of private study and research, and may only be reproduced and copied as permitted by copyright laws or with express written authorization from the copyright owner.

ABSTRACT

A novel Eulerian dispersed-flow Two-Fluid model and an ice accretion model are developed. They are validated for applications involving droplet-air motion and ice interface tracking. Spatially averaged multiphase flow equations are developed and additionally modeled for interfacial form and shear drag forces. Scaling, order of magnitude and similarity methods are adopted for investigation of special near-wall dispersed-flow solutions. A novel multiphase flow exact closed form similarity solution is analytically derived for the droplet flow injected into an airstream at a flat plate. One- and two-phase closed form Lagrangian analytical solutions for dispersed phase/continuous phase (i.e. droplet/air) tracking are developed. Two numerical algorithms, a Control-Volume based Finite-Element dispersed-flow algorithm and an icing algorithm, are developed with a fixed grid approach, and incorporated into an existing PHASES numerical program. Grid and initial condition independence are obtained for several external flow situations, involving frontward steps with straight and curved surfaces. In icing applications at the ice and solid objects, the dispersed-droplet flow is modeled as a group of physical bodies impacting on a surface, while the air flow is modeled as a continuous flow. Drag/gravity is an important ratio when determining the degree of dispersed-flow inertial deflection from a continuous flow and near solid surfaces. An Eulerian, two-dimensional ice interface tracking algorithm is developed for ice shape evolution predictions. It is validated against analytically developed, closed form Lagrangian two-dimensional ice interface solutions.

Furthermore, experimental studies are carried out for droplet and jet flows in the airstream and icing applications, involving water and spray-icing tunnels. Various indoor conditions are considered in the investigation of the droplet flow characteristics (i.e. droplet diameter and impact length geometries). A liquid spray nozzle systems (long and short distances) and liquid stream nozzle system are developed for velocity and trajectory flow measurements. In addition, a *PIV* laser based technique with low and high sense *CCD* chip cameras is used in the spray and stream flow experimental designs to predict the whole-field droplet velocities. Results with numerical, analytical and experimental validations involving droplet motion and ice shape evolution on various surfaces are presented.

ACKNOWLEDGEMENTS

I wish to acknowledge my supervisor, Dr. G. F. Naterer, for granting me the opportunity to work on this *Ph. D.* research project. His technical guidance is thankfully acknowledged. I particularly enjoyed a portion of the time when discussing fundamental aspects of the research.

I wish to thank Dr. G. F. Naterer for his financial support, provided through Westland Helicopters Ltd., Natural Sciences and Engineering Research Council of Canada and the Canada Foundation for Innovation.

I acknowledge Dr. N. Popplewell for his suggestions, especially when discussing fundamental issues and experimental characterization of droplet motion and icing processes. I acknowledge Dr. A. Woodbury for his suggestions when guiding my research work, mostly at our annual meetings. My special appreciation goes to Dr. Tsuboi, for his valuable thoughts about Eulerian and Lagrangian tracking during his stay at the University of Manitoba. I thank the University of Manitoba and Department of Mechanical and Manufacturing Engineering for their support during my *Ph. D.* studies.

I acknowledge Mr. John Finken for his sincere and efficient laboratory assistance.

I extend my special gratitude to Mr. Venn and Dr. G. Richardson from Westland Helicopters, for showing their high appreciation for my scientific and engineering modeling of flow and icing processes.

NOMENCLATURE

Roman Letters

\bar{A}	boundary condition coefficient [-]
A_i	area of deposited ice [m^2]
A_{cylidr}	cross section of a cylinder [m^2]
$[A]$	global coefficient matrix
\bar{B}	local body forces [$kg\ m\ s^{-2}$]
\bar{B}	boundary condition coefficient [-]
B_k	elementary bias limit [-], [%]
a_i	surface of a phase interface [m^2]
a_{kw}	surface of phase k in contact with a wall surface [m^2]
b_k	conserved function
$\langle b_k \rangle$	volume average of a volume integral of a conserved function
$\langle b_k \rangle_i$	volume average of a surface integral of a conserved function
$\{b\}$	vector of known physical quantity
\bar{C}	boundary condition coefficient [-]
C_D	drag coefficient [-]
C_i	drag coefficient in i-th direction [-]
D, D_d	droplet diameter [m]
$D(u_1, u_2)$	Fourier transform of an added noise function

$\det[J]$	determinant of Jacobian transformation
\vec{d}_n	node-to-node distance vector in a finite element [m]
dh	ice shape function [m]
dS	infinitesimal area [m ²]
dV	infinitesimal volume [m ³]
$d(u_1, u_2)$	added noise function
$EBeta$	indicator of the excess ice (excess phase volume fraction) [-]
$ERROR$	error [%]
F	level of measured confidence [-], [%]
Fr	Froude number [-]
$F(\eta)$	similarity function
$F_{D,i}$	components of a drag force [N]
$F(v_1, v_2)$	Fourier transform of interrogation area's light intensity function at time t_0
f	drag factor [-]
f_i	specific body force (volumetric) [m s ⁻²]
f_k	phase fraction (i.e. continuous phase) [-]
$f(x, n)$	scalar function
$f(x, y)$	Gaussian function of the peak in a correlation domain
$f(u_1, u_2)$	interrogation area's light intensity function at time t_0
\vec{G}	phase interaction forces [kg m s ⁻²]
$G(v_1, v_2)$	Fourier transform of interrogation area's light intensity function at time $t_0 + \Delta t$
g	gravity [m s ⁻²]

$g(u_1, u_2)$	interrogation area light intensity function at time $t_0 + \Delta t$
$h(n)$	scalar function
h	height of a peak in a correlation plane, interface position [m]
h_i	measured quantity: [m], [s], [N m ⁻²]
h_k	phase enthalpy [m ² s ⁻²]
\bar{I}	identity tensor
$\bar{i}, \bar{j}, \bar{k}$	unit vectors in x-, y- and z-directions
\bar{j}_k	flux of a general scalar quantity [kg s ⁻¹ m ²]
k_i	measured quantity (i.e. velocity [m s ⁻¹])
L	characteristic length, length of a flat plate [m]
L_{img}	width of a digital image [m]
L_{obj}	width of a camera's view in a object plane [m]
l_{ref}	reference length [m]
m	mass of accreted ice [m]
$\dot{m}_{d,i}$	specific mass flow rate [kg s ⁻¹ m ⁻³]
\dot{m}_k	mass flow rate for a particular phase [kg s ⁻¹ m ⁻²]
N	number of measured samples [-]
$N_i(s, t)$	interpolation shape function ($i = 1, 2, 3, 4$)
n_j	normal vector
$\bar{n}_k, \bar{n}_1, \bar{n}_2$	normal vector for a particular phase
\bar{n}_{kw}	normal vector for a particular phase at the wall surface
P	dimensionless precipitation rate [-]
P_k	precision limit for variable k [-], [%]

Pr	Prandtl number [-]
p	pressure $[kg\ m^{-1}\ s^{-2}]$
p_k	local pressure of phase k $[kg\ m^{-1}\ s^{-2}]$
$\langle p_k \rangle$	volume averaged pressure of phase k $[kg\ m^{-1}\ s^{-2}]$
$\langle p_{ki} \rangle$	volume averaged interfacial pressure of phase k $[kg\ m^{-1}\ s^{-2}]$
Pfl	pre-condition indicator [-]
$Q_{i,j}^*$	scaled flux into/out of a sub-control volume [-]
$q_{convection}''$	convective heat flux $[W\ m^{-2}]$
$q_{evaporation}''$	heat flux of evaporation $[W\ m^{-2}]$
\vec{r}_i, \vec{r}_n	position vectors from origin $(0, 0)$ to a node (CV) $[m]$
$R_{cyl d}$	radius of a cylinder $[m]$
Re	Reynolds number [-]
Re_r	relative Reynolds number [-]
r	ratio $\frac{v_{xd}}{v_{xd\gamma}}$ [-]
S	surface $[m^2]$
S	estimate of a droplet displacement $[m]$
\hat{S}	source term $[s^{-1}]$
$S(u_1, u_2)$	Fourier transform of a spatial shifting function
$s_{k,i}$	coordinate of the trajectory of phase k in i -th direction $[m]$
s	local coordinate within a finite element $[m]$
$s(u_1, u_2)$	spatial shifting function
T	temperature $[K]$
t	time $[s]$, local coordinate within a finite element $[m]$

t_0	initial time [s]
t^*	dimensionless time [-]
t_{ref}	reference time [s]
U_k	total uncertainty for the measured quantity k [-], [%]
u, v	droplet velocities in x - and y - directions, respectively [$m s^{-1}$]
V	volume [m^3]
V	resultant velocity magnitude of droplet flow [$m s^{-1}$]
\bar{v}	phase velocity (\bar{v} - dispersed phase, \bar{v}_a - carrier (air) phase) [$m s^{-1}$]
$v_{d,i}$	component of droplet phase speed in i -th direction [$m s^{-1}$]
$\langle v_{d,i} \rangle^*$	velocity component of volume averaged scaled phase speed in the x - , y - or z -direction [$m s^{-1}$]
$\langle v_{d,i} \rangle^0$	component of volume averaged phase speed at an old time level in x -, y - or z -direction [$m s^{-1}$]
v'_{ki}	fluctuating part of a velocity component of a particular phase [$m s^{-1}$]
v_t	terminal velocity [$m s^{-1}$]
$\langle v \rangle$	volume averaged velocity [$m s^{-1}$]
$\langle \bar{v} \rangle$	specified volume averaged velocity at a boundary (Dirichlet boundary condition) [$m s^{-1}$]
$\langle \bar{v}_0 \rangle$	specified initial volume averaged velocity [$m s^{-1}$]

v_{yd}	droplet velocity in y -direction [$m s^{-1}$]
(v_1, v_2)	coordinates in a frequency domain
$W(u_1, u_2)$	Gaussian window function
W	width of a peak in a correlation domain
x, y, z	Cartesian coordinates and distances [m]
x_i, x_j, x_k	Cartesian coordinates in the x -, y - and z -directions, respectively [m]
x_I	constant [-]
x^*, y^*, z^*	scaled dimensions, locations [-]
$\{x\}$	vector of unknown physical quantities (i. e. velocity vector [m])
(x_0, y_0)	location of a peak in a correlation domain
y	domain elevation [m]
y_0	vertical distance from a horizontal wall [m]
y_0	elevation at an inlet of a computational domain [m]
w	plate width, position [m]

Roman Subscripts

a	air
$ANALY$	analytical
c	continuous phase, carrier phase
cyl_d	cylinder
d	dispersed phase, droplet
i	interfacial, ice
i, j, k	space directions x, y, z , respectively

<i>ip</i>	integration point
<i>IN, INLET</i>	inlet of a domain
<i>k</i>	particular phase, variable
<i>new</i>	new value
<i>NUMER</i>	numerical
<i>old</i>	old value
<i>OUT, OUTLET</i>	outlet of a domain
<i>p</i>	particle
<i>r, rel</i>	relative
<i>UNIT</i>	unit
<i>w</i>	water
<i>x, y, z</i>	Cartesian coordinates

Roman Superscripts

*	scaled (quantity)
-	specified (quantity), mean value (of the quantity)

Greek Letters

α	arbitrary phase fraction [-], angle between phases [$^{\circ}$]
β	phase volume fraction [-]
$\bar{\beta}$	specified phase volume fraction at a boundary (Dirichlet boundary condition) [-]

$\bar{\beta}_o$	specified initial phase volume fraction [-]
β_V	drag parameter $[kg\ m^{-3}\ s^{-1}]$
$\zeta(x, n)$	scalar function
δ	characteristic length, boundary layer thickness, equivalent ice thickness [m]
δ^*	representative conductor thickness [m]
$\delta v_{k,i}$	fluctuating part of a velocity component of a particular phase $[m\ s^{-1}]$
Δ	difference (of the physical quantities)
Δh_i	ice interface distance in i -th direction [m]
Δn	normal distance between two streamlines [m]
Δp	droplet gauge pressure $[kg\ m^{-1}\ s^{-2}]$
$\Delta p_{k,i}$	difference between an average interfacial and average phase pressure $[kg\ m^{-1}\ s^{-2}]$
$\Delta p'_{k,i}$	difference between a local and average interfacial pressure $[kg\ m^{-1}\ s^{-2}]$
Δt	time interval for a droplet pair [s]
$\Delta \tilde{\psi}$	mass flow per unit depth between two streamlines $[kg\ s^{-1}\ m^{-1}]$
$\eta_{d,p}$	normal apparent viscosity for a dispersed component $[kg\ m^{-1}\ s^{-1}]$
$\eta_{d,\tau}$	tangential apparent viscosity for a dispersed component $[kg\ m^{-1}\ s^{-1}]$
η	similarity parameter

$\phi_{f-g}(u_1, u_2)$	discrete cross correlation function
Γ_{md}	(droplet) mass flow rate $[kg\ m^{-3}\ s^{-1}]$
γ	droplet momentum displacement for a reference streamline [m]
$\hat{\gamma}_s$	droplet mass-based displacement up to γ streamline [m]
χ	normalized scalar product [-]
ξ	order of magnitude [-]
$\xi(x)$	scalar function [-]
μ	dynamic viscosity $[kg\ m^{-1}\ s^{-1}]$
ν	kinematic viscosity $[m^2\ s^{-1}]$
∇	gradient operator $[m^{-1}]$
ψ	scalar, quantity of an interest [-]
ρ	density $[kg\ m^{-3}]$
ρ_i	density of ice $[kg\ m^{-3}]$
ρ_j	density of a jet (flow) $[kg\ m^{-3}]$
σ_{ij}	total stress $[kg\ m^{-1}\ s^{-2}]$
σ_k	standard deviation from a measured mean value [-]
τ_{ij}	component of a shear stress $[kg\ m^{-1}\ s^{-2}]$
$\bar{\tau}$	shear stress tensor $[kg\ m^{-1}\ s^{-2}]$
Θ_s	droplet momentum-based displacement up to γ streamline [m]
θ	angle in a conductor's circumferential direction $[0]$

θ_i relative angles between the incoming flow and nodal distances
in each finite element at the node under consideration $[0]$

Greek Subscripts

γ reference streamline

Other Symbols

\tilde{O} order of magnitude

Abbreviations

<i>ANALY</i>	Analytical
<i>AUSM</i>	Advection Upwinding Splitting Method
<i>AUSMD</i>	Advection Upwinding Splitting Method with flux Differences
<i>CCD</i>	Charge Couple Device
<i>CCU</i>	Constant Current Anemometer
<i>CDS</i>	Central Difference Scheme
<i>CFD</i>	Computational Fluid Dynamics
<i>CFX - TASCFLOW</i>	Control-Volume Based Finite-Element Method numerical program
<i>Co</i>	Courant number
<i>CPU</i>	Central Process Unit

<i>CTA</i>	Constant Temperature Anemometer
<i>CV</i>	Control-Volume, Control-Volume method
<i>CVFEM</i>	Control-Volume Based Finite-Element Method
<i>DNS</i>	Direct Numerical Simulation
<i>DRAG</i>	Drag term
<i>EDS</i>	Exponential Difference Scheme
<i>ERR</i>	Error
<i>FAX</i>	Faxen force term
<i>FENSAP - ICE</i>	Finite Element based numerical program
<i>FFT</i>	Fast Fourier Transformation
<i>Fr</i>	Froude number
<i>GRAV</i>	gravity term
<i>HWA</i>	Hot Wire Anemometry
<i>IC</i>	Influential Coefficient
<i>JSPS</i>	Jet flow with Seed Particle Supplier
<i>LES</i>	Large Eddy Scale Simulation
<i>MASS</i>	Mass
<i>N</i>	Number of phases, Interpolation Functions
<i>PDS</i>	Planar Droplet Sizing
<i>PINS</i>	Physical Influence Scheme
<i>PIV</i>	Particle Image Velocimetry
<i>Pr</i>	Prandtl number
<i>PRESS</i>	pressure term
<i>PVC</i>	plastic material
<i>Re</i>	Reynolds number
<i>RSS</i>	Root – Sum – Square
<i>ref</i>	reference
<i>relax</i>	relaxation factor
<i>SAFF</i>	Saffman force term
<i>SCV1, SCV4</i>	Sub-Control Volume 1, Sub-Control Volume 4

<i>SMD</i>	Sauter Mean Diameter
<i>SPS</i>	Seed Particle Supplier
<i>SS1, SS4</i>	Sub-Surface 1, Sub-Surface 4
<i>SW</i>	software
<i>TRANS</i>	transient term
<i>TURB 1</i>	first turbulent term
<i>TURB 2</i>	second turbulent term
<i>UDS</i>	Upwind Difference Scheme
<i>VISC-1</i>	first viscous term
<i>VISC-2</i>	second viscous term
<i>x-CONV</i>	convection term in the <i>x</i> -direction
<i>y-CONV</i>	convection term in the <i>y</i> -direction

TABLE OF CONTENTS

Chapter 1	INTRODUCTION	1-25
1.1	Background	1
1.2	Problem Description	3
1.3	Literature Review	5
1.3.1	Analytical Dispersed-Flow Tracking Leading to Icing	5
1.3.2	Numerical Algorithm for Icing Predictions	11
1.3.3	Experimental Assessment of Droplet Motion and Icing	18
1.4	Scope of Thesis	20

1. 5	Outline of Thesis	21
Chapter 2	MODELING OF MULTIPHASE MOTION WITH DROPLETS AND ICING	26-83
2. 1	Governing Equations	26
2. 2	Method of Eulerian Spatial Averaging in Multiphase Transport	33
2. 3	Modeling of Interfacial Drag Force	51
2. 4	Scaling and Order of Magnitude Analyses	53
2. 5	Special Cases of Analytical Solutions	62
2. 5. 1	Similarity Near-Wall Multiphase Solution	62
2. 5. 2	Lagrangian Analytical Modeling and Solutions of Droplet Trajectories	70
2. 5. 3	Ice Interface Tracking Method	80

Chapter 3	NUMERICAL FORMULATION OF CONTROL-VOLUME BASED FINITE ELEMENT METHOD (CVFEM) FOR MULTIPHASE ICING PREDICTIONS	84-114
3. 1	Definitions and Notation	85
3. 2	Scaled Form of Dispersed Phase Momentum Equations	89
3. 3	Discretization of Dispersed Phase Momentum Equations	92
3. 4	Discretization of the Dispersed Phase Volume Fraction Equations...	100
3. 5	Boundary and Initial Conditions	102
3. 6	Numerical Algorithm and Code Implementation	103
3. 6. 1	Dispersed Flow Algorithm	103
3. 6. 2	Ice Tracking Algorithm	108
3. 6. 3	Continuous Flow Algorithm.....	110
Chapter 4	EXPERIMENTAL INVESTIGATION OF DROPLET MOTION AND ICING	115-139

4. 1	Development of Spray and Jet Nozzle Systems for Droplet Flow and Icing Applications	118
4. 1. 1	Long Distance Nozzle Systems	120
4. 1. 2	Short Distance Nozzle System (Atomizer)	122
4. 1. 3	Jet Flow System with Seed Particle Supplier (<i>JSPS</i>)	124
4. 2	<i>PIV</i> Method and Droplet Flow Measurements in the Water Tunnel	125
4. 2. 1	Preliminary Investigation	126
4. 2. 2	<i>PIV</i> Laser Based Method	128
4. 2. 3	Velocity Measurements of Droplet Trajectories	133
4. 3	Measurement Uncertainties	134
4. 4	Icing on a Helicopter Scoop in the Spray-Icing Tunnel	138

Chapter 5 RESULTS AND VALIDATIONS140-187

5. 1	Freestream Droplet Trajectories (Analytical)	143
5. 2	Near-Wall Droplet Deflection	145

5.3	External Dispersed Phase Flow (Numerical)	147
5.4	Cases of Two-Dimensional Ice Simulations	165
5.5	Experimental Results and Comparisons	180
Chapter 6	CONCLUSIONS AND RECOMMENDATIONS FOR FUTURE RESEARCH	188-192
6.1	Conclusions	188
6.2	Recommendations for Future Research	190
	LIST OF REFERENCES	193-206
	FIGURES AND TABLES	207-295
	APPENDIX	296-312

LIST OF FIGURES

Chapter 1

1. 2. 1:	Sample Ice Accretion on a Surface (Source – Internet: NASA Lewis Research Center, C99-193)	207
1. 2. 2:	Droplet Flow with Helicopter Icing	207

Chapter 2

2. 2. 1:	Schematic of Multiphase Averaging Control Volume	208
2. 4. 1:	Schematic of Near-Wall Droplet Momentum Displacements	

	(Similarity Analysis)	210
2. 5 .3:	Notation for Ice Tracking Algorithm	213
2. 5 .3 .1:	Linear and Non-linear distributions for Pfl	214
2. 5 .3 .2:	Linear and Non-linear distributions for $EBeta$	214
2. 5 .3 .3:	Sample Case of Evolving Ice Interface Based on Analytical Droplet Trajectories	215

Chapter 3

3. 1. 1:	Discretization of Finite Element and Control Volume	216
3. 3. 1. 1:	Construction of the Drag term in the Dispersed Phase Momentum Equation within a $CVFEM$ Control Volume	217
3. 6. 1:	General Solution Algorithm	218
3. 6. 2. 1:	Evolving Ice Interface with Accreted Ice at $t = 119.05 s$ (up) and $t = 500 s$ (down)	219
3. 6. 2. 2:	Droplet x - and y - Velocity Values in the Domain: Before the Ice Interface, at the Ice Interface and in the Region of Accreted Ice, $\beta_d = 1$ at $t = 500 s$	220
3. 6. 2. 3:	Central Part of Ice Redistribution Algorithm	221

Chapter 4

4. 1. 1. 1:	Long Distance Nozzle System with Zero Degree Pressure Washer Nozzles	222
4. 1. 1. 2:	Long Distance Nozzle System with Flare end Cap Nozzles	222
4. 1. 1. 3:	The Atomizer (Airfoil Frame-Left, Water Tubs and Air Tubs-Right)	223
4. 1. 1. 4:	The Atomizer with Droplet-Air Flow	223
4. 1. 1. 5:	The Freezing Nozzles of the Atomizer	223
4. 1. 1. 6:	A Network of Tubes of the New Atomizer	224
4. 1. 1. 7:	Dispersed Droplet Flow is Atomized by the Medium (Left) and the High (Right) Pressurized Air (Premixed Mist Flow in the Nozzle Mixing Chambers)	224
4. 1. 1. 8:	The Experimental Setup of Stream Flow (Up) with the Pulsed Laser (Down)	225
4. 1. 1. 9:	Laser Measurements of Velocity Field of Premixed Water with Seed Particles	226
4. 1. 1. 10:	Laser Measurements of Velocity Field of Dispersed Water (without Seed Particles)	226
4. 1. 1. 11:	Laser Measurements of Velocity Field of Dispersed Water Sprayed from the Outer Duct (no Seed Particles)	227

4. 2. 2. 1:	Estimation of Spatial Shifting – Image Displacement Function $s(u_1, u_2)$	227
4. 2. 2. 2:	<i>PIV</i> Cross – Correlation Technique within the <i>PIV</i> Evaluation Method	228
4. 2. 2. 3:	Loss of Correlation Signal Due to Absence of Particles in the Interrogation Area and Enlargement of Area (Accommodation of Phantom Particles)	229
4. 2. 3. 1:	Schematic of the <i>PIV</i> Laser Based Setup	230
4. 4. 1:	Rime Ice Buildup on the Helicopter Scoop (Case 1)	231
4. 4. 2:	Glaze Ice Buildup on the Helicopter Scoop (Case 2)	231

Chapter 5

5. 1. 1:	Schematic of the Injected Droplet Case	232
5. 1. 2:	Droplet Trajectories through an Air stream [$\vec{v}_a = (0.02, 0)$]; in the Low-Re Regime.....	232
5. 1. 3:	Effects of Varying Droplet Injection Velocity	233
5. 1. 4:	Effects of Varying Droplet Diameters on Droplet Trajectories	233
5. 1. 5:	Gravitational Field Effects on Droplet Trajectories	234

5. 1. 6:	Schematic of Evaporating Droplet Problem Involving Droplet Trajectory	234
5. 1. 7:	Droplet Trajectories with Droplet Diameter of $D = 5e-5 m$ and Varying Droplet Diameter $D(t)$ due to Evaporation of the Droplet (High-Re Regime)	235
5. 1. 8:	Droplet Trajectories with Temperature Dependent Thermophysical Properties and Droplet Diameter of $D = 5e-5 m$	235
5. 2. 1:	Scaling and Similarity Solution for Momentum Deflection Comparison	236
5. 2. 2:	Similarity Function, $F(\eta)$, Solution	236
5. 2. 3:	Droplet Trajectories at Different Ratios, $\frac{v_{xd}}{v_{xdy}}$, and Different x Locations	237
5. 2. 4:	Droplet Trajectories at Different x Locations for Different Ratios of $r = \frac{v_{xd}}{v_{xdy}}$	237
5. 2. 5:	Droplet Trajectories for Different Ratios, $r = \frac{v_{xd}}{v_{xdy}}$, across the Physical Domain	238
5. 2. 6:	Droplet Deflections Based on Similarity Solution and Blasius Solution	238

5. 3. 1:	Problem Schematic (Case 1)	239
5. 3. 2:	Control Volume Grids: 6×6 , 8×8 , 10×10 , 12×12 , 18×18 and 26×26 (Case1)	240
5. 3. 3:	Droplet Velocity Fields for $u_{d,IN} = 2.5 \text{ m/s}$ and Grids: 6×6 , 8×8 , 10×10 , 12×12 , 18×18 , 26×26 (Case 1)	241
5. 3. 4:	Droplet Velocity Fields for $u_{d,IN} = 7 \text{ m/s}$ and Grids: 6×6 , 8×8 , 10×10 , 12×12 , 18×18 , 26×26 (Case 2)	242
5. 3. 5:	Droplet Velocity Fields (Left) Influenced by the Air Field (Right) for Scaled Interfacial Drag of 0.001 (Up) and 0.005 (Down)	243
5. 3. 6:	Droplet Trajectories (12×12 mesh; Case 1)	244
5. 3. 7:	Droplet Trajectories (18×18 mesh; Case 1)	244
5. 3. 8:	Magnitude of Droplet Velocities ($t = 0.5 \text{ s}$; Case 1)	245
5. 3. 9:	Droplet Trajectories (12×12 mesh; Case 1)	245
5. 3. 10:	Grid Refinement Study (Case 1)	246
5. 3. 11:	Initial Condition Independence Study (Case 1, Case 2, Case 3)	246
5. 3. 12:	Numerical Error Distribution of Droplet Position as a Function of Grid Spacing, $\ln(\Delta x)$	248
5. 3. 13:	Problem Schematic (Case 2)	249
5. 3. 14:	Droplet Velocity Fields for $u_{d,IN} = 7 \text{ m/s}$ and Grids 12×12 , 16×16 , 20×20 and 24×24 (Case 2)	250
5. 3. 15:	Air Velocity Fields for $u_{d,IN} = 7 \text{ m/s}$ and Grids 12×12 , 16×16 , 20×20 and 24×24 (Case 2)	251
5. 3. 16:	Droplet Velocity Fields (Left) Influenced by the Air Field (Right) for	

	Interfacial Drag with $D_d = 0.00008\text{ m}$ (Up) and $D_d = 0.00030\text{ m}$ (Down) - (Case 2)	252
5. 3. 17:	Predicted Droplet and Air Velocities based on Interfacial Drag with Droplet Diameter D (Case 2)	253
5. 3. 18:	Predicted Droplet and Air Velocities based on Interfacial Drag with Droplet Diameter D (Case 2)	253
5. 3. 19:	Effects of Droplet Diameter on the Angle Difference Between the Inlet and Step of the Domain (Case 2)	254
5. 3. 20:	Effects of Droplet Diameter on the Angle Difference in the Vertical Position Along the Step of the Domain (Case 2)	254
5. 3. 21:	Grid Refinement Study (Case 2)	255
5. 3. 22:	Problem Schematic (Case 3)	255
5. 3. 23:	Grids of 12×12 , 27×27 , 48×48 and 75×75 (Case 3)	256
5. 3. 24:	Droplet Velocity Fields for $u_{d,IN} = 7\text{ m/s}$ and Grids 12×12 , 27×27 , 48×48 and 75×75 (Case 3)	257
5. 3. 25:	Air Velocity Fields for $u_{d,IN} = 7\text{ m/s}$ and Grids 12×12 , 27×27 , 48×48 and 75×75 (Case 3)	258
5. 3. 26:	Droplet Velocity Fields (Left) Influenced by the Air Field (Right) for Interfacial Drag with $D_d = 0.00008\text{ m}$ (Up) and $D_d = 0.00030\text{ m}$ (Down) - (Case 3)	259
5. 3. 27:	Mesh Refinement Study (Case 3)	260
5. 4. 1:	Boundary Conditions for Droplet Velocity (\vec{v}_d), Air Velocity (\vec{v}_a) and Droplet Volume Fraction (β_d) in Ice Interface Propagation	261
5. 4. 2:	Problem Schematic (Case 1)	262
5. 4. 3:	Spreading Ice with Evolving Ice Interface Position at Times: 417 s ,	

	<i>1042 s, 1667 s and 2292 s (Case 1)</i>	263
5. 4. 4:	The Numerical and Analytical Ice Interface Evolution at Times t [min]	264
5. 4. 5:	Error Distribution for Ice Interface Predictions (Numerical vs. Analytical) at Times t [min].....	264
5. 4. 6:	Ice Interface Numerical Propagation from the Wall Towards the Inlet at Times t [min]	265
5. 4. 7:	Ice Spreading with Ice Interface Evolution at Time Steps: <i>400 s, 600 s,</i> <i>900 s and 1200 s</i>	266
5. 4. 8:	Numerical and Analytical Ice Interface Evolutions at Times t [min]	267
5. 4. 9:	Error Distribution for Ice Interface Predictions (Numerical vs. Analytical) at Times t [min]	267
5. 4. 10:	Air Flow at the Evolving Ice Interface	268
5. 4. 11:	Schematic of the Frontward Step Domain	268
5. 4. 12:	Ice Spreading with Ice Interface Evolution at Time: <i>400 s, 600 s,</i> <i>900 s and 1200 s</i>	269
5. 4. 13:	Ice Spreading with Ice Interface Evolution at Time: <i>400 s, 600 s, 900 s</i> and <i>1200</i>	270
5. 4. 14:	Numerical vs. Analytical Results of Accreted Ice at Frontward Step at Time $t = 500 s$	271
5. 4. 15:	Ice Interface X-Positions at Various Y-Distances from the Bottom at the Frontward Step	272

5. 4. 16:	Numerical Errors at Various Y-Distances from the Bottom at the Frontward Step	272
5. 4. 17:	The Accreted Ice Mass and Error Distributions at the Frontward Step	274
5. 4. 18:	Numerical v. s. Analytical Results of Accreted Ice at Frontward Step at Time $t = 500 s$ (Case 3) – Viscous Terms are Excluded from the Droplet Flow Formulation	274
5. 4. 19:	Distribution of the Droplet Volume Fraction along the bottom of the Domain at the Frontward Step at Various Times (Case 3)	275
5. 4. 20:	Numerical Error Distribution of Accreted Ice Mass at Time $t = 500 s$ as a Function of Grid Spacing, $Ln(\Delta x)$	276
5. 4. 21:	Numerical Simulation of the Droplet (Left) and the Air Flows (Right) with the Scaled Interfacial Drag of 0.05 and the Evolving Ice Interface	277
5. 5. 1:	The Experimental Setup for Vertical Jet Flow (Case 1)	278
5. 5. 2:	Camera Image: Vertical Jet Flow (Case 1)	279
5. 5. 3:	Measured Velocities for Vertical Jet Flow (Case 1). Inlet Velocity Magnitude = $3.215 m/s$	279
5. 5. 4:	Jet Flow Trajectory (Case 2)	280
5. 5. 5:	Illuminated Particles in Flow (Case 2)	280
5. 5. 6:	Measured Droplet Velocities (Case 2), Inlet Velocity Magnitude = $4.251 m/s$	281
5. 5. 7:	Measured Droplet Streamlines (Case 2)	

.....	281
5. 5. 8: Jetl Flow Velocity Components (Case 2)	282
5. 5. 9: Error Distribution for Jet Flow Trajectory (Case 2)	282
5. 5. 10: Error Distributions along the Height of the Camera Interrogation Region for the Jet Flow (Case 2)	283
5. 5. 11: Error Distributions along the Camera Interrogation Region for the Jet Flow (Case 2)	283
5. 5. 12: Measured Droplet Velocities (Case 3). Inlet Velocity Magnitude = 2.092 m/s	284
5. 5. 13: Measured Vertical Velocity Component (Case 3)	284
5. 5. 14: Schematic of Dispersed Droplet Flow Case	285
5. 5. 15: <i>PIV</i> Laser Based Measurements of the Droplet Velocities (Case 3)	286
5. 5. 16: Illuminated Droplets (Case 3; Frame 1 - left and Frame 2 - right)	286
5. 5. 17: Measured Droplet Velocities (Case 4). Inlet Velocity Magnitude = 9.649 m/s	287
5. 5. 18: Droplet Velocity Components (Case 4)	288
5. 5. 19: Droplet Trajectory Components (Case 4)	288
5. 5. 20: Error Distribution for Droplet Trajectories (Case 4)	289
5. 5. 21: Error Distributions for Droplet Trajectories (Case 4)	289
5. 5. 22: Error Distributions along the Height of the Camera Interrogation Region.....	290
5. 5. 23: The Physical and Numerical Domain for Droplet Flow Impact on the Conductor	292

5. 5. 24: Predicted Ice Thickness Distribution, $dh = f(\theta)$, on the Conductor
(in the 1st and 2nd quadrants) at Time $t = 43200$ s.....293

5. 5. 25: Numerical and Experimental Results of the Droplet Volume Fraction
(β) and Maximum Ice Thickness (Δh_{max}) on the Conductor with a
Diameter of $D_c = 0.350$ m294

LIST OF TABLES

Chapter 2

2. 3. 1: Models of the Drag Coefficient209

2. 4. 1: The Parameters for the Scaling, Sensitivity, Order of Magnitude and
Similarity Analyses211

2. 4. 2: Characteristic Parameters in Order of Magnitude Analysis212

Chapter 5

5. 3. 1: Logarithms of Errors of x - and y -Velocity Distributions for Multiphase
Flow with Droplets, Respectively, as Functions of the Time Step Size,
 Δt 247
5. 4. 1: Numerical and Analytical Results of the Mass of the Ice Mass and
Error Based on the Droplet Phase Formulations with/without the
Viscous Terms (Case 3)273
5. 5. 1: Errors for Measured Droplet Velocities at Elevations y and Positions x
in the Camera View Region291
5. 5. 2: Comparison between Results of the Droplet Volume Fraction and the
Ice Thickness with Different Methods for the Conductor with a
Diameter of $D_c = 0.350\text{ m}$ 295

CHAPTER 1

INTRODUCTION

1. 1 BACKGROUND

Multiphase flows with droplets occur in many engineering and scientific problems. Technological examples include icing of aircraft surfaces and structures, spray deposition on surfaces, dispersed condensation on surfaces of heat exchangers, fuel combustion in engines and bio-mass decomposition processes. The other examples involving multiphase flows are convective and diffusive processes of blood movement in human lungs and diffusion in pharmaceutical drug production. Accurate

predictions of multiphase transport (such as droplets, air and ice at a solid surface) have considerable importance in various technological applications.

Modeling techniques for multiphase flows generally fall into two main categories, namely mixture modeling and separated phase modeling for dilute or dense flows. Separate phase modeling is considered in this thesis for both dispersed (i.e. droplet) and carrier (i.e. air) phases in contact. Various past numerical methods (i.e. Finite Difference, Control Volume and Finite Element) were developed within analytical frameworks, such as Eulerian, Lagrangian and their hybrids. Different grid approaches exist, such as fixed and adaptive mesh tracking. Certain advantages and disadvantages exist with each method, which are presented in section (1. 2) below. In this thesis, the dispersed phase momentum equations are modeled numerically within an Eulerian spatially-averaged formulation. A fixed grid approach is adopted in a newly developed Control-Volume Based Finite-Element Method (*CVFEM*) for the dispersed-flow and ice tracking.

Due to limited validation data in the literature, in-house equipment was developed for studying the physical mechanisms. Experimental results were used to validate the numerical simulator. The validation studies in this thesis consist of the following parts.

- Lagrangian analytical solutions were developed for flows involving droplet-air drag resistance in the presence and without the presence of a gravitational field. Special solutions near a flat plate entailed scaling, order of magnitude and similarity analyses, where cross-diffusion effects were studied in the presence of a streaming airflow.
- Experimental studies for droplet flow leading to icing were needed to assess the validity of the numerical results. As a part of the project, while considering the limited relevant measured data in the literature, new experimental equipment, designs and measurements were developed for droplet flow characterization. The goal was to obtain uniform quasi-3-D ice buildup on a helicopter scoop. Experimental studies for droplet flows and icing were conducted in both water and spray-icing tunnels. Droplet flow equipment was

developed to produce the dispersed droplet flows and jet flows under a variety of conditions. The experimental design entailed the *PIV* laser equipment, *CCD* High Sense Camera, and FlowManager software for measurements of flow characteristics, such as whole-field velocities and droplet diameters.

1. 2 PROBLEM DESCRIPTION

The Eulerian method is an efficient approach for tracking a dispersed-flow with co-existing phases. Rather than tracking each particle throughout the domain in a Lagrangian method, the Eulerian method uses dispersed group tracking of droplets within a fixed control volume. In this thesis, Eulerian spatial averaging is used in a *CVFEM*, thus allowing integral flux-based balances to be solved conservatively. Properties of a multiphase flow are spatially-averaged. This concept is adopted in this thesis because the dispersed-carrier phase interactions are assumed to be negligible at the micro-scale level. A dilute multiphase flow formulation is implemented. Unlike Lagrangian tracking of droplets, where the dispersed convective acceleration is not explicitly modeled, a main challenge of the *CVFEM* Eulerian based method is modeling of these convective terms (Chapter 3). This involves additional efforts in the *CVFEM* modeling of convective fluxes at an interface. This thesis develops a new convection model, which focuses on simplicity, robustness and conservative properties of the *CVFEM* in the fixed grid Eulerian tracking.

Based on the methods described in the previous paragraph, a dispersed-flow numerical formulation is developed within a Two-Fluid model. Additional posteriori assumptions are adopted (i.e. interfacial models and sizes of droplets) to close the formulation and the system of equations. The new numerical algorithms are validated analytically and experimentally. Numerical sensitivity studies involving grid and

initial condition independence are performed in different situations, involving different geometrical domains. One of the biggest challenges in numerical simulations exists when a droplet flow weakly interacts (small interfacial drag) with an air flow. The droplet flow behaves considerably different (as a group of bodies) than the air flow (continuum), especially near surfaces. The droplet phase satisfies different boundary conditions at the surfaces than the air stream. This phenomenon makes computations difficult and demanding. Moreover, if a relative drag resistance between phases is small, an influential gravity field appreciably deflects droplet flow from its inertial path and the air stream. These difficulties are addressed in this thesis.

A major problem in numerical ice simulation involves tracking of a spatially evolving ice interface. The multiphase governing equations cannot handle this problem without an additional algorithm. This tracking algorithm predicts the ice buildup in a direction towards the incoming dispersed-flow. Its special features require a variety of dispersed volume fraction distributions when considering various icing conditions at the time-advancing interface. In addition, the algorithm is problem dependent. Certain modeling information should be obtained from experiments.

In addition to theoretical and computational models, this thesis considers experimental studies. A set of nozzle systems, for rime ice applications in the spray – icing tunnel, represented the biggest challenge in these studies. In this thesis, a set of the dispersed droplet-air flow devices (nozzle systems) was developed. Additional preliminary investigations were needed to design the dispersed-flow and icing experiments. A *PIV* laser, *CCD* Cameras and accompanying FlowManager software 4.20.25 met certain requirements regarding the external dispersed-flow measurements. The details are described in Chapter 4. The related numerical results are validated in Chapter 5.

1. 3 LITERATURE REVIEW

In this section, a literature review is presented. The sub-sections are organized according to the methods used in the multiphase icing predictions.

1. 3. 1 ANALYTICAL MULTIPHASE FLOW TRACKING LEADING TO ICING

Multiphase flows with droplets contribute to in-flight icing of helicopter surfaces exposed to impinging droplets. These incoming droplets greatly affect the heat balance with phase change on the iced aircraft surface (Myers, Hammond, [1], 1999) and the other ground-based structures (Naterer [2, 3]). The local, instantaneous transport equations for each phase can be developed in an Eulerian framework [3]. In the majority of practical cases, averaged physical quantities are sufficient for design purposes. Rather than tracking individual trajectories of droplets, the Eulerian approach with volume averaging can significantly reduce computational time by applying conservation balances over fixed control volumes in space.

Previous studies have adopted averaging techniques for multiphase flows (Banerjee, [4, 5], 1980, Hetsroni, [6], 1982). Various types of procedures were documented: (i) time averaging, with no averaging in space, (ii) area or volume averaging, with no averaging in time, (iii) ensemble averaging, with no averaging in space or (iv) combinations of these procedures. Unlike the other two-phase flow

regimes where continuum assumptions may be adopted in both phases, the droplets present unique difficulties since their distribution within a fixed control volume is typically not continuous. In other words, droplets are discrete and not joined with each other to form a continuous phase. In this way, conventional definitions of properties, such as pressure, require special interpretation. These unique physical processes are documented in the thesis, as they arise in Eulerian modeling of multiphase flows.

In the averaging procedures, certain microscopic information is lost through the integration process, especially at the phase interface(s). These inaccuracies can be reduced by better modeling of the physical phenomena throughout the averaging procedure. Information lost through spatial averaging can be supplied back through the other relations (i.e. constitutive or macroscopic – microscopic relationships). Spatial averaging is most effective when integrated quantities do not change significantly over the selected control volume. As mentioned previously, for many cases, the averaged physical quantities are sufficient for design purposes.

Past derivations of the momentum equations for the dispersed phase of multiphase flow were carried out by means of volume averaging (Banerjee, Chan, [4, 5], 1980; Crowe, [7], 1998; Crowe, [8], 1999). These developments include the effects of turbulence, which can have an important role in the dynamics of the dispersed phase (Ainley, [9], 1997). These past formulations served as a basis for associated studies involving droplet impact and icing of helicopters (Milanez et al., [10]).

Most of the predictive models of droplet flows with aircraft icing and Computational Fluid Dynamics (*CFD*) are based on Lagrangian methods of tracking individual droplet trajectories throughout the flow field. An effective alternative, based on an Eulerian *CFD* program called *PHASES* (Naterer, [11], 1995) with entropy based enhancements (Naterer, [12], 1999; [13], 2000, [14], 2001) reduces the computational time by incorporating the droplet dynamics into a finite volume approach. In this approach (see also Tsuboi, Kimura [15]), the droplets are treated as a continuous medium within a discrete volume, with properties analogous to those of a continuous fluid. For instance, the bulk density is regarded as a continuous property.

This approach is based on a control volume that includes a sufficiently large amount of small droplets. The number of droplets in the control volume is assumed to be small enough (i.e. dilute flow) that momentum effects of collisions between droplets are negligible. Thus, the motion of the droplets is controlled by the droplet-fluid interactions, body forces and droplet-wall collisions. In comparison to a dilute flow, a dense flow is a flow in which particle-particle interactions are primarily responsible for the particle motion. For such flows, numerical modeling within a Lagrangian formulation is a good alternative.

In past studies, scaling, sensitivity, order of magnitude and similarity analyses were performed on the governing fluid momentum equations. Unlike conventional approaches to determine similarity parameters and solutions (Schlichting [16], Munson, et al. [17], Naterer [18]), this thesis considers such modeling in the context of the dispersed multiphase flow. Certain parts of the approach are developed based on the literature, i.e., Naterer [18], Oosthuizen, Naylor [19]. However, the new aspects of modeling in this thesis involve the detailed droplet motion near a flat surface.

In this thesis, fundamental issues regarding two-phase droplet-air motion in the vicinity of a flat surface are addressed and novel analytical droplet flow solutions are developed (Milanez et al., [20]). This analytical modeling is viewed to contribute to the physical understanding of droplet behavior in the vicinity of the surfaces. The similarity solution sheds light on fundamental flow behavior near the flat surface, as well as providing droplet trajectories that can be used for validation of numerical models. For example, an analytical solution for a momentum displacement is obtained in Chapter 2. The momentum displacement refers to the displacement of the droplet phase fluid element due to the change of momentum flux arising from interfacial drag forces. The droplet momentum solution and the Blasius boundary layer solution identify certain limits encompassing the expected droplet behaviour. By excluding the viscous diffusion terms from the droplet motion equations, a certain limiting solution can be obtained. This solution is based on outer interfacial drag forces only.

After performing the scaling and sensitivity analyses and establishing the droplet x -momentum equation, a similarity solution is derived. By introducing a stream function, the separable differential equations are solved, thereby establishing self similarity of the droplet motion. From this similarity solution, the droplet velocity profiles and trajectories are obtained. In the cross-stream direction, the droplet flow is mainly controlled by the drag forces. A non-differential drag force between the phases (droplet-air) is modeled through a drag factor, as outlined by Crowe and Sommerfeld [21]. The off-plane displacement of the droplet momentum is also considered in this investigation. Two-dimensionality of the flow is introduced through the droplet y -momentum equation and the droplet phase fraction equation.

Physical parameters selected in this thesis are based on typical conditions encountered during helicopter icing. For example, based on the range of droplet diameters and liquid water contents, as outlined by Bourgault et al. [22], it was assumed and verified that the effects of droplet interactions/collisions were not substantial. The relevant droplet y -velocity is determined based on the volume-averaged phase fraction equation. By inclusion of algebraic forces and a scaling analysis for the momentum equations, the final form of the x -momentum equation is obtained for a group of droplets. With the order of magnitude analysis, a similarity parameter is obtained. Then, the similarity equation is solved by a stream function approach. This differential equation is solved analytically, in order to find the algebraic solution for the similarity function. Droplet velocity profiles in the x and y directions are determined based on this solution of the similarity function. Numerical results are presented and compared against the scaling requirements in Chapter 5.

As described previously, past studies adopted Eulerian volume averaging techniques for various types of multiphase flows (i.e., Banerjee, Chan [4] and Hetsroni [6]). However, their extensions to multiphase flows with droplets often involve modeling approximations without a detailed documented basis of the volume averaging. One particular example of interest in this thesis is the averaged cross-phase pressure interactions in a Two-Fluid model. The cross-phase pressure interactions can have an important role in the dynamics of the dispersed phase [7]. The role of

pressure interactions in multiphase modeling and its physical significance were studied previously, i.e., Sha, Soo [23], Boure [24], Prosperetti, Jones [25], Marchioro, Tanksley, Prosperetti [26] and others.

Various aspects of the representation of the pressure force term (denoted by $P\nabla\beta$) in the phase momentum equations were documented in the literature. Ishii [27] cancels out this term via the interfacial source term when the bulk mean pressure is nearly equal to the interfacial mean pressure. Gidaspow and Solbring [28] pointed out limitations with this partial pressure model, as it can yield unrealistically high pressures. However, Soo [29] suggested that there is no need to drop the $P\nabla\beta$ term for purposes of solution stabilization. Gidaspow and Solbring [28] called this pressure term an “extra type diffusive force” and outlined that the pressure in this expression is not simply the thermodynamic pressure. Jackson et al. [30] and Medlin et al. [31] called the term an “effective force without giving an exact value”. Wallis (Gidaspow [32]) suggested that $P\nabla\beta$ might be dropped for the case of stratified flow, but not in suspensions. Furthermore, Sha and Soo [23] described a significance of the $P\nabla\beta$ term for adiabatic compression of a gas bubble, involving nearly zero velocities of both phases (liquid and gas). Their analysis entailed the kinetic energy and continuity equations with thermodynamic relations for a perfect gas.

A form of the phasic momentum equations for the two-phase flow is discussed by Boure [24]. Volume-averaged phase momentum equations were used and a treatment of the bulk pressure term was shown. However, the pressure deviations at the phase interface were not fully documented. Prosperetti and Jones [25] investigated the volume-averaged dispersed and continuous pressure forces in detail. Although the pressure forces in the continuous phase affect the dispersed phase motion, the pressure within the dispersed phase does not appreciably contribute to the continuous phase motion under certain conditions. This thesis addresses these modeling issues involving the dispersed phase pressure field.

Marchioro, Tanksley and Prosperetti [26] used ensemble averaging to model a mixtures' pressure and viscous stresses in a dispersed two-phase flow. A pressure

force was modeled from the bulk mixture total stress for all phases in contact. Nigmatulin [33] used mixture modeling to address such pressure forces. Park, Drew and Lahey [34] used an ensemble averaging technique for the pressure term in the two-fluid multiphase model. The difference between the averaged pressure in the bulk flow and the interfacial pressure was not fully documented. In addition, the assumptions for inviscid and irrotational flows were made. Joseph and Lundgren [35] used ensemble averaging to derive the relevant transport equations, while the pressure field was assumed to be uniform.

Turbulent fluctuations in single phase flows, represented by single phase Reynolds stresses, appear as a result of the fluctuating velocity field. These Reynolds stresses can be modeled by a Boussinesq gradient assumption. This assumption relates velocity fluctuations to the mean momentum velocities [36]. In multiphase modeling, averaging techniques can be used to describe filtered physical fields, free of deviations [8]. These deviations represent information lost in the averaging procedure. For turbulent flows, the deviating velocity field can be modeled through the multiphase Reynolds stresses. Modeling of these stresses is more complicated than modeling of single phase Reynolds stresses ([8], [9], [34], [37]). For a dilute dispersed-flow, a Boussinesq assumption can be used to relate the deviating velocity to an averaged velocity field.

Both interfacial and volume-averaged pressure forces contribute to the motion of phases in contact. The pressure field in the dispersed phase may affect the continuous phase, particularly if the dispersed phase is moved suddenly from one region to another region that has different bulk pressure. Past studies considered pressure effects at the interface between dispersed and continuous phases. Unlike those previous studies (i.e., Prosperetti, Jones [25]), the interfacial pressure drag and apparent mass force per unit volume are modeled in a more detailed manner in this thesis. For example, a pressure term in the momentum equations, $P\nabla\beta$, is reformulated, while shedding new light on the significance of the interfacial pressure drag and apparent mass force terms.

The newly modeled terms in this thesis, such as interfacial pressure drag and apparent mass, are applied to a droplet/air two-fluid model. This approach (Milanez et al., [38]) differs from previous formulations (i.e., Prosperetti, Jones [25]), where the interfacial pressure drag force per unit volume and apparent mass force per unit volume are assumed to coincide. In this thesis, the terms are grouped under one interfacial surface integral, thereby avoiding certain modeling difficulties associated with the term $P\nabla\beta$ in the momentum equations. After they are grouped with the shear interfacial and shear wall terms, all terms are further modeled by an algebraic term. Pressure deviations at the phase interface are considered, as well as the role of pressure terms in the energy equation [39].

1. 3. 2 NUMERICAL ALGORITHM FOR DISPERSED MULTIPHASE FLOW AND ICING PREDICITONS

Numerous past studies considered numerical modeling of multiphase flows with droplets, including volume-averaged trajectories of impinging droplets in aircraft icing. The studies involved fluid transport in both dispersed and continuous phases (i.e. [4], [22] and [39]). In multiphase flow problems, close similarities arise between dispersed droplets and suspended particles. For example, solid fuel combustion systems, such as pressurized fluidized bed combustors and suspension-fired coal boilers, entail particulate two-phase flow mixtures. A hybrid Eulerian – Lagrangian model was developed by Naik and Bryden [40] for the numerical analysis of dilute particulates, transported through a high curvature duct of a gas turbine combustor. Mixtures with small particle diameters exhibited low inter-phase slip velocities and

low impact probability with the pipe walls. However, higher slip velocities and impact probabilities were observed at particle diameters exceeding 50 microns. In contrast to Lagrangian tracking of particles, this thesis develops a new unified Eulerian formulation for both dispersed and carrier phases.

Commercial codes, such as Fluent-Fidap [41] and CFX-Tascflow [42], generally entail Lagrangian-type methods for dispersed phase tracking. An exact Riemann solver and Gudunov fluxes can be adopted for both carrier and dispersed phases of multiphase flows (Thevand et al., [43]). In Lagrangian methods, the governing equations of motion for each particle are solved in a moving coordinate system for the dispersed phase. Numerical integration of each particle momentum equation along its pathline yields a solution of the particle velocity field (Valentine, Decker [44]). Each particle or group of particles is tracked spatially throughout the computational domain. The method may predict cross-phase interactions more accurately than Eulerian formulations, generally at the expense of significantly higher *CPU* run-time and storage requirements.

For droplet flows in icing applications, the typical *CPU* run-time and storage requirements of conventional droplet tracking (Lagrangian methods) become much higher, due to adaptive re-meshing within each time step to accommodate the moving ice interface. Fixed grid methods offer useful advantages over adaptive re-meshing methods, particularly when predicting flow induced forces on surfaces exhibiting time-varying ice shapes (Naterer, [45]). In contrast to conventional Lagrangian methods, spatial averaging of droplet tracking is generally less time-consuming, since it avoids re-meshing or coordinate transformations at each time step. In addition, Eulerian methods readily accommodate the error indicators from conventional fixed grid solvers, such as Taylor series methods or entropy weighted residuals [46].

This thesis develops a new Eulerian formulation of dispersed phase motion within a *CVFEM* for multiphase flows. The dispersed phase equations are developed separately from the continuous phase system of equations. In the *CVFEM*, a discrete control volume represents a fluid element over which the transported fluxes are balanced. Since each control volume balance is discretized locally within a finite

element, the dispersed-flow equations become independent of the grid configuration, thereby allowing full geometric flexibility in the overall formulation.

In an Eulerian formulation, transport equations of an individual phase become analogous to multi-fluid transport equations. A pressure correction equation was developed by Darwish et al. [47] for multi-fluid flows, based on a mass conservation based algorithm (*MCBA*). The method is tested at various Mach numbers and fluid density ratios. Studies of the single grid (*SG*), prolongation grid (*PG*) and full multi-grid (*FMG*) methods were conducted. For single grids, sub-element quadrature affects both spatial accuracy and transient wave propagation [48]. The convergence history and *CPU* run-time of the *FMG* method are more efficient than the *PG* method, while accelerating the convergence rate over the single grid method [47]. Since this thesis entails a fixed grid formulation of multiphase flows, it is anticipated that similar benefits of the *FMG* methods could be achieved with droplet motion.

Another significant issue addressed in this thesis involves convective droplet transport. For example, icing of helicopter surfaces involves convective exchange between incoming droplets and the co-flowing air stream. Convection of dispersed droplets in multiphase flows depends on various factors, including interfacial drag and droplet breakup [6]. Joseph et al. [49] used a rotating drum camera to investigate the breakup of viscous and viscoelastic droplets in a high speed airstream. Fragmentation of droplets is observed at varying viscosities and Weber numbers. Transition to droplet clouds and vapor occurred in less than 50 micro-seconds. Flattened droplets and Rayleigh/Taylor instabilities arose due to large accelerations from gas to liquid phases. Such studies have significance in various applications involving droplet impingement, including supercooled droplets in icing applications.

In addition to Eulerian and Lagrangian methods, past studies developed hybrid techniques for numerical modeling multiphase convection [50 – 54]. Numerical instabilities may arise when finite elements, generated automatically to follow particle streamlines in a Lagrangian method, become distorted. Examples of alternative hybrid methods include DNS [51, 52, 55], Reynolds-averaged [53] and LES based models [56]. Despite these advances, the methods have certain limitations. For example,

sudden changes of the dispersed phase volume fraction at the interface may lead to false fluctuations of the continuous phase velocity, particularly with refined grids, boundary layer flows and complex geometrical configurations. Convection modeling with a hybrid difference scheme for moving droplet simulations was reported by Huang and Ayyaswamy [57]. Droplet velocities, radii, mass and heating rates were predicted for n-heptane droplets at intermediate Reynolds numbers. In addition, total drag, frictional drag, pressure drag and evaporation drag were evaluated. Each droplet trajectory and terminal velocity was evaluated from a balance of drag and body forces. In contrast, this thesis includes gravitational effects on convective acceleration, when predicting the droplet trajectories.

A Two-Fluid formulation with separate equations of state and volume fraction correlations has been developed for both dense and dilute multiphase convection [58]. Convection modeling with the *AUSM* (Advection Upwinding Splitting Method) and *AUSM* with flux differences (*AUSMD*) were developed. Contact discontinuities and interfaces between phases were accurately modeled by using these convective upwinding formulations.

Ritz and Caltagirone [59] predicted multiphase convection of particles in a dilute suspension. The trajectories of settling particles were initially off-centered between two parallel walls. By assuming pseudo-rigid behavior of the solid particles, only the velocity and pressure remain unknown in the momentum equations. Unlike their staggered finite volume and projection formulations, this thesis develops a collocated convection formulation with both velocity and pressure fields, solved at the nodal points. This approach is viewed to potentially simplify coding, improve solution convergence and robustness and reduce *CPU* run-time, in comparison to Ref. [59].

Past convection models with volume averaging successfully characterized two-fluid systems of gas-particle flows, ranging from dense to dilute flows (Masson, Baliga, [60]). Particle/particle collisions can be predicted with kinetic theory of dense gases. Unlike volume averaging, Direct Numerical Simulations (*DNS*) provides much greater detail regarding the inter-phase mechanisms. *DNS* studies by Marchioli et al. [56] predicted the deposition of inertial particles in vertical upward pipe flows at a

Reynolds number of 337. Interfacial drag, lift and gravitational effects were included in the equations of motion for particles. The particles were assumed to have no influence on the carrier phase (note: same assumption adopted in this thesis). Particle distributions within the boundary layer, particle/wall interactions and deposition of particles were predicted successfully by Marchioli et al. [56].

Boundary conditions lead to additional unique challenges for prediction of multiphase flow patterns. The droplets impinge on the boundary, while the carrier phase is deflected away from the wall. Tsuboi [61] used transparent boundary conditions on the surfaces. During the impact of droplets, the dispersed phase is no longer followed by the carrier phase. This thesis investigates the droplet flow behavior in the airflow near the boundary, involving the transparent boundary conditions for the droplet phase and the no-slip conditions for the airflow. These simultaneous conditions are expected to provide realistic estimates of droplet impact in icing applications. The droplet capture and ice buildup depend on both processes.

Relative motion between phases affects this near-wall impact of droplets. Unlike past modeling of inter-phase relative motion (Morency et al., [62]), in this thesis, a novel separate model for the dispersed phase is developed. A supplementary existing mixture model for the carrier phase is added to the dispersed-phase model. Relative motion between the phases can be especially important during in-flight aircraft icing in clouds, where the supercooled moisture is immersed in the carrier fluid. Phase change of supercooled droplets may arise through varying thermophysical conditions in the carrier phase, thereby affecting the relative motion as droplets impact on the aircraft surface. This thesis develops new modeling of near-wall interactions and relative motion between the phases (Milanez et al. [63]).

In addition to this relative motion, gravity affects the other aspects of the droplet dynamics. For example, it affects droplet impact on an ice surface. Additionally, it affects liquid droplets emitted from a spray combustor, particularly involving the amplitude and self-induced oscillations of the resulting flame structure (Levy, Bulzan, [64]). Gravitational effects on droplets lead to different rates of heat

transfer, evaporation and mass flow in the two-phase fluid. The interface between the fuel nozzle and flame was observed to be largely dependent on gravitational forces. In this thesis, gravitational effects are studied with respect to deflected inertial motion of droplets in a co-flowing airstream.

Gravitational effects on droplet entrainment and stratification in two-phase pipe flows were reported by Williams et al. [65]. Entrainment increases at higher gas velocities, but it does not appear to vary with different pipe diameters. Gravitational settling enhances deposition of droplets at lower gas velocities in vertical pipes. Under certain conditions, quasi-steady creeping flows occur with gravitational settling and coalescence of droplets (Rushton, Davies, [66]). In contrast to these past studies, this thesis considers transient gravitational deflection in a dilute flow, without constrained boundaries of an internal pipe.

Gravitational deflection of droplets affects the impact location of droplets on the surface (Milanez et al. [67]). Hung and Yao [68] investigated impinging droplets on isothermal cylindrical objects. Droplet sizes varied between 110 and 680 microns. Incoming droplet velocities affect the disintegration, dripping and gravity-induced detachment of droplets from the surface. The gravitational effects change at varying Stokes numbers. Additional effects of the Stokes number were reported by Barton [69] for a multiphase flow, with particles, past a backward facing step. Injected particles at low Stokes numbers were shown to raise inlet inertia and strength of the re-circulation cell behind the step. Gravitational effects became dominant at high Stokes numbers. Furthermore, it was shown that differences between multiphase and single-phase flows increased linearly with void fraction. This thesis considers a similar geometry of a front facing half-cylinder step, but with Eulerian volume averaging of droplet motion (unlike Lagrangian droplet tracking). It is shown that volume averaging successfully predicts gravitational effects on deflected groups of droplets in a co-flowing airstream.

In addition to gravity, complex cross-phase interactions arose at the interfacial boundaries, including interfacial drag forces and pressure gradients (Hetsroni, 1982).

This thesis establishes a new iterative algorithm for linking these complex interfacial transport mechanisms of multiphase flow. Impinging droplets on a surface are deflected by near-wall pressure gradients in the carrier phase, gravity and the other interfacial effects. Wang et al. [70] investigated impinging droplets of water, ethanol and water/ethanol mixtures on hot surfaces. Spray breakup and the effectiveness of heat removed from the hot surface due to impinging droplets were reported. Papageorgakis and Assanis [71] included interfacial drag and surface tension forces, when predicting spray breakup under low injection pressures. Internal circulation within moving droplets was investigated by Ayyaswamy et al. [72]. The strength of the internal vortex was observed to have minor impact as a modeling parameter. In dilute multiphase flows with droplets, interactions between droplets are neglected. This thesis considers the interfacial drag forces, particularly their effects on deflected droplet motion near an ice surface.

Frictional drag arises at the interfacial boundaries, due to a relative Reynolds number between dispersed and carrier phases. A numerical formulation called *FENSAP-ICE* [73] applied reduced forms of interfacial drag in both low and high Reynolds number regimes, for the simultaneous prediction of dispersed and carrier phase motion. In contrast, this thesis develops a composite drag model, which simultaneously encompasses a wider range of relative Reynolds numbers, including the transition regime. Unlike past studies [73], sub-element modeling incorporates full elliptical pressure and viscous diffusion effects in the dispersed phase.

For aircraft de-icing, impinging droplets affect the shape and rate of ice growth (Poots, [74]). Latent heat is released and kinetic energy is imparted by incoming droplets (Messinger, [75]). In glaze ice conditions, a flowing supercooled surface film interacts with the impinging droplets during phase change [18]. Past studies outlined the significance of near-wall deflection of droplets on varying collection efficiencies of iced surfaces (Bragg, [76]). Polat et al. [77] investigated a water droplet with surface active agents, in order to enhance the particle and droplet capture efficiency by reducing surface tension. The collection efficiency refers to the ratio of impinging droplet mass flux on the surface, to the mass flux that would occur

on the surface if droplets were not deflected by the airstream. In this thesis, the role of cross-phase interactions in this droplet deflection is investigated.

1. 3. 3 EXPERIMENTAL ASSESSMENT OF DROPLET MOTION AND ICING

In addition to the past numerical methods, described in the previous section, past advances have developed experimental methods of characterizing droplet dynamics in multiphase flows. The *PDS* (Planar Droplet Sizing) is an example of a technique for characterizing droplet diameters in multiphase flows. In the *PDS*, the intensity emitted by a fluorescent dye added to a liquid is proportional to the volume of resulting atomized droplets. Taking the ratio of this intensity with the scattered light intensity yields the *SMD* (Sauter Mean Diameter) of droplets. Past developments [78] predicted the effects of the scattering angle, refractive index, droplet size and dye concentration on the *PDS* method. Unlike dense sprays considered by Domann and Hardalupas [78], this thesis focuses specifically on the dispersed phase of dilute multiphase flows.

Phase Doppler Interferometry, phase-doppler analyzers and Phase Doppler Anemometry are useful techniques for characterizing droplet sizes and velocity distributions in multiphase flows. Jazayeri and Li [79] investigated the spatial distribution of sprays with Phase Doppler Anemometry, including the breakup of liquid sheets in a co-flowing air stream. At the center-line, the authors reported that the mean velocity of droplets reached a maximum value, while the Sauter mean

diameter was a minimum. In the transverse direction, a self-similar distribution of droplet mean velocity was observed. Spatial effects of droplet entrainment, migration, secondary atomization and droplet coalescence at downstream locations affect the momentum exchange between dispersed and carrier phases. In contrast to these liquid sheet breakup mechanisms, this thesis focuses on uniformly dispersed droplets throughout a dilute flow field.

Both deterministic and stochastic aspects of droplet flows in sprays were investigated by Kim et al. [80]. The deterministic portion included unstable wave motion. The breakup length, mean diameter and droplet distributions of the unstable growth at various wavelengths were investigated. In the stochastic approach, a maximum entropy principle was used for the final stage of droplet formation after the liquid bulk breakup. Both deterministic and stochastic parts can be combined through source terms containing liquid/gas interactions.

In aircraft icing applications, droplet collection affects the accreted ice mass and shape [3]. Aerodynamic characteristics are largely dependent on this ice shape, including the drag and lift forces. Such aerodynamic characteristics were measured by a force balance and surface pressure taps connected to an ESP (Electronically Scanned Pressure) system by Lee, Dunn and co-workers [81]. Side windows for laser droplet measurements were utilized by Chintamani and Belter [82]. Impinging droplets on the ice surface affected the ice thickness and transition between rime ice and glaze ice. An ultrasonic pulse-echo technique to measure the ice thickness was reported by Hansmann and Kirby [83]. A transducer was mounted flush with the surface (below the ice), and it emitted a brief compression wave. After the pulse traveled through the ice and was reflected by the external ice surface, it returned to the transducer as an echo signal. Then the resulting ice thickness was calculated, based on the time elapsed and the speed of sound in ice.

In addition to aircraft icing problems, a droplet flow characterization is important in numerous other practical applications. For example, applications include cooling of high temperature surfaces with water/air sprays [84] and spray systems for

fire suppression [85]. Cooling of high temperature surfaces by incoming droplets was studied by using thermocouple data gathered below the surface of a test piece [86]. An experimental study of the flux of droplets delivered from a spray system was performed for controlling and suppressing fires [87]. A *PIV* system (Particle Image Velocimetry) was used to measure the droplet velocities and water densities leaving the sprinkler. It was observed that larger droplets traveled further horizontally from the sprinkler than smaller droplets, since the momentum of larger droplets was proportionally larger than the drag force.

In this thesis, new insight regarding momentum exchange and interfacial drag forces on droplets is provided with data collected from the *PIV* [88, 89, 90]. The *PIV* is a non-intrusive technique, since probes or wires are not directly placed into the flow field [91]. Unlike the other methods of anemometry, where velocity measurements are obtained at a single point, the *PIV* technique permits whole-field measurements of velocity. Past studies mainly applied *PIV* techniques to continuous, single-phase flows [92]. However, in this thesis, applications of the method to dispersed (droplet) phase motion are studied, particularly for applications related to aircraft icing problems.

1. 4 SCOPE OF THESIS

The main goals of this thesis include new physical understanding of multiphase flow and icing processes, as well as development of a numerical formulation and code for dispersed-flow tracking with icing. Validation cases for multiphase droplet motion and ice accretion are developed for the purpose of comparisons with numerical results.

This thesis develops an Eulerian formulation of multiple phases in contact, i.e., the dispersed (droplet), continuous (air), moving wall (ice) and stationary wall (solid

wall). Deeper understanding of interfacial pressure disturbances is gained by modeling of dispersed phase pressures in the governing equations of motion, as they arise from both dispersed and continuous phases. Two-dimensional dispersed-flow and icing numerical algorithms are developed with a Control-Volume Based Finite Element Method (*CVFEM*). Convection, bulk and interfacial diffusion and gravity effects are studied in detail. Furthermore, modeling of boundary conditions at the moving and stationary walls is presented for each phase. Sensitivity analyses for grid and initial condition independence are carried out for a variety of geometrical configurations. Analytical Lagrangian solutions for liquid flows are developed. Scaling, Order of Magnitude and Similarity analyses and solutions are developed for droplet flow characterization in the airstream near a flat plate.

In addition, experimental studies are performed in this thesis. Liquid spray and jet nozzle systems are developed. Experiments with *PIV* (Particle Image Velocimetry) for laser based velocity measurements of spray and stream flows are designed. Comparisons with numerical / analytical results are presented. Icing on a representative helicopter scoop in the newly developed spray-icing tunnel is investigated. Predicted results from the ice tracking models are presented and compared with analytical and experimental data, including Goodwin's law.

1. 5 OUTLINE OF THESIS

This thesis consists of parts involving contributions and validations in modeling of multiphase dispersed/continuous flow with icing. In this introductory text, specific insight regarding individual and connected parts is given. The connected parts are related to the main focus of the thesis (numerical algorithm), as they present its building blocks, sensitivity and validation studies. Analytical, numerical and

experimental methods are constitutive parts of the thesis, where additional contributions are achieved. Both multiphase flow and icing studies are connected with these methods. Analytical (Lagrangian), numerical (Eulerian) and experimental (Eulerian) contributions have been made in dispersed flow and icing modeling. This involves the framework, formulations and analytical solutions. In addition, contributions have been achieved in the experimental multiphase studies, including new devices, designs and results for jet and spray flows. Limited icing experimental work was performed in the spray-icing tunnel (mainly a helicopter scoop). Experimental validation of icing predictions was performed through past measured data from the literature.

In addition, individual contributions to the modeling of multiphase flows are obtained. This includes new analytical modeling, such as dispersed phase pressure modeling, scaling and order of magnitude analyses with a similarity method and solution along a flat plate. These parts are embodied in the text, mainly in the analytical sections.

Chapter (1) equips the reader with necessary background information on the multiphase research work in this thesis. This chapter also emphasizes the important methods involved and their results, as well as comparisons between the results from different methods.

Chapter (2) entails new analytical methods and techniques as they relate to multiphase flow with droplets and icing. It develops the fundamental governing equations for liquid and gas (i.e., droplet / air) motion in an Eulerian framework with spatial averaging. In this process, the role of the bulk and interfacial dispersed phase pressure is investigated in formation of the droplet momentum equations.

The interfacial drag models are studied in section (2. 3) for subsequent derivation of analytical solutions for multiphase droplet/particle motion in section (2. 5).

development of the dispersed phase numerical algorithm.

Section (2. 4) investigates the importance of the physical processes of multiphase flow with air assisted droplets near a flat plate. Scaling, order of magnitude and similarity analyses are used. An order of magnitude method enables derivation of a similarity

variable, which are used in the similarity analysis. It is discovered that the multiphase similarity solution of the droplet flow exists [section (2. 5. 1)]. A closed form exact solution is derived analytically. This section is independent of the numerical algorithms. Section (2. 5. 2) presents investigation of Lagrangian droplet/particle-gas tracking. Closed form exact multiphase analytical solutions for the velocity and trajectory profiles are developed for low- Re_T (i.e. with linear drag model) and high- Re_T (i.e. with quadratic drag model) regimes. Solutions with linear and quadratic drag models and zero gravity, $\bar{g} = \bar{0}$, are used for sensitivity studies of droplet planar motion. Analytical solutions [Eqs. (2. 5. 2. 16) – ((2. 5. 2. 18))] for droplet motion with quadratic drag and $\bar{g} \neq \bar{0}$ are used for validation of the numerical dispersed phase algorithm in a vertical plane. For example, comparisons of the analytical (Lagrangian), numerical (Eulerian) and experimental (*PIV*-Eulerian) velocity profiles for the jet and spray-droplet flows are performed [i.e. Figs. (5. 5. 8) - (5. 5. 9) and Fig. (5. 5. 18) – (5. 5. 22), respectively]. Analytical results [Eq. (2. 5. 2. 25) – (2. 5. 2. 27)] for vertical jet flow [Figs. (5. 5. 1) – (5. 5. 3)] are compared with the numerical and experimental results. Standard analytical solutions for droplet / particle motion with negligible drag [Eqs. (2. 5. 2. 14) – (2. 5. 2. 15)] are compared with the numerical results in section (5. 3) [Figs. (5. 3. 6) – (5. 3. 9)].

Section (2. 5. 3) describes an analytical formulation of the novel numerical ice interface tracking method. It focuses on the backward numerical tracking of the evolving ice towards the incoming flow. This section proposes the pre-conditioning and excess ice re-distribution functions, as they control the ice tracking. In addition, novel analytical solutions for two-dimensional ice tracking are developed for the purposes of validation of the icing part of the numerical algorithm [i.e. equation in Fig. (5. 4. 14)].

Chapter (3) entails description of the *CVFEM* numerical formulation of the multiphase flow with droplets and icing [sections (3. 1) – (3. 5)]. The implementation and architecture of the novel numerical dispersed and icing algorithms into the original Phases program is presented and discussed in sections (3. 6. 1) and (3. 6. 2),

respectively. Section (3. 6. 2) describes additional details of the icing algorithm in the effort to track evolving ice interface with deposited ice behind in the backward direction toward the incoming droplet flow. Droplet flow correction function and excess ice re-distribution functions are discussed. Numerical formulation of the continuous phase is described in sections (3. 6. 3), particularly as it relates to the dispersed phase algorithm with icing and original Phases.

Chapter (4) presents experimental studies of droplet motion and ice accretion in the water and spray-icing tunnels, as well as development of nozzle systems for studies of droplet motion. Long and short distance nozzle systems were developed for droplet (spray) flows. A special nozzle system was developed for the jet flow. The *PIV* laser based Eulerian method with its hardware [i.e. Gemini laser, CCD cameras) and software [FlowManager (2. 2. 25)] was evaluated for its suitability for velocity measurements of jet and particularly dispersed droplet flows. The methods for droplet characterization and the uncertainty method were presented.

Chapter (5) presents results from analytical, numerical and experimental modeling of droplet/air flow motion [Figs. (5. 1. 1) - (5. 3. 27) and Figs. (5. 5. 1) - (5. 5. 22)] and ice tracking [Figs. (5. 4. 1) - (5. 4. 19) and Figs. (5. 5. 23) - (5. 5. 25)]. This chapter involves numerical simulations of multiphase flow with droplets and icing with different computational domains (i. e. vertical and horizontal surfaces, frontward steps with different shapes) and grid discretizations, different boundary conditions, *CPU* time consumptions, etc. The developed analytical solutions and results are used in sensitivity studies and validations of the numerical algorithms, as presented in description of Chapter (2). Validation of the numerical multiphase flow algorithm additionally includes the grid independency studies [Fig. (5. 3. 10), Fig. (5. 3. 21) and Fig. (5. 3. 27)] and the initial condition independency study [Fig. (5. 3. 11)]. Also, the accuracy of the dispersed and icing numerical algorithm is assessed [i.e. Fig. (5. 3. 12) and Fig. (5. 4. 18)].

Section (5. 4) is devoted to temporal one- and two-dimensional numerical simulations with icing algorithm and its validation. Validation of uni-dimensional icing simulations with vertical droplets falling on the horizontal surface is performed [Case

(1) - Figs. (5. 4. 2) - (5. 4. 5)]. Validation of quasi two-dimensional ice growth, caused by horizontally injected two-dimensional droplet flow, impacting on the vertical surface, is presented in Case (2) - Figs. (5. 4. 6) - (5. 4. 10). Simulations of impinging droplets on the evolving ice interface at the frontward step are studied (moving two-dimensional boundary) in Figs. (5. 4. 11) – (5. 4. 18). Presented simulations are validated against the two-dimensional analytical solution at time 500 s [Fig. (5. 4. 14)].

Additional icing experimental validation is presented in section (5. 5). Section (5.5) consists of results from the experimental and analytical studies of droplet / air motion and icing, including laser based *PIV* measurements with the nozzle systems. It compares analytical, numerical and experimental solutions of droplet flow (with drag and gravity terms) and icing (conductor). In jet (vertical and horizontally injected) and droplet flow cases, the results from all methods are compared [i.e. Fig. (5. 5. 8) - (5. 5. 9), Figs. (5. 5. 18) – (5. 5. 21)]. Uncertainty analyses are presented for the jet and spray droplet flows based on the results from experimental *PIV* method. Figures (5. 5. 24) - (5. 5. 25) present additional results from icing studies. The predicted shape of the accreted ice on the conductor, along with the equivalent ice thickness around the conductor, is presented in Fig. (5. 5. 24). The equivalent ice thickness is calculated from the numerically predicted ice shape. Its value is verified through past experimental data from Dr. Popplewell and Goodwin's model [Fig. (5. 5. 24)]. Goodwin's law presents an experimentally validated analytical approximation for ice thickness on the conductor.

Chapter (6) entails the conclusions and recommendations for future research. The suggestions are mainly given to the numerical and experimental parts of the thesis.

CHAPTER 2

MODELING OF MULTIPHASE MOTION WITH DROPLETS AND ICING

2. 1 GOVERNING EQUATIONS

Tracking of droplets throughout a flow field is essential for accurately predicting droplet impingement on iced surfaces (i.e. helicopter scoop). In this chapter, the dispersed (i.e. droplet) and carrier (i.e. air) phases are modeled based on a Two-Fluid formulation. This model describes each phase as a continuous fluid. In this

Chapter 2-MODELING OF MULTIPHASE MOTION WITH DROPLET FLOW AND ICING

section, differential forms of the multiphase conservation laws are presented. An Eulerian approach is used develop and solve the multiphase governing equations with droplets. In this way, a fixed grid can be used and tracking of individual particles is not required (in contrast to a Lagrangian approach). The multiphase/multicomponent governing equations for dispersed and continuous phases are presented first. Constitutive laws for the dispersed and continuous phases are presented and discussed. In the next section, the spatial averaging technique and spatial averaging of governing equations for dispersed flow are presented within the Eulerian framework.

For purposes of aircraft icing applications, the following assumptions in multiphase flow modeling are introduced: (i) incompressible flow; (ii) Two-Fluid model; (iii) disperse phase with droplets is assumed as dilute with droplet volume fraction $\beta_d = 10^{-6}$ in scaling, order of magnitude and similarity analyses. Non-dilute assumption is used in the numerical simulations. Excluding an initial droplet volume fraction of $\beta_d = 0$ in the computational domain, the droplet volume fraction in the simulations was in a range of $\beta_{d,IN} = 0.0001 \leq \beta_d \leq \beta_{d-ice} = 1$; (iv) there is no exchange of phases at the interfaces (i.e. negligible convective or diffusive exchanges of mass and energy), except interfacial exchange between the droplet flow and air flow (drag); (v) droplets in the control volume do not exhibit single body effects; (vi) droplets are spherical and are uniformly distributed within a CV (discrete or differential); (vii) the carrier / continuous phase (air) and droplet velocities are generally different, due to several reasons (such as high velocity gradients in the carrier phase, turbulent fluctuations and/or droplet body forces); (viii) the gravity force acts on droplets in the y -direction; (ix) due to the large density difference between the dispersed and continuous phases, the 'virtual-mass' effect is neglected (note: this effect represents an effective force that is required to accelerate the mass of the surrounding continuous phase, in the immediate vicinity of the dispersed phase when the relative velocity of the phases changes); (x) Coriolis, wall lubrication force, Basset, Magnus, Saffman, Coulomb and London forces are assumed to have negligible effects on the droplet trajectories [see Appendix (1)].

Chapter 2-MODELING OF MULTIPHASE MOTION WITH DROPLET FLOW AND ICING

In this section, general multiphase/multicomponent conservation equations for the transported quantity are presented in a form, independent of an averaging technique (i.e. area averaging, volume averaging and time averaging). An arbitrary fraction quantity, α , is introduced into the equations. Constitutive relations are presented and discussed. In section (2. 2), a spatial averaging technique and spatial averaging of phase/component governing equations is presented. Volume phase fraction β_k for phase k is introduced. A derived phase volume fraction equation is presented. After additional modeling for interfacial pressure within spatial averaging and modeling of interfacial shear drag for droplet flow, the spatially averaged conservation equations for the droplet momentum are developed for icing applications. The spatially averaged terms are denoted with a symbol $\langle \rangle$.

The dispersed phase transport is governed by the following conservation equations for mass, momentum and species distribution:

$$\frac{\partial}{\partial t}(\rho_d) + \frac{\partial}{\partial x_j}(\rho_d v_{d,j}) = 0 \quad (2. 1. 1)$$

$$\begin{aligned} & \frac{\partial}{\partial t}(\alpha_d \rho_d v_{d,i}) + \frac{\partial}{\partial x_j}(\alpha_d \rho_d v_{d,i} v_{d,j}) \\ & = -\frac{\partial}{\partial x_i} \alpha_d (p_d) + \frac{\partial}{\partial x_j} \alpha_d (\tau_{d,ij}) + \alpha_d \rho_d g_i + \alpha_d \rho_d f_i \end{aligned} \quad (2. 1. 2)$$

$$\frac{\partial}{\partial t}(\alpha_d \rho_d) + \frac{\partial}{\partial x_j}(\alpha_d \rho_d v_{d,j}) = -\dot{m}_{d,i} \quad (2. 1. 3)$$

Equations (2. 1. 2) - (2. 1. 3) are averaged. The last term in Eq. (2. 1. 2) represents momentum exchange, similar to Eq. (2. 1. 3), except that it has the opposite sign. In the absence of droplet evaporation, coalescence or collisions, this term becomes negligible. Scalar quantity α_k represents an arbitrary fraction for phase k (d -dispersed or c -continuous), related to the particular method of averaging.

Chapter 2-MODELING OF MULTIPHASE MOTION WITH DROPLET FLOW AND ICING

Once both momentum and mass equations for the dispersed phase are solved, the amount of droplet influx onto a helicopter ice surface can be obtained. This influx is the mass of droplets impinging into control volumes located along the ice surface. Additional modeling of the governing equations for the dispersed-droplet phase is described in the next section. The dispersed motion is developed in the Eulerian framework with spatial averaging and corresponding droplet modeling of interfacial pressure and shear forces.

Each component in the representative control volume has constitutive properties of the viscous phase. These are described by the stress-deformation relationships acting on the infinitesimal phase element. The normal stresses acting on the infinitesimal control volume can be described in the Cartesian coordinate system. For a dispersed phase (denoted by subscript 'd'), it yields

$$\tau_{d,xx} = 2\alpha_d \eta_{d,\tau}(\alpha_d) \frac{\partial v_{d,x}}{\partial x} + \left(\frac{\partial v_{d,x}}{\partial x} + \frac{\partial v_{d,y}}{\partial x} + \frac{\partial v_{d,z}}{\partial x} \right) \left[\left(-\frac{2}{3}\alpha_d \eta_{d,\tau}(\alpha_d) + \alpha_d \eta_{d,p}(\alpha_d) \right) \right] \quad (2.1.4)$$

$$\tau_{d,yy} = 2\alpha_d \eta_{d,\tau}(\alpha_d) \frac{\partial v_{d,y}}{\partial y} + \left(\frac{\partial v_{d,x}}{\partial x} + \frac{\partial v_{d,y}}{\partial x} + \frac{\partial v_{d,z}}{\partial x} \right) \left[\left(-\frac{2}{3}\alpha_d \eta_{d,\tau}(\alpha_d) + \alpha_d \eta_{d,p}(\alpha_d) \right) \right] \quad (2.1.5)$$

$$\tau_{d,zz} = 2\alpha_d \eta_{d,\tau}(\alpha_d) \frac{\partial v_{d,z}}{\partial z} + \left(\frac{\partial v_{d,x}}{\partial x} + \frac{\partial v_{d,y}}{\partial x} + \frac{\partial v_{d,z}}{\partial x} \right) \left[\left(-\frac{2}{3}\alpha_d \eta_{d,\tau}(\alpha_d) + \alpha_d \eta_{d,p}(\alpha_d) \right) \right] \quad (2.1.6)$$

The shear stresses on the element of the component are expressed by the following relations:

$$\tau_{d,xy} = \tau_{d,yx} \quad , \quad \tau_{d,xy} = \alpha_d \eta_{d,\tau}(\alpha_d) \left(\frac{\partial v_{d,x}}{\partial y} + \frac{\partial v_{d,y}}{\partial x} \right) \quad (2.1.7)$$

$$\tau_{d,yz} = \tau_{d,zy} \quad , \quad \tau_{d,yz} = \alpha_d \eta_{d,\tau}(\alpha_d) \left(\frac{\partial v_{d,y}}{\partial z} + \frac{\partial v_{d,z}}{\partial y} \right) \quad (2.1.8)$$

$$\tau_{d,zx} = \tau_{d,xz} \quad , \quad \tau_{d,zx} = \alpha_d \eta_{d,\tau}(\alpha_d) \left(\frac{\partial v_{d,z}}{\partial x} + \frac{\partial v_{d,x}}{\partial z} \right) \quad (2.1.9)$$

Chapter 2-MODELING OF MULTIPHASE MOTION WITH DROPLET FLOW AND ICING

The $\eta_{d,p}$ and $\eta_{d,\tau}$ represent normal and tangential multiphase viscosities of the dispersed component, respectively. In the regions where the volume fraction of the phase does not change appreciably across the cross section of the control volume, the viscosities are assumed to be constant. The multiphase viscosities of a component could be modeled for dilute and (combined)/or (separate) dense regimes for a phase of multiphase flow. If the dispersed phase fraction α_d represents the dispersed phase volume fraction and it does not change considerably across the cross-section of the control volume, the viscosities are assumed to be constant. If that volume fraction is small, the viscosities of the discontinuous fluid should be considered in the constitutive model. Discussion regarding the application of the relations in the incompressible multiphase flow transport equations with droplets and case simulations in the thesis is presented after next two paragraphs.

The carrier phase motion is governed by conservations of mass, momentum and species distribution (phase volume fraction) transport equations as follows:

$$\frac{\partial}{\partial t}(\rho_c) + \frac{\partial}{\partial x_j}(\rho_c v_{c,j}) = 0 \quad (2.1.10)$$

$$\begin{aligned} & \frac{\partial}{\partial t}(\alpha_c \rho_c v_{c,i}) + \frac{\partial}{\partial x_j}(\alpha_c \rho_c v_{c,i} v_{c,j}) \\ & = - \frac{\partial}{\partial x_i} \alpha_c (p_c) + \frac{\partial}{\partial x_j} \alpha_c (\tau_{c,ij}) + \alpha_c \rho_c g_i - \alpha_c \rho_c f_i \end{aligned} \quad (2.1.11)$$

$$\frac{\partial}{\partial t}(\alpha_c \rho_c) + \frac{\partial}{\partial x_j}(\alpha_c \rho_c v_{c,j}) = \dot{m}_{c,i} \quad (2.1.12)$$

The last term in Eq. (2.1.12) represents an interfacial species exchange. The inter-phase mass transfer arises due to mass transfer of the droplet phase across the phase interface. It leads to a momentum change, and therefore a corresponding term appears in the momentum equation, Eq. (2.1.11). In the absence of droplet mass, momentum or energy exchange (i.e. coalescence and collisions), this term becomes negligible.

In the thesis, the super/sub-cooled water droplets with the temperature ranging from $-40^{\circ}C \leq t \leq 0^{\circ}C$ were assumed in the simulations. The data for single and multiphase transport properties of water at $t < 0^{\circ}C$ was not available. A determination of the physical properties of the water at super/sub-cooled conditions represents a challenging endeavor. An overview of considerations regarding the transport properties as they pertain to modeling of the multiphase flow with super/sub-cooled droplets and icing in the thesis is presented below.

With its constitutive relations, a general system of governing equations for a phase entails viscous terms. The equations are used in different forms throughout the thesis, pertaining to the application study. For example:

- (i) in the sections with the similarity solution and the associated scaling and order of magnitude analyses only, the dispersed-droplet flow is assumed dilute. A volume fraction of $\beta_d = 10^{-6}$ with micro droplets is used. The viscous terms of the multiphase flow with the droplets in this study are negligible.
- (ii) In other simulations in the thesis, such as numerical, the multiphase dispersed phase flow with the droplets is assumed non-dilute. In the governing equations of the models, there is no additional modeling of interaction effects between the droplets and there is no additional modeling of interaction effects between the droplets and other phases in contact (i.e. air, moving ice interface and wall), except the interfacial droplet/air momentum exchange (drag).

In the numerical simulations, such as in icing computations an inlet volume fraction $\beta_d = 10^{-4}$ of ejected supercooled droplets into the domain is used. A physical picture considers supercooled droplets impacting on various surfaces (i.e. straight and curved walls and ice interfaces) as discrete physical bodies. The droplet volume fraction increases during the icing process due to an increasing number of supercooled droplets in a group of droplets within the control volume. In quick phase change upon

Chapter 2-MODELING OF MULTIPHASE MOTION WITH DROPLET FLOW AND ICING

increases during the icing process due to an increasing number of supercooled droplets in a group of droplets within the control volume. In quick phase change upon impact on the surface, all supercooled water from the impinging droplets fills the control volume and freeze. In the control volume, occupied by the ice, there is no space left for another phase (i.e. the carrier-air phase is not trapped within the ice). The mass and volume of the freezing supercooled water is assumed the same as the mass and volume of the ice, respectively. The temperature of the freezing water does not change during the phase change.

In spite of the lack of data for the physical properties for multiphase dispersed flow with supercooled droplets, a model of non-dilute multiphase flow with supercooled droplets is considered with the complete viscous terms, involving a single phase dynamic viscosity of the water at $t = 0^{\circ}C$. This is the lowest temperature where the data for water viscosity is available. The assumption of the single phase water viscosity is adopted in order to replace the multiphase flow viscosity of supercooled water droplets for icing processes. A single phase viscosity (i.e. dynamic) of the water non-linearly increases as temperature decreases towards $t = 0^{\circ}C$. It could be anticipated that viscosity of the supercooled water would further increase with decreasing temperature below $0^{\circ}C$. Similarly to single phase dynamic viscosity, the multiphase dynamic viscosity of the water may increase with decreasing temperature, such as below $0^{\circ}C$. Since the droplet flow in the numerical computations is dispersed with $\beta_d < 1$, the multiphase water droplet viscosity is expected to be smaller than the single phase viscosity of water (i.e. at the same, such as sub-cooled conditions). In the icing simulations, there exists a challenging question whether the multiphase viscosity of supercooled flowing and freezing water droplets (i.e. at $-40^{\circ}C$) becomes comparable with or exceeds (i.e. in some stages of icing within the control volume) single phase viscosity of water at $0^{\circ}C$ (at higher temperature).

A point of using viscous terms in the multiphase flow governing equations with droplets is additionally addressed through the case study of the most complete 2D icing example (icing at the frontward step with the 2D flow, 2D wall-step and 2D

viscosity or without the viscous terms in the equations of the multiphase flow with droplets is revealed in section (5. 4) – see also Figs. (5. 4. 18) – (5. 4. 21) and Table (5. 4. 1). The numerical results with the viscous terms seem to be in better agreement with the analytical predictions than the results without the viscous terms.

For the purposes of micro understanding, modeling and coding of the physical properties of water at temperatures below $0^{\circ}C$ into the numerical formulation, detail studies with supported literature are needed. Such studies, which focus on interactions of the flowing and freezing water droplets at supercooled conditions are beyond the scope of the thesis. This involves modeling of the multiphase physical properties (i.e. normal and shear viscosities and pressure) due to translation and collisions of the droplets as a function of the droplet volume fraction and temperature (i.e. different stages of icing). Such modeling may further entail detail description of collisions between the droplets (restitution coefficients of collisions between the droplets, distribution of collisions, etc). Associated studies of possible deformation of the impacting droplets with various surfaces could be additionally conducted for more detail description of the multiphase flow transport equations with droplets.

2. 2 METHOD OF EULERIAN SPATIAL AVERAGING IN MULTIPHASE TRANSPORT

A Eulerian description of fluid motion is adopted for purposes of numerical tracking a group of droplets in icing applications. Details regarding droplet tracking from a numerical modeling perspective are given in Chapter (3). The governing equations of multiphase flow and heat transfer may be obtained by performing

conservation balances over individual phases within a multiphase averaging control volume [see Fig. (2. 2. 1)]. In this section, the general transport equation is spatially averaged, based on the Leibnitz and Gauss theorems for both phases in Cartesian coordinates.

(i) General Scalar Transport Equation

The general transport equation for phase k is

$$\frac{\partial(\rho_k \psi_k)}{\partial t} + \bar{\nabla} \cdot (\rho_k \psi_k \bar{v}_k + \bar{j}_k) - \rho_k \hat{S}_k = 0. \quad (2. 2. 1)$$

Using the Leibnitz and Gauss theorems, respectively, the following relations for each phase are

$$\int_{V_k} \frac{\partial \rho_k \psi_k}{\partial t} dV = \frac{\partial}{\partial t} \int_{V_k} \rho_k \psi_k dV - \int_{a_i} \rho_k \psi_k (\bar{v}_i \cdot \bar{n}_k) dS \quad (2. 2. 2)$$

$$\begin{aligned} & \int_{V_k} \bar{\nabla} \cdot (\rho_k \psi_k \bar{v}_k + \bar{j}_k) dV \\ &= \frac{\partial}{\partial x} \int_{V_k} \bar{n}_x \cdot (\rho_k \psi_k \bar{v}_k + \bar{j}_k) dV + \frac{\partial}{\partial y} \int_{V_k} \bar{n}_y \cdot (\rho_k \psi_k \bar{v}_k + \bar{j}_k) dV + \int_{a_i + a_{k,w}} \bar{n}_k \cdot (\rho_k \psi_k \bar{v}_k + \bar{j}_k) dS, \end{aligned} \quad (2. 2. 3)$$

where the subscript k indicates a specific phase (i.e., droplet or air). The variables $\rho_k \psi_k$, \bar{j}_k and \hat{S}_k refer to the conserved quantity in the k -th phase, the flux of ψ_k and the source of ψ_k . The V_k represents the instant geometric volume of phase k inside the finite multiphase control volume V , fixed in space [see Fig. (2. 2. 1)]. The sum of phase volumes $\sum_k^N V_k$ is equal to V , where N represents the number of phases in V .

Integrating Eq. (2. 2. 1) over the volume of phase k , V_k , and substituting Eqs. (2. 2. 2) and (2. 2. 3) into Eq. (2. 2. 1) yields the following integral equation for the conserved quantity, $\rho_k \psi_k$:

Chapter 2-MODELING OF MULTIPHASE MOTION WITH DROPLET FLOW AND ICING

$$\begin{aligned}
 & \frac{\partial}{\partial t} \int_{V_k} \rho_k \psi_k dV + \frac{\partial}{\partial x} \int_{V_k} \bar{n}_x \cdot (\rho_k \psi_k \bar{v}_k + \bar{j}_k) dV \\
 & + \frac{\partial}{\partial y} \int_{V_k} \bar{n}_y \cdot (\rho_k \psi_k \bar{v}_k + \bar{j}_k) dV - \int_{V_k} \rho_k \hat{S}_k dV \\
 & = \int_{a_i} \rho_k \psi_k (\bar{v}_i \cdot \bar{n}_k - \bar{n}_k \cdot \bar{v}_k) dS - \int_{a_i + a_{kw}} (\bar{n}_k \cdot \bar{j}_k + \bar{n}_{k,w} \cdot \bar{j}_k) dS.
 \end{aligned} \tag{2.2.4}$$

Equation Eq. (2.2.4) outlines the transport processes at the interfacial and wall surfaces. In the first term on the right side, the cross-phase mass transfer can be recognized as:

$$-\dot{m}_k = \rho_k \bar{n}_k (\bar{v}_k - \bar{v}_i). \tag{2.2.5}$$

The spatially averaged scalar equation for the conserved quantity becomes

$$\begin{aligned}
 & \frac{\partial}{\partial t} \beta_k \langle \rho_k \psi_k \rangle + \frac{\partial}{\partial x} \beta_k \langle \bar{n}_x \cdot (\rho_k \psi_k \bar{v}_k + \bar{j}_k) \rangle + \frac{\partial}{\partial y} \beta_k \langle \bar{n}_y \cdot (\rho_k \psi_k \bar{v}_k + \bar{j}_k) \rangle - \beta_k \langle \rho_k \hat{S}_k \rangle \\
 & = -\frac{1}{V} \int_{a_i} (\dot{m}_k \psi_k + \bar{j}_k \cdot \bar{n}_k) dS - \frac{1}{V} \int_{a_{kw}} \bar{n}_{k,w} \cdot \bar{j}_k dS,
 \end{aligned} \tag{2.2.6}$$

where spatial averages of the integrals of a conserved function, i.e., $b_k = \rho_k \psi_k$, are defined as follows,

$$\langle b_k \rangle = \frac{1}{V_k} \int_{V_k} b_k dV, \quad \langle b_k \rangle_i = \frac{1}{V} \int_{a_i} b_k dS. \tag{2.2.7}$$

The parameter $\beta_k = V_k / V$ denotes the phase volume fraction. The sum of phase volume fractions of each phase in the representative control volume is $\sum_k \beta_k = 1$.

(ii) Phase Fraction (Mass) Equation

Substituting $\psi_k := 1$, $\bar{j}_k := \bar{0}$ and $\hat{S}_k := 0$ in Eq. (2. 2. 4), the integral equation for the conserved quantity, ρ_k , becomes

$$\begin{aligned} \frac{\partial}{\partial t} \int_{V_k} \rho_k dV - \int_{a_i} \rho_k (\bar{v}_i \cdot \bar{n}_k) dS + \frac{\partial}{\partial x} \int_{V_k} \bar{n}_x \cdot (\rho_k \bar{v}_k) dV + \frac{\partial}{\partial y} \int_{V_k} \bar{n}_y \cdot (\rho_k \bar{v}_k) dV \\ + \int_{a_i} \bar{n}_k \cdot (\rho_k \bar{v}_k) dS = 0. \end{aligned} \quad (2. 2. 8)$$

The interfacial term can be expressed as

$$\int_{a_i} [\rho_k (\bar{v}_i \cdot \bar{n}_k) - \bar{n}_k \cdot (\rho_k \bar{v}_k)] dS = - \int_{a_i} [\rho_k \bar{n}_k \cdot (\bar{v}_k - \bar{v}_i)] dS = - \int_{a_i} \dot{m}_k dS. \quad (2. 2. 9)$$

Applying the dot products with the unit normal vectors and spatial averaging, Eq. (2. 2. 8) becomes

$$\frac{\partial}{\partial t} (\beta_d \langle \rho_k \rangle) + \frac{\partial}{\partial x} (\beta_d \langle \rho_k v_{k,x} \rangle) + \frac{\partial}{\partial y} (\beta_d \langle \rho_k v_{k,y} \rangle) = - \langle \dot{m}_k \rangle_i. \quad (2. 2. 10)$$

The term on the right side of Eq. (2. 2. 10) represents the inter-phase mass transfer due to mass transfer of the droplet phase across the phase interface. It leads to a momentum change, and therefore a corresponding term appears in the momentum equation. In the absence of droplet evaporation, coalescence or collisions, this term becomes negligible.

(iii) Momentum Equations with Pressure Treatment

The droplet momentum equations can be determined after setting $\psi_k := \bar{v}_k$, $\bar{j}_k := p_k \bar{I} - \bar{\tau}_k$ and $\hat{S}_k := \bar{F}_k$ in Eq. (2. 2. 6). After inserting these relations and taking the dot product with \bar{n}_x , and then with \bar{n}_y , two separate momentum equations in the x [Eq. (2. 2. 20), Eq. (2. 2. 22)] and y [Eq. (2. 2. 23)] directions are obtained.

Chapter 2-MODELING OF MULTIPHASE MOTION WITH DROPLET FLOW AND ICING

Their derivation procedure and final form, with respect to the one-dimensional multiphase equations commonly found in the literature, can be readily extended to three-dimensions by including analogous terms in the z -direction.

For the sake of brevity, the brackets $\langle \rangle$ for spatial averaging and the symbol for the phase volume fraction, β_k , are temporarily dropped in the upcoming discussion. At the end of the averaging procedure, these brackets are included again. For each direction, the linear momentum equation is obtained through the following steps:

- (I) perform the vector operations with the normal vector;
- (II) insert the quantities of interest in the equation, such as $\psi_k := \bar{v}_k$, $\bar{j}_k := p_k \bar{I} - \bar{\tau}_k$ and $\hat{S}_k := \bar{F}_k$;
- (III) multiply all terms from the resulting equation by the normal vector (\bar{n}_x or \bar{n}_y), depending on the direction of interest.

Spatial averaging of the following four terms in Eq. (2. 2. 6) is outlined as follows: (i) second term, (ii) third term, (iii) fifth term and (iv) sixth term (discussed below for the x -momentum equation). In the momentum equations for the droplet flow, it should be noted that many possible forces can be exerted on the droplets, i.e. Coriolis, wall lubrication force, Basset, Magnus, Saffman, Coulomb and London forces. These forces can be modeled in the algebraic source terms of the formulation described later.

(i) Second Term

The second term is simplified as follows:

$$\bar{n}_x (\rho_k \psi_k \bar{v}_k) = \rho_k \psi_k v_{k,x} \quad (2. 2. 11)$$

$$\rho_k (\bar{n}_x \bar{v}_k) v_{kx} = \rho_k v_{k,x} v_{k,x}. \quad (2. 2. 12)$$

For turbulent flows, the velocity component includes both a mean component and a fluctuating component, denoted as δv . As a result,

$$\rho_k (\bar{n}_x \bar{v}_k) v_{kx} = \rho_k (v_{k,x} v_{k,x} + \delta v_{k,x} \delta v_{k,x}). \quad (2. 2. 13)$$

Performing a similar vector operation as presented in Appendix (3), Eq. (A. 3. 8), except that multiplication is here with \bar{n}_x [and not with \bar{n}_y as in Eq. (A. 3. 8)], yields the following result.

$$\bar{n}_x (p_k - \tau_{k,xx}, -\tau_{k,xy}, -\tau_{k,xz}) = p_k - \tau_{k,xx}. \quad (2.2.14)$$

As a result, the second term becomes

$$\begin{aligned} \bar{n}_x \frac{\partial}{\partial x} \bar{n}_x (\rho_k \Psi_k \bar{v}_k + \bar{j}_k) &:= \\ \frac{\partial}{\partial x} [\rho_k (v_{k,x} v_{k,x} + \delta v_{k,x} \delta v_{k,x}) + p_k - \tau_{k,xx}] &. \end{aligned} \quad (2.2.15)$$

(ii) Third Term

$$\bar{n}_y (\rho_k \Psi_k \bar{v}_k) = \rho_k \Psi_k v_{k,y} \quad (2.2.16)$$

$$\rho_k (\bar{n}_x \bar{v}_k) v_{k,y} = \rho_k v_{k,x} v_{k,y}. \quad (2.2.17)$$

Including the turbulent fluctuating component of velocity, δv , in the convection term, and multiplying all terms,

$$\rho_k (\bar{n}_x \bar{v}_k) v_{k,y} = \rho_k (v_{k,x} v_{k,y} + \delta v_{k,x} \delta v_{k,y}) \quad (2.2.18)$$

$$\bar{n}_x (-\tau_{k,yx}, p_k - \tau_{k,yy}, -\tau_{k,yz}) = -\tau_{k,yx}. \quad (2.2.19)$$

As a result, the third term becomes

$$\begin{aligned} \bar{n}_x \left[\frac{\partial}{\partial y} \bar{n}_y (\rho_k \Psi_k \bar{v}_k + \bar{j}_k) \right] &:= \\ \frac{\partial}{\partial y} [\rho_k (v_{k,x} v_{k,y} + \delta v_{k,x} \delta v_{k,y}) - \tau_{k,yx}] &. \end{aligned} \quad (2.2.20)$$

(iii) Fifth Term

$$-\frac{1}{V} \int_{a_i} (\dot{m}_k \psi_k + \bar{j}_k \bar{n}_k) dS :=$$

$$-\frac{1}{V} \int_{a_i} [\dot{m}_k \bar{v}_k + \bar{n}_k (p_k \bar{I} - \bar{\tau}_k)] dS. \quad (2.2.21)$$

Multiplying each term by \bar{n}_x yields

$$\dot{m}_k (\bar{n}_x \bar{v}_k) = \dot{m}_k (\bar{v}_{k,x}) \quad (2.2.22)$$

$$-\int_{a_i} \bar{n}_k (\bar{n}_x p_k) dS = -[\langle p_k \rangle + \Delta p_{ki}] \frac{\partial \beta_k}{\partial x} + \frac{1}{V} \int_{a_i} \bar{n}_k (\bar{n}_x \Delta p'_{ki}) dS. \quad (2.2.23)$$

The extension to include the turbulent fluctuating component of pressure is introduced in order to better account for the pressure effects at the interfacial surface. The term $\Delta p_{ki} = \langle p_{ki} \rangle - \langle p_k \rangle$ accounts for the difference between the average interfacial and average phase pressures. The term $\Delta p'_{ki} = p_k - \langle p_{ki} \rangle$ accounts for the difference between the local and average interfacial pressure.

Assembling the fifth term in the momentum equation yields

$$-\frac{1}{V} \int_{a_i} \bar{n}_x [\dot{m}_k \bar{v}_k + \bar{n}_k (p_k \bar{I} - \bar{\tau}_k)] dS = -\langle \dot{m}_k v_{k,x} \rangle_i$$

$$-[\langle p_k \rangle + \Delta p_{k,i}] \frac{\partial \beta_k}{\partial x} - \langle \Delta p'_{k,i} \rangle_i + \langle \bar{n}_k \bar{\tau}_{kx} \rangle_i. \quad (2.2.24)$$

(iv) Sixth Term

$$-\frac{1}{V} \int_{a_{kw}} \bar{n}_{kw} \bar{j}_k dS := -\frac{1}{V} \int_{a_{kw}} \bar{n}_{kw} (p_k \bar{I} - \bar{\tau}_k) dS \quad (2.2.25)$$

$$\bar{n}_{k,w} \bar{n}_x p_k = 0 \quad (2.2.26)$$

$$-\frac{1}{V} \int_{a_{kw}} \bar{n}_x (\bar{n}_{k,w} \bar{\tau}_{kx}) dS = \langle \bar{n}_{k,w} \bar{\tau}_{kx} \rangle_w. \quad (2.2.27)$$

A similar procedure can be performed for the y -direction momentum equation [see Appendix (3)].

The hydrodynamic forces, such as drag forces (i.e., Stokes, Faxen and Basset), apparent mass force and lift forces (i.e., Magnus and Saffman) [23] are interfacial pressure and interfacial shear forces appearing through the inter-phase terms in the momentum equations, not externally acting or explicitly included forces. These terms represent interfacial interactions between the phases in contact (including wall surfaces). These terms are active terms in the momentum equations for the particular phase. When these forces are evaluated for a specific situation and incorporated into the momentum equations, they can be grouped together with externally acting and explicitly added body volumetric forces (i.e., Coriolis, Coulomb and London) into the source term on the right-hand side of the momentum equations. This can be useful for purposes of numerical modeling. The Basset and apparent mass forces are unsteady interfacial forces. The local difference between phase velocities is not constant, as it changes with time. As a result, the local acceleration changes the interfacial momentum of the dispersed phase.

Both steady-state and unsteady interfacial forces may influence the droplet motion. Unsteady interfacial forces can be introduced on the left-hand side of the momentum equations for the dispersed phase, while the remaining interfacial forces can be grouped with the externally applied body forces in the source term on the right-hand side of the momentum equations. This can provide useful linearization for a numerical formulation, and it allows the equations to be discretized and written in terms of a single active variable, so that standard algebraic solvers can be used. In steady-state motion of the dispersed phase, all interfacial forces can be grouped with externally applied body forces. These forces can then be modeled as a source term.

The velocity field is decomposed into a spatially averaged component, denoted by $\langle v \rangle$, and a deviating component, denoted as δv . In turbulent flow modeling, the deviating velocity component, δv , is related to the spatially averaged velocity $\langle v \rangle$ through the Boussinesq gradient assumption. Then, the second (convective) term in Eq. (2. 2. 6) becomes

$$\vec{n}_x \frac{\partial}{\partial x} \langle \vec{n}_x (\rho_k \Psi_k \vec{v}_k + \vec{j}_k) \rangle := \frac{\partial}{\partial x} \left[\rho_k (\langle v_{k,x} \rangle \langle v_{k,x} \rangle + \langle \delta v_{k,x} \delta v_{k,x} \rangle) + \langle p_k - \tau_{k,xx} \rangle \right]. \quad (2. 2. 28)$$

The pressure part of the fifth term in Eq. (2. 2. 6) is

$$-\frac{1}{V} \int_{a_i} (\dot{m}_k \Psi_k + \vec{j}_k \vec{n}_k) dS := -\frac{1}{V} \int_{a_i} \left[\dot{m}_k \vec{v}_k + \vec{n}_k (p_k \vec{I} - \vec{\tau}_k) \right] dS. \quad (2. 2. 29)$$

Spatial averaging of these terms was not fully documented in past literature, partly due to the difficulties encountered when averaging is performed over a dispersed (rather than a continuous) phase. Rigorous modeling of these terms can shed new light on interactions between the carrier (air) and dispersed (droplet) phases.

Modeling of the fifth term in Eq. (2. 2. 6) outlines the importance of pressure mechanisms at the phase interface. Taking the dot product of the pressure part in the fifth term of Eq. (2. 2. 6) with \vec{n}_x yields the following result:

$$-\frac{1}{V} \int_{a_i} \vec{n}_k (\vec{n}_x p_k) dS = (\langle p_k \rangle + \Delta p_{k,i}) \frac{\partial \beta_k}{\partial x} - \frac{1}{V} \int_{a_i} \vec{n}_k (\vec{n}_x \Delta p'_{k,i}) dS. \quad (2. 2. 30)$$

An assembly procedure of the pressure parts in Eq. (2. 2. 30) is needed. The pressure under the integral on the left-hand side of Eq. (2. 2. 30) is modeled as $p_k = \langle p_k \rangle + \Delta p_{k,i} + \Delta p'_{k,i}$ in order to fully account for the pressure effects at the interface between phases in contact. The term $\Delta p_{k,i} = \langle p_{k,i} \rangle - \langle p_k \rangle$ accounts for the difference between the spatial averaged interfacial and spatial averaged phase pressures. The term $\Delta p'_{k,i} = p_k - \langle p_{k,i} \rangle$ accounts for the difference between the local

and spatially averaged interfacial pressures. These pressure terms can be further modeled and accommodated in the momentum equations, but that modeling is beyond the scope of this thesis. The difference $\Delta p'_{ki}$ represents an additional integral term on the right side of the momentum equation, Eq. (2. 2. 30). In this thesis, the term $\Delta p'_{ki}$ is not modeled and it is left uncombined with other terms in the final momentum equations.

After the remaining parts, such as $\langle p_k \rangle$ and $\Delta p_{k,i}$ under the integral on the left side of Eq. (2. 2. 30) are rearranged, the following expression is obtained,

$$\begin{aligned} \frac{1}{V} \int_{a_i} \bar{n}_k [\bar{n}_x (\langle p_k \rangle + \Delta p_{k,i})] dS &= \frac{1}{V} \int_{V_k} \bar{\nabla} \cdot [\bar{n}_x (\langle p_k \rangle + \Delta p_{k,i})] dV \\ &- \frac{1}{V} \frac{\partial}{\partial x} \int_{V_k} \bar{n}_x [\bar{n}_x (\langle p_k \rangle + \Delta p_{k,i})] dV - \\ &\frac{1}{V} \frac{\partial}{\partial y} \int_{V_k} \bar{n}_y [\bar{n}_x (\langle p_k \rangle + \Delta p_{k,i})] dV. \end{aligned} \quad (2. 2. 31)$$

Performing the necessary vector operations yields the following expression for the interfacial pressure on the right-hand side of the x – momentum equation,

$$\begin{aligned} - \frac{1}{V} \int_{a_i} \bar{n}_k (\bar{n}_x p_k) dS &= \\ \frac{\partial}{\partial x} \langle (\langle p_k \rangle + \Delta p_{k,i}) \rangle \beta_k &- \beta_k \frac{\partial}{\partial x} (\langle p_k \rangle + \Delta p_{k,i}). \end{aligned} \quad (2. 2. 32)$$

The deviating component of pressure is considered here to fully account for the pressure interactions at the interfacial surface. The deviation $\Delta p'_{k,i}$ appears when the term $\Delta p_{k,i}$ is not uniform over the interfacial area. Such differences could arise from velocity non-uniformities around a droplet. In a dilute dispersed flow, the turbulent carrier phase produces a source of pressure deviations at the interface of the dispersed flow (droplets, bubbles, etc.). The interfacial pressure differences are distinct from spatially averaged values in the sixth term of Eq. (2. 2. 6), which

involves their interactions with the physical boundary (wall). Equation (2. 2. 32) is customized in a final form, as the first term on the right side of Eq. (2. 2. 30).

Expressing and assembling the fifth term of the momentum equation, Eq. (2. 2. 6), in terms of the spatially averaged quantities yields:

$$-\frac{1}{V} \int_{a_i} \bar{n}_x \left[\bar{m}_k \bar{v}_k + \bar{n}_k (p_k \bar{I} - \bar{\tau}_k) \right] dS = -\langle \bar{m}_k v_{k,x} \rangle_i \quad (2. 2. 33)$$

$$+ (\langle p_k \rangle + \Delta p_{k,i}) \frac{\partial \beta_k}{\partial x} - \langle \Delta p'_{k,i} \rangle_i + \langle \bar{n}_k \bar{\tau}_{k,x} \rangle_i.$$

Equation (2. 2. 33) is written as a part of the right-hand side of the dispersed phase momentum equation in the x -direction. In Eq. (2. 2. 33), a constant surface tension along the interfacial boundary is assumed. If surface tension inside the droplet surface is not constant, the pressure force balances the inner and outer pressure forces acting on the droplet surface. Bulk pressure internal to the droplet tends to induce the surface tension pressure force in the droplet surface. This occurs when pressure in the droplet (dispersed phase) that acts on the droplet surface and the pressure in the surrounding air (continuous phase) are not equal. In this case, the surface tension is not constant. As soon as the pressure forces at the droplet surface become equal, there is no force acting along the entire droplet surface and the surface tension inside that surface is constant. This is consistent with the dilute phase formulation with small, spherical droplets, where the pressure force acting from the continuous phase approximately equals the pressure force acting inside the droplet on the droplet surface.

When the phase composition or relative velocity between phases changes, an apparent force is created. The third term on the right side of Eq. (2. 2. 33), $\langle \Delta p'_{k,i} \rangle_i$, leads to this apparent mass force, which arises to accelerate the mass of the surrounding continuous phase in the immediate vicinity of the dispersed phase. This term is a force per unit volume in the momentum equation and it affects the change of momentum for both phases.

In Eq. (2. 2. 33), certain waviness between the dispersed and continuous phases may exist along the interfacial boundary, so an apparent mass effect can arise.

However, the large density difference between phases for water droplets in air diminishes this apparent mass effect. If the pressure is assumed to be constant and uniform within both phases in the averaging control volume, then both deviating pressure components become negligible. This means that the pressure terms $\beta_k(\partial\langle p_k\rangle/\partial x)$ and $\beta_k(\partial\langle p_k\rangle/\partial y)$ become valid only within the carrier phase, while the physical effects at the surface of the droplet are lost.

The pressure part of the interfacial surface equation, Eq. (2. 2. 33), is written as

$$-\frac{1}{V} \int_{a_i} \bar{n}_x [\bar{n}_k(p_k)] dS = \langle p_k \rangle \frac{\partial \beta_k}{\partial x} + \Delta p_{k,i} \frac{\partial \beta_k}{\partial x} - \int_{a_i} \bar{n}_x [\bar{n}_k(p_k - \langle p_{ki} \rangle)] dS. \quad (2. 2. 34)$$

By grouping terms together with respect to x - and y -directions, the linear momentum equations for the spatially averaged quantities can be obtained. From the product rule,

$$\frac{\partial}{\partial x} \beta_k \langle p_k \rangle = \beta_k \frac{\partial \langle p_k \rangle}{\partial x} + \langle p_k \rangle \frac{\partial \beta_k}{\partial x} \quad (2. 2. 35)$$

$$\frac{\partial}{\partial y} \beta_k \langle p_k \rangle = \beta_k \frac{\partial \langle p_k \rangle}{\partial y} + \langle p_k \rangle \frac{\partial \beta_k}{\partial y}. \quad (2. 2. 36)$$

the x -momentum equation becomes

$$\begin{aligned} & \frac{\partial}{\partial t} (\beta_k \rho_k \langle v_{k,x} \rangle) + \frac{\partial}{\partial x} (\beta_k \rho_k \langle v_{k,x} \rangle \langle v_{k,x} \rangle) + \frac{\partial}{\partial y} (\beta_k \rho_k \langle v_{k,x} \rangle \langle v_{k,y} \rangle) \\ & + \beta_k \frac{\partial}{\partial x} \langle p_k \rangle - \Delta p_{ki} \frac{\partial \beta_k}{\partial x} - \frac{\partial}{\partial x} (\beta_k \langle \tau_{k,xx} \rangle) - \frac{\partial}{\partial y} (\beta_k \langle \tau_{k,yx} \rangle) - \beta_k \rho_k \langle f_{k,x} \rangle = -\langle \dot{m}_k v_{k,x} \rangle_i \\ & - \langle \Delta p'_{k,i} \rangle_i + \langle \bar{n}_k \bar{\tau}_{k,x} \rangle_i + \langle \bar{n}_{k,w} \bar{\tau}_{k,x} \rangle_w - \frac{\partial}{\partial x} (\beta_k \rho_k \langle \delta v_{k,x} \delta v_{k,x} \rangle) - \frac{\partial}{\partial y} (\beta_k \rho_k \langle \delta v_{k,x} \delta v_{k,y} \rangle). \end{aligned} \quad (2. 2. 37)$$

The momentum equation in the y -direction is derived in a similar manner.

It is worthwhile to consider certain important differences between the current formulation and previous studies, such as that of Prosperetti and Jones [25]. Unlike previous studies, in this thesis the interfacial pressure drag force per unit volume in the fifth term of the differential equation Eq. (2. 2. 37) and the apparent mass force

per unit volume (tenth term of the same equation) do not coincide. This flexibility allows modeling of these terms in various flow conditions independently.

The second term on the right side of Eq. (2. 2. 33) considers the spatially averaged bulk pressure of phase k . With the term $\frac{\partial}{\partial x} \beta_k \langle p_k \rangle$ in the phase momentum equation, it leads to a fourth term of Eq. (2. 2. 15). It is noted that an explicit form of the term $\langle p_k \rangle \frac{\partial \beta_k}{\partial x}$ was removed from Eq. (2. 2. 15). Additionally, this term is grouped with interfacial terms, such as $\Delta p_{k,i} \frac{\partial \beta_k}{\partial x}$, $\langle \Delta p'_{k,i} \rangle_i$ and $\langle \bar{n}_k \bar{\tau}_{k,x} \rangle_i$, and a wall term $\langle \bar{n}_{k,w} \bar{\tau}_{k,x} \rangle_w$ under a surface integral and it is modeled as an algebraic source term in an upcoming momentum equation, Eq. (2. 2. 39). This is a different procedure than that in past studies [25]. The procedure in this thesis distinguishes the interfacial and wall forces per unit volume, thereby allowing useful new insight into the mechanisms of interfacial pressure behavior and its modeling in various multiphase phenomena (i.e., flow separation behind droplets, coalescence or breakup of droplets, etc.).

Also, unlike previous formulations (i.e., Ref. [25]), the dispersed phase pressure is not necessarily equal to the bulk pressure of the continuous phase in the x -momentum equation, Eq. (2. 2. 37). This aspect can be particularly significant if the dispersed phase moves through a continuous phase having rapid pressure variations, or different surrounding continuous phase(s), since there may be insufficient time for the dispersed phase pressure to adjust. An example is that of supercooled droplets being distributed spatially throughout clouds at different elevations and having significantly different characteristics to that in the continuous (air) phase around the helicopter, i.e., down-wash and near-wall regions of a helicopter surface.

The interfacial pressure forces, such as the drag force and apparent mass force per unit volume, would be difficult or inconvenient to evaluate in the current form of Eq. (2. 2. 37). For dispersed phase motion, these forces are assumed to coincide. Therefore, they are grouped together. This procedure is the same as reported in Ref. [25]. For the droplet flow model in this thesis, these interfacial pressure forces are modeled with

the interfacial and wall shear forces under an algebraic drag term. In this way, unlike some previous studies (i.e., Refs. [23], [27] and [32]), the difficulty of addressing the interfacial pressure forces is avoided. This is especially important in a highly non-uniform dispersed flow.

The second integral in Eq. (2. 2. 34) identifies the appearance of the coincidental form drag and apparent mass forces. This derived mathematical expression is recognized as an approximation, which may not always be significant in disperse phase motion, such as a sudden change(s) of uniformity of the pressure of a dilute phase. The general term is kept in a form that offers the description, such as Eq. (2. 2. 34), and additional modeling of these force terms. This is a template for modeling of the disperse phase motion, particularly in the regions of sudden and substantial changes of phase pressure, from a uniform pressure to another non-uniform pressure. The key point here is the existence of the differential term $\langle p_k \rangle \frac{\partial \beta_k}{\partial x}$, which leads to the apparent mass force. In the presence of uniform pressure and vanishing velocity, this term may give rise to motion of the spatially non-uniform dispersed phase. At the same time, the term is vanishing due to the presence of the drag term ($\langle p_k \rangle = p_k$). The implication in this situation is that less disperse phase motion is generated from the onset of uniform pressure.

In dispersed multiphase flows, the Reynolds stresses (analogous to the Reynolds stresses in a single-phase flow) arise from the dispersed phase velocity deviations. These stresses represent information lost in the averaging procedure, which must be supplied back. If the dispersed phase is dilute, the Reynolds stresses arise primarily due to turbulence in the carrier phase. These stresses can be modeled through a Boussinesq assumption. For example, for the y -convective term in the x -momentum equation, this yields

$$\beta_k \rho_k \langle \delta v_{k,x} \delta v_{k,y} \rangle = -\mu_k \left(\frac{\partial \langle v_{k,y} \rangle}{\partial x} + \frac{\partial \langle v_{k,x} \rangle}{\partial y} \right). \quad (2. 2. 38)$$

Chapter 2-MODELING OF MULTIPHASE MOTION WITH DROPLET FLOW AND ICING

The Reynolds stresses in multiphase flows are more complicated to predict than the Reynolds turbulent stresses in a single-phase flow. In certain cases, the averaged Reynolds stresses in the dispersed phase can affect the motion of the carrier phase, particularly for dense multiphase flows.

Spatially averaged deviations of the transported quantities can occur from sources other than turbulence in the carrier phase. For example, the averaged Reynolds stresses may arise from different cross-phase transport processes at the interfacial boundary, such as processes involving variations of droplet velocities and sizes. Such processes may involve coalescence of different sized droplets, with varying dynamic responses to spatial variations in the surrounding continuous (air) phase, thereby affecting the local turbulence. These considerations can be particularly significant in confined regions of a flow, such as a contracted cross-section, where smaller particles tend to follow the local velocity of the continuous phase, while larger particles tend to follow larger velocity scales. In these cases, the solution may require that the averaged equations of motion are solved for each group of droplets.

In Eq. (2. 2. 38), a droplet dynamic viscosity is used with an averaging assumption for the dispersed phase, as this viscosity is a property of the multiphase turbulent flow. Ideally, this viscosity depends on the detailed structure and length scales of the multiphase turbulent flow. Also, the Boussinesq assumption with spatially averaged velocities in Eq. (2. 2. 38) involves certain limitations. Although the droplet velocity deviations exist at the interfacial boundaries, they cannot be fully modeled in a uniform air stream, due to limitations associated with a dilute flow model.

The detailed droplet behavior due to the presence of a wall, such as rotation or splash-back effects, is not fully modeled by the Boussinesq assumption. As droplets approach a surface, the spatially averaged collision effects (droplet/wall and droplet/droplet) become significant, in contrast to assuming droplet/air interactions to be dominant in a dilute flow formulation. In this near-wall case, modifications of the Reynolds stresses are needed. A Boussinesq assumption may be used with an effective viscosity, provided that the near-wall effects can be predicted through

empiricism or other means. The presence of many droplets involves various length scales, droplet diameters, distances between droplets, and so on. Alternatively, the constitutive relations can be modeled by kinetic theory.

In a dilute flow with water droplets (dispersed phase) in air (continuous phase), a large density difference exists between the phases. As a result, the interfacial force of droplets acting to accelerate/decelerate the surrounding air phase is considered to be negligible. After substituting appropriate expressions for the interfacial drag forces (acting on the droplets from the carrier phase) and rearranging the pressure and stress terms, the spatially averaged x -momentum equation for the droplet phase is obtained as follows:

$$\begin{aligned} & \frac{\partial}{\partial t}(\beta\rho\langle v_x \rangle) + \frac{\partial}{\partial x}(\beta\rho\langle v_x \rangle\langle v_x \rangle) + \frac{\partial}{\partial y}(\beta\rho\langle v_x \rangle\langle v_y \rangle) \\ &= \frac{1}{V} \sum v_x \dot{m} - \beta \frac{\partial}{\partial x} \langle p \rangle + \beta \frac{\partial}{\partial x} \langle \tau_{xx} \rangle \\ &+ \beta \frac{\partial}{\partial y} \langle \tau_{yx} \rangle - \frac{\partial}{\partial x} (\beta\rho\langle \delta v_x \delta v_x \rangle) - \frac{\partial}{\partial y} (\beta\rho\langle \delta v_x \delta v_y \rangle) - \beta_V (\langle v_x \rangle - \langle v_{x,a} \rangle). \end{aligned} \quad (2.2.39)$$

This equation governs the motion of the droplets. All symbols refer to the droplet phase, and the phase subscripts, such as d , are omitted, except v_a (air velocity). After including the gravity term, a similar equation is obtained in the y -direction,

$$\begin{aligned} & \frac{\partial}{\partial t}(\beta\rho\langle v_y \rangle) + \frac{\partial}{\partial x}(\beta\rho\langle v_y \rangle\langle v_x \rangle) + \frac{\partial}{\partial y}(\beta\rho\langle v_y \rangle\langle v_y \rangle) \\ &= \frac{1}{V} \sum v_y \dot{m} - \beta \frac{\partial}{\partial x} \langle p \rangle + \beta \frac{\partial}{\partial x} \langle \tau_{yx} \rangle + \beta \frac{\partial}{\partial y} \langle \tau_{yy} \rangle \\ &- \frac{\partial}{\partial x} (\beta\rho\langle \delta v_y \delta v_x \rangle) - \frac{\partial}{\partial y} (\beta\rho\langle \delta v_y \delta v_y \rangle) - \beta_V (\langle v_y \rangle - \langle v_{y,a} \rangle) + \beta\rho g_y. \end{aligned} \quad (2.2.40)$$

The drag parameter is defined as: $\beta_V = \beta f / (D_d^2 / 18\mu_d)$. Unless the droplet phase fraction is $\beta = 1$, the droplet flow depends on the spatial and temporal distribution of the droplets [see also Eq. (2.2.10)]. Such flow is assumed to be discontinuous. Volume fraction dependent, droplet phase viscosities in Eqs. (2.1.4)–(2.1.9)

Chapter 2-MODELING OF MULTIPHASE MOTION WITH DROPLET FLOW AND ICING

represent discontinuous droplet flow. In the current formulation, the viscosities are not dependent on the volume fraction and the constitutive relations for the continuous droplet flow are used (viscosities for the Newtonian continuous flow). The physical interpretation of various terms in the momentum equations [Eqs. (2. 2. 39)–(2. 2. 40)] can be summarized as follows.

- The first term accounts for the local time rate of change of droplet momentum in the control volume.
- The second and third terms account for convection of droplets.
- The fourth term represents cross-phase interactions, such as the momentum change (flux) due to mass transfer from the droplet surface, due to evaporation, coalescence, etc.
- The fifth term refers to spatial pressure gradients acting on the fluid element of the dispersed phase. In dilute flow formulation, this term most probably occur from action of the carrier phase. In dense flow formulation, this term may occur from inner collisions of the constitutive elements of the dispersed phase (i.e. interacting droplets).
- The sixth and seventh terms are viscous forces acting on the dispersed phase at the droplet surface. They contain the unsteady drag force. These viscous terms are modeled based on stress-strain relationships for incompressible Newtonian fluids.
- The eighth and ninth terms are equivalent to the Reynolds stress in single phase flow. These terms can occur due to turbulent velocity fluctuations in the dispersed (droplet) and/or continuous (air) phase. This term is carefully investigated in the near-wall region.
- The tenth term represents diffusive interactions between the phases (effective drag force), due to the relative velocities between the droplets and air.
- The eleventh term (only in the y-momentum equation) accounts for the gravitational force acting on droplets within the control volume.

Closure relations are required for computations based on Eq. (2. 2. 39) and Eq. (2. 2. 40). Such relations are described in Section (2. 3). When evaluating interfacial forces in the numerical formulation, certain thermophysical properties are needed in various terms. Dry air and pure liquid properties are used in the carrier (air) and dispersed (droplet) phases, respectively. However, in practice, the actual co-flowing air stream usually contains moisture, independent from droplet dynamics, as well as evaporative cooling and phase change of thermal interactions between droplets and air. Variations due to moisture content are considered to have minor impact on the resulting properties (see Appendix), when evaluating the cross-phase momentum exchange.

In this section, a detailed spatial averaging procedure leading to Eqs. (2. 2. 39) and (2. 2. 40) is presented, so that modeling assumptions and simplifications of other past models can be identified. For example, Ref. [22] includes only the drag coefficient term of Eq. (2. 2. 40) and gravity force in the y -direction [22], so a comparison with Eq. (2. 2. 40) identifies the assumptions made therein. In that case, the pressure interactions and spatial averaging considerations are neglected. This approach assumes that the droplets are distributed uniformly within the averaging control volume. The gravity force on droplets is introduced in the droplet y -momentum equation. Furthermore, droplets are assumed to be spherically shaped and modeled numerically as solid particles. As a result, a potentially varying shape of droplets, together with a resulting momentum change due to this effect, is not modeled. Also, the cross-phase stresses are assumed to not affect the droplet shape. Evaporation, collisions and coalescence of droplets are neglected, thereby cross-phase mass and momentum exchange due to these effects are also neglected. Although this assumption is often adopted in the free-stream region, its validity in the near-wall region is not well understood in the technical literature. In the near-wall region, the fraction of droplets in the multiphase averaging volume can change appreciably.

2. 3 MODELING INTERFACIAL DRAG

The closure relations are required for computations based on Eq. (2. 2. 39) and Eq. (2. 2. 40). In this section, different drag forms for droplet motion in the air stream are studied, prior to subsequent implementation into the numerical code. Table (2. 3. 1) lists various drag models for drag coefficients, C_D . Drag coefficients from Moody's diagram are investigated.

An approximate transitional form of drag law, which combines low Reynolds and high Reynolds relative number regimes is selected in this study. The form of this multiphase flow drag law is inherently linear and additionally modeled through the drag factor for transitional and high relative Reynolds number regimes. The drag factor, presented below is an approximation function, which entails a cross drag term.

The drag model is implemented in the spatially averaged disperse flow momentum equations. In Eq. (2. 2. 39), the following drag parameter is adopted,

$$\beta_v = \frac{\beta f}{D_d^2 / 18\mu_d} \tag{2. 3. 1}$$

This equation is valid for spherically shaped droplets (i.e micro sized supercooled droplets in the numerical simulations). The function f is the ratio of the drag coefficient to the Stokes drag (note: $f \rightarrow 1$ for Stoke's drag). It is also called a drag factor:

$$f = \frac{C_D}{24} Re_r \tag{2. 3. 2}$$

Alternatively, by expanding the representation for the Reynolds number,

$$f = \frac{C_D}{24} \left(D_d \frac{|\langle \vec{v}_d \rangle - \langle \vec{v}_a \rangle|}{\nu} \right) \tag{2. 3. 3}$$

Chapter 2-MODELING OF MULTIPHASE MOTION WITH DROPLET FLOW AND ICING

Velocity differences between the droplets and air arise due to velocity gradients in the carrier phase, turbulent fluctuations of droplets and/or time varying body forces on the droplets. For both low- Re and high- Re flows, drag factor f can be approximated (Ref. [8]) by

$$f = 1 + 0.15 Re_r^{0.687} + 0.0175 Re_r (1 + 4.25 \cdot 10^4 Re_r^{-1.16})^{-1}. \quad (2.3.4)$$

In the present modeling of droplet flow with icing, the transport quantities of the droplet flow are volume averaged. In the posteriori modeling of the volume averaged governing equations for the droplet flow, an assumption of equal droplet diameters is adopted. Since very small, micron-size spherical super/sub-cooled droplets are assumed in the multiphase flow, the assumption of equal droplets is believed to be realistic.

The droplet diameter measurements in the external flow away from surfaces reveal approximately equal droplet diameters in the core of the flow. A small number of much smaller droplets exist near the core of the flow (i.e. Gaussian distribution). With very small spherical droplets assumed in the present formulation, the remaining droplets are therefore extremely small, with almost negligible inertia. In the current numerical formulation only droplets with the same diameter are considered.

There was no experimental measurement of micro-droplet diameters with approximate diameter of $1 \mu m$ in the newly constructed icing tunnel. Such measurements would require complicated and expensive micro-nozzle systems. This system was planned and designed, but not finished due to infrastructure limitations with high pressure supply lines and freezing.

In rime ice numerical modeling, the droplet impact is modeled as an impact of small discrete objects onto a wall. Similar to modeling of droplet transport, there is no modeling of consequences of the droplet-droplet or droplet-wall collisions, such as droplet splash-back, contraction-elongation, break-up, coalescence, etc. The supercooled droplets impact with their full velocity onto the solid phase (i.e. walls and moving ice interface) and freeze upon impact.

supercooled droplets impact with their full velocity onto the solid phase (i.e. walls and moving ice interface) and freeze upon impact.

The effect of variable diameters of droplets was not experimentally and numerically modeled for the current numerical formulation, presented in Chapter (3). This effect may be important in different flow-icing situations at the walls. It can be introduced and modeled as a measured distribution function in the drag term of the governing momentum equations. Extended experimental measurements should be performed in this regard, accounting for the droplet size distribution, spacing between droplets, time dependent diameter distribution pattern, etc. A special experimentally obtained function of varying droplet diameter in a unit volume can be formed and multiplied with the drag term in that equations of droplet motion.

2. 4 SCALING AND ORDER OF MAGNITUDE ANALYSES

In this section, scaling and order of magnitude analyses are employed to study the important physical mechanisms in droplet transport for a special case (flow near a flat surface). A schematic of the physical problem under consideration is illustrated in Fig. (2. 4. 1). Droplet flow near a solid boundary can affect surface vibrations, heat transfer and ice buildup on the surface [12]. In order to establish the important transport mechanisms and relevant droplet momentum equation for this problem, a scaling analysis is performed in this section. It can be noted than only in the scaling, order and subsequent similarity analyses of the thesis, the assumption of dilute dispersed-droplet multiphase flow is adopted.

(i) Scaling Analysis

This scaling analysis will reveal which terms are most important in the physical model. These terms are chosen based on the largest orders of magnitude. The following parameters are chosen for droplet flow near a flat surface:

$$\begin{aligned} v_{d,x} &= 40.0000 \text{ m/s}, v_{a,x} = 5.0000 \text{ m/s}, v_{a,y} = 0.5000 \text{ m/s} \\ L &= 0.2000 \text{ m}, \gamma = 0.0100 \text{ m}, \beta_d = 10^{-6} \\ \rho_d (t = 0^\circ C) &= 999.8000 \text{ kg/m}^3 \\ \rho_a (t = 120^\circ C) &= 0.8979 \text{ kg/m}^3. \end{aligned} \tag{2.4.1}$$

Complete initial and final calculated data are presented in Table (2.4.1). It can be noted that in this study the physical properties of the droplet flow are considered at temperature $t = 0^\circ C$, which corresponds to slightly supercooled flowing droplets. The flow properties of typical hot air, coming from the engine bay are taken at $t = 120^\circ C$, which resembles a typical anti-icing aircraft application. Unlike in Ref. [104], in this study, the air flows through the surface (through small holes) of a flat plate. Calculating the representative time scale yields: $t = \frac{L}{v_{d,x}} \approx 0.0050 \text{ s}$. The

droplet volume phase fraction is selected as $\beta_d = 10^{-6}$ (Bourgault et al. [22]), which leads to dilute droplet-air two-phase flow. Droplet interactions, such as collisions leading to droplet break-up, coalescence and bouncing from the wall are not modeled, as they are not considered to appreciably affect the droplet motion (Crowe et al. [21]). The chosen droplet diameter of $D_d = 0.000100 \text{ m}$ represents micro size droplets, typically encountered with in-cloud helicopter icing. This diameter suggests a spherical shape for the droplets, equivalent to non-deformable particles in a dilute flow. In this thesis, the droplets have an initial velocity, although it is not necessarily driven by the air stream. The air flow has the same direction as the flowing droplets.

The air can resist the droplet motion, depending on the relative velocity between the air and droplets.

Drag arises between the droplet and air phases. As described previously, the inherently linear form of the drag law is modeled by a transitional drag factor (Crowe et al. [21]). This approximate drag function, f , is the ratio of the drag coefficient to the Stokes drag. In this function, the relative Reynolds number, Re_r , accounts for the exact cross drag term, which entails absolute velocity difference between the droplet and air flow. It is described that velocity differences between the droplets and air usually arise due to velocity gradients in the carrier (air) phase, turbulent fluctuations of droplets and/or time varying body forces on the droplets. In this section, the relative Reynolds number is $Re_r = 140.0760$. Thus, the drag factor from Eq. (2. 3. 4) becomes $f = 5.4911$.

Closure drag relations are required for the analysis of the x - and y - droplet momentum equations, i.e.,

$$\beta_y = \frac{\beta_d f}{\left(\frac{D_d^2}{18\mu_a} \right)}. \quad (2. 4. 2)$$

Substituting the problem parameters into Eq. (2. 4. 2) gives $\beta_y = 0.2236$. The initially established parameters are summarized in Table (2. 4. 1). In Appendix (1), the detailed derivation for establishing these parameters is outlined.

The overall magnitude of the droplet velocity in y -direction is derived from the droplet phase fraction equation. Substituting the values of the scaling parameters, the droplet velocity in the y direction is approximated as

$$v_{d,y} \approx -\gamma \left(\frac{1}{t} + \frac{1}{L} v_{d,x} \right) \Rightarrow v_{d,y} \approx -4 \text{ m/s}. \quad (2. 4. 3)$$

The droplet y -momentum equation is represented as follows

$$\begin{aligned}
 & \frac{\partial}{\partial t} \left(\beta_d \rho_d v_{d,y} \right) + \frac{\partial}{\partial x} \left(\beta_d \rho_d v_{d,y} v_{d,x} \right) + \frac{\partial}{\partial y} \left(\beta_d \rho_d v_{d,y} v_{d,y} \right) \\
 & = \Gamma_{d,m} v_{d,y} - \beta_d \frac{\partial}{\partial x} p_d + 2\beta_d \frac{\partial}{\partial y} \left(\mu_d \frac{\partial v_{d,y}}{\partial y} \right) + \beta_d \frac{\partial}{\partial x} \left[\mu_d \left(\frac{\partial v_{d,y}}{\partial x} + \frac{\partial v_{d,x}}{\partial y} \right) \right] \\
 & - \beta_V \left(v_{d,y} - v_{a,y} \right) + \beta_d \rho_d g_d + \Sigma F_{d,y} - \frac{\partial}{\partial x} \left(\beta_d \rho_d v'_{d,y} v'_{d,x} \right) - \frac{\partial}{\partial y} \left(\beta_d \rho_d v'_{d,y} v'_{d,y} \right),
 \end{aligned} \tag{2.4.4}$$

where $\Gamma_{d,m}$ represents a specific droplet mass flow rate [kg/s/m³]. The tenth term in Eq. (2.4.4) represents the sum of other non-differential forces (Crowe et al. [21]) acting in y -direction, i.e., Faxen, Saffman and Magnus forces. The last two terms in Eq. (2.4.4) are modeled by the Boussinesq hypothesis.

After approximating all terms by the scaling parameters from Eqs. (2.4.1) and (2.4.3), the values are substituted into the droplet y -momentum equation [see Table (2.4.1)]. By assembling and showing each term in its order of magnitude from Eq. (2.4.4), the final expression representing the term-by-term magnitudes is

$$\begin{aligned}
 & (0.7998), (0.7998), (1.5997) = \\
 & (0.0000), (10^{-4} \cdot p_d), (1.4328 \cdot 10^{-4}), (3.5621 \cdot 10^{-5}), \\
 & (1.0061), (0.0098), (6.6588 \cdot 10^{-14}), \\
 & (5.6644 \cdot 10^{-8}), (1.4328 \cdot 10^{-4}), (3.5621 \cdot 10^{-5}).
 \end{aligned} \tag{2.4.5}$$

From Eq. (2.4.5), the droplet dynamic pressure is deduced, such that $p_d = 0.10157 \cdot 10^5 \text{ kg} / (\text{m s}^2)$ (order of magnitude).

Using this value for the droplet dynamic pressure and performing a similar procedure as above, the following droplet x -momentum magnitudes are obtained,

$$\begin{aligned}
 & (7.9984), (7.9984), (15.9968) = \\
 & (0.0000), (0.0507), (3.5800 \cdot 10^{-6}), (7.1242 \cdot 10^{-4}), \\
 & (7.8252), (0.0000), (3.3294 \cdot 10^{-15}), \\
 & (7.2827 \cdot 10^{-9}), (3.5800 \cdot 10^{-6}), (7.1242 \cdot 10^{-4}).
 \end{aligned} \tag{2.4.6}$$

Chapter 2-MODELING OF MULTIPHASE MOTION WITH DROPLET FLOW AND ICING

From left to right, the terms represent: transient, x -convection, y -convection, momentum flux due to phase change, pressure, normal stress, shear stress, algebraic drag, Faxen, Saffman and two turbulent terms. Table (2. 4. 1) shows the summarized magnitudes of the terms in the x and y droplet momentum equations. Dividing each term in Eq. (2. 4. 6) by the most significant drag term, the relative magnitudes of the terms of Eq. (2. 4. 6) are shown in percentages in Table (2. 4. 1). The detailed analysis term-by-term is presented in Appendix (1).

Based on this scaling analysis, it is concluded that the following terms in the droplet x -momentum equation are the most important: *transient*, *convection* and *source drag* terms. The scaling analysis was applied to the terms based on certain finite dimensions [Eq. (2. 4. 1)]. For single phase flow, the Blasius similarity solution (documented in Ref. [18]) outlines the boundary layer growth due to diffusion of momentum along a flat surface. Although self similarity of velocity profiles is also expected in multiphase boundary layers with droplets (or particles), such analytical solutions are not available in the technical literature. In section (2. 5. 1), it is shown that a similarity solution exists, when considering the forces due to interfacial resistance (drag) of droplets. The main forces of interest are (i) interfacial resistance (drag), (ii) viscous diffusion and (iii) gravity. The first term is dominant outside of the boundary layer, while the second term is significant near the wall. The purpose of the similarity analysis is determining the extent of droplet momentum displacement, due to interfacial drag alone in a dilute dispersed multiphase flow. In order to maintain consistency when comparing the new solution against the Blasius solution, a no-slip boundary condition is applied. Furthermore, the gravity term is not included in the droplet momentum equations, except for the equation corresponding to the direction of gravity. The other directions are called “off-plane” or “cross-stream” directions.

Based on these considerations, the spatially averaged x -momentum equation becomes

$$\frac{\partial}{\partial x} \langle \beta_d \rho_d v_{d,x}^2 \rangle + \frac{\partial}{\partial y} \langle \beta_d \rho_d v_{d,x} v_{d,y} \rangle = -\beta_v (\langle v_{d,x} \rangle - \langle v_{a,x} \rangle). \quad (2. 4. 7)$$

In the next sub-section, this equation is investigated further with an order of magnitude analysis. The brackets $\langle \rangle$ represent spatially averaged terms (note: for the sake of brevity, they are dropped in subsequent equations). The similarity analysis [see section (2. 5) and Appendix] provides the similarity parameter and establishes whether self-similar velocity profiles exist along the flat surface. A separable differential equation for the similarity function, $F(\eta)$, is derived to describe this self similarity. If self-similar profiles of the droplet velocity field exist, then all velocity profiles collapse into one single curve, after a change of coordinates.

(ii) Order of Magnitude Analysis

In this sub-section, an analysis of the orders of magnitude (denoted by symbol \tilde{O}) is performed on the main terms in the x -momentum equation. This analysis derives the relevant terms in the droplet momentum equations. It also determines how the stream function and momentum displacement for a reference streamline are found, as well as their limitations. The analysis defines a momentum displacement, γ , and similarity parameter, η , and it uses them in a subsequent similarity analysis, in order to develop the similarity solution of multiphase flow with droplets at the flat plate. A more detailed derivation procedure is presented in Appendix (2).

In many cases, it is not necessary or it is not feasible to calculate exact physical processes. Initial useful insight into the physical processes can be gained through the orders of magnitude, which give an insight of the scale of the problem. In this analysis, a similarity variable will be developed, without exact insight into the processes of continuity and convection of the droplet phase, as well as drag interactions between the dispersed droplet and continuous air phase near a flat plate. Table (2. 4. 2) presents the relevant variables with dimensional and non-dimensional orders of magnitudes.

Chapter 2-MODELING OF MULTIPHASE MOTION WITH DROPLET FLOW AND ICING

From the steady-state continuity requirement for the droplet phase without mass transfer of the droplet phase across the phase interface:

$$\frac{\partial}{\partial x}(\beta_d \rho_d v_{d,x}) + \frac{\partial}{\partial y}(\beta_d \rho_d v_{d,y}) = 0 \quad (2.4.8)$$

the orders of the geometrical (x, y) and physical quantities $(v_{d,x}, v_{d,y})$, can be estimated by

$$\frac{\tilde{O}(1)}{\tilde{O}(1)}, \frac{\tilde{O}(?)}{\tilde{O}(\xi)} \quad (2.4.9)$$

The second term in Eq. (2.4.9) should have the same order, $\tilde{O}(1)$, as the first term in Eq. (2.4.9), in order to satisfy Eq. (2.4.8). From this conclusion,

$$v_d \Rightarrow \tilde{O}(\xi). \quad (2.4.10)$$

Inserting the orders of magnitude from Table (2.4.2), Eq. (2.4.8) and Eq. (2.4.9) into the droplet momentum equation, Eq. (2.4.7), yields expressions with the following orders of magnitude,

$$\frac{\tilde{O}(1) \tilde{O}(1)}{\tilde{O}(1)}, \frac{\tilde{O}(1) \tilde{O}(\xi)}{\tilde{O}(\xi)}, [\tilde{O}(1), \tilde{O}(1)]. \quad (2.4.11)$$

It can be concluded from Eq. (2.4.11) that each term in Eq. (2.4.7) should have the same order of magnitude, which is $\tilde{O}(1)$. This conclusion of the same magnitude of the physical processes enables two separate equations, Eqs. (A.2.2) – (A.2.3), presented in Appendix (2).

Based on the discussion above, the droplet x -momentum equation is written in an algebraic order of magnitude form and all terms in the equation have the same order of magnitude. Individual terms are grouped and compared. The droplet x -velocity, $v_{d,x}$, represents a reference velocity at an outer droplet momentum

displacement streamline. The x -momentum equation can be expressed by orders of magnitudes, such as

$$\tilde{O}\left(\frac{\beta_d \rho_d v_{d,x\gamma}^2}{x}\right) + \tilde{O}\left(\frac{\beta_d \rho_d v_{d,x\gamma} v_{d,y}}{\gamma}\right) = \tilde{O}\left[-\beta_v (v_{d,x\gamma} - v_{a,x})\right]. \quad (2.4.12)$$

Equalization of the order of terms in Eq. (2.4.12) enables comparisons of the transport processes on an individual basis. The investigation, starting from section (2.4) - (i), Scaling Analysis, and involving Eqs. (2.4.8) - (2.4.12), revealed the originality of these comparisons that lead to the establishment of the unique similarity parameter. In this steady-state case, the local transport processes, such as inertia of the dispersed phase and dispersed-continuous phase resistance (outer forces) equally act on a dispersed fluid element. Omission of either term in Eq. (2.4.12) [or Eq. (A.2.1)] would drastically affect the transport process of the dispersed phase. In comparing the orders of magnitudes of particular terms in Eq. (2.4.12), two cases were considered. Firstly, the change of the x -inertia in the x -direction [x -momentum x -convective term, Eq. (A.2.2), left] comes from the action of inertia on the cross-section of the fluid element. This is related to the dispersed part of the drag force, which acts on the surfaces, parallel to the motion. Secondly, the change of x -inertia in the y -direction [x -momentum y -convective term, Eq. (A.2.3) in Appendix (2), left] comes from the action of y -inertia, which acts at the side surface of the fluid element. It is related with the air part of the drag force [Eq. (A.2.3), Appendix (2), right], which also acts at these surfaces.

Following this procedure, the x -convective term (first part of the first term on the left side) is equated with the droplet part of the drag force (first term on the right side). From the first equality, the droplet x -velocity on the reference streamline is obtained as:

$$v_{d,x\gamma} = \tilde{O}(-C x). \quad (2.4.13)$$

The parameter C is determined as follows [see Table (2. 4. 1)]:

$$C = \frac{f}{\frac{D_d^2 \rho_d}{18\mu_a}}. \quad (2. 4. 14)$$

Secondly, from Eq. (2. 4. 12), the x -momentum y -convective term (second term on the left side) is equated with the air part of the drag force (second part of the first term on the right side). From the second equality, the droplet momentum displacement for the reference streamline, γ , is obtained as a function of $v_{d,y}$, $v_{d,x,\gamma}$, $v_{a,x}$, β_d , ρ_d and β_v . Inserting the expression for $v_{d,x,\gamma}$ from Eq. (2. 4. 13), the following result for the droplet momentum displacement of the reference streamline is obtained:

$$\gamma = \tilde{O}\left(-\frac{v_{d,y}}{v_{a,x}} x\right). \quad (2. 4. 15)$$

Thirdly, the droplet y -velocity is obtained from droplet y -momentum equation (similarly to x -direction).

A similar order of magnitude analysis is performed on the constituent parts of the droplet y -momentum equation. The y -convective y -momentum term is equated with the air component of the y -direction drag term. Therefore, the droplet y -velocity component is obtained as

$$v_{d,y} = \left[\tilde{O}\left(\frac{\beta_v}{\beta_d \rho_d} v_{a,y} \gamma\right) \right]^{\frac{1}{2}}. \quad (2. 4. 16)$$

The expression in Eq. (2. 4. 16) is inserted into Eq. (2. 4. 15), thus yielding the equation for γ . By squaring this result on both sides, canceling the extra γ terms, and dropping the order symbol (\tilde{O}), the final equation for the momentum displacement of the reference streamline becomes

$$\gamma = C \frac{v_{a,y}}{v_{a,x}^2} x^2. \quad (2.4.17)$$

2. 5 SPECIAL CASES OF ANALYTICAL SOLUTIONS

The development of Eulerian and Lagrangian analytical solutions is presented in this section. Special cases are studied to provide deeper understanding of the multiphase flow interactions, when building and validating the numerical formulation and assessing the experimental results. Applications with droplet and air motion were examined with/without the presence of a wall.

2. 5. 1 SIMILARITY NEAR-WALL MULTIPHASE SOLUTION

In this section, a multiphase flow similarity solution for dispersed phase transport in the airstream along a flat plate is developed based on characteristic values of the droplet flow in Section (2. 4). In the similarity analysis, and associated scaling and order of magnitude analyses, the assumption of dilute dispersed-droplet multiphase flow is adopted in this thesis only.

The similarity parameter is an independent parameter, which contains all the other independent parameters of the problem. In this way, the number of the independent parameters reduces to one. This enables observing the droplet multiphase

physical processes in this (one) direction only. In the following similarity analysis, the similarity parameter is recognized based on the previously uniquely developed momentum displacement of the reference streamline γ . Unlike others, who guessed the single phase similarity parameter in ahead and confirmed it afterwards through the procedure, this original multiphase similarity parameter is developed from physical assumptions, scaling and order of magnitude analyses (γ). It is also shown that the parameter is confirmed afterwards through the similarity procedure. The similarity analysis reveals the existence of the multiphase similarity solution for droplet flow along the flat plate. The developed similarity differential equation is solved afterwards in a unique exact analytical manner, yielding a closed form analytical solution. It is shown that all derived droplet velocity profile and trajectory multiphase solutions collapse into the similarity solution.

(i) Similarity Analysis

The focus here is to observe similarity behavior of the x -velocity profile of droplets in the y -direction along the surface [see (Fig. 2. 4. 1)]. The ratio of this droplet x -velocity to a reference droplet x -velocity is defined as a similarity function:

$$\frac{v_{d,x}}{v_{d,x,\gamma}} = F\left(\frac{y}{\gamma}\right), \quad F(\eta) \equiv F\left(\frac{y}{\gamma}\right). \quad (2. 5. 1. 1)$$

Inserting the previously determined parameters into Eq. (2. 5. 1. 1), yields the following expressions:

$$\frac{v_{d,x}}{-[\beta_V/(\beta_d \rho_d)] x} = F\left(\frac{y}{x^2} G\right), \quad (2. 5. 1. 2)$$

where

$$G \equiv \left[\frac{I}{C v_{a,y} / v_{a,x}^2} \right]. \quad (2.5.1.3)$$

From Eq. (2.5.1.3), the similarity parameter is recognized as follows:

$$\eta = \frac{y}{x^2} G. \quad (2.5.1.4)$$

As mentioned, this non-dimensional parameter represents the independent variable in the subsequent similarity analysis. In terms of this parameter, the droplet velocity profiles do not change with respect to the similarity variable, despite the fact that droplet velocity profiles change with respect to the x -direction.

In this similarity analysis, a stream function approach is introduced. The stream function for multiphase flow is derived from the two-dimensional continuity relation. The mass flow per unit depth between two streamlines is defined as:

$$\Delta\tilde{\psi} = \beta_d \rho_d V \Delta n, \quad (2.5.1.5)$$

where V is the resultant velocity magnitude of the droplet flow and Δn is the normal distance between two streamlines. Sub-dividing Eq. (2.5.1.5) into components and expressing the result in terms of differential scales yields

$$d\tilde{\psi} = \beta_d \rho_d (v_{d,x} dy - v_{d,y} dx). \quad (2.5.1.6)$$

Comparing Eq. (2.5.1.6) with the expression for the total differential of $d\tilde{\psi}$, and replacing $\tilde{\psi}$ with $\tilde{\psi} / \rho_d$, the following expressions are obtained:

$$\beta_d v_{d,x} = \frac{\partial \psi}{\partial y} \quad (2.5.1.7)$$

$$\beta_d v_{d,y} = -\frac{\partial \psi}{\partial x}. \quad (2.5.1.8)$$

Chapter 2-MODELING OF MULTIPHASE MOTION WITH DROPLET FLOW AND ICING

Substituting the expressions from Eqs. (2. 5. 1. 7) - (2. 5. 1. 8) into the phase volume fraction equation, an identity is obtained, so that the phase fraction equation is automatically satisfied. Inserting the droplet velocities as a function of the stream function gradients into Eq. (2. 5. 1. 1), while employing the earlier order of magnitude analysis, yields the following expression for the droplet flow stream function:

$$\psi = -\beta_d \left(\frac{C}{G} x^3 \right) F(\eta). \quad (2. 5. 1. 9)$$

Expressing the droplet velocity in terms of ψ in droplet x -momentum equation, Eq. (2. 4. 7) yields the following expression:

$$\frac{\partial}{\partial x} \left[\frac{1}{\beta_d} \left(\frac{\partial \psi}{\partial y} \right)^2 \right] + \frac{\partial}{\partial y} \left[-\frac{1}{\beta_d} \left(\frac{\partial \psi}{\partial y} \right) \left(\frac{\partial \psi}{\partial x} \right) \right] = -\frac{\beta_y}{\rho_d} \left[\left(\frac{1}{\beta_d} \frac{\partial \psi}{\partial y} \right) - v_{a,x} \right]. \quad (2. 5. 1. 10)$$

Equation (2. 5. 1. 10) can be evaluated based on Eq. (2. 5. 1. 4) and Eq. (2. 5. 1. 9). Differentiating the similarity parameter, (Eq. 2. 5. 1. 4), with respect to x and y , and evaluating the derivatives in the droplet x -momentum equation, Eq. (2. 5. 1. 10), yields the following result:

$$3 F(\eta) [F(\eta)]'' - [F(\eta)']^2 + F(\eta)' = -\frac{v_{a,x}}{C x}. \quad (2. 5. 1. 11)$$

The left-hand side of Eq. (2. 5. 1. 11) is a function of the similarity parameter, η , alone, while the right-hand side of the same equation is a function of x alone. Both sides of Eq. (2. 5. 1. 11) must then be equal to the same constant. Equation (2. 5. 1. 11) consists of two separable ordinary differential equations. It is second-order and it needs two boundary conditions to find its solution. Equation (2. 5. 1. 11) indicates that self similarity of the profile, $v_{d,x} / v_{d,x,\eta}$, exists along the plate and a similarity solution exists. This result confirms the initial hypothesis that a similarity solution for the droplet flow exists next to the flat surface.

The similarity solution can now be developed. The similarity equation is simplified, since in this case, the condition $v_{a,x} \ll C x$ [see Table (2. 4. 1)] is satisfied from the physical model in most of the region, except very close to the leading edge in Fig. (2. 4. 1). Accounting for this condition, Eq. (2. 5. 1. 11) becomes

$$3 F(\eta) [F(\eta)]'' - [F(\eta)']^2 + F(\eta)' = 0. \quad (2. 5. 1. 12)$$

An analytical solution of Eq. (2. 5. 1. 12) exists. It is performed in the next subsection. Graphical results from the solution are shown in Chapter (5).

(ii) Similarity Solution

Based on the following substitution, $F(\eta)' = z$, Eq. (2. 5. 1. 12) becomes

$$3 F(\eta) z \frac{dz}{d[F(\eta)]} - z^2 + z = 0. \quad (2. 5. 1. 13)$$

By introducing a substitution, $u = z^2$, in Eq. (2. 5. 1. 13), separating variables, integrating and then introducing another substitution $g = u^{1/2}$ and integrating again,

$$3 \ln|g - 1| = \ln[F(\eta)] + C_1. \quad (2. 5. 1. 14)$$

Back substitutions are applied in reverse order, and a constant, $C_2 \equiv e^{C_1/3}$, is introduced. Then, integrating the resultant equation and inclusion of another substitution, $z = C_2 [F(\eta)]^{1/3} + 1$, yields an integral equation. From an additional back substitutions and integrations,

$$\frac{3}{2C_2} [F(\eta)]^{2/3} - \frac{3}{C_2^2} [F(\eta)]^{1/3} - \frac{9}{2C_2^3} + \frac{3}{C_2^3} \ln\{1 + C_2[F(\eta)]^{1/3}\} = \eta + C_3. \quad (2. 5. 1. 15)$$

Chapter 2-MODELING OF MULTIPHASE MOTION WITH DROPLET FLOW AND ICING

The constants C_2 and C_3 are determined with the following two boundary conditions:

$$1) \eta = 0, \quad F(\eta) = 0 \quad (2.5.1.16)$$

$$2) \eta = 1, \quad F(\eta) = 1, \quad (2.5.1.17)$$

where the similarity parameter is

$$\eta = \frac{y}{x^2} \frac{v_{a,x}^2}{v_{a,y} C} \approx \eta = 0.2236 \frac{y}{x^2}. \quad (2.5.1.18)$$

From the boundary conditions, $C_2 = 0.008$ and $C_3 = -8789062.500$, so that

Eq. (2.5.1.15) becomes

$$187.500 [F(\eta)]^{2/3} - 46875.000 [F(\eta)]^{1/3} - 8789062.500 + 5859375.000 \ln\{1 + 0.008[F(\eta)]^{1/3}\} = 0.2236 \frac{y}{x^2} - 8789062.500. \quad (2.5.1.19)$$

Inserting the boundary conditions back into Eq. (2.5.1.19), where $\gamma = y$ and $v_{d,x} = v_{d,x\gamma}$ along the reference streamlines [see Fig. (2.4.1)], yields

$$187.500 - 46875.000 + 5859375.000 \ln(1 + 0.008) = 0.2236 \frac{\gamma}{x^2}. \quad (2.5.1.20)$$

This yields the following momentum displacement for the reference streamline:

$$\gamma = 4.4458 x^2. \quad (2.5.1.21)$$

The steady-state solution of the droplet trajectories is obtained from the similarity solution as follows:

$$y = 4.4724 \frac{v_{d,x}}{v_{d,x\gamma}} x^2. \quad (2.5.1.22)$$

Chapter 2-MODELING OF MULTIPHASE MOTION WITH DROPLET FLOW AND ICING

The droplet mass-based displacement up to the γ streamline is denoted here by $\hat{\gamma}_s$. From the similarity variable, Eqs. (2. 5. 1. 1) and (2. 5. 1. 20), similarity function and the similarity solution, $F(\eta) = \eta$, the mass-based displacement up to the γ streamline, $\hat{\gamma}_s$, can be calculated. Since the droplet x -velocity profile exists in the momentum displacement layer, a velocity deficit, $v_{d,x,\gamma} - v_{d,x}$, exists. Therefore, the flow rate across the flow section at a particular x -position is less than it would be across the same section, if the flow had a uniform relative velocity profile. Thus, an actual droplet velocity profile in the vicinity of the flat surface is compared with the velocity profile of the flow corresponding to slip boundary conditions at the surface.

The flow rate balance across the momentum thickness at a certain x -location can be written as

$$\hat{\gamma}_s w v_{d,x,\gamma} = \int_0^{\infty} (v_{d,x,\gamma} - v_{d,x}) w dy, \quad (2. 5. 1. 23)$$

where w represents the plate width. Dividing both sides of Eq. (2. 5. 1. 23) by the constant plate width, Eq. (2. 5. 1. 23) can be rearranged as follows:

$$\hat{\gamma}_s = \int_0^{\infty} \left(1 - \frac{v_{d,x}}{v_{d,x,\gamma}}\right) dy \Rightarrow \hat{\gamma}_s = \int_0^{\gamma} \left(1 - \frac{v_{d,x}}{v_{d,x,\gamma}}\right) dy. \quad (2. 5. 1. 24)$$

The droplet x -velocity profile from the similarity solution is inserted with the γ function into Eq. (2. 5. 1. 24). Once Eq. (2. 5. 1. 24) is integrated along the y direction, it gives the following expression for the droplet mass-based displacement up to the γ streamline:

$$\hat{\gamma}_s = 2.2229 x^2. \quad (2. 5. 1. 25)$$

The droplet momentum-based displacement up to the γ streamline is defined by Θ_s . Due to the velocity deficit ($v_{d,x,\gamma} - v_{d,x}$), the momentum flux across the flow section at a particular x -location is less than it would be across the same section, if the flow

Chapter 2-MODELING OF MULTIPHASE MOTION WITH DROPLET FLOW AND ICING

had a uniform relative velocity profile. In this study, the deficit of the droplet momentum flux is called the droplet momentum-based displacement up to the γ streamline, Θ_s . It can be calculated as

$$\Theta_s \rho w v_{d,x\gamma}^2 = \rho w \int_0^{\infty} v_{d,x} (v_{d,x\gamma} - v_{d,x}) dy. \quad (2.5.1.26)$$

Dividing both sides of Eq. (2.5.1.26) by $\rho w v_{d,x\gamma}^2$ and integrating along the y -direction of the momentum displacement, yields

$$\Theta_s = \int_0^{\gamma} \frac{v_{d,x}}{v_{d,x\gamma}} \left(1 - \frac{v_{d,x}}{v_{d,x\gamma}}\right) dy. \quad (2.5.1.27)$$

Inserting the similarity solution ratio of Eq. (2.5.1.1) into Eq. (2.5.1.27), substituting the γ function and proceeding with the integration, yields the following expression for the momentum based displacement up to the γ (reference streamline) streamline,

$$\Theta_s = 0.7410 x^2. \quad (2.5.1.28)$$

Based on the Blasius solution (Munson et al. [17]), the boundary layer thickness is expressed as

$$\delta = 5 \sqrt{\frac{v_d x}{v_{d,x}}} \Rightarrow \delta = 0.0011 \sqrt{x}. \quad (2.5.1.29)$$

The boundary layer displacement thickness is

$$\hat{\delta} = \frac{1.721}{\sqrt{\frac{D_d}{v_d x}}} \Rightarrow \hat{\delta} = 0.2303 \sqrt{x}. \quad (2.5.1.30)$$

The boundary layer momentum thickness is

$$\Theta = \frac{0.664}{\sqrt{\frac{D_d}{v_d x}}} \Rightarrow \hat{\delta} = 0.0888 \sqrt{x}. \quad (2.5.1.31)$$

The purpose of this comparison is to establish the region between drag and diffusion-based displacement of droplets [see Fig. (2.4.1)]. The current analysis has considered the extent of droplet momentum displacement, due to interfacial drag between droplets and air. In addition to providing analytical solutions for validation of numerical modeling, it sheds light on certain 3D processes. For example, 2D icing predictions that miss off-stream trends of droplet capturing, by the potentially iced surface area, may be better understood through the droplet momentum displacement. Blowing air through the holes of a profiled surface of an airfoil deflects the droplets away from the surface, thus preventing icing on the surface. Due to the non-deforming, small droplets being considered, the analysis and results are also applicable to multiphase flows with solid particles.

Graphical results from these similarity solutions are re-calculated and presented in Chapter (5), entitled "Validation and Results".

2.5.2 LAGRANGIAN ANALYTICAL MODELING AND SOLUTIONS OF DROPLET TRAJECTORIES

In this section, Lagrangian multiphase analytical solutions are developed for cases of dispersed phase-droplet motion. Spherically shaped droplets are considered. The time-dependent analytical solutions are obtained for low Reynolds and high

Chapter 2-MODELING OF MULTIPHASE MOTION WITH DROPLET FLOW AND ICING

Reynolds number droplet-air regimes. These solutions are derived for different numbers of the drag coefficient (discussed below).

Consider a force balance with interfacial drag and gravity acting on a droplet (subscript d) in an airstream (subscript a). The equations of motion in the x - and y -directions are

$$m_d \frac{d}{dt} (v_{d,x}) = -F_{D,x} + m_d g_x \quad (2.5.2.1)$$

$$m_d \frac{d}{dt} (v_{d,y}) = -F_{D,y} + m_d g_y, \quad (2.5.2.2)$$

where $F_{D,x}$, $F_{D,y}$, g_x and g_y represent drag forces in x - and y -directions and gravity in x - and in y -directions, respectively.

The non-linear (quadratic) drag law predicts drag on the sphere in high- Re_r number flow regime, i.e.,

$$-F_{D,i} = -\frac{1}{2} \rho_a |v_{d,i} - v_{a,i}| (v_{d,i} - v_{a,i}) C_D \frac{\pi D_d^2}{4}, \quad (2.5.2.3)$$

where symbol i represents Cartesian components in x - and y -directions. It can be noted that drag in Eq. (2.5.2.3) entails the cross drag term. For *low- Re* number flow regimes, the linear drag law in each direction, i , is used, i.e.,

$$-F_{D,i} = -3\mu\pi D_d (v_{d,i} - v_{a,i}). \quad (2.5.2.4)$$

The relative Reynolds number between phases in contact in each direction, Re_r , is defined as

$$Re_r = \frac{\rho_a |v_{d,i} - v_{a,i}| D_d}{\mu_a}. \quad (2.5.2.5)$$

Table (2.3.1) represents different drag coefficients. Several closed form analytical solutions to Lagrangian two-phase droplet motion are developed, yielding droplet

velocity profiles and trajectories for four different applications [Case (i) – Case (iv)], presented below. Drag law is used in different forms in the presented cases. The following symbols are used below: s - trajectory, v_a – air velocity, v_d - droplet velocity, D_d - droplet diameter, ρ_d - droplet density, ρ_a - air density and t - time.

(i) Case 1

Gravitational effects are neglected in this (horizontal) x - y plain motion. It is assumed that droplets reach a sufficient distance from the wall, so the effects of the near-wall air boundary layer on droplet motion can be neglected. The uniform air streams next to the wall horizontally.

(a) Newton's law of motion [Eqs. (2. 5. 2. 1) - (2. 5. 2. 2), $g_y = 0$] for a flowing droplet subjected to interfacial drag in high Reynolds relative number flow regime ($Re_r < 1000$, i.e. $C_D=0.3$) is considered. The droplets are injected through a tiny hole at the beginning (left side) of a flat plate into a co-flowing air stream [Fig. (5. 1. 1)]. The droplets can be injected into the domain under various angles.

Since the developed temporal closed form velocity (trajectory) analytical solutions for the droplet phase are to be expected dependent on constant velocity (trajectory) initial conditions of each phase (only), these conditions are first examined with respect to the quadratic drag law. By injecting the droplets into the domain with the same horizontal velocity as the air horizontal velocity, the drag in x -direction becomes negligible, $F_{D,x} = 0$. Only drag in y -direction between the phases exists.

Due to the horizontal air stream velocity only, the vertical drag is therefore reduced to

yield a simplified form of exact drag law $F_{D,y} = \frac{\rho_a (v_{d,y})^2}{2} C_D \frac{\pi D_d^2}{4}$. It can be

observed that in this case, there is no cross drag term involved in neither of the directions. Using the physical considerations in this paragraph (above), the simplified

Chapter 2-MODELING OF MULTIPHASE MOTION WITH DROPLET FLOW AND ICING

equations for the exact drag law above can be inserted into the droplet equations of motion [Eqs. (2. 5. 2. 1)-(2. 5. 2. 2)] and integrated twice to yield the analytical solutions for the droplet velocity profiles [Eq. (2. 5. 2. 6)-(2. 5. 2. 7)] and the droplet trajectories [Eqs. (2. 5. 2. 8)-(2. 5. 2. 9)]. Instead, a different form of the drag form, an

approximated quadratic form in i -th direction $F_{D,i} = \frac{\rho_a (v_{d,i} - v_{a,i})^2}{2} C_D \frac{\pi D_d^2}{4}$ is

adopted in the study. It can be noted that this form accommodates the simplified exact drag law and can be also used as an arbitrary approximation of the drag law (the speeds in all directions are included). Because of this robust property, this approximated form of the drag law is used within equations of motion [Eqs. (2. 5. 2. 1)-(2. 5. 2. 2)] when the droplet velocity and trajectory profiles in the air stream are developed. Two subsequent separated time integration processes of the equations of motion yield the velocity distributions in Eqs. (2. 5. 2. 6)-(2. 5. 2. 7) and droplet trajectories in Eqs. (2. 5. 2. 8)-(2. 5. 2. 9), presented below. The droplet velocity profiles are

$$v_{d,x}(t) = v_{a,x} + \frac{[v_{d,x}(t_0) - v_{a,x}]}{1 - \left(-\frac{6}{8} C_D \frac{\rho_a}{\rho_d D_d}\right) (t - t_0) [v_{d,x}(t_0) - v_{a,x}]} \quad (2. 5. 2. 6)$$

$$v_{d,y}(t) = v_{a,y} + \frac{[v_{d,y}(t_0) - v_{a,y}]}{1 - \left(-\frac{6}{8} C_D \frac{\rho_a}{\rho_d D_d}\right) (t - t_0) [v_{d,y}(t_0) - v_{a,y}]} \quad (2. 5. 2. 7)$$

The solutions for droplet trajectories at an initial time $t_0 = 0$ are developed, such as

$$s_{d,x}(t) = s_{d,x}(t_0) + v_{a,x} t - \frac{1}{\left(-\frac{6}{8} C_D \frac{\rho_a}{\rho_d D_d}\right) C} [v_{d,x}(t_0) - v_{a,x}] \text{LN} \left[-\left(-\frac{6}{8} C_D \frac{\rho_a}{\rho_d D_d}\right) C t + 1 \right] \quad (2. 5. 2. 8)$$

Chapter 2-MODELING OF MULTIPHASE MOTION WITH DROPLET FLOW AND ICING

$$s_{d,y}(t) = s_{d,y}(t_0) + v_{a,y}t$$

$$- \frac{1}{\left(-\frac{6}{8}C_D \frac{\rho_a}{\rho_d D_d}\right) C} [v_{d,y}(t_0) - v_{a,y}] \text{LN} \left[-\left(-\frac{6}{8}C_D \frac{\rho_a}{\rho_d D_d}\right) C t + 1 \right].$$

(2. 5. 2. 9)

Parameter C represents a relative component velocity between the initial droplet velocity and air velocity. The C has a unit of $[m/s]$ (i.e. $C = 1 \text{ m/s}$).

(b) For low Reynolds number regimes ($Re_r < 1$, $C_D=24/Re_r$), the droplet velocity profiles are derived from Newton's law of motion [Eqs. (2. 5. 2. 1) - (2. 5. 2. 2), $g_y = 0$], i.e.,

$$v_{d,x}(t) = v_{a,x} + [v_{d,x}(t_0) - v_{a,x}] \text{EXP} \left[-\frac{18\mu_a}{\rho_d D_d^2} (t - t_0) \right] \quad (2. 5. 2. 10)$$

$$v_{d,y}(t) = v_{a,y} + [v_{d,y}(t_0) - v_{a,y}] \text{EXP} \left[-\frac{18\mu_a}{\rho_d D_d^2} (t - t_0) \right]. \quad (2. 5. 2. 11)$$

The solutions of the corresponding droplet trajectories are

$$s_{d,x}(t) = s_{d,x}(t_0) + v_{a,x}(t - t_0) + [v_{d,x}(t_0) - v_{a,x}] \left(-\frac{\rho_d D_d^2}{18\mu_a} \right) \times \text{EXP} \left(-\frac{18\mu_a t_0}{\rho_d D_d^2} \right) \left[\text{EXP} \left(-\frac{18\mu_a t}{\rho_d D_d^2} \right) - \text{EXP} \left(-\frac{18\mu_a t_0}{\rho_d D_d^2} \right) \right] \quad (2. 5. 2. 12)$$

$$s_{d,y}(t) = s_{d,y}(t_0) + v_{a,y}(t - t_0) + [v_{d,y}(t_0) - v_{a,y}] \left(-\frac{\rho_d D_d^2}{18\mu_a} \right) \times \text{EXP} \left(-\frac{18\mu_a t_0}{\rho_d D_d^2} \right) \left[\text{EXP} \left(-\frac{18\mu_a t}{\rho_d D_d^2} \right) - \text{EXP} \left(-\frac{18\mu_a t_0}{\rho_d D_d^2} \right) \right]. \quad (2. 5. 2. 13)$$

If only gravity acts on the droplet, droplet y -velocity and droplet trajectory become

$$v_{d,y}(t) = v_{d,y}(t_0) - g_y t \quad (2.5.2.14)$$

$$s_{d,y}(t) = s_{d,y}(t_0) + v_{d,y}t + \frac{g_y}{2} \left[\frac{s_{d,x} - s_{d,x}(t_0)}{v_{d,x}} \right]^2 \quad (2.5.2.15)$$

(ii) Case 2

Consider another example with a droplet flowing through air under the influence of gravity ($g_y \neq 0$) in vertical plane x - y . A Lagrangian analytical formulation of droplet/air motion over a range of relative Reynolds numbers (Re_r) is derived. Consider a force balance with interfacial drag and gravity acting on a droplet (subscript d) in the airstream (subscript a) in high Re_r and low Re_r number multiphase regimes.

(a) For high Reynolds number multiphase regimes ($Re_r < 1000$, i.e. $C_D=0.3$), the droplet is flowing in quiescent air ($\vec{v}_a = \vec{0}$) and the initial time is set to zero value ($t_0 = 0$). In this case, an approximate form of the drag law is adopted within Eq. (2.5.

2.3) to yield drag in i -th direction $F_{D,i} = \frac{\rho_a (v_{d,i} - v_{a,i})^2}{2} C_D \frac{\pi D_d^2}{4}$. It can be noted

that this approximate form of drag law does not include the cross drag term (with two-phase velocities in each direction). The cross drag term would couple the multiphase droplet momentum equations into a system of non-linear differential equations. Rather, the approximate form of drag law considers the relative velocities between droplet and air in each direction separately. Since in this case study air is assumed stationary, only a dispersed part of the cross drag term is lost. For multiphase droplet flow with moderate inertia, a non-linear aspect of the drag law is not significant and the errors due to the approximate form of the drag law are viewed to be acceptable (i.e. referred to the comparisons with the experimental results).

Chapter 2-MODELING OF MULTIPHASE MOTION WITH DROPLET FLOW AND ICING

Newton's law of droplet motion in moving air [Eqs. (2. 5. 2. 1) - (2. 5. 2. 2), $g_y \neq 0$] subject to the approximate form of drag law is integrated over time to yield the velocity distribution

$$v_{d,x}(t) = v_{a,x} + \frac{v_{d,x}(t_0)}{1 - \left(-\frac{6}{8} C_D \frac{\rho_a}{\rho_d D_d} \right) (t - t_0) v_{d,x}(t_0)} \quad (2. 5. 2. 16)$$

$$v_{d,y}(t) = v_{d,y}(t_0) + \sqrt{\frac{g}{\frac{6}{8} C_D \frac{\rho_a}{\rho_d D_d}}} \operatorname{TANH} \left(\frac{6}{8} C_D \frac{\rho_a}{\rho_d D_d} \sqrt{\frac{g}{\frac{6}{8} C_D \frac{\rho_a}{\rho_d D_d}}} t \right). \quad (2. 5. 2. 17)$$

For the droplet velocity in y -direction, an alternative equation is developed, yielding

$$v_{d,y}(t) = \frac{\sqrt{\frac{g}{\frac{6}{8} C_D \frac{\rho_a}{\rho_d D_d}}} \left[\frac{\left(1 + \frac{v_{d,y}(t_0)}{\sqrt{\frac{g}{\frac{6}{8} C_D \frac{\rho_a}{\rho_d D_d}}}} \right)}{\left(1 - \frac{v_{d,y}(t_0)}{\sqrt{\frac{g}{\frac{6}{8} C_D \frac{\rho_a}{\rho_d D_d}}}} \right)} \operatorname{EXP} \left(2 \frac{6}{8} C_D \frac{\rho_a}{\rho_d D_d} \sqrt{\frac{g}{\frac{6}{8} C_D \frac{\rho_a}{\rho_d D_d}}} t \right) - 1 \right]}{1 + \frac{\left(1 + \frac{v_{d,y}(t_0)}{\sqrt{\frac{g}{\frac{6}{8} C_D \frac{\rho_a}{\rho_d D_d}}}} \right)}{\left(1 - \frac{v_{d,y}(t_0)}{\sqrt{\frac{g}{\frac{6}{8} C_D \frac{\rho_a}{\rho_d D_d}}}} \right)} \operatorname{EXP} \left(2 \frac{6}{8} C_D \frac{\rho_a}{\rho_d D_d} \sqrt{\frac{g}{\frac{6}{8} C_D \frac{\rho_a}{\rho_d D_d}}} t \right)} \quad (2. 5. 2. 18)$$

Chapter 2-MODELING OF MULTIPHASE MOTION WITH DROPLET FLOW AND ICING

The droplet positions in x - and y -directions represent the trajectories for droplet motion in air stream. This analytical trajectory becomes

$$s_{d,x}(t) = s_{d,x}(t_0) + v_{a,x}t - \frac{\rho_d D_d}{\frac{6}{8} C_D \rho_a C} [v_{a,x} - v_{d,x}(t_0)] \text{LN} \left(\frac{\frac{6}{8} C_D \rho_a v_{d,x}(t_0)}{\rho_d D_d} t + I \right) \quad (2.5.2.19)$$

$$s_{d,y}(t) = s_{d,y}(t_0) + v_{d,y}(t_0) t + \frac{I}{\frac{6}{8} C_D \frac{\rho_a}{\rho_d D_d}} \left\{ \text{LN} \left[\text{COSH} \left(\frac{6}{8} C_D \frac{\rho_a}{\rho_d D_d} \sqrt{\frac{g}{\frac{6}{8} C_D \frac{\rho_a}{\rho_d D_d}}} t \right) \right] \right\}. \quad (2.5.2.20)$$

(b) For low Reynolds number regimes ($Re_r < 1$, $C_D=24/Re_r$), integrating Newton's law of motion [Eqs. (2.5.2.1) - (2.5.2.2), $g_y \neq 0$] over time yields two separate equations for the droplet velocity field,

$$v_{d,x}(t) = v_{a,x} + [v_{d,x}(t_0) - v_{a,x}] \text{EXP} \left[-\frac{18\mu_a}{\rho_d D_d^2} (t - t_0) \right] \quad (2.5.2.21)$$

$$v_{d,y}(t) = v_{a,y} + g \frac{\rho_d D_d^2}{18\mu_a} + \left[v_{d,y}(t_0) - v_{a,y} - g \frac{\rho_d D_d^2}{18\mu_a} \right] \text{EXP} \left[\frac{18\mu_a}{\rho_d D_d^2} (t_0 - t) \right]. \quad (2.5.2.22)$$

The droplet positions in x - and y -directions become

$$s_{d,x}(t) = s_{d,x}(t_0) + v_{a,x} (t - t_0) + [v_{d,x}(t_0) - v_{a,x}] \left(-\frac{\rho_d D_d^2}{18\mu_a} \right) \times \text{EXP} \left(-\frac{18\mu_a t_0}{\rho_d D_d^2} \right) \left[\text{EXP} \left(-\frac{18\mu_a t}{\rho_d D_d^2} \right) - \text{EXP} \left(-\frac{18\mu_a t_0}{\rho_d D_d^2} \right) \right] \quad (2.5.2.23)$$

$$\begin{aligned}
 s_{d,y}(t) = & s_{d,y}(t_0) + v_{a,y}(t - t_0) + \frac{\rho_d D_d^2}{18\mu_a} g (t - t_0) \\
 & + \left[v_{d,y}(t_0) - v_{a,y} - \frac{\rho_d D_d^2}{18\mu_a} g \right] \left(-\frac{\rho_d D_d^2}{18\mu_a} \right) \\
 & \times \text{EXP} \left(\frac{18\mu_a}{\rho_d D_d^2} t_0 \right) \left[\text{EXP} \left(-\frac{18\mu_a}{\rho_d D_d^2} t \right) - \text{EXP} \left(-\frac{18\mu_a}{\rho_d D_d^2} t_0 \right) \right].
 \end{aligned}
 \tag{2. 5. 2. 24}$$

(iii) Case 3

In a third example, the droplet is falling through a quiescent ambient air. Two velocity solutions are obtained: droplet reaching the terminal velocity and droplet impact on a wall. Different drag models are enabled in the drag coefficient, C_D .

(a) Balancing the upward force and drag with the weight of the spherical droplet, the following expression for the droplet terminal velocity is obtained,

$$v_t = + \sqrt{\left\{ \frac{8}{\rho_a C_D} \left[\frac{g D_d}{6} (\rho_d - \rho_a) \right] \right\}}.
 \tag{2. 5. 2. 25}$$

Balancing the upward and drag forces with the weight of a cylinder (representing a vertical jet flow), yields the following expression for the terminal velocity,

$$v_t = + \sqrt{\left\{ \frac{2}{\rho_a C_D} \left[g L (\rho_j - \rho_a) \right] \right\}}.
 \tag{2. 5. 2. 26}$$

where ρ_j represents the specific density of a jet (flow).

diameter in the airstream, smaller interfacial drag occurs. As a result, the droplet reaches a smaller distance into the airstream, as opposed to the larger droplet. Also, the thermophysical properties for the moist air are functions of temperature. They usually need to be determined from physical experiments.

2. 5. 3 ICE INTERFACE TRACKING

METHOD

In this final section of Chapter (2), a mathematical formulation of ice interface tracking is presented. In order to facilitate better understanding in upcoming chapters, the discussion is given in a context of a Control-Volume Based Finite Element Method (*CVFEM*).

Consider incoming droplets impacting on a solid surface (i.e., wall or ice interface). After impact, the droplets adhere to the solid surface(s) and create ice. The ice gradually fills an area and produces a typical two-dimensional ice interface. Various multiphase processes at the interface affect the ice shape evolution. In this section, two parameters are introduced for modeling of these ice evolution processes: 1) a pre-conditioned parameter (*Pfl*) and 2) an excess volume fraction (*EBeta*). A special value is assigned to these parameters within each time step and volume fraction iteration. When conditions for ice growth are established, *Pfl* is given a special value of 0, which allows ice growth. The ice gradually fills appropriate neighboring control volumes, while maintaining a unit value for the ice volume fraction in those iced control volumes. The excess amount of accumulated ice (when the volume fraction exceeds 1) must be spatially re-distributed into the detected neighboring control volumes.

Detection of potentially iced areas and transfer of excess ice are predicted as a function of direction and magnitude of the incoming droplet flow. Figure (2. 5. 3)

AND ICING

(b) The expression for impact velocity of an object as a function of vertical distance from the horizontal wall, y_0 , is obtained as follows,

$$v_{imp} = +v_t \sqrt{1 - \text{EXP}\left(-\frac{2g y_0}{v_t^2}\right)}. \quad (2.5.2.27)$$

These expressions are used in upcoming chapters for analytical studies of Lagrangian multiphase droplet/air tracking, involving numerical and experimental validations of Eulerian tracking of droplet and liquid jet flows in the air.

(iv) Case 4

This final example involves droplet evaporation. Evaporative effects and effects of varying thermophysical properties on droplet motion are studied analytically in this sub-section.

Evaporative cooling (evaporation) is a phase change process. It develops when the gas molecules exchange mechanical energy and thermal energy with the molecules on the surface of a liquid. In this study, the uniform air (gas) stream flows over the droplet (liquid) surface [see Fig. (5.1.6)]. When the energy received by the air is greater than the energy required to sustain the liquid phase together, evaporation from the droplet surface occurs. The latent heat of vaporization of liquid is released from the liquid surface, in order to make phase change possible. The evaporation affects the droplet diameter and its trajectory through the streaming air. The vaporization of the droplet can be simulated by a decreasing droplet diameter in time, i.e.,

$$D_d(t) = 2 \left[0.5(10^{-5}) - (10^{-6})t \right]. \quad (2.5.2.28)$$

The droplet diameter is a function of time, $D_d(t)$. At high-Re numbers, the evaporation is more significant than at low-Re regimes. Due to the reduced droplet

Chapter 2-MODELING OF MULTIPHASE MOTION WITH DROPLET FLOW AND ICING

presents a typical arrangement of interconnected control volumes (*CV*) and finite elements (*FE*) with corresponding nodal droplet velocities. The local coordinate system is placed in each *FE*, while the global coordinate system is placed outside the grid. The control volume nodes are numbered locally (i. e. $i=1, 2, 3, 4$) and globally with respect to the computational domain. The position vectors $\vec{r}_i, \vec{r}_{n+1}, \vec{r}_{n+2}$ and \vec{r}_{n+3} point from the origin of the global coordinate system to each local node of the *CV* under consideration [see Fig. (2. 5. 3); local node $n = 1$]. The position vector \vec{r}_{n+1} points to local node 2, position vector \vec{r}_{n+2} points to local node 3 and position vector \vec{r}_{n+3} points to local node 4.

Droplets impact onto an arbitrary wall with a full volume-averaged droplet velocity $\langle \vec{v}_d \rangle$. Figure (2. 5. 3) presents an example of the central control volume under examination, i , and its surrounding control volumes, at a certain time and certain iteration of a volume fraction. The algorithm searches a range of relative angles between the incoming droplet velocities and nodal distances ($\vec{d}_{n+1}, \vec{d}_{n+2}, \vec{d}_{n+3}$) from the local node under consideration, within each finite element. The algorithm creates a dot product between the incoming velocity and position vectors, i.e.,

$$\langle \vec{v}_d \rangle_i \cdot \vec{d}_{n+1} = \left| \langle \vec{v}_d \rangle_i \right| \left| \vec{d}_{n+1} \right| \cos(|\theta_i - \theta_{n+1}|), \quad (2. 5. 3. 1)$$

In component form, Eq. (2. 5. 3. 1) yields:

$$\begin{aligned} \begin{Bmatrix} \langle v_d \rangle_{i,x} \\ \langle v_d \rangle_{i,y} \end{Bmatrix} \begin{Bmatrix} r_{n,x} - r_{n+1,x} \\ r_{n,y} - r_{n+1,y} \end{Bmatrix} = \\ \sqrt{\langle v_d \rangle_{i,x}^2 + \langle v_d \rangle_{i,y}^2} \cdot \sqrt{(r_{n,x} - r_{n+1,x})^2 + (r_{n,y} - r_{n+1,y})^2} \cos(|\theta_i - \theta_{n+1}|) \end{aligned} \quad (2. 5. 3. 2)$$

The algorithm considers two limited cases, such as:

Chapter 2-MODELING OF MULTIPHASE MOTION WITH DROPLET FLOW AND ICING

$$\cos(\theta_i - \theta_{n+1}) = 1 \Rightarrow \chi = \frac{\langle \vec{v}_d \rangle_i \cdot \vec{d}_{n+1}}{\|\langle \vec{v}_d \rangle_i\| \|\vec{d}_{n+1}\|} = 1 \quad (2.5.3.3)$$

$$\cos(\theta_i - \theta_{n+1}) = 0 \Rightarrow \chi = \frac{\langle \vec{v}_d \rangle_i \cdot \vec{d}_{n+1}}{\|\langle \vec{v}_d \rangle_i\| \|\vec{d}_{n+1}\|} = 0 \quad (2.5.3.4)$$

The processes of *Pfl* conditioning and *EBeta* re-distribution between the limits [Eqs. (2.5.3.3) – (2.5.3.4)] are controlled by two generated functions. These functions are presented in Figs. (2.5.3.1) – (2.5.3.2). The functions for *Pfl* and *Ebeta* in Figs. (2.5.3.1) – (2.5.3.2) are needed in the icing algorithm for backward ice tracking. They can be additionally modeled for specific physical processes related to the ice interface evolution. These icing processes are problem-dependent and they generally need to be studied in conjunction with experimental data. They depend on many parameters, such as the size and shape of droplets and shape of the accreted ice, as well as the precipitation rate of the incoming dispersed flow, and droplet impact velocity.

For validation purposes, analytical solutions of the ice interface motion were established based on the analytical solution of droplet trajectories for rime ice. Figure (2.5.3.3) represents a sample case of idealized two-dimensional ice interface evolution at a time of $t = 0.04$ s. The inlet droplet velocity is $u_d = 2.50$ s. This interface is obtained solely based on the analytical droplet trajectories [Eqs. (2.5.2.1) - (2.5.2.2)]. In this case, there is no influence of the phase volume fraction (droplet influx) on the evolving interface. This case represents only the introductory schematics.

The two-dimensional analytical solutions for ice interface propagation for the case in Fig. (5.4.14) is given by the following expressions

$$f(x, n) = \begin{cases} \xi(x), & x_0 \leq x \leq x_1 \\ \zeta(x, n), & x = x_1, n \in \mathbb{N} \end{cases} \quad (2.5.3.5)$$

Chapter 2-MODELING OF MULTIPHASE MOTION WITH DROPLET FLOW
AND ICING

$$\xi(x) = (0.676)x + (-3.357)x^2 + (8.706)x^3 + (-7.415)x^4 \quad (2.5.3.6)$$

$$\zeta(x, n) = \xi(x) + h_1(n) \quad (2.5.3.7)$$

$$h_1(n) = 0.083n \quad (2.5.3.8)$$

$$x_1 = 0.720 \quad (2.5.3.9)$$

This analytical solution corresponds to the ice interface at a time of $t = 700$ s.

CHAPTER 3

NUMERICAL FORMULATION OF CONTROL-VOLUME BASED FINITE ELEMENT METHOD (CVFEM) FOR MULTIPHASE ICING PREDICTIONS

In this chapter, a numerical formulation for the volume averaged, dispersed (droplet) and carrier (air) phases is developed with a Control-Volume Based Finite-Element Method (*CVFEM*). The formulation performs spatial averaging of droplets within a control volume centered around a node in the finite element mesh. The computational domain is sub-divided into quadrilateral, bi-linear finite elements. The governing discrete equations are obtained by spatial integration of the multiphase

equations over discrete control volumes (*CVs*) and time steps. These equations are developed locally within each element and independently of the overall mesh configuration. The motion of the supercooled droplets is controlled by droplet-air phase interactions, viscous effects, body forces and boundary conditions at droplet / wall or droplet / ice interface impact. As mentioned in section (2. 1), the multiphase dispersed flow with water droplets is assumed non-dilute in the numerical simulations. Excluding an initial droplet volume fraction of $\beta_d = 0$ in the computational domain, the droplet volume fraction in the simulations was in a range of $\beta_{d,IN} = 0.0001 \leq \beta_d \leq \beta_{d-ice} = 1$. Other droplet interactions with the phases are not additionally modeled in the governing transport equations.

In the following section, preliminary definitions and notations for the *CVFEM* are described.

3. 1 DEFINITIONS AND NOTATION

The computational domain is sub-divided into quadrilateral, bi-linear finite elements. For the *CVFEM*, a corner node of a finite element represents the center point of a corresponding control volume [see (Fig. 3. 1. 1)]. Isoparametric quadrilateral finite elements are used in this thesis, with bi-linear approximation of the physical and geometrical variables. Each finite element is sub-divided into four internal *Sub-Control Volumes (SCV)*. Each *SCV* belongs to a corresponding full control volume associated with the central node. At the boundaries of the problem domain, a boundary of the *SCV* coincides with the finite element exterior boundaries.

Local coordinates at the surfaces of the *SCV* are defined by $s = 0$ and $t = 0$. The physical variables of interest, such as a general scalar variable, (s, t) , and

spatial coordinates, i.e., $x(s,t)$ and $y(s,t)$, of any point within the finite element are interpolated with bi-linear shape functions and with nodal values, ψ_i , or global coordinates, x_i and y_i , as follows:

$$(s,t) = \sum_{i=1}^4 N_i(s,t)\psi_i \quad (3.1.1)$$

$$x(s,t) = \sum_{i=1}^4 N_i(s,t)x_i \quad (3.1.2)$$

$$y(s,t) = \sum_{i=1}^4 N_i(s,t)y_i. \quad (3.1.3)$$

The interpolation shape functions, $N_i(s,t)$, are expressed in terms of local geometrical coordinates, s and t . With reference to the control volume in Fig. (3.1.1):

$$N_1(s,t) = \frac{1}{4}(1+s)(1+t) \quad (3.1.4)$$

$$N_2(s,t) = \frac{1}{4}(1-s)(1+t) \quad (3.1.5)$$

$$N_3(s,t) = \frac{1}{4}(1-s)(1-t) \quad (3.1.6)$$

$$N_4(s,t) = \frac{1}{4}(1+s)(1-t). \quad (3.1.7)$$

These shape functions are needed for interpolation of dependent variables and geometrical coordinates at internal positions within a finite element. The shape functions give a geometrical weighting for the dependent and geometrical quantities, based on the distance between nodal and internal points. Using the shape functions,

the local coordinates within a finite element, (s, t) , can be expressed with respect to the global coordinate system, (x, y) .

The final global system of equations, for all physical quantities at the centers of the control volumes, can be written in the following matrix form

$$[A]\{x\} = \{b\}, \quad (3.1.8)$$

where $\{x\}$ and $\{b\}$ represent the vector of unknowns (solutions) and the vector of known physical quantities (i.e. boundary conditions). Since the global matrix $[A]$ is typically banded for a finite element formulation, it can be readily solved with a direct solver. Faster calculations for a large system of equations (i.e. typically more than 3,000 nodes) would require an iterative solver.

Derivatives of the scalar physical quantity (i.e. components of a dispersed phase velocity) at any location within the *SCV* can be expressed in terms of their nodal values through the shape functions. For the x -direction and y -direction:

$$\frac{\partial \psi(s, t)}{\partial x} = \sum_{i=1}^4 \frac{\partial N_i(s, t)}{\partial x} \psi_i \quad (3.1.9)$$

$$\frac{\partial \psi(s, t)}{\partial y} = \sum_{i=1}^4 \frac{\partial N_i(s, t)}{\partial y} \psi_i. \quad (3.1.10)$$

The derivatives of the shape functions are expressed in the following relation:

$$\begin{Bmatrix} \frac{\partial N_i(s, t)}{\partial x} \\ \frac{\partial N_i(s, t)}{\partial y} \end{Bmatrix} = \frac{1}{\text{Det}[J]} \begin{vmatrix} \frac{\partial y}{\partial t} & -\frac{\partial y}{\partial s} \\ -\frac{\partial x}{\partial t} & \frac{\partial x}{\partial s} \end{vmatrix} \begin{Bmatrix} \frac{\partial N_i(s, t)}{\partial s} \\ \frac{\partial N_i(s, t)}{\partial t} \end{Bmatrix}, \quad (3.1.11)$$

where the determinant of the Jacobian transformation in Eq. (3.1.11) is defined as follows:

$$Det[J] \equiv \frac{\partial x}{\partial s} \frac{\partial y}{\partial t} - \frac{\partial y}{\partial s} \frac{\partial x}{\partial t} \quad (3.1.12)$$

The outward normal surface vector is presented for a two-dimensional control volume, acting outwards at its *Sub - Surface (SS)*, i.e.,

$$\Delta \vec{n} = \Delta y \vec{i} - \Delta x \vec{j} \quad (3.1.13)$$

Typically, it is used in evaluation of momentum fluxes at the integration points of the *SS*. The elemental volume within the finite element (or the *SCV*) is defined as

$$dV = |Det[J]| ds dt \quad (3.1.14)$$

In this notation, the surface momentum terms (called momentum fluxes across the *SS*) act perpendicular to the *SS*, at an "integration point". Incoming fluxes are directed into a particular *SCV* (i.e. $Q_{2,I}$), whereas the outgoing fluxes point out of a particular *SCV* (i.e. $Q_{4,I}$). The volumetric forces act directly at the center of the *CV*.

The *CVFEM* formulation is element based, so the local stiffness equations become independent of the grid structure in a computational domain. This provides a useful benefit over other conventional finite volume or finite difference methods, where the discretized equations are derived for a particular grid format in the computational domain. Due to this grid flexibility, the *CVFEM* is suitable for distorted geometries with unstructured grids.

3. 2 SCALED FORM OF DISPERSED FLOW MOMENTUM EQUATIONS

In the numerical formulation, scaling and non-dimensionalization are performed before the equations are fully discretized. This scaling is performed for purposes of creating better numerical stability, solution convergence, and flexibility for testing various ranges of flow conditions. Dependent variables are non-dimensionalized with respect to certain reference values, which are selected from input data involving the actual physical problem. The time, spatial coordinates and velocities are scaled as follows:

$$t = t^* t_{ref} \quad (3. 2. 1)$$

$$x = x^* l_{ref}; \quad y = y^* l_{ref} \quad (3. 2. 2)$$

$$\langle v_x \rangle = \langle v_x \rangle^* \langle v_x \rangle_{ref}; \quad \langle v_y \rangle = \langle v_y \rangle^* \langle v_y \rangle_{ref}. \quad (3. 2. 3)$$

In Eqs (3. 2. 1 – 3. 2. 3), the dimensional variables of time, coordinates and volume averaged velocities are denoted by t , x , y , $\langle v_x \rangle$ and $\langle v_y \rangle$, respectively. The non-dimensional values are designated with an asterisk superscript, while reference values are denoted by subscript “ ref ”.

Then, individual terms in the volume averaged momentum equations can be evaluated, provided that empirical correlations for the interfacial drag terms are supplied [5]. These substitutions are performed and each term is non-dimensionalized, so that the x -momentum equation becomes

$$\frac{\partial \beta_d \rho_d^* \langle v_{d,x} \rangle^*}{\partial t^*} + \langle v_{d,x} \rangle^* \frac{\partial \beta_d \rho_d^* \langle v_{d,x} \rangle^*}{\partial x^*} - \langle v_{d,y} \rangle^* \frac{\partial \beta_d \rho_d^* \langle v_{d,x} \rangle^*}{\partial y^*} = -\beta_d \frac{\partial}{\partial x^*} \langle p_d \rangle^*$$

$$\begin{aligned}
 & + \frac{18l_{ref}^2 \beta_d \mu_a}{Re_{ref} D_d^2 \mu_d} \left(\langle v_{a,x} \rangle^* - \langle v_{d,x} \rangle^* \right) \left(1 + 0.15 \left(6.3 \sqrt{\left(\langle v_{a,x} \rangle^* - \langle v_{d,x} \rangle^* \right)^2 + \left(\langle v_{a,y} \rangle^* - \langle v_{d,y} \rangle^* \right)^2} \langle |\bar{v}_d| \rangle_{ref} \right) \right)^{0.687} \\
 & + \frac{18l_{ref}^2 \beta_d \mu_a}{Re_{ref} D_d^2 \mu_d} \left(\langle v_{a,x} \rangle^* - \langle v_{d,x} \rangle^* \right) \\
 & \times \left[\begin{aligned}
 & \left(0.0175 \left(6.3 \sqrt{\left(\langle v_{a,x} \rangle^* - \langle v_{d,x} \rangle^* \right)^2 + \left(\langle v_{a,y} \rangle^* - \langle v_{d,y} \rangle^* \right)^2} \langle |\bar{v}_d| \rangle_{ref} \right) \right. \\
 & \left. \times \left[1 + 42,500 \left(6.3 \sqrt{\left(\langle v_{a,x} \rangle^* - \langle v_{d,x} \rangle^* \right)^2 + \left(\langle v_{a,y} \rangle^* - \langle v_{d,y} \rangle^* \right)^2} \langle |\bar{v}_d| \rangle_{ref} \right)^{-1.16} \right] \right)
 \end{aligned} \right] \\
 & + \frac{\beta_d \mu_d^*}{Re_{ref}} \left(\frac{\partial^2 \langle v_{d,x} \rangle^*}{\partial x^{*2}} + \frac{\partial^2 \langle v_{d,x} \rangle^*}{\partial y^{*2}} \right) + \left(\frac{l_{ref}}{\langle |\bar{v}_d| \rangle_{ref}^2} \right) \langle g_x \rangle^* . \tag{3. 2. 4}
 \end{aligned}$$

The normalized equation, Eq. (3. 2. 4), contains the bulk pressure term to accommodate the pressure gradient of the droplet phase. The dispersed pressure term is numerically formulated as a flux, acting on the sub-surfaces of the control volume [see Eq. (3. 3. 1. 6), Eq. (3. 3. 1. 9) and Eq. (3. 3. 1. 10) below]. In the numerical simulations, the pressure terms of the dispersed (droplet) and carrier (air) phases are assumed to be equal. This corresponds to a variety of realistic situations, involving the interactions between phases [i.e. helicopter downwash effects, where the droplets are immersed and carried with(in) the air flow]. The dispersed phase system of equations is closed. The continuous (air) pressure term is placed in a location of the dispersed pressure term. In the absence of air, the dispersed pressure gradient is zero. The pressure term of the carrier phase (i.e. air) is formulated within the original *Phases* program (see Ref. [11]). It is calculated based on a simultaneous solution of the mass and momentum equations in the carrier phase. The pressure is not recovered from the velocity field at the nodes explicitly. Rather, the pressure term is formulated and solved directly from the continuity equation, which relates the mass flux across the surface of a control volume to the nodal pressures. Local changes in density due to droplets are accommodated by the mass transport equation for droplets, which tracks variations of droplet volume fraction throughout the flow field.

Similarly, in the y -direction,

$$\begin{aligned}
 & \frac{\partial \beta_d \rho_d \langle v_{d,y} \rangle^*}{\partial t^*} + \langle v_{d,x} \rangle^* \frac{\partial \beta_d \rho_d \langle v_{d,y} \rangle^*}{\partial x^*} - \langle v_{d,y} \rangle^* \frac{\partial \beta_d \rho_d \langle v_{d,y} \rangle^*}{\partial y^*} = -\beta_d \frac{\partial}{\partial y^*} \langle p_d \rangle^* \\
 & + \frac{18 l_{ref}^2 \beta_d \mu_a}{Re_{ref} D_d^2 \mu_d} \left(\langle v_{a,y} \rangle^* - \langle v_{d,y} \rangle^* \right) \left(1 + 0.15 \left(6.3 \sqrt{\left(\langle v_{a,x} \rangle^* - \langle v_{d,x} \rangle^* \right)^2 + \left(\langle v_{a,y} \rangle^* - \langle v_{d,y} \rangle^* \right)^2} \langle |\bar{v}_d| \rangle_{ref} \right) \right)^{0.687} \\
 & + \frac{18 l_{ref}^2 \beta_d \mu_a}{Re_{ref} D_d^2 \mu_d} \left(\langle v_{a,y} \rangle^* - \langle v_{d,y} \rangle^* \right) \\
 & \times \left[\begin{aligned} & 0.0175 \left(6.3 \sqrt{\left(\langle v_{a,x} \rangle^* - \langle v_{d,x} \rangle^* \right)^2 + \left(\langle v_{a,y} \rangle^* - \langle v_{d,y} \rangle^* \right)^2} \langle |\bar{v}_d| \rangle_{ref} \right) \\ & \times \left[1 + 42,500 \left(6.3 \sqrt{\left(\langle v_{a,x} \rangle^* - \langle v_{d,x} \rangle^* \right)^2 + \left(\langle v_{a,y} \rangle^* - \langle v_{d,y} \rangle^* \right)^2} \langle |\bar{v}_d| \rangle_{ref} \right)^{-1.16} \right] \end{aligned} \right] \\
 & + \frac{\beta_d \mu_d}{Re_{ref}} \left(\frac{\partial^2 \langle v_{d,y} \rangle^*}{\partial x^{*2}} + \frac{\partial^2 \langle v_{d,y} \rangle^*}{\partial y^{*2}} \right) + \left(\frac{l_{ref}}{\langle |\bar{v}_d| \rangle_{ref}^2} \right) \langle g_y \rangle^* . \tag{3.2.5}
 \end{aligned}$$

The reference Reynolds number is defined as

$$Re_{ref} = \frac{\rho_{d,ref} l_{ref} \langle |\bar{v}_d| \rangle_{ref}}{\mu_{d,ref}} . \tag{3.2.6}$$

The reference dispersed phase velocity, $\langle |\bar{v}_d| \rangle_{ref}$, is defined based on the specific problem. For example, $\langle |\bar{v}_d| \rangle_{ref} = |\bar{v}_d|_{in}$ (inlet velocity) is used for incoming droplets in external flow problems.

3. 3 DISCRETIZATION OF DISPERSED FLOW MOMENTUM EQUATIONS

In this section, discretization of the dispersed phase momentum equations is presented. These equations are developed by spatial integration of the equations over a discrete control volume. Approximations for discrete fluxes and source terms are presented. In addition, implementation of the drag term is given and boundary conditions are presented. Code implementation is presented with other important issues regarding the numerical algorithms.

Since the momentum equations are written in a divergence (conservation) form, the Gauss theorem of calculus can be used to transform the integrated divergence terms to surface momentum fluxes. Performing spatial integration over a discrete control volume, V , yields the following system of integral equations for the dispersed phase momentum equations:

$$\begin{aligned} & \iiint_V \frac{\partial}{\partial t} [\beta_d \rho_d \langle v_{d,i} \rangle] dV + \iint_S [\beta_d \rho_d \langle v_{d,j} \rangle \langle v_{d,i} \rangle] dn_j = \\ & \frac{1}{V} \iiint_V [\sum v_i m_i] dV - \beta_d \iint_S \langle p_d \rangle dn_j + \beta_d \iint_S [\langle \tau_{d,ij} \rangle + \langle \tau_{d,ji} \rangle] dn_j - \\ & \iint_S [\beta_d \rho_d \langle \delta v_{d,j} \delta v_{d,i} \rangle] dn_j - \iiint_V \beta_{v,i} [\langle v_{d,i} \rangle - \langle v_{a,i} \rangle] dV + \iiint_V [\beta_d \rho_d \langle g_i \rangle] dV. \end{aligned} \quad 3. 3. 1. 1)$$

Modeling of individual terms in this equation will now be considered.

(i) Transient Term

The lumped mass approach is adopted for this term. The dispersed volume averaged velocities are placed at the center of CV , yielding

$$\iiint_{SCV_I} \frac{\partial}{\partial t} [\beta_d \rho_d \langle v_{d,x} \rangle] dV = \beta_d \rho_d \left[\frac{\langle v_{d,x} \rangle_I - \langle v_{d,x} \rangle_I^0}{\Delta t} \right]. \quad (3.3.1.2)$$

The transient term is evaluated with a backward difference scheme in time. The formulation of the term is first-order accurate. It uses a “lumped mass” approximation with implicit evaluation of all flux terms. The spatially integrated transient term contains the droplet velocities at both current and previous time steps. An implicit time-marching scheme is adopted. Unlike a second-order Crank-Nicholson scheme, this scheme provides a stable performance without requiring additional storage of flux terms and nodal values at an intermediate time level. The most sensitive phase in the multiphase flow simulations with icing dictates the numerical computation with a constant time step. Therefore, the same time step for all phases was selected based on the most sensitive phase (air) in the contact with the other phases in the computational domain and the smallest grid spacing (upper time step size estimate based on the Courant number).

(ii) Convection Terms

The convection terms in Eq. (3.3.1.1) are linearized by the convecting velocities at the old (previous) time iteration values. These velocities constitute a mass flux, which acts at the *SS*. Integration point values for the convecting velocity components are obtained from the interpolated nodal velocity values and integration point coefficients. These coefficients are calculated from the upstream and downstream positions on the finite element surfaces. These locations are passed by the streamlines of the flow, with an arbitrary angle.

When assembling the convective terms in Eq. (3.3.1.3) into the global system of equations, the integration point velocities must be related to corresponding nodal values. Many past schemes were developed for such relations. Some examples include the central difference scheme (*CDS*), upwind difference scheme (*UDS*) and the exponential difference scheme (*EDS*). They calculate the physical value at the

integration point by interpolation, using an upstream value (*UDS*), upstream and downstream adjacent nodal values (*CDS*) or a hybrid combination of these methods (*EDS*). The latter method provides a continuous transition between the former methods. However, these schemes lack information on certain physical processes at the integration points, such as transient and diffusion processes. Thus, this section uses a *PINS* scheme (Physical Influence Scheme) for all phases in contact. This scheme includes all transport processes from the momentum balances for each direction. Additional details regarding the *PINS* are documented in Ref. [6]. Then the convective term at the *SSI* becomes

$$\iint_{SSI} [\beta_d \rho_d \langle v_{d,j} \rangle \langle v_{d,x} \rangle] dn_j \approx \beta_d \rho_d \langle v_{d,x} \rangle^0 \langle v_{d,x} \rangle \Delta y - \beta_d \rho_d \langle v_{d,y} \rangle^0 \langle v_{d,x} \rangle \Delta x. \quad (3.3.1.3)$$

These terms would not appear in a Lagrangian tracking method. In this respect, the Eulerian method is more difficult. The multiphase convection terms cause more difficulties than a single phase formulation, due to cross-phase effects within a time step. If old values of the velocity are not updated with effects of the surrounding phase within a time step, the time step needs to be reduced. These velocities are additionally dependent on the integration point coefficients (discussed further after Eq. (3.3.1.7) in an upcoming section).

(iii) Diffusion Terms

Using the constitutive approximation for Newtonian fluids, the diffusion term can be approximated as follows,

$$\begin{aligned}
 & \iint_{SS1} \beta_d \mu_d \left[\frac{\partial \langle v_{d,i} \rangle}{\partial x_j} + \frac{\partial \langle v_{d,j} \rangle}{\partial x_i} \right] dn_j - \iint_{SS1} [\beta_d \rho_d \langle \delta v_{d,j} \delta v_{d,i} \rangle] dn_j \approx \\
 & 2\beta_d \mu_d \left[\frac{\partial \langle v_{d,x} \rangle}{\partial x_x} \right]_{ip1} \Delta y - \beta_d \mu_d \left[\frac{\partial \langle v_{d,x} \rangle}{\partial y} + \frac{\partial \langle v_{d,y} \rangle}{\partial x} \right]_{ip1} \Delta x \\
 & - [\beta_d \rho_d \langle \delta v_{d,j} \delta v_{d,i} \rangle]_{ip1} \Delta y + [\beta_d \rho_d \langle \delta v_{d,j} \delta v_{d,i} \rangle]_{ip1} \Delta x.
 \end{aligned} \tag{3.3.1.4}$$

The shape functions for the bi-linear quadrilateral elements are introduced in the gradient components of the Eq. (3.3.1.4), thereby yielding Eq. (3.3.1.5). The fluxes in this diffusion term are illustrated in Fig. (3.3.1.1). These momentum fluxes are calculated from the nodal point contributions and then placed at the integration points of the control volume. Apart from Refs. [19] - [24], this term is a newly modeled formulation of the dispersed phase diffusion term. If only one component of the dispersed phase velocity is expressed in the momentum equation, a simplified expression for the diffusion term can be obtained.

$$\begin{aligned}
 & \iint_{SS1} \beta_d \mu_d \left[\frac{\partial \langle v_{d,i} \rangle}{\partial x_j} + \frac{\partial \langle v_{d,j} \rangle}{\partial x_i} \right] dn_j - \iint_{SS1} [\beta_d \rho_d \langle \delta v_{d,j} \delta v_{d,i} \rangle] dn_j \approx \\
 & 2\beta_d \mu_d \left[\sum_{j=1}^4 \frac{\partial N_j}{\partial x_x} \langle v_{d,x} \rangle_j \right] \Delta y - \beta_d \mu_d \left\{ \sum_{j=1}^4 \left[\frac{\partial N_j}{\partial y} \langle v_{d,x} \rangle_j + \frac{\partial N_j}{\partial x} \langle v_{d,y} \rangle_j \right] \right\} \Delta x \\
 & - [\beta_d \rho_d \langle \delta v_{d,j} \delta v_{d,i} \rangle]_{ip1} \Delta y + [\beta_d \rho_d \langle \delta v_{d,j} \delta v_{d,i} \rangle]_{ip1} \Delta x.
 \end{aligned} \tag{3.3.1.5}$$

(iv) Pressure Term

CVFEM modeling of this term also represents a new contribution over past methods. It is calculated at the sub-surfaces of the sub-control volume as follows,

$$\beta_d \iint_{SS1} \langle p_d \rangle dn_j \approx \beta_d \langle p_d \rangle \Delta y \tag{3.3.1.6}$$

For moderate relative *Re*-number flows, the pressure in both phases in contact is similar. But if the phases in contact move with different speeds or at different angles, this pressure becomes much different. Pressures in both phases may not have enough time to adjust themselves in each phase. For example, if the dispersed phase moves away from the carrier phase, it starts creating a lower pressure next to the other phase. As a result, the phase lowers its pressure by mass replacement, while the other phase opposes this adjustment. The phases start adjusting to the pressure losses at the interface, while deforming the interface. In this thesis, the dispersed phase is modeled with spherical droplets. Their shape (interfaces) is not deformed.

(v) Source Terms

The source terms, such as drag and gravity are calculated at the centers of the *SCVs*. For the *x*-dispersed momentum equation, the source term becomes

$$\frac{1}{V} \iiint_{SCV1} [\sum v_x \dot{m}_d] dV - \iiint_{SCV1} \beta_{v,x} [\langle v_{d,x} \rangle - \langle v_{a,x} \rangle] dV + \iiint_{SCV1} [\beta_d \rho_d \langle g_x \rangle] dV = \left\{ \left[\sum v_{d,x} \dot{m}_d \right]_{\frac{1}{2}} - \beta_{v,x} [\langle v_{d,x} \rangle - \langle v_{a,x} \rangle]_{\frac{1}{2}} + [\beta_d \rho_d \langle g_x \rangle]_{\frac{1}{2}} \right\} det[J]. \quad (3.3.1.7)$$

These terms are placed entirely at nodes on the right-hand side of the system of equations. The dispersed phase part of the steady-state drag term is represented in Fig. (3.3.1.1). The construction is shown based on the velocity vectors. The dispersed part of the drag term can also be placed at the integration point, if a more stable formulation is needed (i.e. for higher relative Reynolds number flows). Such formulation would require larger computational effort.

(vi) Approximation of Convection Terms

After the previous terms are integrated as discrete sums, they are further approximated for a particular control volume. For example, the non-linear convective

terms are evaluated from the product of a linearized convected velocity (from the previous iteration) and an active convecting velocity at the integration point. More specifically, at integration point I [ip1 on Fig. (3. 3. 1)], the convective flux in the dispersed x -momentum equation becomes

$$Q_{2,I}^* = + \sum_{i=1}^4 \left\{ \int_{t^*=0}^{t^*=I} \beta_d \rho_d^* \left[\langle v_{d,x} \rangle^* \frac{\partial y^*}{\partial t^*} - \langle v_{d,y} \rangle^* \frac{\partial x^*}{\partial t^*} \right] N_i|_{s^*=0} dt^* \right\} \langle v_{d,x} \rangle^* \quad (3. 3. 1. 8)$$

Unlike past upwind schemes, a local approximation of transport processes with the *PINS* was constructed at the integration point, in order to calculate this convecting velocity. This local balance involves convective upstream differencing, diffusion and local pressure gradients. Assembling these operators together produces an implicit relationship between nodal and integration point variables. The resulting coefficient matrix was inverted, thereby yielding integration point velocities explicitly in terms of nodal quantities. This coefficient matrix is used for the convecting velocity in the momentum flux term. Since the matrix includes effects of nodal variables on the convecting velocity, a sub-element pressure/velocity link is established.

(vii) Approximation of Pressure and Diffusion Terms

Both diffusion and pressure terms in the momentum equations are discretized with the shape functions and bilinear interpolation of nodal values. An implicit formulation is adopted, so that all terms are evaluated at the current time level. For example, at integration point I , the pressure terms become

$$Q_{2,I}^* = - \int_{SS1} \beta_d \langle p_d \rangle^* dS^* + \sum_{i=1}^4 \left\{ \int_{t^*=0}^{t^*=I} \beta_d \left[\frac{\partial y^*}{\partial t^*} \right] N_i|_{s^*=0} dt^* \right\} \langle p_d \rangle^* \quad (3. 3. 1. 9)$$

$$Q_{4,1}^* = \int_{SS4} \beta_d \langle p_d \rangle^* dS^* = + \sum_{i=1}^4 \left\{ \int_{s=0}^{s=1} \beta_d \left[\frac{\partial y^*}{\partial s^*} \right] N_i \Big|_{t^*=0} ds^* \right\} \langle p_d \rangle^* . \quad (3.3.1.10)$$

Although the dispersed phase pressure appears in the droplet flow equations, this thesis assumes identical pressures in both phases.

The form of the diffusion term is rearranged in the numerical code afterwards, in order to reduce the computational time (discussed further in the section entitled "Code Implementation"). The representation of this term is illustrated in Fig. (3.3.1.1). For example, the cross-phase momentum exchange due to interfacial drag forces in the dispersed x -momentum equation is calculated at each surface of the SCV . For $SCV 1$,

$$Q_{2,1}^* = - \int_{SCV1} \beta_d (\langle \tau_{d,xx} \rangle^* \vec{i} + \langle \tau_{d,xy} \rangle^* \vec{j}) d\vec{n} \quad (3.3.1.11)$$

Substituting the Newtonian constitutive relations and expanding the surface normal vector with respect to the component directions,

$$Q_{2,1}^* = - \int_{SCV1} \beta_d \mu_d^* \left[2 \frac{\partial \langle v_{d,x} \rangle^*}{\partial x^*} dy^* \vec{i}^2 - \left(\frac{\partial \langle v_{d,x} \rangle^*}{\partial y^*} + \frac{\partial \langle v_{d,y} \rangle^*}{\partial x^*} \right) dx^* \vec{j}^2 \right], \quad (3.3.1.12)$$

which becomes

$$Q_{2,1}^* = - \int_{t^*=1}^{t^*=0} \beta_d \mu_d^* \left[2 \frac{\partial \langle v_{d,x} \rangle^*}{\partial x^*} \frac{\partial y^*}{\partial t^*} - \left(\frac{\partial \langle v_{d,x} \rangle^*}{\partial y^*} + \frac{\partial \langle v_{d,y} \rangle^*}{\partial x^*} \right) \frac{\partial x^*}{\partial t^*} \right] \Big|_{s^*=0} dt^* . \quad (3.3.1.13)$$

The interfacial diffusive flux at *Sub-Surface 1 (SS1)* becomes

$$Q_{2,1}^* = + \sum_{i=1}^4 \left\{ \int_{t^*=0}^{t^*=1} \beta_d \mu_d^* \left[2 \frac{\partial N_j}{\partial x^*} \langle v_{d,x} \rangle^* \frac{\partial y^*}{\partial t^*} - \left(\frac{\partial N_j}{\partial y^*} \langle v_{d,x} \rangle^* + \frac{\partial N_j}{\partial x^*} \langle v_{d,y} \rangle^* \right) \frac{\partial x^*}{\partial t^*} \right] \Big|_{s^*=0} dt^* \right\}. \quad (3.3.1.14)$$

In a similar manner for *SS 4*,

$$Q_{4,1}^* = + \sum_{i=1}^4 \left\{ \int_{s^*=0}^{s^*=1} \beta_d \mu_d^* \left[2 \frac{\partial N_j}{\partial x^*} \langle v_{d,x} \rangle^* \frac{\partial y^*}{\partial s^*} - \left(\frac{\partial N_j}{\partial y^*} \langle v_{d,x} \rangle^* + \frac{\partial N_j}{\partial x^*} \langle v_{d,y} \rangle^* \right) \frac{\partial x^*}{\partial s^*} \right] \Big|_{t^*=0} ds^* \right\}. \quad (3.3.1.15)$$

(viii) Approximation of Source Terms

In this sub-section, modeling of source terms in the momentum equations is presented. An algebraic drag term in the dispersed *x*-momentum equation and a gravity term in the dispersed *y*-momentum equation are modeled as examples. Rather than placing the drag term at the center of the *CV*, it is placed in the middle of each *SCV*, so that

$$\begin{aligned} \int_{SCV1} \int_{s^*=0}^{s^*=1} \beta_{v,x}^* \left(\langle v_{a,x} \rangle^* - \langle v_{d,x} \rangle^* \right) \left| Det[J^*] \right| ds^* dt^* \\ = \beta_{v,x}^* \left(\langle v_{a,x} \rangle^* - \langle v_{d,x} \rangle^* \right) \Big|_{s^*=1/2, t^*=1/2} Det[J^*]. \end{aligned} \quad (3.3.1.16)$$

Details of the numerical implementation of the drag term are illustrated in Fig. (3.3.1.1).

The gravity term is modeled similarly to the drag term, i.e.,

$$\int_{SCV1} \int_{s^*=0}^{s^*=1} \rho_d^* \langle g_y \rangle^* ds^* = \int_{s^*=1/2, t^*=1/2} \rho_d^* \langle g_y \rangle^* \left| Det[J^*] \right| ds^* dt^* = \rho_d^* \langle g_y \rangle^* \Big|_{s^*=1/2, t^*=1/2} Det[J^*]. \quad (3.3.1.17)$$

3.4 DISCRETIZATION OF THE DISPERSED FLOW VOLUME FRACTION EQUATION

The dispersed phase volume fraction equation, Eq. (2. 2. 10), is discretized in this section. The approximation for each term is presented below.

(i) Transient Term

A lumped mass approach is adopted for this term. The droplet phase volume fractions are placed at the center of a CV , yielding

$$\iiint_{SCV_I} \frac{\partial}{\partial t} [\beta_d \langle \rho_d \rangle] dV = \langle \rho_d \rangle \left[\frac{\beta_{d,I} - \beta_{d,I}^o}{\Delta t} \right]. \quad (3. 4. 1)$$

The transient term is evaluated with a backward difference in time. The term is a first-order accurate Eulerian approximation and it is called a “lumped mass” approximation. The spatially integrated transient term contains the droplet volume fraction at both current and previous time steps. An implicit time-marching scheme is used.

(ii) Advection Term

The advection term in Eq. (2. 2. 10) contains mass conserving velocities. Integration point values for the convecting velocity components are obtained from the interpolated nodal velocity values and influence coefficients. These coefficients are

calculated with the *PINS* scheme, similarly to the dispersed and carrier integration velocities (see section (3. 6) and Ref. [11]).

Then the advection term at the *SSI* becomes

$$\iint_{SSI} [\rho_d \langle v_{d,j} \rangle \beta_d] dn_j \approx \rho_d \langle v_{d,x} \rangle_I \beta_d \Delta y_I - \rho_d \langle v_{d,y} \rangle_I \beta_d \Delta x_I. \quad (3.4.2)$$

(iii) Source Term

The source term, specific mass flow rate is calculated at the center of the *SCVs*, i.e.,

$$-\frac{1}{V} \iiint_{SCV_I} \langle \dot{m}_k \rangle_i dV = -\langle \dot{m}_k \rangle_i |_{I/2, I/2} \det[J]. \quad (3.4.3)$$

(iv) Approximation of the Advection Term

The integrated terms above are approximated for a particular control volume. The advection flux at integration point *I* becomes

$$Q_{2,I}^* = + \sum_{i=1}^4 \left\{ \int_{t^*=0}^{t^*=I} \rho_d^* \left[\langle v_{d,x} \rangle^* \frac{\partial y^*}{\partial t^*} - \langle v_{d,y} \rangle^* \frac{\partial x^*}{\partial t^*} \right] N_i |_{s^*=0} dt^* \right\} \beta_d. \quad (3.4.4)$$

(v) Approximation of Source Term

Modeling of the source term in the volume phase fraction equation is presented below.

$$-\int_{SCV_I} \int \langle \dot{m}_k \rangle_i dS^* = - \int_0^1 \int_0^1 \langle \dot{m}_k \rangle_i |_{Det[J^*]} ds^* dt^* = -\langle \dot{m}_k \rangle_i |_{s^*=1/2, t^*=1/2} Det[J^*]. \quad (3.4.5)$$

3. 5 BOUNDARY AND INITIAL CONDITIONS

When all parts of the control volumes are assembled throughout the computational domain, the interior discretized conservation balances are established. The system of equations is not closed yet, since the fluxes across the boundary control volumes must still be determined. It will be closed after the fluxes are prescribed at the boundaries of the domain. In this section, the boundary conditions are represented in the form of a standard Robin-type condition applied to external surfaces of the physical domain.

For both dispersed and continuous phases, the same type of boundary conditions is used. For the continuity and momentum equations of both phases, Dirichlet and Neumann types of boundary conditions are used. Boundary conditions on the boundary, S , of the physical domain and initial conditions inside the physical domain, V , are expressed as

$$\langle \bar{v} \rangle = \langle \bar{v} \rangle, \quad \beta = \bar{\beta} \quad \text{at } t > t_o \quad (3. 5. 1)$$

$$\frac{\partial \langle \bar{v} \rangle}{\partial \bar{n}} = \frac{\partial \langle \bar{v} \rangle}{\partial \bar{n}}, \quad \frac{\partial \beta}{\partial \bar{n}} = \frac{\partial \bar{\beta}}{\partial \bar{n}} \quad \text{at } t > t_o \quad (3. 5. 2)$$

$$\langle \bar{v} \rangle = \langle \bar{v}_o \rangle, \quad \beta = \bar{\beta}_o \quad \text{at } t = t_o, \quad (3. 5. 3)$$

where $t = t_o$ (initial time). In the current formulation, the dispersed phase (i. e. droplets) impinges on a surface (i.e. wall and ice evolving interface) as a group of physical bodies [Neumann type of boundary conditions in Eq. (3. 5. 2) is applied],

with their full impact velocity. A continuous phase (i. e. air) impinges on a surface as a fluid [Dirichlet type of boundary conditions in Eq. (3. 5. 1) is applied]. This enables the fluid, that after impingement on a surface where its velocity is zero, moves away / along / around the surface.

Implementation of the boundary conditions for the dispersed and continuous phases [Eqs. (3. 5. 1 - 3. 5. 3)] for each physical situation is discussed in Chapter (5).

3.6 NUMERICAL ALGORITHM AND CODE IMPLEMENTATION

In this section, further details about the dispersed flow, ice tracking and continuous flow numerical algorithms are presented. The overall multiphase algorithm and common features of particular algorithms are presented in this section, while other specifics are presented separately in sections (3. 6. 1), (3. 6. 2) and (3. 6. 3). The overall procedure of the computer code is depicted in Fig. (3. 6. 1). Many additional subroutines that communicate with different input and output files are part of the original *PHASES*. Such constitutive parts of the pre-processor are subroutines for mesh, boundary and initial condition generation. A typical part of the post-processor is a viewer. These additional subroutines are used to their full extent.

3.6.1 DISPERSED FLOW ALGORITHM

The derived governing equations for the dispersed-droplet flow are scaled differently than the governing equations for the continuous-air flow [see also section

(3. 6. 3) for details]. This leads to different computer programming when discretizing the terms of equations and subsequent different behavior of the numerical algorithms. Different scaling may affect the stability of the numerical simulations. It may temporarily shift a steady-state solution, especially when the droplet and air flows are solved together under conditions of large spatial gradients (i.e. near-corner effects). Thermophysical property variations are assumed to not affect the motion of phases in this thesis, so the additional temperature dependent term in the air equations becomes unnecessary. Nevertheless, it is retained in the present calculations.

After the input data is specified, the governing equations of dispersed phase motion are solved sequentially. These equations entail non-linear convective terms, thereby requiring inter-equation iterations until solution convergence is reached. Then, the governing equations of the carrier phase are solved simultaneously. The non-linear terms of the carrier phase also require inter-equation iterations. Further inter-equation iterations are performed between the dispersed and carrier phases. For example, the updated air velocity affects the relative Reynolds number and interfacial drag factor in calculation of the dispersed phase motion. The time step is successfully completed when a convergence tolerance is met within each equation (and set of equations) of all predicted physical quantities (i.e. velocity and fraction of phases)

The approximated discretized terms in the dispersed phase momentum equations [section (3. 3)] are implemented into the subroutines of the numerical algorithm. The global matrix of elements for the specific quantity (i.e. velocity) is created first. The assembly matrix $[A]$ is formulated from the elemental stiffness matrices. Then, the right side vector, $\{b\}$, is formulated at the boundaries of the domain. Then, the solver finds the solution vector field $\{x\}$ of the particular quantity. The residual of the solution between two successive iterations is calculated next (with relaxation) and compared with the residual convergence tolerance criteria (tol).

The *CVFEM* is an elemental based method. Conservation balances are formed at a sub-control volume (*SCV*) level and then assembled throughout the computational domain in the global matrix. The passive coefficients of terms in section (3. 3) are

created therefore in the local stiffness matrices, where each quantity has its own stiffness subroutine within the assembly subroutine.

The transient term in Eq. (3. 3. 1. 2) is implemented into the numerical algorithm as a part of the right-side of equations at the local node. The convective term in Eq. (3. 3. 1. 8) is implemented as a directed mass flux at the integration point, $ip1$, at surface SSI of $SCVI$. The mass fluxes are multiplied with the influence coefficients (IC) at each integration point. Momentum convection in each direction and volume fraction advection terms are implemented within an existing $PINS$ scheme (see section (3. 3), (ii) Convection terms and Ref. [11]). This scheme uses local transport equations for each physical quantity, which consist of its diffusion, advection and source terms through influence coefficients IC . From this local balance, the integration point values at each integration point (at each SS of a SCV) are obtained and the final convective fluxes can be determined. Unlike other schemes (i.e. UDS , EDS and hybrid), which account for the direction of the flow only, $PINS$ formulates all local transport processes, including the local pressure gradient (i.e. velocity-pressure link). Since the convective term is a non-linear term, the term is linearized by placing the convecting integration point velocities at the previous time level (old) in each direction into that mass flux. The final convected velocity (i.e. x -directed momentum velocity) is calculated at the center of the CV .

In the numerical formulation, the droplet pressure term in Eq. (3. 3. 1. 6) is implemented as a flux acting at the center ($ip1$) of the SS in a SCV . Air is the carrier phase of a non-dilute droplet phase small spherical droplets. The droplet volume fraction in the simulations was in a range of $\beta_{d,IN} = 0.0001 \leq \beta_d \leq \beta_{d-ice} = 1$ (with an initial droplet volume fraction of $\beta_d = 0$). As mentioned, it is assumed that a pressure of the air phase is the same as the pressure within the droplet phase. The pressure of the air is implemented into the formulation of droplet flow pressure $\langle p_d \rangle$. The air pressure term is taken at the previous time level for calculation of the droplet pressure and velocities at the current time level.

Re-formulation of the original diffusion terms [Eqs. (3. 3. 1, 14) - (3. 3. 1, 15)] in the scaled discretized dispersed flow equations was needed to stabilize and improve efficiency of the numerical calculations. These terms were re-developed in terms of a single velocity variable. For example, accounting for a Newtonan fluid and incompressible flow, the diffusion term of x -dispersed phase momentum equation at SSI ($ip1$) of SCV 1 became

$$Q_{2,1}^* = + \sum_{i=1}^4 \left\{ \int_{t^*=0}^{t^*=1} \beta_d \mu_d^* \left[\left(\frac{\partial N_j}{\partial x^*} \langle v_{d,x} \rangle^* \right) \frac{\partial y^*}{\partial t^*} - \left(\frac{\partial N_j}{\partial y^*} \langle v_{d,x} \rangle^* \right) \frac{\partial x^*}{\partial t^*} \right] \Big|_{s^*=0} dt^* \right\}. \quad (3. 6. 1. 1)$$

Similarly, the diffusion term at $SS4$ ($ip4$) of SCV 1 became

$$Q_{4,1}^* = + \sum_{i=1}^4 \left\{ \int_{s^*=0}^{s^*=1} \beta_d \mu_d^* \left[\left(\frac{\partial N_j}{\partial x^*} \langle v_{d,x} \rangle^* \right) \frac{\partial y^*}{\partial s^*} - \left(\frac{\partial N_j}{\partial y^*} \langle v_{d,x} \rangle^* \right) \frac{\partial x^*}{\partial s^*} \right] \Big|_{t^*=0} ds^* \right\}. \quad (3. 6. 1. 2)$$

The terms in Eqs. (3. 6. 1. 1) - (3. 6. 1. 2) are now more suitable for coding and computing than the forms of Eqs. (3. 3. 1, 14) - (3. 3. 1, 15). This approach requires less computational effort, since there is no mixed term for x - and y -velocities. For example, there is no vertical droplet velocity in the droplet x -momentum equation. In this way, only one type of shape function derivative of one component of the active droplet velocity (i.e. $\langle v_{d,x} \rangle^*$) at the current time level is calculated in both directions, in each and separate stiffness matrices (i. e. for $\langle v_{d,x} \rangle^*$ and $\langle v_{d,y} \rangle^*$ velocities). The diffusion term in Eq. (3. 6. 1. 1) is coded as a flux, acting on the SCV in the stiffness matrix, on the left hand side of the momentum equation.

The source terms in Eqs. (3. 3. 1. 16) - (3. 3. 1. 17) are coded as passive source terms of the droplet x -momentum equation, placed on the right hand side of the equations. The drag term in Eq. (3. 3. 1. 16) contains old droplet and air

velocities, from the previous time iteration. The drag term is not updated within the inner or intra iteration loops. The gravity term in Eq. (3. 3. 1. 17) is similarly coded like a drag term, besides the transient term on the right hand side of the equation. The gravity term is constant and it always updates the solution in each time step. This may cause minor and temporary instability within the propagated droplet wake of the convected momentum velocity, before the wake impacts on the surface and stabilizes. But this usually only happens at the interface of the evolving wake. If the inertia of the droplet flow is strong, the stabilization of such temporary instabilities is almost instantaneous. Reduction of the dispersed droplet velocities at an evolving ice interface [see discussion with Figs. (3. 6. 2. 1) - (3. 6. 2. 2)] is implemented in both droplet momentum equations, in their stiffness subroutines.

The boundary conditions are implemented and synchronized with the dispersed phase numerical algorithm through the general transport equation, i.e.,

$$\bar{A} \frac{\partial \psi}{\partial t} + \bar{B} \psi = \bar{C} . \quad (3. 6. 1. 3)$$

The scalar ψ in Eq. (3. 6. 1. 3) is interchangeably used for different quantities, such as x -, y -velocities of phases and the phase volume fractions, u , v and β_d , respectively. The formulation existed previously for air velocities and the phase volume fraction in the *PHASES* program. The boundary conditions are structured in segments for each physical quantity, according to the constants \bar{A} , \bar{B} , \bar{C} and orientation of the corresponding *CV*. Each phase contains its own segment of physical quantities. For example, for the scalar quantity of ψ , “1, 0, 0, R” means at the right side of the region (usually an outlet), the Neumann boundary condition is implemented. Also, for scalar quantity ψ , “0,1,0,1, L” means at the left side of the region (usually an inlet of the domain), the Dirichlet boundary condition is implemented

3.6.2 ICE TRACKING ALGORITHM

Figures (3. 6. 2. 1) - (3. 6. 2. 2) focus on the distribution of the phase velocities (i.e. droplet) in the vicinity of the evolving ice interface. The numerical algorithm corrects the phase velocities at the ice interface as a function of varying droplet volume fraction. As discussed previously in section (2. 5. 3), these functions are needed, in order to prevent deposition of excess ice after control volumes are entirely filled. This enables the re-distribution algorithm presented in Fig. (3. 6. 2. 3) to respond with backward spatial re-distribution of excess ice into detected *CVs*. The re-distribution algorithm is accommodated in the section after the dispersed volume fraction equation is solved. The pre-condition indicator, *Pfl*, detects a potential control volume (*CV*) where ice may accumulate. This potential region is searched close to the propagating ice interface at every iteration of the dispersed-flow equations, within the current time step [refer to section (2. 5. 2)]. Afterwards, the algorithm allows and controls excess ice (*EBeta*) to be gradually deposited into these *CVs* [see Fig. (3. 6. 2. 3)]. Droplet velocities, air velocities and phase volume fractions at the evolving ice interface and properties within the ice are simultaneously adapting during the calculations, depending on the conditions around the ice interface.

After a *CV* is filled with the ice, the algorithm calculates the excess ice and re-distributes it in the vicinity (in front) of the evolving ice interface, leaving the iced area behind [see section (2. 5. 3) and re-distribution functions in Figs. (2. 5. 3. 1) – (3. 5. 3. 2)]. In the iced region, the algorithm maintains the phase volume fraction unchanged. After establishing the ice interface between the flow and iced region, the ice tracking algorithm starts re-distributing the excess ice (ice backward tracking). At the point of establishing the ice interface, the flow algorithm suppresses the droplet inertia at the moving ice interface. This prevents the droplets from coming into the iced regions and freezing. The droplet flow and the droplet phase fraction algorithm are tightly connected with the ice tracking algorithm in a special flow-icing loop.

For illustrative purposes, the functioning of the algorithm is shortly discussed in reference to section (5. 4), Case (iii), in the paragraphs below. In section (5. 4), a whole case study is presented.

Figure (3. 6. 2. 1) presents two instances of droplet volume fraction distribution at the bottom wall of the front step, at times $t = 119.05 s$ and $t = 500 s$, respectively. The upper part of the figure presents a droplet phase fraction wave, as it propagates throughout the domain and hits the step at the right wall of the domain. The bottom wall consists of a series of control volumes, filled with accumulating supercooled droplets. The droplets immediately freeze upon impact onto the wall and start filling the area of the last control volume, adjacent to the step. The ice interface has just formed, leaving a small area of accreted ice behind, with $\beta_d = 1$. This area presents the first series of control volumes at the right wall surface, at a location of $0.96154 m$ from the inlet of the domain. It can be noted on the figure that large temporal and spatial gradients of the volume fraction exist at the evolving ice interface, which have to be accommodated by the algorithm and modeling of the simulation (i.e. boundary conditions and an appropriate time step). The reasons for the gradients are in the velocity field distribution at the interface, discussed in the next paragraph. The droplets impact onto the spreading interface with their full velocity. The algorithm imposes a zero gradient Neumann boundary condition for the droplet volume fraction and the droplet velocities at the moving ice interface.

In Fig. (3. 6. 2. 2), two droplet velocity profiles in the domain at the time $t = 500 s$ are presented. The upper part presents the x -directed velocity profile, while the lower part shows the y -directed velocities. Droplets are impinging onto the wall or ice interface. As soon as the droplet concentration-volume fraction reaches 1 ($\beta_d = 1$), the ice region is detected by the ice algorithm. In the next time iteration, the algorithm changes the droplet velocities in that region to $\vec{v}_d = \vec{0}$. In the case of an impinging airflow, the algorithm imposes $\vec{v}_a = \vec{0}$ at the interface and in the iced area. It can be noted that large spatial and temporal velocity gradients exist at the interface. These changes are accommodated in the flow algorithm. For orientation, the spatial x -

directed sensitivities for droplet x - and y -directed velocities in the numerical calculations have values: $\Delta u / \Delta x = 26.8 / s$ and $\Delta v / \Delta x = 16.1 / s$. The values for the velocity and distance are normalized based on a reference velocity of $u_{ref} = 4 m / s$ and a reference distance of $l_{ref} = 1 m$, respectively. Temporal sensitivities for droplet x - and y - directed velocities are: $\Delta u / \Delta t = 102.9 m / s^2$ and $\Delta v / \Delta t = 62.0 m / s^2$. Droplet phase fraction sensitivities for droplet x - and y -directed velocities are: $\Delta u / \Delta \beta = 12994.7 m / s$ and $\Delta v / \Delta \beta = 7830.3 m / s$. The algorithm successfully stabilizes the changes of velocities at the ice interface within the iteration loops of the numerical algorithm.

3.6.3 CONTINUOUS FLOW ALGORITHM

The continuous flow algorithm used in this thesis originates as a part of a previous *PHASES* algorithm. The continuous conservation equations for species (phase fraction), mass, momentum and energy transport have the following form [11]:

$$\frac{\partial(\rho C)}{\partial t} + \vec{\nabla} \cdot (\rho \vec{v} C) = \left(\frac{1}{Le}\right) \vec{\nabla} \cdot \left(\sum_{k=1}^2 f_k \rho_k D_k \vec{\nabla} C_k \right) + \vec{\nabla} \cdot \left(\rho \vec{v} C - \sum_{k=1}^2 f_k \rho_k \vec{v}_k \nabla C_k \right) \quad (3.6.3.1)$$

$$\frac{\partial \rho}{\partial t} + \vec{\nabla} \cdot (\rho \vec{v}) = 0 \quad (3.6.3.2)$$

$$\begin{aligned} \frac{\partial(\rho u)}{\partial t} + \vec{\nabla} \cdot (\rho \vec{v} u) = \\ -\frac{\partial p_d}{\partial x} + Pr \vec{\nabla} \cdot \left[\sum_{k=1}^2 v_k \vec{\nabla} \cdot (f_k u_k) \right] + \left(\frac{Pr Re}{Fr^2} \right) \delta_{1j} \frac{\partial h}{\partial x} + \vec{\nabla} \cdot \left[\rho \vec{v} u - \sum_{k=1}^2 f_k \rho_k \vec{v}_k u_k \right] + B_x + G_x \end{aligned} \quad (3.6.3.3)$$

$$\begin{aligned} \frac{\partial(\rho v)}{\partial t} + \vec{\nabla} \cdot (\rho \vec{v} v) = \\ -\frac{\partial p_d}{\partial y} + Pr \vec{\nabla} \cdot \left[\sum_{k=1}^2 v_k \vec{\nabla} \cdot (f_k v_k) \right] + \left(\frac{Pr Re}{Fr^2} \right) \delta_{1j} \frac{\partial h}{\partial y} + \vec{\nabla} \cdot \left[\rho \vec{v} v - \sum_{k=1}^2 f_k \rho_k \vec{v}_k v_k \right] + B_y + G_y, \end{aligned} \quad (3.6.3.4)$$

where

$$p = \sum_{k=1}^2 \left[f_k p_k - \frac{1}{3} \mu_k \vec{\nabla} \cdot (f_k \vec{v}_k) \right] \equiv p_0 + \rho g (h - y) + p_d. \quad (3.6.3.5)$$

The parameters Fr , Pr , Re , B , G and f_k in Eq. (3.6.3.1) represent the Froude number, Prandtl number, Reynolds number, local body forces, phase interaction forces and fraction of phase k , respectively. The transport of enthalpy, h , is governed by the following equation,

$$\begin{aligned} \frac{\partial(\rho h)}{\partial t} + \vec{\nabla} \cdot (\rho \vec{v} h) = \\ \vec{\nabla} \cdot (k \vec{\nabla} T) + \vec{\nabla} \cdot \left(\rho \vec{v} h - \sum_{k=1}^2 \rho_k \vec{v}_k h_k \right), \end{aligned} \quad (3.6.3.6)$$

where

$$h_k(C, T) = \int_{T_0}^T c_{r,k}(\zeta) d\zeta + h_{r,k}(C, T). \quad (3.6.3.7)$$

Unlike the dispersed momentum equations, the continuous phase momentum equations involve energy transport processes. Scaling of the continuous phase momentum equations is different than scaling of the dispersed phase equations. Such scaling of the air system of equations [11] requires different coding for referencing of the terms, as well as synchronization with the dispersed phase equations. The system of continuous phase equations [Eqs. (3. 6. 3. 1) - (3. 6. 3. 7)] is not presented in the form for coding. The system is closed by supplementary equations for the interphase liquid fraction, momentum phase interactions (interfacial drag) and the enthalpy [11]. The pressure term still exists in the equations. Closure of the continuous phase equations for the mass and momentum equations consists of a simultaneous pressure-velocity (within *PINS* numerical scheme at integration point, described below) and segregated temperature-velocity coupling through the buoyancy source terms. The buoyancy term uses the temperature field in the momentum equations.

Additional explanation regarding the closure of the carrier phase equations and pressure-velocity coupling is described in Ref. [11]. For the implementation of the dispersed phase convective and advective phase fraction terms, the local momentum equation for each direction is also used within *PINS*. This convection scheme includes physical effects of diffusion, advection and source terms in the form of influence coefficients. The local carrier phase equation for the convecting integration point velocity is

$$\frac{\partial \vec{v}}{\partial t} + C(\vec{v}) = -\vec{\nabla} p + D(\vec{v}) + \vec{S}. \quad (3. 6. 3. 8)$$

By introducing the transient, convection, pressure and diffusion operators,

$$\left. \frac{\partial \phi}{\partial t} \right|_{ip} \approx \frac{\phi_{ip}^{n+1} - \phi_{ip}^n}{\Delta t} \quad (3. 6. 3. 9)$$

$$C(\phi) = \rho V \frac{\partial \phi}{\partial s} \approx \rho V \left(\frac{\phi_{ipi} - \phi_u}{L_c} \right) \quad (3. 6. 3. 10)$$

$$\left. \frac{\partial p}{\partial x} \right|_{ip} \approx \sum_{i=1}^4 \frac{\partial N_i}{\partial x} P_i \quad (3.6.3.11)$$

$$D(\phi) \Big|_{ip} = \nabla^2(\phi) \Big|_{ipi} \approx \frac{\sum_{j=1}^4 N_j \Phi_j - \phi_i}{L_d^2}, \quad (3.6.3.12)$$

respectively, into Eq. (3.6.3.8) and inverting four integration point equations for \bar{v}_{ip} (for each element), the integration carrier integration point velocities can be written in terms of the nodal values as follows,

$$\{v_{x,ip}\} = [IC^{v_x v_x}] \{v_{x,n}\} + [IC^{v_x p}] \{P_n\} + \{S^{v_x}\} \quad (3.6.3.13)$$

$$\{v_{y,ip}\} = [IC^{v_y v_y}] \{v_{y,n}\} + [IC^{v_y p}] \{P_n\} + \{S^{v_y}\}. \quad (3.6.3.14)$$

The parameters $C(\phi)$, $D(\phi)$, ϕ , ϕ_u , Φ , ipi , s , V , L_c , L_d , \bar{S} , IC and P_n in Eqs. (3.6.3.8) - (3.6.3.14) refer to the convection operator, diffusion operator, integration point value, upwind value, nodal value, integration point “ v ”, local streamwise direction, magnitude of the resultant fluid velocity, convection length scale, diffusion length scale, external forces (source term), influence coefficient and nodal pressure, respectively. The upstream value, ϕ_u , was determined by two different schemes, namely a skew upwind scheme (for the mass and momentum equations and a mass-weighted scheme for the volume fraction equation [11]).

Velocities $v_{x,ip}$ and $v_{y,ip}$ at integration points at each SS appear in the convection term of the momentum equations and the advection terms of mass and phase fraction equations. It can be noted that these velocities contain the nodal pressure values, so nodal pressure is placed in the convection and advection terms of the conservation equations. In addition, regular pressure terms exist in the momentum

equations as fluxes, similar to the droplet flow formulation in Eqs. (3. 3. 1. 9) - (3. 3. 1. 10). They act at the *SS* of a *SCV*. For example, for the carrier *x*-directed momentum equation, the corresponding pressure term is added to the term constructed above in Eq. (3. 5. 3. 13), as a part of the convection modeling within the integration point *x*-directed velocity. Both pressure contributions are combined into the convection flux of the *x*-momentum equation. Similar construction exists for the *y*-momentum equation. It can be noted that the pressure term exists in the momentum equations, mass equation and phase fraction equation. The system of equations is closed and the equations with the pressure-velocity coupling are solved simultaneously. As mentioned above, the solution of that carrier pressure field is used in the dispersed phase momentum equations.

CHAPTER 4

EXPERIMENTAL INVESTIGATION OF DROPLET MOTION AND ICING

In this chapter, new insight regarding droplet momentum exchange and interfacial drag forces is gained with experimental data collected from Particle Image Velocimetry (*PIV*). Theoretical and practical physical background of the problems regarding the droplet motion and icing are addressed. Newly developed devices and experimental methods are described. In addition, results of novel experimental designs are presented. In the following chapter [Chapter (5)], additional experimental results and validation of the numerical code will be presented.

As discussed previously, the practical motivation for this research project is to create a better understanding of droplet motion and impact on iced helicopter surfaces [see Fig. (1. 2. 2)]. The main objective of the spray and jet flow experiments and

measurements was to validate the numerical code. Since there was inadequate experimental infrastructure, new devices had to be developed. This fact has brought an additional purpose of the experimental studies, to simulate practical field conditions. Along with the infrastructure, the experimental instrumentation was developed for field simulations. There were high demands on experimental devices to satisfy numerical formulations and different benchmark cases. Examples include dilute and micro droplet flows with smooth long trajectories. Also, there were high demands to satisfy the field conditions of supercooled droplets. Furthermore, rime ice conditions and rime ice buildup is far more difficult to produce in the icing tunnel than glaze ice conditions. The short distance spray nozzle system was selected in the *PIV* trajectory experiments. The measured velocity field was successfully compared with results from numerical simulations.

Ice protection of the engine bay cooling intake involves active or passive methods. Active methods of de-icing involve electrical heating elements, or hot bleed air re-directed from the compressor of the engine system. On the other hand, passive methods include alteration of the surface geometry to reduce droplet capturing and water adherence to the surface. Controlled surface roughness, such as specially designed microchannels embedded within the surface, may allow the local air stream to eject water from the surface before it re-freezes downstream [18]. In each method, a main purpose is deflecting droplets away from the ice surface and reducing the collection efficiency, thereby reducing the mass of ice accretion. Compromises involving effects of aerodynamic performance, manufacturing and so forth must be considered. Developing new de-icing methods requires a detailed understanding of droplet impact and droplet momentum exchange between the dispersed (droplet) and carrier (air) phases. The droplet velocities near the ice surface contribute to the collection efficiency of the surface. This efficiency refers to a ratio of mass flow of impinging droplets on the upstream side of the iced surface, to the mass flow that would contact the same surface if the droplets were not deflected by the airstream. By measuring droplet velocities in assessment of the collection efficiency, the detailed effects of surface shape on droplet capturing can be better understood. In this way,

individual aircraft components can be designed to become less ice prone during in-flight icing conditions.

In this chapter, a method involving Particle Image Velocimetry (*PIV*) is discussed for purposes of studying droplet tracking and momentum exchange in multiphase flows. In particular, experimental studies of ice accretion on a helicopter scoop are performed. In this application, the droplet flow must be understood, created and assessed by the experimental method. The practical goal was producing a uniform (two-dimensional) ice accretion on the wide scoop surface. This goal presented major challenges, mainly regarding uniformity of the incoming multiphase flow. For example, some specific issues regarding the droplet flow and ice accretion are listed below as follows:

- the external flow is prone to unstable behavior and dispersion.
- Micro-droplets with droplet diameters of $D_d = 10\ \mu m - 500\ \mu m$ must be produced and sprayed as a uniform continuous flow.
- A high pressure is needed in the nozzles to produce micro-droplets and launch them over a long distance towards the test piece.
- Both long distance and short distance dispersed (droplet) flow trajectories are needed for experiments in the spray-icing tunnel.
- The trajectories must be uniform, smooth and parallel.
- Dilute droplet flow conditions must be maintained, since the physical model neglects droplet interactions and deformations.
- Phase change may occur during droplet motion.

During the experiments, rime ice conditions arise at air temperatures lower than $-30\ ^\circ C$. Droplets must reach the ambient air temperature and solidify before impact onto surfaces, in order to properly replicate conditions in actual icing problems. This requirement becomes difficult for a $10\text{-}m$ distance in rime ice conditions, even with a chilled water supply for droplets. Furthermore, long duration tests at $-40\ ^\circ C$ require heat sources for the nozzle systems inside the tunnel to prevent them from freezing.

When the above requirements are combined, some challenges became difficult to overcome. Several requirements were investigated and satisfied before performing the droplet flow measurements. These requirements involved the following issues simultaneously: flow environment (spray-icing tunnel), incoming flow and instrumentation. The droplet flow needed to be produced correctly to satisfy dispersed (droplet) flow requirements and two-dimensional icing. The long distance and short distance nozzle systems needed to be developed in this regard [see Section (4. 1)].

The existing *PIV* instrumentation (hardware and software) has certain limitations. It was not originally designed for applications involving droplets in an icing tunnel. A sufficient number of droplets cannot be produced by the long distance nozzle system in the icing tunnel to allow the *PIV* system to execute an Eulerian-based algorithm for velocity measurements. Nevertheless, the following sections describe other useful studies conducted with *PIV* and droplet motion.

4. 1 DEVELOPMENT OF SPRAY AND JET NOZZLE SYSTEMS FOR DROPLET FLOW AND ICING APPLICATIONS

Two long distance (first project) and short distance (second project) nozzle systems were developed for liquid spray and stream flow in icing applications mainly within two undergraduate projects. Supervision and extended assistance in the two undergraduate projects took place. Two students, Jared Kozub: [first undergraduate project: May-August, 2003, section (4. 1. 1) below] and Mike Koupriyanov [second undergraduate project: May-August, 2004, section (4. 1. 2 – 4. 1. 3 below)], were mainly responsible for buying and manufacturing the parts of the devices.

The main goal in these developments was production of a uniform ice shape on a helicopter scoop in the spray-icing tunnel. This required connection and operation of the chilled-water supply system. The lowest temperature of the water in the chilled-supply is $1^{\circ}C$, as lower temperatures would lead to freezing in the supply lines. The maximum gauge line pressure of the water was 60 Psi . Also, the maximum gauge pressure of the water in the chilled-supply was 75 Psi .

The diameter of droplets and space between droplets were measured with two methods: (i) Oil bath method and (ii) *PIV* method. The spacing between droplets was measured in the core of the flow. Outside that region, the droplet diameters were significantly smaller.

(i) Oil bath method

Based on suggestions from a committee member (Dr. Popplewell), the emitted droplets from the nozzle system were captured into an oil bath. Their diameters and distances between droplets, as well as the droplet diameter's variation, were measured. A Digital Caliper ($8'' / 200\text{ mm}$) was used for the measurements of droplet diameter. Diameters of $1 / 100\text{ mm}$ ($10\ \mu\text{m}$) can be measured with this Caliper. The oil layer was sufficiently thick to prevent direct impact of droplets on the bottom wall of the bath and their elongation. For example, droplets were emitted from the long-distance nozzle system at low-temperature measurements (icing conditions). The temperature in the spray-icing tunnel was approximately $-30^{\circ}C$. The droplets partially solidified during flight towards the test piece (i.e. scoop). They were captured at (before) the scoop, at approximately 10 m from the nozzles (with an inner diameter of 0.00140 m). The droplet diameter was about 0.00265 m . The spacing between droplets was found to be between 2-4 diameters of droplets. Outside the core region of the flow, the droplets have smaller diameter than in the core of the flow. Their diameters were in the range between 0.00020 m to 0.00060 m .

(ii) PIV method with Flow Manager (4. 20. 25)

In addition, the emitted droplets from the nozzle system were captured on the camera and processed by the FlowManager software. The droplet diameters and distances between them were measured during the data acquisition from the computer screen [i.e. with resolution between 0.0001 m (μm scale) to 0.001 m (mm scale)]. For example, the droplets emitted from the spray bar in a water tunnel at low pressure (55 Psi) were approximately 0.0040 m in a diameter [see section (5. 5)]. In the similar experiment, the diameter of droplets was measured in the spray-icing tunnel (0.0050 m) under slightly lower pressure than in the previous experiment in the water tunnel. The spacing between the droplets was approximately between one diameter of a droplet ($1 \times D_d$) to five diameters of droplets ($5 \times D_d$). A spacing pattern was not fixed, as it changes over time. Outside the core region of the flow, the droplets have significantly smaller diameter than in the core of the flow. Their diameters were in the range between 0.0001 m to 0.0005 m .

4. 1. 1 LONG DISTANCE NOZZLE SYSTEM

A new long-distance nozzle system was developed [see Figs. (4. 1. 1. 1) - (4. 1. 1. 2)]. It produces a droplet flow, which can be injected from a long distance ($L \approx 10\text{ m}$) and nearly uniform ice shape on quasi-3D surfaces [i.e. test piece of the helicopter scoop, see Fig. (4. 4. 1)]. Icing experiments were conducted with different nozzles (i.e. exit diameters of 0.91 mm , 1.15 mm and 1.45 mm) to study the droplet flow characteristics and flow impact on the ice surfaces. The average droplet diameter at the location of the test pieces was $D = 2.65\text{ mm}$ (with the largest nozzle diameter and low temperature measurements: $-33\text{ }^\circ\text{C}$). The control parameters of the experiment and characteristics of the newly developed spray-icing tunnel were observed during these studies.

The new chilled water supply was used. The spray tunnel was cooled by the inner duct airflow. A temperature of $-30\text{ }^\circ\text{C}$ was reached in approximately three

hours. During the experiment, water was flowing at the minimum flow rate from the nozzles, in order to prevent the nozzle exits from freezing. After the desired temperature was reached, the water was turned to its maximum flow rate through the nozzles and sprayed onto different cylindrical and squared surfaces.

The droplet diameters of $D = 1.45 \text{ mm}$ are too large for droplets to reach certain low temperatures in the tunnel (minimum air temperature of $-33 \text{ }^{\circ}\text{C}$) at the maximum traveling distance (10 m). Such droplets are typically not encountered in in-cloud icing. This implies that long-duration rime ice experiments can not be performed satisfactorily. If the droplet diameters were considerably reduced, then much higher pressures in finer nozzles would be needed. This would considerably increase the expenses of the needed equipment (i.e. booster pumps, new nozzles), while reducing the quality of the droplet flow. With such a flow, uniform quasi-3D ice shape may not be obtained. Such flow is difficult to control. The trajectory can split into many trajectories in many directions. It is known that the droplet trajectory can be appreciably different from the trajectory of a solid particle. It is difficult in the experimental setup to produce exactly the same droplet trajectory as a solid particle trajectory (assumed in the numerical simulations). Due to the constitutive law of water, the friction forces on the injected water stream do not balance with the gravitational forces over the entire traveling distance. A crucial point is the maximum height of the trajectory, where the y -component of the droplet velocity is zero. For an instant after this point is reached, the gravity force tends to split the water elements apart into many trajectories. Splitting a trajectory may occur before or after the maximum height is reached, due to several other influences. Such influences are an elliptic action of pressure in the suddenly contracted nozzle exit, influences of the drag due to the surrounding air flow, and varying droplet diameters over the traveling distance. It is anticipated that these difficulties can be minimized by long and smooth needles with a micro-scale diameter at the nozzle exit. In this case, a large liquid pressure must be supplied at the entrance of the nozzles. This would ensure large pressure drop in the needles, long traveling distance of the droplets (10 m) and a sufficient volume flow rate.

It was discovered that the chilled water supply did not produce sufficient pressure to allow the droplets to reach the test pieces. Removing the chilled water supply from the experiment diminished the possibility to produce the rime ice conditions in the tunnel. Since the nozzle system did not have heat sources, the pressure from the chiller was too low and the cooling stage of the tunnel was too long. For example, before the water was sprayed with its maximum flow rate, three nozzle exits froze. However, such difficulties were not entirely unexpected, in view of the new tunnel's unique design.

Due to the considerably higher costs needed to produce the rime ice accretion in the spray-icing tunnel (due to lower temperatures, higher pressure, smaller droplets, longer distances and longer duration experiments), the nozzle system was developed to a level of spraying droplets at moderate distances ($5m$) and higher temperatures (greater than $-15^{\circ}C$). Due to the water spray limitations inside the tunnel (up to 28 gal/hr), a relatively small number of nozzles was used. A final set-up with four nozzles is shown in Fig. (4. 1. 1. 1).

The further development of this nozzle system was suspended due to the challenging problems with the spray-ice tunnel floor. The major parts of the novel long needle nozzle system were planned and bought. The system is viewed to have better capability to effectively control the long range droplet trajectories.

4. 1. 2 SHORT DISTANCE NOZZLE SYSTEM (ATOMIZER)

Existing atomizer (old atomizer) was made by Anderson [94]. Various challenges were encountered with this existing in-duct atomizer, i.e., spatially uncontrolled droplet flow with unequal mass flow rates from the nozzles, inability to work under $-7^{\circ}C$ [see Figs. (4. 1. 1. 4) – (4. 1. 1. 5)]. Such flow could not produce two-dimensional uniform rime ice shapes on quasi-3D surfaces, made from different materials (i.e.

helicopter test scoop). For a lower thermal conductivity of the surface material in the test piece, thicker (rime) ice is produced. More supercooled droplets must be sprayed in order to produce rime ice accretion on the surfaces.

After preliminary tests with the old atomizer [see Fig. (4. 1. 1. 3)], the system was modified. The modified system produces controllable droplet flow and mass flows in the range of droplet diameters of $D_d \leq 11\text{ mm}$, depending on the pressure of assisted air. The old atomizer [Fig. (4. 1. 1. 3)] was tested under various conditions in the spray/icing tunnel, in order to discover its limitations and requirements for droplet flows and icing applications. These conditions involved low pressure and high pressure of the droplet flow and air flows, and different temperatures in the spray tunnel. The tests focused on the droplet flow and the airflow, sprayed separately from different inlet housings. The droplets were sprayed with water from the chilled water supply system and the air was supplied from a compressed air supply. At the nozzle exits, the compressed air was injected into the droplet flow. The droplet flow was further dispersed and assisted by the air motion. The third flow (air stream) was coming from the inner duct. It controlled both flows from the nozzles.

The atomizer behaved unexpectedly under certain conditions and tests. Two representative droplet-air flow cases will be discussed from these tests. These cases involved simulations of flows under varying ambient temperatures. During initial tests, nozzles pointed in different directions and the flow was not dispersed horizontally [see Fig. (4. 1. 1. 4)]. As a result, new tubs and a control system for the nozzles were developed. The dispersed droplet flow and the assisting air flow from the nozzle system were injected into the cooling air flow. The temperature in the spray tunnel was gradually decreased by increasing the speed of the cooling air flow. At -3°C , the nozzles started freezing at their exits [Fig. (4. 1. 1. 5)]. The dispersed droplet flow gradually became highly distorted. At -5°C , almost all nozzles were plugged with ice and at -7°C all nozzles stopped functioning. The freezing around the nozzle exits happened despite the compressed air supplied at the nozzle exits.

For purposes of droplet flow control from each nozzle, a *PVC* network of water and air tubs was replaced by a stiffer network system with brass connectors and

flow valves [Fig. (4. 1. 1. 6)]. In this setup, the water pressure and mass flow rate can be regulated by a set of reduction valves [smaller picture in Fig. (4. 1. 1. 6)].

The atomizer was planned to operate under rime ice conditions (temperatures below about $-10\text{ }^{\circ}\text{C}$). In order to prevent the nozzle exits from accumulating water and freezing, heating strips were bought to be placed inside the frame of the airfoil of this nozzle system. The atomizer was developed for general use in a variety of conditions involving different air pressures, mass flow rates and droplet diameters for a specific nozzle within the atomizer. For example, sample tests of the atomizer are shown in Fig. (4. 1. 1. 7). Figure (4. 1. 1. 7) shows reflected *PIV* laser light from the flowing atomized droplets, which were assisted by pressurized air (online *PIV* droplet velocity measurements). This atomizer does not have a supply system for seed particles, as the droplets are assumed to be small enough. It is inappropriate for the atomizer to run with seeding particles, since the nozzle may clog. Also, a sufficient number of droplets is assumed to co-exist in the camera interrogation region for successful *PIV* velocity measurements.

A heating system with heat strips, swiveling valves and tests with final adjustments of all nozzles for the nozzle system were not completed for this undergraduate project in time. For, example, the unavailable spray-icing tunnel underwent floor reconstruction at that time.

4. 1. 3 JET STREAM WITH SEED PARTICLE SUPPLY (JSPS)

This JSPS device was developed for two main reasons:

- (i) to measure the velocity field of the controlled jet flow with continuously supplied seeding particles and

- (ii) to obtain comparable reference velocity measurements for atomized flow in the spray-icing tunnel.

The JSPS is shown in Fig. (4. 1. 1. 8). The vertical pipe in Fig. (4. 1. 1. 8) is supplied by a constant water mass flow from the top. The horizontal pipe (below) can be replaced with pipes of different diameters, in order to produce a jet flow with different characteristics. The mass flow, pressure and pipe diameters are the main parameters that control the stream (jet) flow characteristics, such as the final length, thickness, continuance and the shape of the flow.

A Seeding Particle Supplier (*SPS*) with premixed seeding particles can continuously supply the jet flow during its operation and thus allow *PIV* velocity field measurements. Seed particles with diameters of $10\mu m - 20\mu m$ are used to perform velocity measurements of the jet flow. The *SPS* supplies the flow with particles under gravitational and low pressure effects in the horizontal pipe.

4. 2 PIV METHOD AND DROPLET FLOW MEASUREMENTS IN A WATER TUNNEL

The *PIV* laser based measurements of flow trajectories were carried out with the short distance nozzle and jet systems. Dispersed-flows and liquid streams were injected into the ambient air and the velocities in the trajectories were measured. In the next section, the accompanying instrumentation and issues associated with these studies will be briefly described.

4. 2. 1 PRELIMINARY INVESTIGATION

A goal was to design an experiment for external dispersed-flow measurements with the existing equipment, i.e., *PIV* Gemini laser, High and Low Sense *CCD* (Charge Couple Device) Cameras (Dantec and Kodak), FlowManager software [Dantec Dynamics Flow Manager (4.20.25)], nozzle systems (long distance and short distance), water and spray-icing tunnels. The external flow (i.e. droplet flow) *PIV* measurements were found to be more difficult than internal flow measurements in many aspects (i.e. acquiring and processing of the signals).

Various issues regarding interaction of the flow and equipment were encountered. For example, this included the flow characteristics, i.e., number and size of droplets that pass the camera view region to receive sufficient light illumination, 3-*D* shape of trajectories for related alignments with the laser light sheet. Another issue involved the capabilities of the equipment, i.e., laser light spread angle, laser light intensity, focal length of the camera lenses, sensitivity of the cameras and their safety, FlowManager tracking method. In addition, arrangement of the experimental design (positions, interactive usage) was investigated. In the following three cases, the equipment performance was tested inside the icing – spray tunnel to obtain experimental information for subsequent droplet flow measurements. The low sensitive Kodak camera was used.

In the first experiment [see Fig. (4. 1. 1. 9)], a glass container filled with water and polyamide seed particles ($D_p = 20 \mu m$) was placed approximately one meter beneath the laser. The camera was placed less than *300 mm* away from the glass box (inside the spray flow tunnel). With this setup, reasonably small distances between the laser, camera and object were ensured. The laser light intensity was found to be sufficient and the camera was sufficiently sensitive to capture good images of the moving particles. The corresponding velocity field and particle diameters were successfully processed.

In the second experiment [see Fig. (4. 1. 1. 10)], the droplets (not particles) were sprayed from the nozzle manually, less than 300 mm from the camera inside the spray tunnel and approximately 3 m (maximum distance) from the *PIV* laser. The number and diameter of droplets were large enough to reflect sufficient light from the laser to the camera. In this case, the droplets and the droplet velocity field could be captured digitally on the computer screen. The laser light intensity was sufficient to illuminate light from the droplets, despite that distance from the flow. On the other hand, the droplets were bigger than previously used seed particles.

The third experiment [Fig. (4. 1. 1. 11)] used the long distance nozzle system. The droplets were sprayed from a 10 m distance in the outer duct of the spray – icing tunnel. The camera was placed more than 300 mm from the sprayed droplets outside of the tunnel. The droplet trajectories crossed the laser light plane approximately 1.5 m to 3 m from the laser. Several reasons for not capturing the droplets digitally were investigated. It was discovered that an insufficient number of sprayed droplets with small diameters was captured by the low-sense camera, mainly due to the distorted trajectories (inadequate alignment with the laser light sheet).

For the given experimental setup (i.e., laser and camera distances, diameter and number of droplets, etc.) and laser/camera performance, several steps for improving the measurement capabilities were studied. The following methods could possibly produce more intense laser light and additional camera sensitivity for capturing the images digitally:

1. smaller light spreading angle, based on custom-made cylinder laser lenses for $5\text{-}10$ degrees;
2. larger light sheet thickness (from 700 to 3000 mm);
3. larger lenses (focus of approximately 150 mm) with $4\text{ x} - 8\text{ x}$ camera sensitivity;
4. more powerful laser ($150 - 200\text{ mJ/s}$), as current laser system is inadequate;
5. combinations of aforementioned options.

The problems encountered were addressed to the best extent possible, but it was discovered that the current FlowManager system is not the most suitable for the

long distance dispersed-flow measurements in the spray-icing tunnel. It is even more problematic in icing applications, where the dispersed, transitional and film flows need to be measured simultaneously at the helicopter scoop. This *SW* does not use the conventional Lagrangian method for processing the measurements, so motion of an insufficient number of droplets cannot be tracked properly with Eulerian-based instrumentation in icing applications. In addition, the main concern in icing applications is near-wall droplet impact. Due to insurmountable problems with near-ice distortion of laser light, the current system is incapable of these measurements. As a result, the experimental studies were limited to non-icing problems.

4. 2. 2 PIV LASER BASED METHOD

In assessment of fluid flows, two main characteristics make Particle Image Velocimetry (*PIV*) attractive. Unlike other conventional anemometry methods [*HWA*- (Hot Wire Anemometry): *CTA*, *CCU*], the *PIV* method:

- is a non-intrusive technique and
- it is a whole-field method. The measured velocity field is not obtained at a single point, such as with the *HWA*.

Image maps were processed by a *PIV 2000* Processor from the *CCD* camera directly into velocity vector maps. A laser sheet is formed by a laser beam. A problem in *PIV* is in determining the displacement field of a group of particles/droplets using *FFT*/Correlation techniques. Alternatively, in particle tracking, individual particles are identified and algorithms match the initial and final locations. Interrogation areas constitute the camera image. Two camera frames are correlated within each interrogation area to predict an average displacement vector.

In these experimental studies, a velocity field is determined from single exposed images by cross-correlation of corresponding interrogation regions between

two successive frames. The average displacement of the illuminated particle is obtained based on the location of the highest correlation peak.

The pulsed laser is used to produce high light energy during a short period of time. The laser light sheet is pulsed twice. The time interval between pulses can be set. The experimental setup reflects a laser plane sheet into the flow, where particles within the flow (such as seed particles or droplets) are illuminated. A video or photographic camera acquires two single exposed images of the flow at two instants. A full-frame interline transfer progressive scan *CCD* was used.

Since the time interval is very short with respect to the measured velocity of the flow (even for high velocities $> 100 \text{ m/s}$), the images are practically frozen. The first image from the first laser pulse is rapidly transferred to dark areas on the *CCD* chip, which stores the image. The image from the second pulse is not stored. After the second pulse, both images are transferred to the computer for evaluation. The displacement field of a group of particles is determined, typically by dividing the image plane into small interrogation regions and cross-correlating images from two time exposures. The displacement that yields the maximum cross-correlation, based on statistical analysis, approximates the average displacement of the particles in the interrogation region. By dividing the displacement associated with each interrogation cell by the time between laser pulses, the measured velocity field is calculated. The conventional *PIV* method typically measures velocities on a 100×100 grid with accuracy between approximately 0.2 % and 5 % and a spatial resolution of about 1 mm. Extensions of this technique to 3-D flows can be accomplished with a stereographic system using two lenses.

(i) Cross – Correlation

An auto-correlation method measures the initial and final positions of the particles within a single frame in the interrogation area. On the other hand, the cross – correlation method measures the initial particle position in the first and final particle position of the second single exposure frame. Interrogation areas from both images

are cross-correlated, thereby yielding a single peak particle displacement function. A high cross-correlation value means that many of the same particles are found at initial and shifted positions (counter-parts). The average particle displacement is directly determined from the location of the peak of a function.

Figure (4. 2. 2. 1) presents the definition of the displacement function used in the *PIV* analysis, where the interrogation area light intensity at time t_0 is a function, $f(u_1, u_2)$, and the function $g(u_1, u_2)$ is the light intensity at time $t_0 + \Delta t$. The function $s(u_1, u_2)$ is the spatial shifting function and $d(u_1, u_2)$ is the added noise function. The $F(v_1, v_2)$, $G(v_1, v_2)$, $S(v_1, v_2)$ and $D(v_1, v_2)$ functions are the Fourier transforms of functions $f(u_1, u_2)$, $g(u_1, u_2)$, $s(u_1, u_2)$ and $d(u_1, u_2)$. The pair (v_1, v_2) represents coordinates in the frequency domain. The input and output functions, $f(u_1, u_2)$ and $g(u_1, u_2)$, define the particle displacement function, which directly corresponds to the flow and two time recordings of the particles.

A discrete cross - correlation function is defined as

$$\phi_{f-g}(u_1, u_2) = \sum_{l_1=-\infty}^{l_1=\infty} \sum_{l_2=-\infty}^{l_2=\infty} f(l_1, l_2) g(u_1 + l_1, u_2 + l_2) \quad (4. 2. 2. 1)$$

Figure (4. 2. 2. 2) shows a processing chart of the *PIV* method. Equation (4. 2. 2. 1) is established by an inverse *FFT* transformation. The *FFT* technique is used only to process the calculation of the correlation plane efficiently. The correlated values are transferred from the frequency domain, in order to calculate the location of the correlation peak. This location will be used in the subsequent final calculation of the real velocity field.

(ii) Peak Interpolation

After the peaks in the correlation plane are detected, a curve-fit is applied to estimate the width (w), height (h) and location (x_0, y_0) of the peak. A sample Gaussian function in this regard is presented as follows:

$$f(x, y) = h \text{ EXP} \left[-4 \frac{(x - x_0)^2 + (y - y_0)^2}{w^2} \right] \quad (4. 2. 2. 2)$$

In Eq. (4. 2. 2. 2), (x_0, y_0) is initially known. After images are sampled by the *CCD* camera, the function $f(x, y)$ is known for each integer value and estimation of (x_0, y_0) can be carried out. Following the calculation of the local maximum of the position, the pair (x_0, y_0) is calculated from that maximum and two neighbor local maximums for each direction separately.

(iii) Window and Filter Weighing Functions

The *FFT* method is embedded into the *PIV* algorithm to ensure fast correlation calculations. As cyclic patterns around the interrogation region are assumed, it includes phantom particles in its calculations. The phantom particles are particles that exist outside the interrogation area. Phantom correlations exist between any positions where phantom particles are involved [see Fig. (4. 2. 2. 3)]. Particles/droplets that are not present in either stage of the interrogation area, when the first or second image is recorded, do not contribute to the true correlation. They reduce the signal/noise ratio. In order to eliminate phantom correlations near the edges of the interrogation area, the size of the area is increased by special window functions (input filter to the *FFT*). These functions re-evaluate the camera images. For example, a Gaussian window function is defined as follows:

$$W(u_1, u_2) = EXP \left\{ - \left(\frac{I}{k} \right)^2 \left[\left(\frac{2u_1}{M} \right)^2 + \left(\frac{2u_2}{N} \right)^2 \right] \right\} \quad (4.2.2.3)$$

The $(M, N), (u_1, u_2)$ and k values in Eq. (4.2.2.3) represent the size of the interrogation region, pixel positions inside the interrogation region and width of the window.

Similar to Window functions in the real domain, Filter functions act in the frequency domain, before the inverse *FFT* is performed [see also Fig. (4.2.2.2)]. Many such functions are adopted to remove the noise during successful identification and processing of the measured data (i.e. background noise when acquiring the illuminated laser light).

An important piece of information in the *PIV* measurements is the size of particles, which contributes to the accuracy of velocity measurements. The particles must be small enough to follow the flow closely, while at the same time, not too small to reflect sufficient light. Excessively large structures may reflect too much light for the camera, if the full intensity of the laser is applied. In gas applications, particles must be smaller than fluid applications (smaller than $10 \mu m - 20 \mu m$) to follow the flow. The velocity of the particle is actually measured, not the velocity of the flow. The buoyancy force in the surrounding liquid must equal the weight of the particle, so the particle will not settle during its movement through the liquid. In addition to the physical size of the particles, the properties of the imaging optics affect the particle image diameter [Adrian (1991)].

Past studies predominantly applied *PIV* techniques to continuous, single-phase flows [90]. Software (i.e. Flow Manager; Dantec Dynamics) for dispersed-flow motion in a multiphase control volume has not been previously developed. In this section, applications to external droplet motion are considered. External multiphase flow measurements bring many accompanying issues that are not found in internal flow cases [see previous discussions at the beginning of Chapter (4)]. For example, the flow is usually not circulating in a closed loop, so corresponding equipment with a

continuous particle supply must be developed. External flow is usually injected into the less dense liquid (i.e. air), which reduces diffusion of the reflected laser light through the air. This increases the intensity of the illuminated light and requirements of camera protection. Since the external flow is prone to instability and transition regions, different flow structures may reflect the laser light differently. Thus, the light may be illuminated differently than illumination from the seed particles.

4. 2. 3 VELOCITY MEASUREMENTS OF DROPLET TRAJECTORIES

In this section, applications of the *PIV* laser based method are described for velocity measurements of external dispersed (droplet) and continuous (jet) flows in the water tunnel. Results of these measurements are presented in Chapter (5). Unlike conventional applications of the *PIV* to continuous, single-phase flows, this section considers how measurements can be performed for dispersed droplets in dilute multiphase flows [see Fig. (4. 2. 3. 1)]. Various setups are considered. Large droplets (up to about 1 mm diameter) are seeded with polyamide particles ($20\ \mu\text{m}$ diameter) and emitted horizontally in quiescent air [see Fig. (4. 1. 1. 8)]. Also, small droplets (on the order of $10\ \mu\text{m}$ diameter) are sprayed from a series of air atomizing nozzles [see Figs. (4. 1. 1. 6) - (4. 1. 1. 7)].

In these cases, the *PIV CCD* camera is aligned perpendicularly to the planar laser sheet. The test section is contained within a plexiglass region within an empty water tunnel, which collects water after it is sprayed. Reflecting optics below the test section are adjusted, so that the emitted laser light is reflected at the proper angle relative to the camera positioning. Once the camera matches a sequential pair of images of dispersed droplets, the average displacement of a group of droplets within an interrogation region is calculated. This approach yields a grid of measured velocity vectors in the plane of the laser sheet.

In the large droplet case [see Fig. (4. 1. 1. 8)], a vertical pipe is fed by a constant water mass flow rate from the top. The horizontal pipe can be replaced with pipes of different diameters, in order to produce a jet-type flow with various emitted droplet characteristics. The mass flow, pressure and diameter of the pipes are the main parameters controlling the flow characteristics (i.e. droplet breakup diameter). The seed particle supplier (upright mixer at the midpoint of the horizontal pipe) mixes polyamide seeding particles of $20\ \mu\text{m}$ diameter with the water stream, thereby immersing particles within the emitted droplets for *PIV* measurements. The seed particle supplier feeds particles into the water stream by gravitational and pressure effects induced within the adjoining horizontal pipe. Without particle seeding of large droplets, it was observed that an inadequate number of droplets passed through the interrogation region for *PIV* image analysis. The flow with the *PIV* on-line measurements can be seen in Figs. (5. 5. 4) – (5. 5. 5).

In the small droplet case [see Figs. (4. 1. 1. 6) - (4. 1. 1. 7)], the droplets are emitted from the atomizer containing nozzles and atomizers. The velocity field of dispersed droplets was measured with the *PIV* setup, without the seeding particle supplier. Additional measures were studied to improve the measurement capabilities. These steps would ensure additional camera sensitivity for capturing the images digitally. For example, a smaller spreading angle of laser light could be achieved by using a custom-made cylinder type laser lens. The droplet flow with the *PIV* on-line measurements can be seen in Figs. (5. 5. 13) – (5. 5. 14).

4. 3 MEASUREMENT UNCERTAINTIES

The experiment operated for some time before the velocity data acquisition was performed due to adjustment of necessary settings, such as the water line, nozzle

mass flow, *PIV* laser equipment (i.e. different alignments: flow-laser light-camera view) and *CCD* HighSense camera settings. Each experiment with the spray and jet flows was conducted under the closest possible steady-state conditions.

Several sources of experimental errors were investigated. Initial relative alignment of the objects in the experimental design is important to minimize adverse effects on measured results. Perpendicular alignment in all three dimensions for combinations of all entities, such as the laser plane/camera view and camera view/flow, must be successfully performed. Various other factors affect the accuracy of captured images from the seeded droplets. These factors include light intensity from the laser and different droplets, droplet diameters, number of droplets, camera sensitivity, camera distance from the laser sheet, and errors associated with the equipment (transfer of the signal within the laser equipment). The line pressure and water mass flow rates at the line outlet and nozzle exits were measured. The repeatability of the daily and weekly measurements was ensured by setting equal water mass flow rates. More information in these regards is given in Section (5. 5).

The *AIAA* standard [93] was used to perform an uncertainty analysis for the measured dispersed phase velocity results. Bias, precision and total uncertainty errors were calculated from the measured results. The calculated error estimates are presented here for trajectories at different elevations of the camera – view Region.

(i) Bias Limit

The Bias limit of a measured variable k is a Root – Sum – Square (*RSS*) of the elementary Bias limits, such as

$$B_k^2 = \kappa_{\Delta L_0}^2 B_{\Delta L_0}^2 + \kappa_{\Delta L_i}^2 B_{\Delta L_i}^2 + \kappa_{\Delta S}^2 B_{\Delta S}^2 + \kappa_{\Delta t}^2 B_{\Delta t}^2 + \kappa_{\Delta p}^2 B_{\Delta p}^2. \quad (4. 3. 1)$$

In Eq. (4. 3. 1), k denotes the following measured quantities:

$$k = k_i(v_{d,x}, v_{d,y}). \quad (4. 3. 2)$$

The variables $v_{d,x}$ and $v_{d,y}$ are the droplet horizontal and vertical velocities at the point of measurement.

The sensitivity coefficients, κ_k , for each measured quantity are defined as follows:

$$\kappa_k = \frac{\partial k_i}{\partial h}, \quad (4.3.3)$$

where h represents a set of measured quantities, i.e.,

$$h = h_i(L_{obj}, L_{img}, S, \Delta t, \Delta p). \quad (4.3.4)$$

In Eq. (4.3.4), the quantities L_{obj} , L_{img} , S , Δt and Δp are the width of the camera view in the object plane, width of the digital image, estimate of the droplet displacement, time interval for a droplet pair, and droplet gauge pressure. In addition, the L_{obj} , L_{img} , S , Δt are specified by the *PIV* equipment manufacturer (Dantec Dynamics). The mean droplet flow gauge pressure was 55 Psi . A fluctuating part of the pressure was $\pm 5 \text{ Psi}$ (9.091 % of the mean value).

Evaluating Eq. (4.3.1) for the elementary bias limits and taking a square root of the bias limit of the quantity k gives a combined bias error of $B_k = 0.01060$. The pressure fluctuation is found to have the biggest influence on the measured droplet velocity field. Its contribution to the bias error is appreciable (81.792 %). This corresponds to the observed disturbances of the dispersed droplet flow.

(ii) Precision Limit

The precision limit of a measured variable k is defined as

$$P_k = \frac{F \cdot \sigma_k}{N}. \quad (4.3.5)$$

The variables F , σ_k and N in Eq. (4. 3. 5) represent a level of measured confidence, standard deviation from the measured mean value and the number of measured samples. For a 95 % confidence level of measured data, the constant is $F = 2$. The standard deviation is evaluated from the following definition:

$$\sigma_k = \left[\frac{1}{N-1} \sum_{i=1}^N (k_i - \bar{k})^2 \right]^{1/2}. \quad (4. 3. 6)$$

The mean value of a measured quantity k in Eq. (4. 3. 6) is defined as

$$\bar{k} = \frac{1}{N} \sum_{i=1}^N k_i. \quad (4. 3. 7)$$

(iii) Total Uncertainty

The total uncertainty for the measured quantity k is defined as the RSS of combined bias and precision limits, i.e.,

$$U_k = [B_k^2 + P_k^2]^{1/2}. \quad (4. 3. 8)$$

The precision limit and total uncertainty are evaluated in the whole domain of the camera view region [discussed further in Chapter (5)]. The minimum precision limit and total uncertainty are calculated as 0.72774 % and 1.66605 %, within 95 % of the measured confidence. These values are obtained at $x = 45 \text{ mm}$ and an elevation of $y = 40 \text{ mm}$ in the camera view region. The location corresponds to the center of the flow, which passes the camera view region. Other data is presented in Table (5. 5. 1). Additional discussion is presented in Section (5. 5).

Several nearly identical experiments were performed for each experimental design under the same conditions to test repeatability of each experiment. The possible sources of experimental errors were examined. Negligible discrepancy between repeated tests was considered. Every input of a measured quantity (i.e.

pressure and mass flow rate) or output of a measured quantity (i.e. droplet velocities) in one test agrees with the corresponding quantity in the other test by within 0.5 %. The measured data from the experiments was found to be repeatable.

4. 4 ICING ON THE HELICOPTER SCOOP IN THE SPRAY-ICING TUNNEL

As discussed previously, practical motivation of this project was better understanding of droplet impact and ice buildup on a helicopter surface scoop. Ice accretion on a scoop in the spray-icing tunnel is presented in this section. Icing experiments under rime ice and glaze ice conditions were carried out. For example, water droplets were sprayed from a set of nozzles in the outer duct onto a replicated model of a helicopter scoop. At the beginning, the air flowed at full speed. This provided a maximum rate of cooling of the tunnel. In the cooling stage, the droplets were sprayed from the nozzles at their minimum velocities, in order to prevent water freezing in the supply lines. Nozzles were supplied with water from the pipe line system with water temperature of approximately $10^{\circ} C$. After a temperature below $0^{\circ} C$ was reached, the droplets were sprayed with their final velocities onto the scoop. The air speed was reduced, in order to remove effects of the air flow on droplet trajectories. The air speed was low enough, as to not produce shearing of the droplet flow on the scoop surface.

The first experiment ran for 2.25 hours. The nozzle system used in this experiment is shown in Fig. (4. 1. 1. 1). The ambient air temperature was $-30^{\circ} C$. By observation, the droplet flow and air flow were not entirely uniform across the width and height of the tunnel. The airflow was significantly reduced (to maintain the ambient temperature) right before droplets were ejected from the nozzle system and

started impacting the test piece. The droplets were not influenced by the air. The created ice was nearly uniform and rime [see Fig. (4. 4. 1)]. The degree of uniformity of the impacting droplet flow can be seen from the degree of uniformity of accreted ice on the test piece. The rate of ice growth was approximately 0.028 mm/s . Since the droplets did not solidify upon impact on the airfoil surface the remaining unfrozen water was sheared by the air and run-off from the airfoil surface. This situation demonstrates a lack of ice mass in the impact area. Such conditions and results are unacceptable for comparison with rime ice numerical results. This situation would be acceptable for validation of glaze ice numerical predictions. It can be seen in Fig. (4. 4. 1) that the scoop surface was covered by the ice almost uniformly.

The second experiment was performed with the nozzle system, shown in Fig. (4. 1. 1. 2). Once the ambient air flow at full speed reached temperature of $-17 \text{ }^\circ\text{C}$, the droplet flow was injected through the nozzles at the maximum flow rate. Then, the air speed was reduced. Glaze ice was created on a scoop test piece [see Fig. (4. 4. 2)]. The core of the droplet flow impinged on the scoop surface. The droplet inertia and gravity effects sheared the droplets toward the back of the scoop, where the droplets gradually accumulated over time. The glaze ice grew towards the direction of the incoming droplets. At both sides of the core of the droplet flow, the remaining droplets impinged and froze. Due to smaller inertia of droplets, the flow on both sides of the scoop froze faster than a region in a core of the flow.

CHAPTER 5

VALIDATIONS AND RESULTS

This chapter encompasses analytical, numerical and experimental results. Validation of the numerical code for droplet/air flow and ice interface predictions is presented.

The transient simulations in the thesis are highly nonlinear multiphase flow simulations with phase change. The phases in contact (droplets/air/ice-walls) have significantly different physical properties and spatial motion, which imposes challenging demands on the numerical algorithms. Examples include the frontward flows and backward ice tracking algorithms, especially at sudden changes in geometry of the test piece. They incorporate a variety of element shapes and test pieces, *CPU* times, grid / initial condition refinements and so forth. For some simulations, it is almost impossible or highly impractical to find analytical or experimental solutions.

Chapter 5-VALIDATIONS AND RESULTS

Icing at the frontward step [Figs. (5. 4. 12) - (5. 4. 14)] is considered as the most complete and comprehensive icing example in the thesis. Three essential aspects are supplied for this case: (i) corresponding analytical and/or experimental validation, (ii) realistic modeling and geometry of the test piece and (iii) grid sensitivity analyses. Multiphase flow with droplets and icing are two major components of the algorithm that were validated. A previously developed graphical user interface was not sufficiently capable of producing complex geometries, especially not smooth and curved surfaces. The frontward step cases have elements of complex geometry [see Figs. (5. 3. 12) - (5. 3. 15)], involving different shapes and sizes of the *CV*. From the perspective of the physics of icing and the numerical algorithms, the frontward step case exhibits complete two-dimensionality. Analytical Lagrangian [section (2. 5)], Eulerian experimental (*PIV*) results [section (5. 5)] for multiphase flows with droplets and combined flow-icing two-dimensional analytical solutions [i.e. in Fig. (5. 4. 14)] were developed by the author. They were used to validate the multiphase flow and icing numerical algorithms. This allowed determination of numerical accuracy, success of the scheme and corresponding *CPU* times.

A fixed grid formulation was adopted in the numerical simulations for the presented examples. There is no adaptive mesh tracking and the grid is created in advance. The examples involve a wide range of quadrilateral element shapes. Icing at the frontward step is the only case, which is completely two-dimensional with respect to the problem geometry, physical phenomena (flow and icing), numerical tracking algorithms and boundary conditions. However, there are difficulties associated with the frontward step case, when evaluating the final “success”. Namely, the case is non-steady. There is no steady state solution, so ice shapes in both directions are compared with the temporal analytical solutions. Accuracy was evaluated by comparing the mass flows and shape locations, based on $ERROR(\%) = f[(l/\Delta x)]$ [i.e. see Figs. (5. 4. 15) – (5.4.17) and Table (5.4.1)].

Icing on the sample helicopter scoop (near the engine cooling bay) is not a complete *2D* case, in terms of icing numerical algorithm and boundary conditions. Furthermore, there is no experimental validation data or analytical

Chapter 5-VALIDATIONS AND RESULTS

solution. Furthermore, the *Phases* graphical viewer had limitations in this case. The viewer allows only grids up to $1\text{ m} \times 1\text{ m}$, with a refinement scale of 0.02 m , which is insufficient to create the detailed curved surface.

Icing on the *conductor* is also an incomplete-quasi $2D$ case, in terms of the icing numerical algorithm and boundary conditions. The numerical icing part of the code lacks experimental re-distribution icing functions [see Chapter (6), Recommendations for Future Research]. Therefore, the numerical results could not be sufficiently validated. Also, similar problematic issues with the *Phases* viewer were encountered.

Different success criteria were used to assess the success of solutions. Within the numerical method: the grid independence of the solution was tested and the error distribution function was obtained: $ERROR (\%) = f [(1/\Delta x)]$. Similarly, within the experimental method, an uncertainty analyses were performed.

With respect to other methods, such as analytical and experimental methods, the success criteria for a particular physical quantity $\psi_{numerical}$ were used as follows,

$$ERROR (\%) = 100x \left[1 - \left(\frac{\Psi_{analytical}}{\Psi_{experimental}} \right) \right] \quad (5.1)$$

$$ERROR (\%) = 100x \left[1 - \left(\frac{\Psi_{numerical}}{\Psi_{analytical}} \right) \right] \quad (5.2)$$

$$ERROR (\%) = 100x \left[1 - \left(\frac{\Psi_{numerical}}{\Psi_{experimental}} \right) \right]. \quad (5.3)$$

Stability is a necessary condition for convergence. Convergence is a sufficient condition for a numerical solution and its accuracy. Additional discussion of how much computational effort is needed to produce sufficient accuracy is presented below.

There are two criteria to control numerical convergence. Firstly, stability is addressed through the time marching (outer iterations). A Courant (Co) condition was

used to estimate a maximum time step for stable computations (see section 3. 3). The Courant number condition is defined as $Co = \langle |\vec{v}_d| \rangle_{ref} \Delta t / \Delta x < 1$. Although an implicit method was used, the Courant number provided a useful criterion regarding the permissible time steps.

Secondly, stability within the spatial discretization was addressed in the inner iterations. Possible high spatial gradients of physical quantities (such as velocity gradients) were managed by the relaxation criteria, which consider the old value (converged solutions from the previous time step) and the new values. For example, $\vec{v}_{new} = \vec{v}_{old} + relax(\vec{v}_{old} - \vec{v}_{new})$. A relaxation factor of $relax = 0.5$ was successfully applied.

Once both time and spatial stabilities were achieved during the iterations, the convergence and subsequent accuracy of the solution were automatically ensured.

5. 1 FREESTREAM DROPLET TRAJECTORIES (ANALYTICAL)

Fundamental study of droplet motion was an initial step for developing the icing numerical code. Consider an example whereby liquid droplets are injected into an incoming horizontal air stream [see Fig. (5. 1. 1)]. In the presented cases, the maximum nominally constant velocity of the horizontal air flow is 4 m/s, while the minimum is 0.02 m/s. Different droplet velocity values are examined. Droplets are modeled as discrete spherical particles. The results are generated from analytical trajectories outlined in Section (2. 5. 2). The elapsed simulation time for all cases is 10 seconds. In all cases, droplets are injected at a distance of $x = 0.1$ m from the origin ($x = 0$ m, $y = 0$ m).

Droplets with a diameter of $D_d = 50 \mu m$ are injected into the air stream [see Fig. (5. 1. 2)] vertically (upwards arrow in the figure). A *low-Re* flow regime is considered. A uniform airstream flows horizontally along the flat plate with a speed of 0.02 m/s . As opposed to the high-Re flow regime [see for example Fig. (5. 1. 3)], the droplet trajectories [see Eqs. (2. 5. 2. 12) – (2. 5. 2. 13)] have a step-like shape. As the droplet injection velocity increases, the droplet penetration distance into the freestream increases.

For the *high-Re* flow regime at different velocities, the droplets with a diameter of $D_d = 10 \mu m$ are injected into the air freestream [see Fig. (5. 1. 3)]. The airstream velocity is 4 m/s . As the droplet injection velocities [u, v in Fig. (5. 1. 3)] increase, the droplet penetration distance into the freestream increases. The trajectories [Eqs. (2. 5. 2. 8) – (2. 5. 2. 9)] are parabolically shaped.

In Fig. (5. 1. 4), various droplet diameters influence each trajectory [Eqs. (2. 5. 2. 8) – (2. 5. 2. 9)]. Droplets are injected at horizontal velocity 4 m/s and vertical velocity 1 m/s into the air freestream. The horizontal airstream velocity is 4 m/s . Larger droplets have more inertia and they can travel further in the y -direction into the airstream. It was observed that bigger droplets propagated less distance downstream than smaller droplets, due to higher drag resistance. The impact of varying initial velocities in the gravitational field on droplet trajectories [Eq. (2. 5. 2. 15)] is presented in Fig. (5. 1. 5).

A schematic of an evaporating droplet in motion is presented in Fig. (5. 1. 6). An analysis of results reveals that for the higher-Re number case [Fig. (5. 1. 7)], the evaporative cooling effect on droplets is more influential than on droplets at low Re numbers, as expected. Due to the reducing droplet diameter [Eq. (2. 5. 2. 28)], the droplets impose smaller resistance than larger droplets. As a consequence, they travel a smaller distance (y -direction) in the inflow air region than bigger droplets. A thermal analysis of the evaporative cooling process provides a proper variation of droplet diameter with time and position along the droplet trajectories.

Temperature-dependent thermophysical properties, i.e. ρ_{air} , ρ_d and μ_{air} , are obtained from existing tables for the low-Re number values. Sample trajectories [Eqs. (2. 5. 2. 12) – (2. 5. 2. 13) with temperature dependent physical properties – i.e. $\rho_d(t)$ and $\mu_a(t)$] from these cases are shown in Fig. (5. 1. 8). The results with the temperature-dependent thermophysical properties for the non-evaporating and evaporating droplets are similar. The evaporative cooling effect slightly decreases the y -distances reached by the droplets in the air flow region.

5. 2 NEAR-WALL DROPLET DEFLECTION

It was established earlier that self-similarity of the droplet velocity profile exists in the vicinity of a flat surface [see Chapter (2), Section (2. 5. 1) and the appendices]. In this section, aspects of validation and analysis of these results are shown. A comparison of Eq. (2. 5. 1. 21) with the scaling requirements, Eq. (2. 5. 1. 25), requires that

$$\gamma = 24.918 \cdot x^2. \quad (2. 5. 1. 25)$$

Figure (5. 2. 1) confirms close agreement between the similarity analysis and the scaling requirements. Differences between both methods are less than 1.0 %.

A plot of the $F(\eta)$ function, expressed through Eq. (2. 5. 1. 19), is presented in Fig. (5. 2. 2). Since the similarity function represents the velocity ratio, the droplet x -velocity is shown on the x -axis as a portion of the droplet x -velocity on the reference

streamline. The relation between the similarity function and the similarity parameter is linear. This ratio stays constant at all x locations in the vicinity of the flat surface.

A plot of the function $y = f(F)$ is shown in Fig. (5. 2. 3). At each location x , there is a corresponding profile of the x -component of the droplet velocity, v_{xd} , along the y -direction. These profiles are equivalent, since for each x location, the edge of the droplet flow field is further away from the surface. Therefore, the same number of y positions across the flow need to be stretched by the factor $y \sim (x_2/x_1)^2$. It can be concluded that all of these specific functions, $y = f(F)$, at each x location across the y field, collapse into the same line. This confirms that self-similarity of the function is maintained throughout the droplet flow field.

The profiles of Eq. (2. 5. 1. 22) are presented in Fig. (5. 2. 4). At $x = 0$ m and $y = 0$ m, a zero droplet velocity solution exists, due to the no-slip boundary condition at the wall. At any position $x > 0$, two-dimensionality of the droplet flow appears. Inertia deflects a fluid parcel at the top of the droplet in the x -direction, while accommodating the no-slip condition at the bottom of the fluid parcel. Also, the interfacial drag force in the x -direction opposes the motion of the fluid parcel at the top (in the x -direction). Since the opposing resistance contributes to droplet inertia, due to the viscous no-slip condition at the wall, it is larger than the drag in the x -direction. The fluid parcel also experiences drag forces in the y -direction, so that the fluid parcel is also deflected in the y -direction. The consequence of these effects is that the fluid parcel is moved away from the wall. This is modeled in the mathematical formulation [see Chapter (2) and Appendix]. Due to the 2-D droplet motion and external forces exerted on each fluid parcel, a corresponding mass flow in the y -direction appears. This mass flow causes a change of x -momentum in the y -direction. This momentum displacement in the y -direction represents the off-plane trajectories of droplets, as they are induced by interfacial drag forces.

Sample droplet trajectories are presented in Fig. (5. 2. 5). These results are used in the subsequent numerical study. The physical problem consists of an open inlet region, outlet region and the top side of the domain. At the inlet, the boundary condition for the droplet velocity is specified as v_{xd} and v_{yd} at each location. The

droplets are resisted slightly by the air motion, due to its lower velocity. Throughout the domain, the drag force between droplets and air acts on the droplets to deflect each fluid parcel over time. The droplet equation incorporates this effect. The droplets move through the air and reach a distance of $L = 0.2 \text{ m}$ at the end of the helicopter surface, where the outlet is located.

The droplet mass-based displacement up to the γ streamline from Eq. (2. 5. 1. 21) is plotted in Fig. (5. 2. 6). If the thickness of the body is increased by an amount represented by Eq. (2. 5. 1. 21), the actual droplet flow will have the same flow rate as the inviscid (uniform) flow field. If this thickness is added to the plate surface, the flow over the thickened body can be treated as an inviscid flow. The droplet momentum-based displacement up to the γ streamline Θ_s [Eq. (2. 5. 1. 28)] is plotted in Fig. (5. 2. 6), along with a comparison of all displacements.

Displacements based on the droplet similarity solution from Eqs. (2. 5. 1. 21), (2. 5. 1. 25) and (2. 5. 1. 28), and the displacement based on the Blasius single-phase solution are compared. These results provide useful insight regarding physical interactions between droplet motion and air flow near a stationary boundary.

5. 3 EXTERNAL DISPERSED PHASE FLOW (NUMERICAL)

This section focuses on droplet velocity modeling in a co-flowing airstream with the newly developed Eulerian numerical formulation of multiphase flow. Past studies have documented the carrier (air) phase modeling [16]. It has been shown that spatial averaging of the dispersed phase momentum equations can accurately predict the trajectories of droplets moving under gravity in a co-flowing air stream. In

droplets, rather than individual droplets. It is viewed that the current approach provides a useful basis, from which less time-consuming predictions of impinging droplets in various multiphase flow applications (such as aircraft icing and other applications) can be realized.

The numerical model is validated for three geometrical cases [see Fig. (5. 3. 1), Fig. (5. 3. 12) and Fig. (5. 3. 17)]. The analytical one-phase and two-phase Lagrangian solutions for droplet motion are developed and grouped in section (2. 5. 2).

Comparisons between analytical and predicted results were performed at various locations, including the walls of the domain. The discrepancy between results for the velocity fields and droplet trajectories, respectively, are represented as

$$ERROR_{\langle |\vec{v}| \rangle} = \frac{\langle |\vec{v}| \rangle_{num}}{|\vec{v}|_{analy}} \times 100 \quad [\%] \quad (5. 3. 1)$$

$$ERROR_{\langle |y| \rangle} = \frac{\langle |y| \rangle_{num}}{|y|_{analy}} \times 100 \quad [\%]. \quad (5. 3. 2)$$

In addition, studies involving sensitivity to grid spacing and initial conditions are performed. Grid independence of results requires that the results do not appreciably change with any further refinements of the grid spacing. Each case was validated for grid independence. It was verified that numerical predictions were independent of initial conditions for different droplet and air velocities (as expected), provided that grid convergent results were achieved.

The Courant number was used as an estimate to determine the upper limit of the time step for each phase with respect to the smallest grid spacing in the computational domain. Although an implicit method was used and the Courant number condition usually corresponds to explicit schemes, it was viewed as a useful indicator regarding the general order of magnitude of permissible time steps. The Courant number condition is defined as $Co = \langle |\vec{v}_d| \rangle_{ref} \Delta t / \Delta x < 1$. The phase should not propagate more than one grid space distance within a time step. On the

other hand, the lower limit of the time step in particular multiphase simulation (i.e. droplet/air flow) was determined based on the most sensitive phase in contact (air). Namely, solutions for the continuous (air) and dispersed (droplet) phases have different sensitivities to a given time step size (different material and transport characteristics of the phases and phase flows in different sections of the domain). Since the most sensitive phase in contact (air) dictates the time step needed for disturbances to be successfully propagated through the computational domain, the same time step for all phases was selected based on the most sensitive phase and the smallest grid spacing in the computational domain. Within the time step, there are different inner equation iteration loops for each phase and an extra intra equation iteration loop. These additional iterations ensure the convergence of the solutions for each phase within the time step.

Grid refinement at the locations of significant changes of physical quantities (i.e. at a step) was carried out for each case. The grid refinement was extended into other parts automatically. The focus was to study accuracy of the solutions and grid independence, rather than optimization of the overall *CPU* time for each case. A constant time step was selected for the most sensitive phase, with respect to the smallest grid spacing. In the region of coarser grid spacing, the time advancing solutions would not be faster. For example, the ice interface is not allowed to propagate more than one element width in a single time step. When the grid was not refined, coarser grids maintain conservation accuracy in the *CVFEM* formulation. The cases were performed with non-uniform grids. Additional studies with various non-uniform grid arrangements are not presented in this thesis. Also, there are a large number of cases created and tested. Some were very difficult or time consuming. The most convenient way was to simulate cases involving uniform grids.

(i) Case 1

The geometrical configuration and boundary conditions are illustrated in Fig. (5. 3. 1). The length and height of the domain are 1 m . The following different grids were tested: 6×6 , 8×8 , 10×10 , 12×12 , 18×18 and 26×26 elements (Fig. 5. 3. 2). The results for the velocity fields are presented for inlet droplet and air velocities of $v_x = 2.5\text{ m/s}$ and $v_y = 0.0\text{ m/s}$ in Fig. (5. 3. 3). The results for the velocity fields are presented for inlet droplet and air velocities of $v_x = 7\text{ m/s}$ and $v_y = 0.0\text{ m/s}$ in Fig. (5. 3. 4). It can be noted in Fig. (5. 3. 3) and in Fig. (5. 3. 4) that the droplet velocity profiles are parallel across (in vertical direction) the width of the domain, along (in horizontal direction) the domain for all grids. The impacting droplet flow onto the wall (right side of the domain) is uniform. This observation of the velocity field is important for subsequent icing studies. From such flow, the uniform ice interface propagation is correctly to be expected. In addition, the study shows that under smaller inlet horizontal droplet velocity in Fig. (5. 3. 3)] than the inlet horizontal droplet velocity in Fig. (5. 3. 4)], the gravity needs less time to deflect the droplets from their initial horizontal direction. The results in Figs. (5. 3. 3)-(5. 3. 4) are free of downstream-upstream influence of droplet motion on the flow near the inlet (Dirichlet boundary condition) of the domain.

Figure (5. 3. 5) shows a comparative study of the effects of interfacial drag resistance of droplets (for droplet and air velocity fields). The inlet velocities are equivalent for both phases, but varying interfacial drag has noticeable effects on droplet motion throughout the domain, especially at the wall because of different motion of droplets and air in that region. Different droplet diameters lead to varying interfacial diffusion, thereby affecting the domain and near-wall deflection of droplets.

In the upper section of Fig. (5. 3. 5), the mean droplet diameter (same inlet phase fraction of droplets) is about 2.24 times smaller than the lower section of the same figure. Therefore, in the lower section of Fig. (5. 3. 5), the interfacial drag is five times higher than that in the upper section. Different motion of droplets and air arise from different interfacial drag, near-wall effects and other effects. Droplets hit the

wall with a full impact velocity, while air moves away after it reaches the wall. Due to the no-slip air velocity Dirichlet type of boundary conditions at the wall, the boundary layer exists. The air stream decelerates as it approaches the wall, while pushing against the wall and building the adverse pressure gradient. This adverse effect deflects the near air motion away from the wall. The elliptic nature of the pressure causes it to propagate in the upstream direction, against the flow. The longer the propagation, the larger is the distance of the air deflection before it reaches the wall. The droplet velocity field is sheared by interfacial drag imparted by the flowing air stream. When this interfacial drag becomes sufficiently large, the droplets are deflected upwards against gravity, which is expected. Additional studies have verified that this droplet deflection varies for different incoming air velocities. The validation case involving interfacial droplet-air drag interactions is presented in experimental studies in section (5.5).

The Dirichlet boundary conditions at the inlet and at the wall are ‘strong’ conditions and the confined flow between them may become affected by such conditions. Closer observation of upstream adverse pressure gradient influence in this case study reveals that despite a distance of 1 m from the right wall, the air flow slightly affects the coupled droplet and air flows next to the inlet boundary condition at the left side of the domain. The computer algorithms seem to execute stable calculations. The results of this case study are reasonable. Similar micro accurate studies of the droplet/air flows near the vertical wall with associated available independent validation results seem to become complicated or insurmountable. For most accurate studies, a long inlet section may be needed and the relatively narrower airflow may need to be driven against the wall to ensure air flow turn along the vertical walls and its vertical exit at the sides of the computational domain. Such air flow is expected to be additionally disturbed by the maximum droplet velocity at the wall.

Figures (5. 3. 6) – (5. 3. 7) show close agreement between analytical [Eq. (2. 5. 2. 15)] and numerical (predicted) droplet trajectories for both 12×12 and 18×18 grid

discretizations. In this cases, although phases are calculated simultaneously, it is assumed that negligible drag between the droplet and air phases exist.

In Fig. (5. 3. 8), close agreement between the predicted and analytical [Eq. (2. 5. 2. 14)] droplet velocities is observed at different elevations. Droplets impinge on the wall at $x = 1 m$, while the air stream decelerates as it approaches the wall. The air stream turns parallel to the wall after decelerating near the stagnation point, symmetrically in opposite directions. Adverse pressure gradients and inertia affect the air motion near the wall. It was verified that the droplet trajectories become more horizontal when the incoming velocities increase, while falling faster under gravity when these velocities become smaller (as expected). Figures (5. 3. 6) – (5. 3. 8) represent an intermediate value of relative Reynolds number, whereby both inertia and gravity contribute to droplet deflection from its incoming horizontal pathline.

The analytical trajectories [Eq. (2. 5. 2. 15)] and predicted trajectories are plotted in Fig. (5. 3. 9) for two different inlet velocities, namely $v_x = 2.5 m/s$, $v_y = 0.0 m/s$ and $v_x = 7.0 m/s$, $v_y = 0.0 m/s$. The predicted results illustrate the expected trends. At higher inlet velocities, the inertial forces are larger than in the case of the smaller velocities. As a result, gravitational deflection of trajectories is larger for the case of lower inlet velocities. In Fig. (5. 3. 9), reasonably close agreement is achieved between predicted results and the analytical solutions [Eq. (2. 5. 2. 15)] for both cases and initial elevations of injected droplets ($0.5 m$ and $0.67 m$). Figure (5. 3. 10) illustrates that the numerical error regarding predicted droplet impact position on the right wall diminishes to below 1% when the grid spacing is reduced to an 18×18 grid.

Figure (5. 3. 11) presents an initial condition sensitivity study. For each computational simulation of the numerical code, different initial velocities were specified throughout the computational domain. The resultant velocity field at the wall of the domain (opposite to the inlet side) is observed for each calculated case. In Fig. (5. 3. 11) for Case (1), the solution at the wall is almost insensitive to the specified initial conditions in the domain. The initial conditions have only a minor

effect on the results at the wall of the domain. All computed errors fall below about 2 %.

The solution accuracy is addressed hereafter for the simulation cases in section (5. 3).

The linear time derivative term governs the transient process, such as the droplet flow velocity in the x -momentum equation. This first order derivative is numerically formulated as first order accurate in time. Therefore, the transient numerical calculations are first-order accurate in time. The backward Eulerian approximation of that temporal term is formulated as a "lumped" approximation, yielding fully implicit and stable transient calculations. There is no update at the intermediate time level. Thus, additional storage of computational effort of a Crank-Nicholson temporal scheme are not incurred. Due to the scheme's robustness and implicit implementation, the current Eulerian formulation is tolerant regarding the permissible size of time step. One should also consider the nature of the flow, as modeled with this time approximation. Generally, if the flow exhibits small transient changes or it is predominately steady, a linear approximation of the time derivative is sufficient. But if the flow is highly non-steady (i.e. turbulent dispersed flow), a higher order temporal scheme may be adopted. This would be needed if the time increments (i.e. time steps in the outer-loop of the numerical code) are not sufficiently small. In this thesis, the droplet flow problems are predominately steady, especially at impact locations on the surface of the domains (i.e. walls), where the examples below are referred to. The time steps are optimized with respect to the grid and the sensitivity of the phases.

In addition, the flow reaches the wall opposite to the inlet in fairly short times. For example, in cases of droplet inlet velocity $\bar{v}_d = (7,0)$ m / s, the traveling time of the droplet wave (convected droplet velocity field) is: (i) Case (1), 0.143 s; (ii) Case (2), 0.089 s and (iii) Case (3), 0.071 s. This droplet flow propagation wave is the only relatively major transient part. It is quite short for all cases under consideration due to the inlet velocity ($u_d = 7$ m/s) and inlet-wall (i.e. step) distance.

In the investigations, the main focus is to observe numerical accuracy of the steady-state solutions of the velocity fields at the wall of the domain (droplet impact

locations), as a function of the time step size. In addition, the overall accuracy of the numerical solution is presented, with respect to time accuracy. All cases in section (5. 3) have approximately the same characteristics, in terms of temporal performance. In particular, time accuracy of the numerical solutions is assessed through the x - and y -direction droplet impact velocities at the wall of the computational domain [Case (1), Section (5. 3)]. The interfacial air resistance is negligible and gravity is the external force acting on the droplets. In this case, the corresponding analytical solutions are presented in Eqs. (2. 5. 2. 14) - (2. 5. 2. 15). As mentioned above, after the droplets propagate throughout the computational domain and hit the wall, the steady state solution is obtained. For each time step, the numerical solution is compared with the analytical solution. The results are presented in terms of logarithmic values of velocity errors. The slope of the curve approximates the order of accuracy of the temporal solutions for each case.

Table (5. 3. 1) presents the solution error for a variety of time steps, ranging from 0.005 s - 0.500 s . It can be observed that the time step has small impact on the accuracy of the predicted droplet velocities, which suggests that there is no or negligible temporal non-linearity in this flow and/or the selected time steps are sufficiently small for this flow. Similar trends are obtained for Case (2) and Case (3) [see also Fig. (5. 3. 11), where independence of initial conditions on the final steady-state solution of the droplet flow at the wall is presented]. The errors for Case (2) and Case (3) for x - and y -droplet velocities are approximately 0.42% and 3.66% , respectively. Given the first order transient term, this observation indicates small infrequent changes in time, as the flow is predominately steady-state. Steady-state solutions were sought at the wall, when the droplet flow becomes fully developed. This happened after the droplet wave propagated throughout the computational domain, hit the surface and stabilized. If the flow was transient such as time-varying turbulence in combustion processes, the numerical solution would respond and become largely dependent on the size of the time step. In such cases, a sufficiently small time step is needed to capture non-linearities in the temporal solution. Otherwise, a second-order scheme should be implemented. The time step was

optimized for good solution convergence. Flow disturbances cannot propagate more than the approximate length of the control volume within the time step.

The next example in Fig. (5. 3. 12) presents the investigation on the quality of the numerical droplet flow solutions. The accuracy of the (overall) numerical solution is assessed through error in the numerical solution as a function of grid spacing. The error is presented in terms of the droplet impact position on the wall for Case (1) in Fig. (5. 3. 1). An analytical expression (Eq. [2. 5. 2. 15]) is used for comparison with the numerical results. A logarithmic coordinate system is used to assess the accuracy of the numerical solutions. By decreasing the grid spacing, $Ln(\Delta x)$, the solution error, $Ln(Error)$, decreases. The solution error is approximately a 3-rd order function. The lowest solution error, 0.57%, is obtained for grid spacing, which is represented by the fifth point on the diagram, $Ln(Error) = Ln(Error) [Ln(\Delta x)]$. The solution function is further approximated, yielding a linear function, $Ln(Error) = 3.42 Ln(\Delta x) + 9.84$. The slope of this function represents the order of accuracy of the numerical solution. It can be observed that the slope of the linear function is approximately 3, which suggests that the accuracy of the numerical solution is approximately 3rd order. Numerical solutions for the same kind of impacting droplet flow on surfaces in section (5. 3), such as in Case (2) and Case (3), do not lose accuracy.

(ii) Case 2

For this case, the geometrical configuration and boundary conditions of a frontward step domain are illustrated in Fig. (5. 3. 13). This case resembles external flow over a helicopter intake scoop. The total height of the domain is 1 m. The step height is 0.25 m. The distance from the left boundary and the step is 0.625 m. The following different grids were tested: 12 × 12, 16 × 16, 20 × 20, 24 × 24, 34 × 34 and 52 × 52 elements. The droplets are injected into the co-flowing air stream at the left boundary.

The resultant velocity fields are presented for the following inlet droplet and air velocities: $v_{d,x} = 7 \text{ m/s}$, $v_{d,y} = 0.0 \text{ m/s}$ [Fig. (5. 3. 14)] and $v_{a,x} = 7 \text{ m/s}$, $v_{a,y} = 0.0 \text{ m/s}$ [Fig. (5. 3. 15)]. The droplet flow and air flow are not coupled in this case study. The flows are studied separately as they impinge on the step. A group of droplets moves under gravity and impinges at a certain angle onto the step. The step is modeled with a zero-gradient Neumann type of conditions for incoming droplets, i.e., $\partial \bar{v}_d / \partial \bar{n} = 0$. This condition is particularly important for impinging droplets on an accreting ice surface, as droplets adhere onto the wall upon impact. The air stream moves around the step, while droplets impact on the step.

For the air flow, the step is modeled with no-slip boundary conditions, i.e., $\bar{v}_a = \vec{0}$. After the decelerating air approaches the wall, the near-wall adverse pressure gradient contributes to deflection of the air away from the impinging droplets and step surface. The droplet flow is free of downstream-upstream influence of the air adverse pressure gradient [see Fig. (5. 3. 14)]. It can be noted in Fig. (5. 3. 15) that the adverse pressure gradient may reach the vicinity of the inlet section and insignificantly affect the air flow to turn away from its initial horizontal direction. The solver did not experience difficulties in computing the flows. The results near the inlet seem not to be notably affected by the adverse air pressure. It appears that the air velocity results may not appreciably differ from those, obtained with larger inlet section of the domain. After impinging the step, the air flow turns around the step and accelerates towards the exit, where its bulk velocity varies approximately with inverse proportionality to the cross-sectional area (due to mass conservation requirements).

Numerical accuracy versus elapsed *CPU* time, *accuracy / CPU [% / s]*, was compared for the situations of multiphase flow impacting on the frontward step for the results with different grids. Criteria used to assess the success of the simulations is defined as $accuracy [\%] = 100 - 100 \times \left(1 - \psi_{numerical} / \psi_{analytical} \right)$. The convergence of the numerical solution to the analytical solution was observed during the time iterations. The details for each case are reported below. Once the transient

Chapter 5-VALIDATIONS AND RESULTS

numerical calculations reach the steady-state at the wall, the results were compared with the analytical solutions for the droplet flow [Eqs. (2. 5. 2. 14) – (2. 5. 2. 15)].

Stability and convergence of the solution within the inner and intra iterations were controlled and ensured by the relaxation factor and residual tolerance, $relax = 0.5$ and $tol = 0.001$, respectively. During the simulations, the tolerance criteria was almost instantly satisfied. The flow solutions converged to the tolerance criteria within each time step. This indicated stable numerical calculations. There was no need to observe how the difference between the successive inner solutions approached the tolerance criteria, as a function of the number of inner iterations.

The details of the numerical solution based on grids of 12×12 , 20×20 and 24×24 are reported next. The algorithm is very stable, even for coarser grids than 12×12 (i.e. grid 6×6). Generally, if the time step is not sufficiently small, the solution may diverge. An estimate for the maximum time step allowed for each grid is needed beforehand. The flow cannot propagate through more than one CV within a given time step. Finer grids, along with smaller time steps require more iterations and therefore larger computational CPU times. The sensitivity analysis regarding the aspect ratio and $accuracy / CPU$ is presented hereafter. The distance from the inlet to the step wall is $0.625 m$.

The droplet impact position at the wall, y , of the frontward step is considered for three grids. These simulations were tested on an *Intel Pentium Processor III* (865 MHz, 512 MB of RAM). The systems of droplet and air phase governing equations were run simultaneously. The position was compared with the analytical solution in Eq. (2. 5. 2. 15). For a grid of 12×12 , the simulation time step, number of time iterations and simulation time were $\Delta t = 0.0090 s$, $it = 45$ and $t = 0.405 s$, respectively. The approximate corresponding CPU real time consumption was $CPU = 108.000 s$. The error in droplet position at the wall was calculated as $ERR = 5.247 \%$, yielding an $accuracy / CPU = 0.877 \% / s$. For a grid of 20×20 , the simulation time step, number of time iterations and simulation time were $\Delta t = 0.0090 s$, $it = 45$ and $t = 0.405 s$, respectively. The approximate

Chapter 5-VALIDATIONS AND RESULTS

corresponding real time was $CPU = 142.100$ s. The error in droplet position at the wall was calculated as $ERR = 4.496$ %, yielding a ratio of $accuracy / CPU = 0.672$ %/s. For a grid of 24×24 , a simulation time step, number of time iterations and simulation time were $\Delta t = 0.0090$ s, $it = 70$ and $t = 0.630$ s, respectively. The approximate corresponding real time was $CPU = 233.300$ s. The error in droplet position at the wall was calculated as $ERR = 0.097$ %, yielding a ratio of $accuracy / CPU = 0.428$ %/s.

From the information given above, it can be concluded that the coarser grid provides the highest ratio of $accuracy / CPU$. The biggest computational effort is needed for the most accurate result (grid of 26×26). With grid refinement, computational effort rises faster than accuracy. By grid refinement, computational expense may exceed the accuracy reached. It seems that there is no optimum with cheap and accurate numerical simulations, when grid refinement is involved. This is partially due to the nature of the *CVFEM* method, which offers stable and reasonably good results, even for very coarse grids. It is an elemental based formulation, with conservation balances at the sub-elemental level. It gives conservation and grid flexibility. The user should ultimately decide how much computational time and accuracy are acceptable.

Figure (5. 3. 16) investigates drag-induced deflection of droplets near a wall past the frontward step. Grid converged results of droplet and air velocities are presented in Fig. (5. 3. 16) for two different interfacial drag forces with two different diameters of droplets. Lower interfacial drag [Fig. (5. 3. 16); upper section] leads to more droplets deflected upwards against gravity. Air motion is deflected around the step, while cross-phase diffusion exceeds gravitational acceleration. The interfacial drag is calculated based on a droplet diameter of $D_d = 0.00008$ m. In a lower section [Fig. (5. 3. 16)], the interfacial drag is larger than in upper section. It is calculated based on droplet diameter $D_d = 0.00030$ m. Near the wall, cross-phase diffusion becomes particularly significant (over gravity) and smaller droplets are most readily deflected, due to the rapidly changing air stream near the step. Due to the geometrical

wall-step effect, droplets become immersed into the air stream and gravitational effects become negligible. This phenomenon may also arise in cases when gravity deflects droplets from the air stream in the region without the presence of a wall.

An upper case in the figure shows a situation where the droplet flow with $D_d = 0.00008\text{ m}$ is more affected by the air flow than in a case with $D_d = 0.00030\text{ m}$. In this case study, it can be noted that the second column of velocity vectors from the inlet in the figure may be insignificantly affected by the air pressure. The numerical solver did not show problems with calculation stability and convergence. The results of this case study seem to be reasonable good. Additional micro study of the flows around the step with available validation results of the flows around the step may not reveal considerable difference with respect to the presented results of the case study.

Figure (5. 3. 17) depicts the droplet and air velocity fields, presented in Fig. (5. 3. 16), down from the inlet to 0.0781 m before the step (wall). The x - and y -relative velocities between phases are small and the small diameter droplets ($D = 0.00008\text{ m}$) are almost entirely immersed into the airflow and they closely follow the airflow. Due to the relatively small diameter of droplets, gravitational effects are almost negligible. The x -component and resultant velocities rapidly decrease as the flow decelerates, when approaching the frontward step. The y -component velocities increase, since the flows turn upward around the step. Figure (5. 3. 18) presents the droplet and air velocity fields, presented in Fig. (5. 3. 16), vertically from the bottom of the computational domain to the elevation of 0.3500 m [above the step (wall)]. The distance before the step is 0.0781 m . The x - and y -relative velocities between phases in contact are small and $D = 0.00008\text{ m}$. Similarly as previous figures, droplets are almost entirely immersed in the airflow. The x -component and resultant velocities of both flows increase, as the flows at larger vertical elevations do not decelerate as much as lower elevations, due to the presence of the step.

The change of relative angles between the corresponding velocities of the droplet and air phases is presented in Fig. (5. 3. 19), as a function of droplet diameter.

The droplet and air velocity angles are calculated as $\alpha_d = \arctan(v_{d,y} / v_{d,x})$ and $\alpha_a = \arctan(v_{a,y} / v_{a,x})$, respectively. The relative difference between angles is denoted as $\Delta\alpha$. It can be noted in Fig. (5. 3. 19) that the smaller droplets have smaller relative angles with the airflow throughout the domain, in front of the step. Larger droplets progressively increase the relative difference in flow angle, as they move in the co-flowing airstream toward the forward step. This means that the gravitational effect becomes larger for such droplets in the airstream. Equal and larger droplets than $D = 0.00014 \text{ m}$ developed an increasingly negative vertical component of velocity, $v_{d,y} < 0$, as they approach the step.

Another sensitivity study of varying droplet diameter is shown in Fig. (5. 3. 20), where the change of relative angle between droplet / air velocities is shown as a function of droplet diameter. In Fig. (5. 3. 20), curves are presented in a vertical direction at the distance of 0.0781 m from the step wall. The droplet and air velocity angles are calculated as $\alpha_d = \arctan(v_{d,y} / v_{d,x})$ and $\alpha_a = \arctan(v_{a,y} / v_{a,x})$, respectively. As described previously, the relative difference between angles is denoted as $\Delta\alpha$. It can be noted in Fig. (5. 3. 20) that smaller droplets have smaller relative angles at the specified vertical distance in front of the step. It can be observed that relative angles decrease faster for larger droplets in the vertical direction.

It appears that the newly developed Eulerian formulation can successfully predict effects of cross-phase diffusion on deflected droplets in multiphase flows. In icing applications, the impinging supercooled droplets on the wall may lead to glaze ice accumulation. In practical problems such as de-icing of a helicopter engine cooling bay, downstream freezing of runback flow is highly undesirable. The current predictions provide useful insight regarding the role of cross-stream diffusion on deflected droplets and runback flow along the walls.

The newly developed Eulerian formulation contains various effects which are modeled differently than Lagrangian tracking of droplets, such as spatial averaging of diffusive and gravitational effects on the impinging droplet motion. Numerical errors

of predicted droplet velocities and positions on the step surface for various grids are plotted in Fig. (5. 3. 21). The discrepancy between analytical and predicted results diminishes for the finer grid (as expected). Sensitivity studies were conducted until grid independence of results was achieved. For the finest grid, agreement between predicted results and the analytical solution is within 0.2 %. For coarser grids, the non-linear convective terms lead to greater difficulty in reaching solution convergence. Although numerical errors diminish with refined grids, certain discrepancies arise with coarse grids. The analytical solution involves Lagrangian tracking, while excluding the convective acceleration associated with Eulerian spatial averaging.

In contrast to this Lagrangian solution, the Eulerian method applies a momentum balance to droplets over a fixed control volume, through which the dispersed phase passes. These convective terms are evaluated implicitly, with first-order accuracy in time. If the linearized convective terms are calculated at a time level between the previous and current time (i.e., Crank–Nicholson type of higher order temporal scheme), this would improve the accuracy and convergence of the method, but at the expense of added *CPU* time and computer storage.

Figure (5. 3. 11) shows an initial condition independence study. For Case (2), the solution at the sharp frontward step is almost independent of the specified initial conditions in the computational domain. The initial conditions have only a minor effect on the results at the wall of the domain. All computed errors are approximately 0.15 %.

(iii) Case 3

A multiphase flow around a half-cylindrical step is studied in Case (3). The geometrical configuration and boundary conditions of the half-cylinder surface domain are illustrated in Fig. (5. 3. 22). This case also resembles external flow over a helicopter scoop. The total height the domain is 1 m. The height of the half-cylindrical

Chapter 5-VALIDATIONS AND RESULTS

step is 0.175 m . The distance from the left boundary and the step is 0.5 m . Droplets are injected into the domain with co-flowing air. The results are presented for inlet droplet and air velocities of $v_{d,x} = 7\text{ m/s}$, $v_{d,y} = 0.0\text{ m/s}$ and $v_{a,x} = 7\text{ m/s}$, $v_{a,y} = 0.0\text{ m/s}$ in Figs. (5. 3. 18) - (5. 3. 20).

Different spatial discretizations of the problem domain, including discretizations with 12×12 , 27×27 , 48×48 and 75×75 elements are presented. The discretizations are presented in Fig. (5. 3. 23). Sample droplet velocity vectors are plotted in Fig. (5. 3. 24), while corresponding air velocity vectors are predicted in Fig. (5. 3. 25). A group of droplets moves in the gravitational field and impinges at a certain angle onto the half-cylinder step [see Fig. (5. 3. 24)]. Although gravitational deflection is small with incoming air velocities of 7 m/s , the degree of downward deflection can be observed in Fig. (5. 3. 24), based on the y -component of droplet velocity at the walls. Both convective inertia and gravity contribute to droplet acceleration. After the decelerating air flow reaches the half-cylinder step, the adverse pressure gradient deflects the air stream past the step towards the exit region [Fig. (5. 3. 25)]. Due to mass conservation requirements, the bulk velocity of the air stream increases with approximately inverse proportion to the smaller cross-sectional area of the exit region.

Closer observation of Figure (5. 3. 25) reveals that the air adverse pressure gradient hardly reaches the vicinity of the inlet section, where the Dirichlet boundary velocity condition is imposed. This may slightly affect the confined air between two Dirichlet boundary conditions (inlet-step) to start turning away from the horizontal direction near the inlet section. The solver did not show difficulties in calculating the flows and the results of this case study seem to be reasonable. Additional micro studies of the flows streaming around the step may require longer inlet section of the domain and available validation results in the vicinity of the step. It seems that such studies may not produce significantly better results over the existing results of the presented cases study.

Results of predicted droplet and air velocities are illustrated in Fig. (5. 3. 26) for different rates of interfacial drag between droplets and air. Similarly to the previous study in Fig. (5. 3. 16), in this case study, lower interfacial drag leads to more droplets ($D_d = 0.00008 \text{ m}$) being deflected upwards against gravity. Air flow is deflected around the step, while cross-phase diffusion almost entirely exceeds gravitational acceleration. In the lower section of Fig. (5. 3. 26), the interfacial drag is calculated based on a diameter of droplets $D_d = 0.00030 \text{ m}$, which yields higher interfacial drag between the droplets and air. In both cases, the same inlet phase fraction of droplets is used in the numerical simulations. Near the wall, cross-phase diffusion becomes particularly significant and smaller droplets are most readily deflected, due to the rapidly changing air stream near the step.

The curved wall of the right step is at 0.500 m distance from the inlet, which is smaller distance than in the case in Fig. (5. 3. 16). Due to air pressure buildup next to the wall, the droplet flow is slightly affected in downstream-upstream direction. The adverse pressure gradient influence extends to the vicinity of the inlet with Dirichlet boundary conditions. This can be seen by slight deflection of the velocities near the inlet as they start turning away from the cylindrical step. The deflections seem not to affect the solver performance. Additional micro accurate studies of the flows around the cylinder with associated available validation results may require fully parallel air flow next to the inlet conditions. This could be achieved by the larger domain distance between the inlet and the step or/and with the lower-smaller step.

Numerical errors of predicted droplet velocities for various grids (12×12 , 27×27 and 48×48) are plotted in Fig. (5. 3. 27) on the half-cylinder surface. As expected, the discrepancy between numerical and analytical results diminishes with finer grids and it almost entirely disappears for a 48×48 grid. Close agreement (within $\pm 0.2\%$) is observed between analytical and predicted results [in Fig. (5. 3. 27)]. Grid independence of the predicted results has been achieved.

However despite low errors at finer grids, certain sources of numerical error arise when discretizing equations for coarse grids and time steps. For example, the

Chapter 5-VALIDATIONS AND RESULTS

discretized transient term requires a sufficiently small time step. If a small time step is not used, unstable and divergent computations may occur. As described previously, a useful criterion for characterizing the general order of magnitude of time step is the Courant number condition. This condition requires that the time step is smaller than the grid spacing divided by a characteristic flow velocity. The implicit formulation is first-order accurate in time. If a second-order temporal scheme is applied, added time accuracy is obtained. However, this benefit comes at the expense of a longer simulation time and more storage, due to variables saved at the previous time step in a Crank-Nicholson scheme.

Stable transient predictions of droplet motion are challenging, due to varying time scales between air and droplet flows. The air flow sensitivity to time step size behaves differently from the droplet motion. This occurs because of different physical properties and boundary conditions, as compared to the droplet flow. Also, equations for both phases are scaled differently, thereby implying a different ideal time step for each phase. Numerical simulations are computed with the smallest time step required to satisfy all phases simultaneously. This smallest time step size prolongs calculations, but improves overall robustness of the formulation. Alternatively, variable time steps could be used in the algorithm, but at the expense of added complexity.

In these simulations, particle/wall interactions such as reflected droplets, splashback or droplet breakup were not modeled. These mechanisms could be incorporated with volume-averaged source terms in the formulation. However, unlike Lagrangian methods of tracking the detailed interactions between individual particles, the Eulerian formulation represents volume-averaged interactions. As a result, it would need suitable correlations for these interactions. This approach could provide useful advantages over Lagrangian methods, particularly regarding cost savings (*CPU* run-time and storage) due to volume averaging of the droplet trajectories.

Figure (5. 3. 11) shows an initial condition independence study. The solution at the cylindrical step for Case (3) is almost independent of the specified initial conditions in the computational domain. The initial conditions have only a minor

Chapter 5-VALIDATIONS AND RESULTS

effect on the results at the wall of the domain. All computed errors are between approximately 0.15% and 0.20% .

5. 4 CASES OF TWO-DIMENSIONAL ICE SIMULATIONS

Different physical cases were simulated using the newly developed numerical model and code of droplet flow and icing. Due to a noticeable lack of validation data in past literature, analytical one-dimensional and two-dimensional solutions were developed to assess results from the numerical code. In this chapter, it is considered that the temperature of droplets, air and test piece surface is low enough to yield rime ice conditions and rime ice (not glaze ice). Thus, droplets freeze immediately upon impact on the ice surface. In this section, the specified inlet droplet volume fraction is $\beta_m = 0.0001$.

An important aspect of the numerical simulations is phase impact modeling using the developed coupled flow/ice code. Upon impact, the dispersed flow is modeled as a group of 'physical bodies', while the carrier flow is solely modeled as a continuous flow. This modeling allows simulations with significantly different behavior of phases in contact. This becomes especially important at the solid surface, when droplets exhibit different behavior than the air phase.

The boundary conditions in this section are presented in Fig. (5. 4. 1). This figure shows an ice region with a moving ice interface. Droplets are transported throughout the field. Depending on the level of interfacial drag, they may also be assisted by the surrounding air stream. Upon impact on the ice surface, they freeze, while at the same time the air moves along the ice interface. After impact, the droplet motion is considerably different than the air motion, regardless of the level of interfacial drag effects. While phase flows are supplying the solute (droplets) into the *CV*, the droplet flow inertia is altered due to the re-distributive diffusion effects. This spatial activity inside the *CV* reduces the theoretically expected time deposition of the freezing droplets.

A variable time step was not implemented. There are different phases in contact, which may move simultaneously in very different (even opposite) directions. There are two types of algorithms, namely frontward tracking (dispersed and continuous flows with

a volume fraction) and backward tracking (evolving ice based on the flow direction). The algorithms are synchronized within a single time step. While the first type of algorithm sufficiently follows the physics of the flow, the second type needs additional modeling based on experimental data. Such simultaneous tracking of phases in all directions, under various conditions, makes the attempt to simultaneously search and accommodate the appropriate time step for each phase seem inefficient. For example, within the same time step, there may exist different physical processes simultaneously at the same location. These include convection of droplets into the potential freezing region, freezing of droplets in that region and re-distribution of excess ice into the region in front of the evolving ice interface.

(i) Case 1

This case represents full droplet impact on the top of a test piece [see Fig. (5. 4. 2)]. The boundary conditions are depicted in Fig. (5. 4. 2). Before incoming droplets reach the inlet section of the computational domain, they already fall at their terminal speed. This speed was calculated in Chapter (2) by Eq. (2. 5. 2. 13), based on the droplet diameters (0.0015 m) and a balance of the forces: weight, upthrust, and interfacial drag. The numerical results in Fig. (5. 4. 3) show the ice interface evolution at various times. Droplets impact the horizontal surface at a distance of 1 m from the inlet at their terminal velocity. Gravity affects the direction and magnitude of the droplet velocity at the evolving interface. Despite the air algorithm runs alongside droplet flow and icing algorithms, there is no air or air flow presence between the inlet and interface. Therefore, the ice interface does not affect the flow near the inlet Dirichlet boundary conditions. This can be also observed by unchanged droplet velocity vectors near the inlet and reasonably good validations of the results [Figs. (5. 4. 4) – (5. 4. 5)]. In addition, the solver did not show difficulties calculating the flow, including the flow near the inlet-top Dirichlet boundary conditions.

In real icing cases with the droplet and air flows, the air builds the pressure against the moving (the Dirichlet boundary velocity condition for the air) ice interface. Regardless of its magnitude, the adverse pressure gradient would as a consequence

sooner or later influence the vicinity of the inlet (Dirichlet boundary condition) top section of the domain and affect the coupled droplet and air flows in the entire domain. This situation forces the flows to be deflected towards the open (Neumann boundary condition) vertical sides of the domain. If the air builds appreciable pressure against the interface and consequently against the inlet section (i.e. high-Re air flow or quickly moving ice interface), the incompressible flow numerical algorithms may experience insurmountable difficulties. In such situations, the flows may become compressible, which requires an employment of the compressible governing equations of phase motion and possible additional modeling of the droplet interactions.

The results in Fig. (5. 4. 4) represent the evolving ice interface at various time steps computed with the numerical code and the analytical method ($\Delta h_y = \beta_d v_{d,y} \Delta t$). For each time step, the numerical ice interface closely agrees with the analytical ice interface.

Figure (5. 4. 5) shows the differences between numerical and analytical predictions of the evolving ice interface at various time steps. The solution agreement is reasonably good for the evolving ice interface. The relatively large error at the beginning arises due to the relatively large half of the near-wall CV_w . As expected, this error diminishes for the finer grid.

(ii) Case 2

This problem is depicted in Fig. (5. 3. 1) and in Section (5. 3). The inlet droplet velocity is 10 m/s . The simulation time step is $\Delta t = 0.01 \text{ s}$. The schematic of the problem and the numerical results are presented in Fig. (5. 4. 6) at three different times 240.0 s , 540.0 s and 960.0 s . The inertia of droplets is mainly controlled by the gravity and diffusive effects. The droplets impact at a certain angle on the vertical surface of the test piece. The droplet flow becomes stable and well developed after droplets impact on the surface. It can be seen at first two presented times (4.0 min and 9.9 min) that the ice interface is not yet fully developed. The current numerical CVs at the interfaces are not yet fully occupied by the ice. This is denoted by the less inclined slope of the upper part of the two interfaces at the two different times. At time 9.9 s , the upper part of the

interface is steeper than the upper part of the interface at time 4.0 s . Similarly, the numerical results from the same case are presented in Fig. (5. 4. 7) in two-dimensions and at four different times. The selected numbers of iterations are 16667 , 41667 , 66667 and 91667 . It can be observed in the figure that the ice interface is parallel to the inlet boundary, which indicates that the droplets uniformly impact at the evolving ice interface across the domain. The highlighted vertical line presents the reduced volume fraction at the developing ice interface. Similar situation is presented by the slopes (reduced droplet volume fraction at evolving ice interface) in Fig. (5. 4. 6).

The droplet flow has typical parabolic upstream-downstream dominated motion during entire icing simulation. There is no air presence in this case study. The ice interface does not affect the flow near the inlet with Dirichlet boundary conditions. This can be also observed by expectedly changed droplet velocity near the inlet. The results are in reasonably good agreement with the analytical results [see Figs. (5. 4. 4) – (5. 4. 5)]. The solver did not experience difficulties with the flow calculations (near the inlet of the domain).

In real icing situation with droplet and air flows, the moving ice interface (Dirichlet zero velocity boundary conditions for the air) would push slightly pressurized air flow and consequently the droplet flow (flow coupling is dependent on the drag strength) against the inlet of the domain (with Dirichlet boundary conditions). As a consequence, the degree of deflection of the coupled droplet and air flows become a function of the ice interface position and the magnitude of the adverse air pressure gradient. The droplet and air flows become more deflected towards the open horizontal sides of the domain (with Neumann boundary conditions) once the ice interface propagates closer to the inlet and the adverse air pressure gradient becomes larger. If the air builds significant adverse pressure between the inlet and the ice interface, the coupled droplet and air flows may become compressible. This situation requires an employment of the compressible phase governing equations of motion and possible special additional modeling of the interactions within droplet flow. The ice interface may become distorted such that impinging air may become trapped between the inlet and interface. This situation and appreciable deflection of the flows near the inlet and

especially in the situation when the ice interface is very (too) close to the inlet may affect solver performances.

Figure (5. 4. 8) presents numerical and analytical results for the evolving ice interface at different times, ranging from 166.8 s to 916.8 s . Analytical results are calculated and plotted based on expression $\Delta h_x = \beta_d v_{d,x} \Delta t$. The variables Δh_x and Δt are counted at the moment when the droplet flow hits the wall surface, at the right side of the computational domain.

Figure (5. 4. 9) presents the discrepancy between numerical and analytical ($\Delta h_x = \beta_d v_{d,x} \Delta t$) predictions for the evolving ice interface at various time steps. The solution agreement becomes better as the ice interface evolves. Similarly to the previous example, the relatively large error at the beginning arises due to the relatively large half of the near-wall CV_w .

In addition to the previous droplet flow results, results for the incoming air flow near the evolving ice interface are depicted in Fig. (5. 4. 10). In this problem, Neumann boundary conditions are applied at the top and bottom of the domain. The predictions confirm that the ice interface propagates accurately in a single direction. Extensions to full two-dimensionality are considered in the following problem [Case (3)].

The incoming air arrives at the wall (right side) and appreciably deflects from its initial horizontal path. Unlike the droplet flow, which impinges onto the wall with its full inertia, the air flow behaves quite differently. The propagating ice interface additionally affects the incoming air flow. Numerical stability is more sensitive to the air flow calculations, so that this phase dictates the establishment of the time step criterion.

(iii) Case 3

For this case, the schematic is shown in Fig. (5. 4. 11). The dimensions of the computational domain, which encompasses a frontward step, is $1\text{ m} \times 1\text{ m}$. The droplets are injected into the domain with the velocity $\vec{v}_d = (4, 0)$ m/s, prescribed at the inlet. The droplets impact onto the wall with their full velocity and freeze instantly, while forming evolving ice interface. This case involves a fully two-dimensional ice shape evolution.

The two-dimensional aspects are covered, such as two-dimensional droplet flow, two-dimensional impact of droplets onto the two-dimensional stationary wall and two-dimensional moving (temporal) ice interface and two-dimensional coupled forward fluid-droplet (impacting objects) flow and backward moving solid ice interface with phase change. Temporal analytical solutions of ice growth are developed from the droplet flow analytical solutions. Numerical results for two-dimensional ice interface position are compared with the analytical solutions of ice interface position [i. e. see solution in Fig. (5. 4. 14)].

In all numerical simulations, pertaining to (iii) Case (3) with different grids (see also the text throughout this section), the droplet flow has typical parabolic upstream-downstream directed motion during the entire icing simulation. There is no air flow involved in this case study. Therefore, the ice interface does not affect the flow near the inlet (boundary conditions of a Dirichlet type). This can be also observed by expectedly changed droplet velocity profiles near the inlet. Reasonably good agreement of the results is met with the analytical results [see Figs. (5. 4. 14) – (5. 4. 17)]. In addition, the solver did not experience the difficulties computing the flow (near the inlet).

In more comprehensive real icing simulation with droplet and air flows at the forward step, the spreading ice interface (Dirichlet boundary conditions) pushes the air and consequently the adopting droplet flow against the inlet section (Dirichlet boundary conditions) through the upper-open side of the domain (with Neumann boundary conditions). As a result, the slightly pressurized air flow, which would build the adverse pressure gradient against the moving ice interface may deflect the incoming coupled flows away from their inlet direction (well) before they reach the interface. In the case of propagating ice interface very close to the inlet, the flows between the two Dirichlet boundary conditions (inlet-interface) may exhibit large deflection. In order to avoid such situation, the results of the icing case studies may be addressed at the ice interface positions (stages) far enough from the inlet. In the case of largely deflected and compressed air and/or droplet flows, the incompressible solver may experience difficulties. In such situations, the compressible algorithms with additional modeling of phase (i.e. droplet) interactions could be implemented.

The results in Fig. (5. 4. 12) show the numerical simulations with a 12×12 grid. Since the horizontal droplet inertia is dominant over the vertical, ice starts occupying a majority of the region in a vertical direction. The corner region is spatially and temporally sensitive to two-dimensional predictions of ice growth in the direction of the incoming droplets. Complex interactions with the phases in contact (i.e. supercooled droplets and ice in formation by phase change) are predicted successfully with the preconditioning coefficient and excess droplet redistribution functions, described in Chapter (2).

A similar example of ice spreading at the frontward step is studied with a 26×26 grid [Fig. (5. 4. 13)]. Different stages of the moving ice interface across the domain are shown for the same time step, $\Delta t = 0.01 s$, and the following number of iterations: 4000, 6000, 9000 and 12000. The accuracy of the ice growth predictions (i.e. the positions and accumulated mass of the ice) is assessed through comparisons with the analytical solutions [Fig. (5. 4. 14)]. The analytical ice interface solutions are developed based on the analytical trajectories described in Eqs. (2. 5. 2. 6) - (2. 5. 2. 7). In these equations, both spatial and transient aspects of ice growth were incorporated.

Figure (5. 4. 14) shows the accreted ice on the frontward step at time $t = 500 s$. Numerical and analytical predictions for two-dimensional evolving ice interface positions and the total mass of the accreted ice are shown at time $t = 500 s$. Positions of the ice interface are numerically predicted with grids of 6×6 , 12×12 , 18×18 and 26×26 . The analytical solution of the ice interface position is also presented in Fig. (5. 4. 14). Accounting for the nature of both predictions and excluding additional physical modeling, the ice interface positions based on each of the developed method are expected. It can be observed that the resultant ice interface position with the finer grid is closer to the analytical ice interface than in the case of the coarse grid solution. Better accuracy of the numerical solution with respect to the analytical solution is obtained with the finer grid. The numerical simulations account for close iterative interactions between the flow and droplets within the interfacial region. On the other hand, the analytical method is based on exact droplet flow solutions, which makes this method accurate and therefore insensitive to complexities associated with interactions near the interface. In the analytical method, there is no phase change or backward tracking of the moving interface into the direction of incoming droplets.

Numerical accuracy v. s. elapsed *CPU* time, $accuracy / CPU [\% / s]$, was compared for the situation of droplet flow impacting on the frontward step and freezing [see Case (3) in section (5. 4)]. The distance from the inlet to the step wall is 1 m . Criteria used to assess the success of the simulations are defined as $accuracy [\%] = 100 - 100 \times (1 - \psi_{numerical} / \psi_{analytical})$. Unlike other multiphase flow cases in the thesis, the cases with icing have no steady-state solution. Since the flow and icing processes are entirely transient, the convergence of the overall numerical solution is sought in regards to the two-dimensional analytical solutions. The numerical results are compared with the analytical solution in Fig. (5. 4. 14) at time $t = 500\text{ s}$.

Stability and convergence of the solution within the inner (and intra) iterations were controlled and ensured by the relaxation factor and residual tolerance, $relax = 0.5$ and $tol = 0.001$, respectively. During the simulations, the flow and icing solutions instantly converged to the tolerance criteria within each single time step. This indicated stable numerical calculations and no need to observe the change of the difference between the successive inner solutions, as a function of the number of inner iterations, as it approaches to the tolerance criteria. The details of the representative numerical calculations for cases of droplet flow and droplet flow-icing are reported later.

The ratio of $accuracy / CPU [\% / s]$ is examined for the case of ice interface evolution at the frontward step. These simulations were tested on an *Intel Pentium Processor III (865 MH, 640 MB of RAM)*. The numerical accuracy of the total accreted mass of ice was compared against the analytically obtained mass of ice. The analytical solution for the accreted ice mass was calculated from the region under the analytical solution in Fig. (5. 4. 14).

For a grid of 6×6 , the simulation time step, number of time iterations and simulation time were $\Delta t = 0.1000\text{ s}$, $it = 5000$ and $t = 500.0000\text{ s}$, respectively. The approximate corresponding real simulation time was $CPU = 1595.5900\text{ s}$. The calculated accreted mass of ice at the frontward step was calculated as $m = 318.3530\text{ kg}$. The error in the accreted mass of ice was calculated as $ERR = 17.2883\%$. This yields $accuracy / CPU = 0.0518\% / s$. For a grid of 12×12 , the simulation time step, number

of time iterations and simulation time were $\Delta t = 0.1000$ s, $it = 5000$ and $t = 500.0000$ s, respectively. The approximate corresponding real simulation time was $CPU = 1931.0120$ s. The calculated accreted mass of ice at the frontward step was calculated as $m = 292.6560$ kg. The error in the accreted mass of ice was calculated as $ERR = 7.8207$ %. This yields $accuracy / CPU = 0.0477$ % / s. For a grid of 18×18 , simulation time step, number of time iterations and simulation time were $\Delta t = 0.0100$ s, $it = 50000$ and $t = 500.0000$ s, respectively. The approximate corresponding real simulation time was $CPU = 16793.9260$ s. The calculated accreted mass of ice at the frontward step was calculated as $m = 287.1130$ kg. The error in the accreted mass of ice was calculated as $ERR = 5.7789$ %. This yields $accuracy / CPU = 0.0056$ % / s. For a grid of 26×26 , the simulation time step, number of time iterations and simulation time were $\Delta t = 0.0100$ s, $it = 50000$ and $t = 500.0000$ s, respectively. The approximate corresponding real time was $CPU = 25655.6179$ s (≈ 7.1 h). The accreted mass of ice at the frontward step was calculated as $m = 272.5440$ kg. The error in the accreted mass of ice was calculated as $ERR = 0.4112$ %. This yields $accuracy / CPU = 0.0039$ % / s. It can be concluded that the coarser grid (6×6) provides the highest ratio $accuracy / CPU$ among all cases examined above ($accuracy / CPU = 0.0518$ % / s). The biggest computational effort is needed for the most accurate result. Finer grids produce the best results at the progressive expense of the computational effort. Finer grids have more nodes and generally require smaller time steps. In the case of ice accretion, the ice interface can propagate into the domain at a maximum of one CV within the time step. Similar criteria were valid for the flow simulations. From the perspective of the $accuracy / CPU$ ratio, calculations with finer grids become less efficient. There seem to be no optimal point, where the finer grid would require smaller computational effort and better accuracy than in the case of the coarser grid. It is up to the user to decide how much effort is needed for a desired accuracy of the numerical solution.

The ice interface positions at the frontward step were evaluated at different locations. For example, Figure (5. 4. 15) shows the x -positions of the interface at various y -positions

(distances) from the bottom at the frontward step [see also Fig. (5. 4. 14)]. Numerical ice interface predictions for 6×6 , 12×12 , 18×18 and 26×26 grids are compared with the analytical interface positions. The discrepancies in the positions are larger at the bottom of the frontward step at the corner [left section in Fig. (5. 4. 14)], since the interface gradually spreads in the opposite direction. The errors in such ice interface positions are presented in Fig. (5. 4. 16). The errors are calculated with respect to the analytical predictions. The error difference between numerical calculations with the 6×6 and 26×26 grids starts at approximately 20 % (29.107 % for the grid 6×6 and 8.352 % for the grid 26×26) in the corner region at the frontward step and it gradually diminishes to the top of the step [right section in Fig. (5. 4. 16)].

The mass of accreted ice at the frontward step is calculated from the region under the solution functions of the interface positions. The predicted mass of the accreted ice is calculated as

$$\frac{m_{NUMER}}{m_{UNIT}} \cong \rho_i \left[\int_{A_x} f(x, n) dA \right]. \quad (5. 4. 1)$$

The analytical prediction of the accreted mass of the ice is calculated under the analytical curve of the ice interface as follows,

$$\frac{m_{ANALY}}{m_{UNIT}} = \rho_i \left[\int_{A_x} f(x, n) dA + \int_{A_y} f(x, n) dA \right]. \quad (5. 4. 2)$$

The predicted results of accumulated ice mass and the discrepancies between numerical and analytical results are plotted in Fig. (5. 4. 17)—see also the summarized results in Table (5. 4. 1)—see formulation with viscous terms. The discrepancy in the results of predicted ice mass diminishes with grid refinement (17.288 % \rightarrow 0.411 %). The accreted ice mass calculated with the finer grid 26×26 (272.544 kg) is closer to the analytical result (271.428 kg) than the ice mass calculated with the coarser grid 6×6 (318.353 kg), as expected.

Figures (5. 4. 18)-(5. 4. 19), along with the information in Table (5. 4. 1) present a study of the icing results at the frontward step in regards to two different numerical formulations of multiphase equations with flowing and freezing non-dilute droplets in supercooled icing conditions. The first formulation considers the viscous terms with a single phase dynamic viscosity of water at $t = 0^{\circ}C$, whereas the second formulation excludes the viscous terms from the equations. The differences between the results are briefly addressed below.

Figure (5. 4. 18) presents the numerical predictions of shape of the evolving ice interfaces at an instant of $t = 500 s$. In this set of simulations with different grids, the viscous terms in the multiphase momentum equations with droplets are excluded from the formulations. The ice interface shapes are similar than the shapes, predicted with the viscous terms in Fig. (5. 4. 14). The numerical results of accreted ice mass at time $500 s$ with and without the viscous terms and the differences between the numerical and analytical results are presented in Table (5. 4. 1). The results from icing simulation with the finest grid are in the best agreement (below 1 %) with the analytical results. The differences between the ice mass results of the both formulations are within an absolute range of 0.300 %.

Unlike formulation without the viscous terms, it can be noted that formulation with the viscous terms provides the results, which are in closer agreement with the analytical temporal solution. It appears that the results without the viscous terms slightly over predict the ice accretion results, obtained by the formulation with the viscous terms and analytical prediction. It appears that the viscous terms play a positive role and could be successfully used in the predictions of the icing simulations. This suggests that small room between the simulation results from the numerical formulations with and without the viscous terms is available for modeling of the dispersed phase viscous terms. The differences between the numerical results can probably be larger (closer agreement with the independent analytical solution), when considering the assumption that the multiphase dynamic viscosities of supercooled flowing or freezing water droplets are larger than the available and used single phase dynamic viscosity of water at $t = 0^{\circ}C$ [see also introduction in section (2. 1)]. The further investigation in regards to the above

mentioned modeling of the viscous terms in the governing equations for the multiphase flow with supercooled droplets is beyond the scope of the thesis.

Figure (5. 4. 19) presents an assessment of time dependent droplet phase distribution along the bottom (wall) of the domain, neighboring the vertical wall (a first series of the CV s in the computational domain) at the forward step. The results of the droplet volume fraction are obtained from two numerical formulation with and without droplet phase viscous terms. The differences between the results from the two formulations are slightly increasing along the domain in the direction to the right wall. The differences are also increasing in time, as the supercooled droplets accumulate and freeze at the walls and evolving ice interface [i.e. see the 4-th nodal values from the right wall (side) of the domain in the figure]. It can be noted that although not significant, the viscous processes are not negligible in these processes of droplet transport and accumulation, leading to the ice accretion.

Similar complementary numerical studies of differences among the temporal numerical solutions as a function of i.e. inlet droplet inertia, droplet phase volume fraction and temperature for the viscosity of water with each grid of a particular case can produce additional useful data. The comprehensive bank of such data may provide further insight on the viscous processes and modeling of the multiphase water droplet dynamic viscosity during the droplets transport with icing.

Figure (5. 4. 20) presents the order of accuracy for the numerical solution of ice interface evolution and mass of the accreted ice at the forward step. This solution is obtained from the logarithmic error distribution of the accreted mass of the ice at time 500 s as a function of the logarithmic grid spacing. Numerical solutions with grids of 6×6 , 12×12 , 18×18 and 26×26 are compared against the analytical solution, presented on Fig. (5. 4. 14). A logarithmic coordinate system is used to assess the order of accuracy of the icing simulation. By decreasing the grid spacing, $\ln(\Delta x)$, the solution error, $\ln(\text{Error})$, decreases. The logarithmic error solution function is approximated, yielding a linear function, $\ln(\text{ERROR}) = 2.2404 \ln(\Delta x) + 7.2821$. The slope of this linear function is approximately 2, which suggests that the numerical solution is approximately 2^{nd} order accurate.

(iv) Case 4

This simulation case study entails interfacial drag resistance imparted on the supercooled droplets flowing in an air stream, impinge on the wall and moving ice interface and freeze [see Fig. (5. 4. 21)]. The distance of the vertical wall at the right of the domain is 1.000 m from the inlet. The droplets are injected at the inlet of the domain horizontally at a speed of $u = 2.5\text{ m/s}$ (Dirichlet type of boundary condition). The air velocity is initially the same as the droplet velocity, but it becomes gradually different throughout the domain. The whole flow field is changing due to the droplet/air flow interactions and due to the moving ice interface. The Neumann zero gradient type of boundary condition for the droplet flow is imposed at the wall and at the ice interface. The Dirichlet type ($\vec{v}_a = \vec{0}$) of boundary condition for air flow is imposed at the wall and at the ice interface. At the top and bottom of the domain, the Neumann zero gradient type of boundary conditions is imposed for the droplet and air flows. The droplets are heavier than the air and have appreciable smaller volume fraction. The air has almost no mass (with respect to droplets) and at the same time satisfies continuity requirement instantly. The air flow is very sensitive flow. It changes directions quickly. As the most sensitive phase in the simulation, the air flow requires the smallest time step. Since the time step in the computation is constant, it dictates a computation of all phases in the contact. The time step size for this simulation is determined as $\Delta t = 9.10^{-3}$. The results in Fig. (5. 4. 21) are shown for time 1000 s . The scaled drag resistance is 0.05 (normalized in regards to the constant part of the drag term and actual droplet diameter). Since the droplets are not fully immersed in the air flow, the behavior of this flow is significantly different than in the previous cases. Due to situation of three moving phases in contact, this case study entails many aspects of a realistic comprehensive icing situation. The droplet flow tends to exhibit a parabolic type of motion in the gravitational field. The shearing incoming air, which is slightly pressurized at the wall (where forms a boundary layer) and at the moving ice interface, progressively deflects the droplets flow and itself in the upstream direction. Every deflection of the droplet flow field affects the shape of the evolving ice interface. The deflected droplet flow arrives at the ice interface with its full velocity and freeze non-symmetrically. It can be also emphasized that due to influence of drag and

moving ice interface, air flow does not deflect (move away) from the wall nor from moving ice interface symmetrically. It can be observed in Fig. (5. 4. 21) that air flow turns upwards and carries droplets, despite gravity forcing the droplets downwards. The droplets have a slightly larger horizontal velocity component in the upper part of the domain, since the gravitational deflection of droplets in the lower part of the domain is larger than the upper part of the domain, Therefore, the ice interface grows slightly faster in that region, as compared with the lower region of the domain. In the lower part, the air turns downward, carrying the droplets with additional inertia downwards.

Some other aspects of the dynamics of the phases are discussed here. The ice accretes instantly and propagates gradually into the domain in the upstream direction, pushing the air flow in front of it, against the inlet and through the bottom and top side exits of the domain. As the ice interface (moving Dirichlet air velocity boundary condition) approaches the inlet section (stationary Dirichlet boundary conditions), the droplet and the air flows become more deflected (near the inlet). Such progressive deflection of the flows, especially at the inlet may negatively affect the solver performances. In spite of the complexity of this case study involving the sensitive phases with significantly different motion, the algorithms execute stable calculations. The results seem to be reasonable.

Elaborate detailed study of this case with coupled droplet-air motion near the moving ice interface and associated validations with an independent method seems to be complicated or impossible. Avoiding the air adverse pressure gradient influence and flow deflection near the inlet may require long computational domain and presenting the ice accretion results at location far from the inlet section. Proper modeling of the impinging air onto the vertical wall with its turn along the wall and closely vertical exit through the sides of the domain may require narrow air stream and relatively long vertical wall. Since the moving ice interface changes its unsymmetrical shape, the problem of most accurate modeling of the flows in the domain and at the interface may become insurmountable. In the situation with compressed flows, an employment of the compressible equations of multiphase motion is needed.

5. 5 EXPERIMENTAL RESULTS AND COMPARISONS

For the purpose of experimental validations of the numerical code, several experiments were performed and results are presented in this section. The velocity fields associated with droplet trajectories are measured with the *PIV* laser-based experimental technique [Chapter (4)]. Furthermore, predicted results of ice accretion on a conductor are compared with Goodwin's law. Past experimental studies by Lu, Popplewell and co-workers [94] have shown close agreement between Goodwin's law and measured data for rime ice accretion on a circular conductor.

(A) Droplet Flow Trajectories

Three cases are selected for presentation in this section:

- Case (1): Vertically injected stream flow into the air,
- Case (2): Horizontally injected stream flow into the air,
- Case (3): Horizontally injected stream flow into the air,
- Case (4): Horizontally injected droplet flow into the air.

The stream flow consists of a disintegrating jet flow with droplets. In these cases, seed particles are added into the stream. The dispersed droplet flow is fully formed.

Some results [especially in Case (4)] correspond to the camera view region (HighSense camera view), when presenting the locations [especially in Figs. (5. 5. 15) - (5. 5. 18)]. The computational domain for numerical simulations is the same as that in the camera view region. A typical camera view region with units is presented in Fig. (5. 5. 6). In this figure, the dimensions can be read (directions: x -horizontal, y -vertical).

(i) Case 1

The schematic of this experimental design is presented in Fig. (5. 5. 1). A liquid water jet with premixed seeding particles falls vertically under gravity in free flow from a liquid supply container. The surrounding ambient air is quiescent. The exit mass flow rate of water is 53.3 mL/s . From classical mechanics, the expected fluid velocity in the view region of the camera image can be predicted without a drag model, yielding the analytical value of 3.679 m/s . The measured average velocity at this location was 3.821 m/s , which corresponds to an error of approximately 3.7 %, when compared with the analytical solution $v = \sqrt{2g\Delta h}$. Employing drag models in the analytical [Eqs. (2. 5. 2. 25) - (2. 5. 2. 27)] and numerical [Eqs. (2. 3. 1) - (2. 3. 4)] predictions produces lower discrepancies with measured results.

A sample photographic image of the vertically falling jet with seed particles is illustrated in Fig. (5. 5. 2). The measured steady state velocity vectors within this vertical jet flow are presented in Fig. (5. 5. 3). The flow is stable across its width at different locations along the stream. A central conglomeration of white spots in Fig. (5. 5. 2) presents flow structures and seed particles. Although seed particles were premixed, some segments of a group of particles existed. Such particles may be attracted with the flow structures. Since flow structures and particles reflect the laser light more than a smooth jet without particles, the central conglomeration of white spots appeared.

(ii) Case 2

In this case, a liquid water stream (jet) is emitted horizontally from the jet nozzle system into the quiescent air [Fig. (5. 5. 4)]. Internal jet flow transforms into external flow. Apart from the initial pressure force, the dominant external forces that govern its inertia become jet/air resistance and gravity. The jet with large droplets is fed with seed particles. The jet passes HighSense CCD Camera from the right side, while the camera takes two images from two subsequent laser pulses. The corresponding image of the jet is shown in Fig. (5. 5. 5). Spatial windows used in Figs. (5. 5. 5) - (5. 5. 7) are created from the middle section of the most intense reflective laser light from the jet, shown in Fig. (5. 5. 4). A slight overexposure of the camera can be seen in the middle part of the image,

which did not affect the accuracy of the measured velocity field. At the exit of the nozzle, the liquid stream has a diameter of approximately 0.020 m . Without seed particles in this jet, an insufficient level of illumination is provided in order to successfully implement the *PIV* laser method. In this problem, the exit mass flow rate of water is 55.6 mL/s and the supply line pressure is $55\text{ Psi} \pm 5\text{ Psi}$. As a result, the jet flow is not perfectly uniform, as it slightly oscillates due to the varying pressure field.

Results of the velocity field for this flow are shown in Figs. (5. 5. 6), Fig. (5. 5. 8) and Fig. (5. 5. 9). Corresponding streamlines are depicted in Fig. (5. 5. 7). From right to left in Fig. (5. 5. 8), it can be observed that the horizontal component of fluid velocity decreases. Diffusion through the liquid layer, adjacent to the quiescent air stream contributes to momentum exchange and the resulting velocity variations. Similar trends are observed for the vertical velocity component, except that gravity contributes to acceleration of the fluid from right to left. The analytical results are generated from analytical solutions Eqs. (2. 5. 2. 16) - (2. 5. 2. 17), where the quadratic drag resistance is considered between the droplets and adjacent air. A comparison of the results from three methods is presented in Fig. (5. 5. 9). The numerical results are generated by the computer code, based on the transitional drag model. The analytical and numerical results are expected for this external jet flow. All results agree within 10% , while a majority agrees within 6% . This is reasonable agreement with the *PIV* measured data.

The precision limit and total uncertainty of the jet flow are presented in Fig. (5. 5. 10) and Fig. (5. 5. 11) for the jet flow x - and y - directed velocity components (in [%]). Details of error evaluation are presented in section (4. 3). The results of performed uncertainty analysis are presented in the camera view region. The results are evaluated within 95% of the measured confidence.

Figure (5. 5. 10) presents uncertainty analysis of the jet flow at location $x = 85\text{ mm}$ and at 15 different elevations. The elevations are ranging from $y = 5\text{ mm}$ to $y = 75\text{ mm}$. The presented minimum / maximum values of the precision limit and total uncertainty for x -directed jet velocity are calculated as $1.03851\% / 1.52962\%$ and $1.82336\% / 2.14126\%$, respectively. The minimum / maximum values are obtained at elevation $45\text{ mm} / 65\text{ mm}$, respectively. The presented minimum / maximum values of the precision limit and total uncertainty for y -directed jet velocity are calculated as $0.61372\% / 0.83267\%$ and

1.61950 % / 1.71448 %, respectively. The minimum / maximum values are obtained at elevation 25 mm / 75 mm, respectively. The precision limit and total uncertainty are reasonably low. The flow is expected to fluctuate, since the line pressure fluctuation is about 9.1 %. The uncertainty analysis revealed that this fluctuation has the biggest effect on the accuracy of the measured velocity field (about 82 %) among all parameters.

Fig. (5. 5. 11) presents the uncertainty analysis for the jet flow at an elevation of $y = 25$ mm along the domain of the camera view region (horizontal positions). Results are presented at x -locations, ranging from $x = 5$ mm (outlet) to $x = 95$ mm (inlet). The presented minimum / maximum values of the precision limit and total uncertainty for x -directed jet velocity are calculated as 1.05654 % / 1.50211 % and 1.82336 % / 2.12190 %, respectively. The minimum / maximum values are obtained at elevation 25 mm / 15 mm, respectively. The presented minimum / maximum values of the precision limit and total uncertainty for y -directed jet velocity are calculated as 0.00519 % / 0.00917 % and 0.51617 % / 1.75718 %, respectively. The minimum / maximum values are obtained at elevations 25 mm / 5 mm, respectively. The precision limit and total uncertainty are reasonably low. The flow exits the *JSPS* system horizontally [see Fig. (4. 1. 1. 8)]. Larger fluctuations occur in horizontal x -direction due to the fluctuating pressure that exists in the jet system. This partly explains why the errors of the uncertainty analyses for the horizontal components of the flow are slightly larger than for the vertical components.

(iii) Case 3

A case, similar to that in Case (2) is considered, but with lower pressure in the supply line. Measured results for this case are shown in Figs. (5. 5. 10) – (5. 5. 11). At a lower supply pressure, the horizontal velocity component decreases in this case [Fig. (5. 5. 10)]. Despite the influence of drag on each droplet, the magnitude of the vertical component of velocity increases from right to left. This is due to relatively larger gravitational acceleration [see also Fig. (5. 5. 11)], acting on droplets. Similar trends in the x -direction are observed at different elevations throughout the jet flow. Figure (5. 5. 11) illustrates these variations at positions of 5, 10, 15 and 20 mm from the base of the camera view region.

(iv) Case 4

In this case, dispersed droplets are emitted from the nozzles of the atomizer into the ambient air. Droplet motion upstream from the helicopter engine bay is studied [see Fig. (5. 5. 14)]. The *PIV*-based measurements of the droplet velocity field are performed. Unlike Cases (1) – (3), seed particles are not used within this flow. Laser light is reflected from the droplets themselves [see Fig. (5. 5. 15)], before their motion is analyzed by the *PIV* software.

Two camera images were needed for each velocity result [see Fig. (5. 5. 16)]. The first image shows the positions of droplets at one time. Then, after a time step, a matching second image of the final positions of droplets determines the movement of the fluid. Both camera images are divided into interrogation regions, which are used to measure the displacement of groups of dispersed droplets (based on a *FFT* correlation technique).

The measured droplet velocity field is presented in Fig. (5. 5. 17). Measured values for the droplet velocities are presented in Figs. (5. 5. 18) – (5. 5. 19) at different locations in the camera view region. The droplet flow is injected into the air from the right of the domain. Close agreement between experimental, numerical and analytical [Eqs. (2. 5. 2. 16) – (2. 5. 2. 18)] results are obtained for the horizontal and vertical components of the droplet velocities. Differences in the results are presented in Figs. (5. 5. 20) – (5. 5. 21). The numerical results generally agree with experimental data within 2 %. The relative difference between horizontal velocities is smaller than between the vertical velocities. The discrepancies between results are relatively smaller at the lower elevation than at higher elevation. This is expected, since gravity appreciably deflects the flow in the vertical direction.

Uncertainty analyses are presented for measured droplet velocity fields in Fig. (5. 5. 22) and Table (5. 5. 1). Evaluation details are presented in section (4. 3). The precision limit and total uncertainty for horizontal (x) and vertical (y) droplet velocities are presented in [%]. The results are evaluated within 95 % of the measured confidence. Figure (5. 5. 22) presents the distribution of precision limit and total uncertainty for measured droplet velocities $v_{d,y}$ across the width of the domain at three horizontal locations $x = 0.085 \text{ m}$ (\sim the inlet of the domain), $x = 0.045 \text{ m}$ (\sim the center of the

domain) and $x = 0.010 \text{ m}$ (\sim outlet of the domain). The droplets are scattered around the core region of the flow [see Fig. (5. 5. 22)]. The core of the flow changes - moves downward (depicted in the smaller schematics of that flow in Fig. [5. 5. 22]) as the droplets travel from the inlet to the outlet of the domain (camera view region). This can be observed in the figure: Sections with the minimum errors at each x -location are decreasing in y -direction as flow passes from the inlet to the outlet of the domain. In the regions outside the core of the flow, there is a lack of sample data, which increases the precision limit and total uncertainty. The presented minimum / maximum values of the precision limit and total uncertainty for at location $x = 0.085 \text{ m}$ in Fig. (5. 5. 22) are calculated as $0.28772 \% / 5.41698 \%$ and $1.52607 \% / 5.62048 \%$, respectively. At location $x = 45 \text{ mm}$, the presented minimum / maximum values of the precision limit and total uncertainty are calculated as $0.72774 \% / 9.19297 \%$ and $1.66605 / 9.31434$, respectively. At location $x = 10 \text{ mm}$, the presented minimum / maximum values of the precision limit and total uncertainty are calculated as $1.26500 \% / 6.97534 \%$ and $1.96121 \% / 7.13453 \%$, respectively.

The results from the uncertainty analysis for the x -directed droplet velocities are presented in Table (5. 5. 1). The precision limit and total uncertainty are evaluated along the domain ($x = 0.010 \text{ m}$, $x = 0.045 \text{ m}$ and $x = 0.085 \text{ m}$) at elevations $y = 35 \text{ mm}$ and $y = 40 \text{ mm}$. At an elevation of $y = 35 \text{ mm}$, the minimum / maximum values for the precision limit and total uncertainty are evaluated as $3.28292 \% / 4.83967 \%$ and $3.60884 \% / 5.0664 \%$, respectively. At an elevation of $y = 40 \text{ mm}$, the minimum / maximum values for the precision limit and total uncertainty are evaluated as $1.59799 \% / 4.52032 \%$ and $2.19082 \% / 4.76229 \%$, respectively. The total uncertainty is reasonably low. The droplet flow is expected to fluctuate to some extent, since this quite narrow flow is dispersed and mainly controlled by the line pressure. The droplets are scattered around the core region where there is a lack of sample data, which increases the precision limit and total uncertainty.

(B) Icing on a Conductor

This case represents another droplet flow, which is vertically injected into the surrounding air, while falling onto the conductor. The schematic of the physical situation and numerical setup is presented in Fig. (5. 5. 23). Due to the symmetry of the physical problem, only 1/4 of the domain was numerically simulated. The droplet diameter is $D_d = 1.5 \text{ mm}$. The inlet boundary conditions are $\vec{v}_d = (0, -5.241) [m/s]$, $\vec{v}_a = (0, 0) [m/s]$ and $\beta_a = 0.0001$. The initial conditions are set to zero (normalized) values for all physical quantities. Droplets are injected into quiescent air at their terminal velocity. This velocity was analytically predicted beforehand. Droplets are exposed to gravity, drag and buoyancy. The numerically calculated impact velocity at the cylinder is slightly larger than the velocity prescribed at the inlet of the computational domain.

The shape of the evolving ice interface was numerically predicted. The results of the predicted ice shape with radial ice distribution on the cylinder at a time of $t = 12 \text{ h}$ are presented in Fig. (5. 5. 24). The fastest ice buildup occurs where the angle between the flow and the cylinder is maximum. Subsequently, the slowest or no ice accretion appears where the angle is smallest, as expected. It appears to be a general observation that higher droplet volume fractions in the air and bigger diameters of the cylinder lead to less uniformly distributed ice around that object. This corresponds to the situation in Fig. (5. 5. 24).

Furthermore, a process of comparing the ice shape on the conductor in Fig. (5. 5. 24) with experimental data is presented in this section. The numerical results are compared with Goodwin's law and measured data through the dimensionless time and equivalent thickness of ice around the cylinder. The iced area around the cylinder was transformed into an equivalent ice area and the ratio was used to determine the dimensionless parameters. The ice shape is presented as a cylindrical angular function, $dh = f(\theta)$. It is plotted with the radius of the cylinder ($R_{cyl} = 0.175 \text{ m}$). This height distribution encompasses the numerically predicted ice area. The area between the curves, $dh = f(\theta)$ and $R_{cyl} = 0.175 \text{ m}$ [see Fig. (5. 5. 24)], is the numerically predicted area of deposited ice (A_i). From the ratio $\frac{A_i}{A_{cyl}}$, the equivalent ice thickness, δ , was

calculated. The variable δ represents the uniformly distributed ice around the conductor. The thickness δ was further scaled and a representative conductor thickness, δ^* , was determined based on Ref. [91].

Then, δ^* is calculated as

$$\delta^* = \frac{\delta}{R_{cylidr}}. \quad (5.5.1)$$

The dimensionless time, t^* , was determined from Goodwin's law [see Fig. (5.5.25)], i.e.,

$$t^* \approx 2\delta^*. \quad (5.5.2)$$

From Eq. (5.5.2), the dimensionless precipitation rate of droplets was calculated as

$$P = \frac{t^* \rho_i \pi R_{cylidr}}{2 \rho_w t}, \quad (5.5.3)$$

where the densities of water and ice are $\rho_i = 1000 \text{ kg/m}^3$ and $\rho_w = 800 \text{ kg/m}^3$ respectively. The experimental ice thicknesses on the conductor and the droplet volume fractions in the air are calculated from Eq. (5.5.3). The experimental values are compared with corresponding numerical and analytical values in Table (5.5.2). The values show relatively good agreement. These results suggest that the numerically calculated area of the ice on the conductor and maximum thickness of the accreted ice exhibit reasonably good agreement with measured data.

At this point, the code does not contain experimental data for predictions of re-distribution of excess ice (ice shape evolution for a variety of realistic situations). The icing algorithm works alongside the flow algorithms. It uses information from the flow and volume fraction fields to track an evolving ice interface. Experimental data for modeling of droplet flow at the evolving interface should be developed in the icing tunnel. The temporal - spatial evolution of ice buildup and re-distribution of excess ice towards impinging flows should be further studied for different objects and conditions, according to experimental functions incorporated into the numerical code.

CHAPTER 6

CONCLUSIONS AND RECOMMENDATIONS FOR FUTURE RESEARCH

6.1 CONCLUSIONS

A focus of this *Ph.D.* research work was to develop deeper understanding of multiphase flow processes with icing on surfaces and to develop a 2-D icing numerical simulator. Two parts of this research were completed: dispersed flow and ice modeling. The parts were assessed with analytical, numerical and experimental methods. The validation tools and case studies were mainly developed. The main conclusions of this thesis are summarized as follows.

- Scaling, Order of Magnitude and Similarity analyses were applied to assess and quantify the physics of dispersed flow in a uniform airstream. A closer analysis was performed for the droplet flow within a parallel air stream near the flat surface. Analytical solutions were developed for this special case (i.e. similarity solutions).
- Lagrangian analytical tools and two-dimensional solutions were developed for validation of the numerical dispersed flow and icing predictions. The analytical results agreed with numerical results.
- A numerical Eulerian based *CVFEM* method was developed for two-dimensional dispersed (droplet) flow and rime ice applications. It was accommodated into an existing PHASES numerical program. Wall and ice interface conditions for the dispersed flow were modeled as Neumann conditions, while the air flow was simulated with Dirichlet boundary conditions. A transitional drag model was implemented into the code to simulate a variety of low-Re and high-Re regimes. A momentum-diffusion function for the droplet velocity at the interface was introduced to suppress its effect, when ice completes its growth in the control volume. A two-dimensional rime ice evolution method, with linear and parabolic tracking of ice interface preconditioning and excess ice distribution, was developed. Grid independence and initial condition independence of results were obtained. Validations were carried out for a variety of droplet flows, air flows and icing conditions for various geometries (straight walls and channels, sharp steps, cylindrical steps and cylinders). The most sensitive phase (air) was observed to strongly affect computational stability of all other phases. The effects of relative resistances between phases in contact were studied (i.e., full and zero gravitational deflection of droplets in the air stream; freestream and near-wall regions). The numerical results for dispersed droplet flow and ice interface evolution were successfully compared against analytical and experimental results.

- Experimental work was carried out for dispersed and jet flow applications, as well as for the icing on a helicopter scoop. Three nozzle systems (two systems for long distances and one system for short distances), and a stream-jet system were developed for injection of dispersed and continuous liquid flows (droplet and jet flows). Several experiments were designed for droplet flow and icing with the *PIV* laser based technique and with FlowManager software 4. 20. 25. The experiments were conducted in closed-loop water and spray-icing tunnels. The dispersed (droplet) and continuous (jet) velocities and droplet diameters were measured. The results agree well with numerical velocity results. Goodwin's law for ice thickness measurements on a curved surface (conductor) showed close agreement with the numerical results.

6. 2 RECOMMENDATIONS FOR FUTURE RESEARCH

Recommendations for numerical and experimental parts of the future research are outlined below.

(1) The following extensions to the numerical research work are suggested:

- modeling of additional forces acting on droplets at the iced aircraft surfaces with respect to the experimentally obtained data (i.e. drag, lift and electromagnetic forces);
- modeling of droplet diameter distribution in the non-differential drag term in the momentum equation, based on experimental data;

- modeling of break-up and splash-back mechanisms for dispersed phase motion. The former mechanism can be modeled in the entire region, while the latter mechanism mainly applies after the flow impacts on the evolving ice interface;
- development of ice tracking algorithms for different droplet flows, air flows and icing conditions and geometries. Experimental data from the spray-icing tunnel can be incorporated into the numerical model;
- experimental data can be produced in the tunnel for modeling droplet flow at the ice interface (such as diffusion processes);
- development of the numerical algorithm for two-dimensional glaze ice modeling with run-off and run-back flows;
- improvement of pre- and post-processing of the numerical results.

(2) The following extensions to the experimental work are suggested:

- determination of single and multiphase flow physical properties (i.e. transport, such as dynamic viscosity) of super/sub-cooled water and incorporation into the numerical algorithms;
- investigation of forces acting on droplets in the vicinity of their impact on the ice interface and other solid surfaces in the icing tunnel. Some effects, such as electromagnetic influences on the surfaces, can be studied in the tunnel;
- investigation of icing processes of ice interface propagation, including processes under varying temperatures;
- the atomizer should be finalized for rime ice applications (such as anti-freezing);

Chapter 6-CONCLUSIONS AND RECOMMENDATIONS FOR FUTURE WORK

- the long distance pressurized nozzles with micro diameters should be finalized and used for accurate droplet flow measurements in the tunnel;
- the novel *PIV* FlowManager for dispersed flow applications should be used for droplet flow velocity measurements. This would improve the quality of results, especially in the transition region (droplet flow to film flow in glaze ice applications).

LIST OF REFERENCES

- [1] Myers, T. G., Hammond, D. W., 'Ice and Water Film Growth from Incoming Supercooled Droplets', *International Journal of Heat and Mass Transfer*, vol. 42, pp. 2233 - 2242, 1999.
- [2] Naterer, G. F., 'Energy Balances at the Air / Liquid and Liquid / Solid Interfaces with Incoming Droplets at a Moving Ice Boundary', *Int. Comm. Heat Mass Transfer*, vol. 29, no. 1, pp. 57 - 66, 2002.
- [3] Naterer, G. F., 'Multiphase Flow with Impinging Droplets and Airstream Interaction at a Moving Gas / Solid Interface', *Int. J. Multiphase Flow*, vol. 28, no. 3, pp. 451 - 477, 2002.
- [4] Banerjee, S., Chan, A. M. C., 'Separated Flow Models - I, Analysis of the averaged and local instantaneous formulations', *Int. J. Multiphase Flow*, vol. 6, pp. 1 - 24, Pergamon / Elsevier, Great Britain, 1980.
- [5] Banerjee, S., Chan, A. M. C., 'Separated Flow Models - II, Analysis of the averaged and local instantaneous formulations', *Int. J. Multiphase Flow*, vol. 6, pp. 1 - 24, Pergamon / Elsevier, 1980, Great Britain, 1980.
- [6] Hetsroni, G., *Handbook of multiphase systems*, Hemisphere Publishing Corp., McGraw - Hill Book Company, USA, 1982.
- [7] Crowe, C., 'Modeling Fluid - Particle Flows: Current Status and Future Directions', AIAA 30th Fluid Dynamics Conference, Norfolk, VA, 1999.

LIST OF REFERENCES

- [8] Crowe, C. T., Sommerfeld M., Tsuji, Y., *Multiphase flows with droplets and particles*, CRC Press LLC, Florida, 1998.
- [9] Ainley, S., Coppen, S., Manno V. P., Rogers, C. B., 'Modeling particle motion in a turbulent air flow', FEDSM '97, ASME, June 22 - 26, 1997.
- [10] Milanez, M., Naterer, G. F., Venn, G., Richardson, G., 'Eulerian Formulation for Droplet Tracking in Dispersed Phase of Turbulent Multiphase Flow', AIAA Paper 2002-3182, AIAA 32nd Fluid Dynamic Conference, St. Louis, MO, June 24 - 26, 2002.
- [11] Naterer, G. F., Schneider, G. E., 'PHASES Model of Binary Constituent Solid - Liquid Phase Transition, Part 1. Numerical Method', *Numerical Heat Transfer*, vol. 28, no. 2, pp. 111 - 126, 1995.
- [12] Naterer, G. F., 'Constructing an Entropy Stable Upwind Scheme for Compressible Fluid Flow Computations', *AIAA Journal*, vol. 37, no. 3, pp. 303 - 312, 1999.
- [13] Naterer, G. F., 'Predictive Entropy Based Correction of Phase Change Computations with Fluid Flow - Part 2: Application Problems', *Numerical Heat Transfer B*, vol. 37, pp. 415 - 436, 2000.
- [14] Naterer, G. F., 'Applying Heat - Entropy Analogies with Experimental Study of Interface Tracking in Phase Change Heat Transfer', *International Journal of Heat and Mass Transfer*, vol. 44, no. 15, pp. 2917 - 2932, 2001.

LIST OF REFERENCES

- [15] Tsuboi, K., Kimura, S., 'Numerical Study of the Effect of Droplet Distribution in Incompressible Droplet Flows', AIAA Paper 98-2561, AIAA 29th Fluid Dynamics Conference, Albuquerque, NM, 1998.
- [16] Schlichting, H., *Boundary-Layer Theory*, McGraw-Hill, New York, 1979.
- [17] Munson, B. R., Young, D. F., Okiishi, T. H., *Fundamentals of Fluid Mechanics*, John Wiley & Sons, Inc., USA, 1994.
- [18] Naterer, G. F., *Heat Transfer in Single and Multiphase Systems*, CRC Press, Boca Raton, FL, 2002.
- [19] Oosthuizen, P. H., Naylor, D., *An Introduction to Convective Heat Transfer Analysis*, McGraw-Hill Co., Inc., USA, 1999.
- [20] Milanez, M., Naterer, G. F., Venn, G., Richardson, G., 'Self Similarity of Cross-Stream Droplet Momentum Displacement in Dispersed Multiphase Flow', *Particle and Particle Systems Characterization*, vol. 20, no. 1, pp. 62 - 72, 2003.
- [21] Crowe, C. T., Sommerfeld, M., Tsuji, Y., *Multiphase Flows with Droplets and Particles*, CRC Press, Boca Raton, FL, 1998.
- [22] Bourgault, Y., Habashi, W. G., Dompierre, J., Baruzzi, G. S., 'A Finite Element Method Study of Eulerian Droplets Impingement Models', *Int. J. Num. Meth. in Fluids*, vol. 29, pp. 429 - 449, 1999.
- [23] Sha, W.T., Soo, S.L., 'On the Effect of $PV\alpha$ Term in Multiphase Mechanics', *International Journal of Multiphase Flow*, vol. 5, pp. 153 - 158, 1979.

LIST OF REFERENCES

- [24] Boure, J. A., 'On the Form of the Pressure Terms in the Momentum and Energy Equations of Two - Phase Flow Models', *International Journal of Multiphase Flow*, vol. 5, pp. 159 - 164, 1979.
- [25] Prosperetti, A., Jones, A. V., 'Pressure Forces in Disperse Two - Phase Flow', *International Journal of Multiphase Flow*, vol. 10, pp. 425 - 440, 1984.
- [26] Marchioro, M., Tanksley, M., Prosperetti, A., 'Mixture Pressure and Stress in Disperse Two - Phase Flow', *International Journal of Multiphase Flow*, vol. 25, pp. 1395 - 1426, 1999.
- [27] Ishii, M., *Thermo - Fluid Dynamic Theory in Two - Phase Flow*, Eyrolles, Paris, 1975.
- [28] Gidaspow, D., Solbring, C. W., 'Transient Two - Phase Flow Models in Energy Productions', *Proceedings, AIChE 81st National Meeting*, Kansas City, 1976.
- [29] Soo, S. L., 'Fluid Mechanics of Non - Equilibrium Systems', *Proc. 17th Congr. Int. Astro Fed.*, vol. 3, 1976a.
- [30] Jackson, R., *Fluid Mechanical Theory in Fluidization* (Eds. J. F. Davison and D. Harrison), Ch. 3, pp. 65-119, Academic Press, New York.
- [31] Medlin, J., Wong, H., W., Jackson, R., 'Fluid Mechanical Description of Fluidized Beds - Convective Instabilities in Bounded Beds', *Ind. Engng Chem. Fundam.*, vol. 13, pp. 247 - 259, 1974.
- [32] Gidaspow, D., 'Modelling of Two - Phase Flow', 5th International Heat Transfer Conference, 7, pp. 163 - 169, 1974.

LIST OF REFERENCES

- [33] Nigmatulin, R. I., 'Spatial Averaging in the Mechanics of Heterogeneous and Dispersed Systems', *International Journal of Multiphase Flow*, vol. 5, pp. 353 - 385, 1979.
- [34] Park, J. W., Drew, D. A., Lahey, R. T., 'The Analysis of Void Propagation in Adiabatic Mono - Dispersed Bubbly Two - Phase Flows Using an Ensemble - Averaged Two - Fluid Model', *International Journal of Multiphase Flow*, vol. 24, pp. 1205 - 1244, 1998.
- [35] Joseph, D.D., Lundgren, T. S., 'Ensemble Averaged and Mixture Theory Equations for Incompressible Fluid - Particle Suspensions', *International Journal of Multiphase Flow*, vol. 16, pp. 35 - 42, 1990.
- [36] Wilcox, D. C., *Turbulence Modeling for CFD*, 2nd Edition, DCW Industries, Inc. 1998.
- [37] Crowe, C., 'Review - Numerical Models for Dilute Gas-Particle Flows', *ASME Journal of Fluids Engineering*, vol. 104, pp. 297 - 303, 1982.
- [38] Milanez, M., Naterer, G. F., Venn, G., Richardson, G., 'Volume Averaged Pressure Interactions for Dispersed Droplet Phase Modeling of Multiphase Flow', *AIAA Journal*, vol. 42, no. 5, pp. 973 - 979, 2004.
- [39] Naterer, G. F., 'Eulerian Three-Phase Formulation with Coupled Droplet Flow and Multimode Heat Transfer', *Numerical Heat Transfer B*, vol. 43, pp. 331 - 352, 2003.

LIST OF REFERENCES

- [40] Naik, S., Bryden, I. G., 'Prediction of Turbulent Gas-Solids Flow in Curved Ducts Using the Eulerian - Lagrangian Method', *International Journal for Numerical Methods in Fluids*, vol. 31, no. 3, pp. 579 – 600, 1999.
- [41] FIDAP 7.62, Example Manual 7.0, Fluid Dynamics International, 1993.
- [42] TASCflow, Version 2.4.1-3, Advanced Scientific Computing, Waterloo, Ontario, 1996.
- [43] Thevand, N., Daniel, E., Loraud, J. C., 'On High-Resolution Schemes for Solving Unsteady Compressible Two-Phase Dilute Viscous Flows', *International Journal for Numerical Methods in Fluids*, vol. 31, no. 4, pp. 681 – 702, 1999.
- [44] Valentine, J. R., Decker, R. A., 'Lagrangian - Eulerian Scheme for Flow Around an Airfoil in Rain', *International Journal of Multiphase Flow*, vol. 21, pp. 639 - 648, 1995.
- [45] Naterer, G. F., 'Pressure Weighted Upwinding for Flow Induced Force Predictions: Application to Iced Surfaces', *International Journal for Numerical Methods in Fluids*, vol. 44, no. 9, pp. 927 – 956, 2004.
- [46] Naterer, G. F., Rinn, D., 'Towards Entropy Detection of Anomalous Mass and Momentum Exchange in Incompressible Fluid Flow', *International Journal for Numerical Methods in Fluids*, vol. 39, no. 11, pp. 1013 - 1036, 2002.
- [47] Darwish, M., Moukalled, F., Sekar, B., 'A Robust Multi-grid Pressure-based Algorithm for Multi-fluid Flow at All Speeds', *International Journal for Numerical Methods in Fluids*, vol. 41, no. 11, pp. 1221 – 1251, 2003.

LIST OF REFERENCES

- [48] Naterer, G. F., 'Sub-Grid Volumetric Quadrature Accuracy for Transient Compressible Flow Predictions', *International Journal for Numerical Methods in Fluids*, vol. 25, no. 2, pp. 143 - 149, 1997.
- [49] Joseph, D., Belanger, J., Beavers, G., 'Breakup of a Liquid Drop Suddenly Exposed to a High-Speed Airstream', *International Journal of Multiphase Flow*, vol. 25, pp. 1263-1303, 1999.
- [50] Valentine, J. R., 'Application of a Lagrangian Particle Tracking Scheme in a Body-Fitted Coordinate System', *Numerical Methods in Multiphase Flows*, ASME-FED 185, pp. 39 - 46, 1994.
- [51] Nadaoka, K., Nihei, Y., Yagi, H., 'Grid Averaged Lagrangian LES model for Multiphase Turbulent Flow', *International Journal of Multiphase Flow*, vol. 25, pp. 1619 - 1643, 1999.
- [52] Murai, Y., Kitagawa, A., Song, X-Q., Yamamoto, F., Ohta, J., 'Inverse Energy Cascade Structure of Turbulence in a Bubbly Flow (Numerical Analysis using Eulerian - Lagrangian Model Equations)', *JSME International Journal Series B*, vol. 43, no. 2, pp. 197 - 205, 2000.
- [53] Moissette, S., Oesterle, B., Boulet, P., 'Simulation of Particle Temperature Fluctuations in Eulerian - Lagrangian Predictions of Heat Transfer in a Turbulent Gas - Solid Pipe Flow', *Proceedings of the ASME 2000 Fluids Engineering Division Summer Meeting*, No. 11143/CD-ROM, pp. 1 - 8, 2000.
- [54] Reutsch, G. R., Meiburg, E., 'Two-way Coupling in Shear Layers with Dilute Bubble Concentration', *Physics of Fluids A*, vol. 6, pp. 2656 - 2670, 1994.

LIST OF REFERENCES

- [55] Marchioli, C., Giusti, A., Salvetti, M. V., Soldati, A., 'Direct Numerical Simulation of Particle Wall Transfer and Deposition in Upward Turbulent Pipe Flow', *International Journal of Multiphase Flow*, vol. 29, no. 6, pp. 1017 – 1038, 2003.
- [56] Decker, S., Sommerfeld, M., 'Numerical Calculations of Two-Phase Flows in Agitated Vessels Using the Euler / Lagrange Approach', Proceedings of the ASME 2000 Fluid Engineering Division Summer Meeting, No. FEDSM2000-11154/CD-ROM, pp. 1 - 8, 2000.
- [57] Huang, L. J., Ayyaswamy, P. S., 'Evaporation of a Moving Liquid Droplet: Solutions for Intermediate Reynolds Numbers', *International Communications in Heat and Mass Transfer*, vol. 17, no. 1, pp. 27 – 38, 1990.
- [58] Niu, Y. Y., 'Advection Upwinding Splitting Method to Solve a Compressible Two-Fluid Model', *International Journal for Numerical Methods in Fluids*, vol. 36, no. 3, pp. 351 – 371, 2001.
- [59] Ritz, J. B., Caltagirone, J. P., 'A Numerical Continuous Model for the Hydrodynamics of Fluid Particle Systems', *International Journal for Numerical Methods in Fluids*, vol. 30, no. 8, pp. 1067 – 1090, 1999.
- [60] Masson, C., Baliga, B. R., 'Simulation of Gas-Solid Particle Flows Over a Wide Range of Concentration', *International Journal for Numerical Methods in Fluids*, vol. 28, no. 10, pp. 1441 – 1479, 1998.
- [61] Tsuboi, K., 'Computational and Analytical Study on Particle Flow Field Around a Circular Cylinder', AIAA Paper 2001-2650, AIAA Fluid Dynamics Conference, Anaheim, CA, 2001.

LIST OF REFERENCES

- [62] Morency, F., Beaugendre H., Baruzzi, G. S., Habashi, W. G., 'FENSAP-ICE: A Comprehensive 3D Simulation System for In-Flight Icing', *International Journal for Numerical Methods in Fluids*, vol. 29, pp. 429 – 449, 1999.
- [63] Milanez, M., Naterer, G. F., 'Eulerian Cross-Phase Diffusive Effects on Impinging Droplets and Phase Change Heat Transfer' (in press), *International Communications in Heat and Mass Transfer*, 2004.
- [64] Levy, Y., Bulzan, D. L., 'On the Oscillation of Combustion of a Laminar Spray', *International Journal of Multiphase Flow*, vol. 22, no. 1, pp. 105, 1996.
- [65] Williams, L. R., Dykhno, L. A., Hanratty, T. J., 'Droplet Flux Distributions and Entrainment in Horizontal Gas-Liquid Flows', *International Journal of Multiphase Flow*, vol. 22, no. 1, pp. 1 – 18, 1996.
- [66] Rushton, E., Davies, G. A., 'The Slow Motion of Two Spherical Particles Along Their Line of Centres', *International Journal of Multiphase Flow*, vol. 4, no. 4, pp. 357 - 381, 1978.
- [67] Milanez, M., Naterer, G. F., Venn, G., Richardson, G., 'Dilute Gas/Droplet Flow Past a Frontward Facing Step', AIAA Paper 2005-0002, AIAA 43rd Aerospace Sciences and Exhibit, Nevada, January 10 - 13, 2005.
- [68] Hung, L., Yao, S. C., 'Experimental Investigation of the Impaction of Water Droplets on Cylindrical Objects', *International Journal of Multiphase Flow*, vol. 25, pp. 1545 – 1559, 1999.

LIST OF REFERENCES

- [69] Barton, I. E., 'Computation of Dilute Particulate Laminar Flow Over a Backward Facing Step', *International Journal for Numerical Methods in Fluids*, vol. 22, pp. 211 – 221, 1996.
- [70] C. Wang, H., Sun, C. J., Kuo, H. C., *International Communications in Heat and Mass Transfer*, vol. 24, 65, 1997.
- [71] Papageorgakis, G. C., Assanis, D. N., *International Communications in Heat and Mass Transfer*, vol. 23, 1, 1996.
- [72] Ayyaswamy, P., Sadhal, S., Huang, L., *International Communications in Heat and Mass Transfer*, vol. 17, 689, 1990.
- [73] Poots, G., *Ice and Snow Accretion on Structures*, John Wiley and Sons Inc, 1996.
- [74] Messinger, B. L., *Journal of the Aeronautical Sciences*, vol. 20, 29, 1953.
- [75] Bragg, M. B., *Aircraft Icing*, Yearbook of Science and Technology, McGraw-Hill, New York, pp. 183 - 185, 1999.
- [76] M. Polat, H. Polat, S. Chander, R. Hogg, *Particle and Particle Systems Characterization*, vol. 19, 38, 2002.
- [77] Domann, R., Hardalupas, Y., 'A Study of Parameters that Influence the Accuracy of the Planar Droplet Sizing (PDS) Technique', *Particle and Particle Systems Characterization*, vol. 18, no. 1, pp. 3 – 11, 2001.
- [78] Jazayeri, S. A., Li, X., 'Structure of Liquid-Sheet Sprays', *Particle and Particle Systems Characterization*, vol. 17, no. 2, pp. 56 – 65, 2000.

LIST OF REFERENCES

- [79] Kim, W. T., Mitra, S. K., Li, X., Prociw, L. A., Hu, T. C. J., 'A Predictive Model for the Initial Droplet Size and Velocity Distributions in Sprays and Comparison with Experiments', *Particle and Particle Systems Characterization*, vol. 20, no. 2, pp. 135 – 149, 2003.
- [80] Lee, S., Dunn, T., Gurbacki, H. M., Bragg, M. B., Loth, E., 'An Experimental and Computational Investigation of Spanwise-Step-Ice Shapes on Airfoil Aerodynamics', AIAA Paper 98-0490, AIAA 36th Aerospace Sciences Meeting, Reno, NV, January 12 – 15, 1998.
- [81] Chintamani, S. H. Belter, D. L., 'Design Features and Flow Qualities of the Boeing Research Aerodynamic Icing Tunnel', AIAA Paper 94-0540, AIAA 32nd Aerospace Sciences Meeting and Exhibit, Reno, NV, January 10 – 13, 1994.
- [82] Hansman, R. J., Kirby, M. S., 'Comparison of Wet and Dry Growth in Artificial and Flight Icing Conditions', *AIAA Journal of Thermophysics and Heat Transfer*, no. 3, pp. 215 – 221, 1987.
- [83] Buckingham, F. P., Haji-Sheikh, 'Cooling of High Temperature Cylindrical Surfaces Using a Water – Air Spray', *ASME Journal of Heat Transfer*, vol. 117, pp. 1018 – 1027, 1995.
- [84] Sheppard, D. T., Gandhi, P. D., Lueptow, R. M., 'Understanding Sprinkler Sprays: Trajectory Analysis', Fifteenth Meeting of the UJNR Panel on Fire Research and Safety, vol. 1, pp. 281 – 288, March 1 – 7, 2000.
- [85] Dantec Measurement Technology A/S, *FlowMap Particle Image Velocimetry Instrumentation – Installation & Users's Guide*, 1998.

LIST OF REFERENCES

- [86] Dantec Dynamics, 'Web-Site: \\www.dantecmt.com'.
- [87] Buchhave, P., 'Particle Image Velocimetry - Status and Trends', *Experimental Thermal and Fluid Science*, vol. 5, pp. 586 - 604, 1992.
- [88] Yu, S. C. M., 'Steady and Pulsatile Flow Studies in Abdominal Aortic Aneurysm Models Using Particle Image Velocimetry', *International Journal of Heat and Fluid Flow*, pp. 74 – 83, vol. 21, 2000.
- [89] Milanez, M., Naterer, G. F., Venn, G., Richardson, G., 'Droplet Momentum Characterization With Particle Image Velocimetry in Helicopter Icing Studies', AIAA Paper 2005-0001, AIAA 4th theoretical Fluid Mechanics Meeting, Toronto, June 6 - 9, 2005.
- [90] Naterer, G. F., Chomokovski, S. R., Friesen, C., Shafai, C., 'Micro-machined Surface Channels Applied to Engine Intake Flow and Heat Transfer', AIAA Paper 2003-4054, AIAA 36th Thermophysics Conference, Orlando, FL, June 23 - 26, 2003.
- [91] Naterer, G. F., Deng, H., Popplewell, N., 'Predicting and Reducing Glaze Ice Accretion on Electric Power Lines with Joule heating: Theory and Experiments', *Transactions of the CSME*, Vol. 23, No. 1A, 1999.
- [92] AIAA Standard, 'Assessment of Wind Tunnel Data Uncertainty', AIAA S – 071 - 1995, 1995.
- [93] Lu, M. L., Popplewell, N., Shah, A. H., Barrett, W., Au, A., "Mass of Ice Accretion from Freezing Rain Simulations", *Proceedings, 8th IWAIS, Reykjavik, Iceland, 1998.*

LIST OF REFERENCES

- [94] Anderson, J., 'Calibration of Wind Tunnel Icing Spray Nozzle', B.Sc. Thesis, Department of Mechanical and Manufacturing Engineering, University of Manitoba, Winnipeg, Canada, April, 2002.
- [95] Naterer, G. F., Popplewell, N., Barrett, W., Anderson, J., Faraci, E., McCartney, D., Lehmann, W., "Experimental Facility for New Hybrid Ice / Spray Flow Tunnel with Laser Based Droplet Measurement", AIAA Paper 2002-2867, AIAA 32nd Fluid Dynamics Conference, St. Louis, Missouri, June 24 - 27, 2002.
- [96] Stokes, G. G., "On the Effect of internal Friction of Fluids on the motion of pendulum", Trans. Comb. Phil. Soc., Vol. 9, p. 8-27, 1851.
- [97] Mei, R., and Klausner, J. F. "Shear Lift Force on a spherical bubble", International Journal Heat and Fluid Flow, Vol. 15, p. 62-65, 1974.
- [98] Moeller, J., "Trajectory Analysis of Dust Particles Ejected by the Augustine Volcano on March 27 and 28, 1986", Math Modeling, September, 2000.
- [99] Szilder, K., Lozowski, E. P. and Gates, E. M., "Modelling ice accretion on non-rotating cylinders — The incorporation of time dependence and internal heat conduction", Math Cold Regions Science and Technology, Vol. 13, 2, p. 177-191, 1987.
- [100] Fox, R. W., McDonald, A. T. and Pritchard, P. J., "Introduction to Fluid Mechanics", Six-th Edition, Wiley & Sons, Inc., Danvers, MA, USA, 2004.
- [101] Li, C., Mosyak, A. and Hetroni, G., "Direct Numerical Simulation of Particle-Turbulence Interaction", International Journal of Multiphase Flow, Vol. 25, p. 187-200, 1999.

LIST OF REFERENCES

- [102] Clift, R., Gauvin, W. H., "The Motion of Particles in Turbulent gas streams", Chemeca, p. 14-28, 1970.
- [103] Clift, R., Grace, J. R., Weber, M. E., *Bubbles, Drops and Particles*, Academic Press, 1978.
- [104] Khalil, M., Keith, T. G., DeWitt, K. J., "New Concept in Runback Water Modeling for Anti-Iced Aircraft Surfaces", Journal of Aircraft, Vol. 30, No. 1, p. 41-49, 1993.

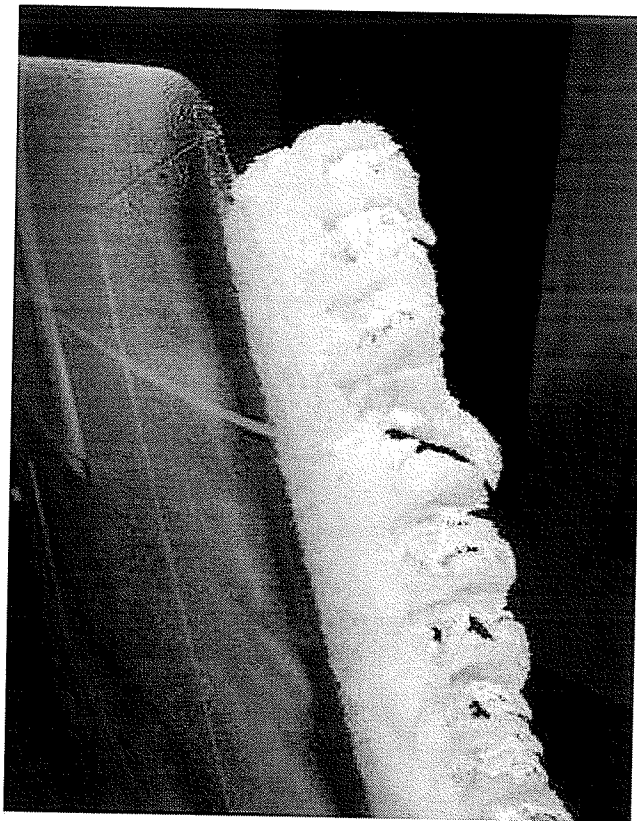


Figure 1. 2. 1: Sample Ice Accretion on a Surface (Source – Internet: NASA Lewis Research Center, C99-193)

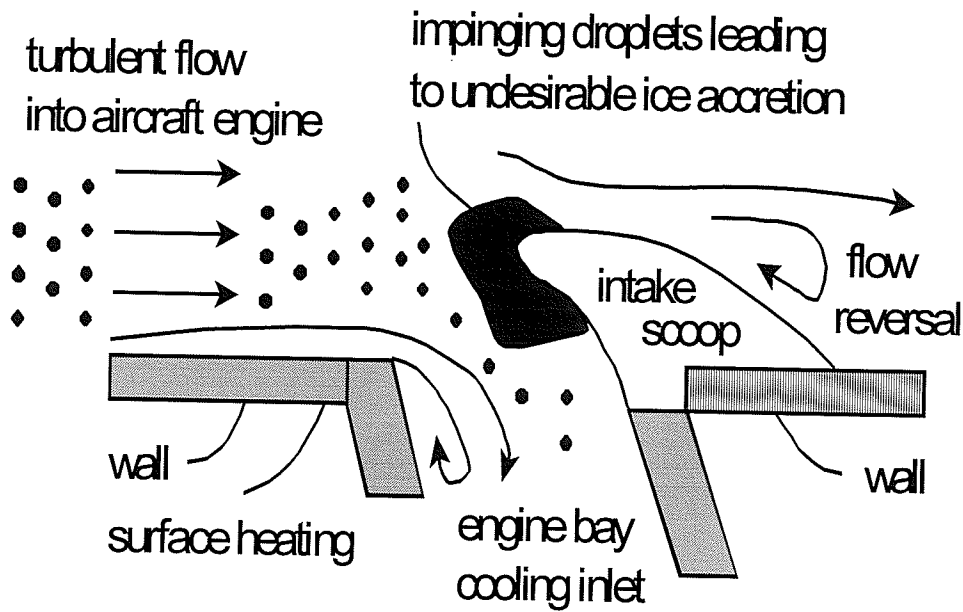


Figure 1. 2. 2: Droplet Flow with Helicopter Icing

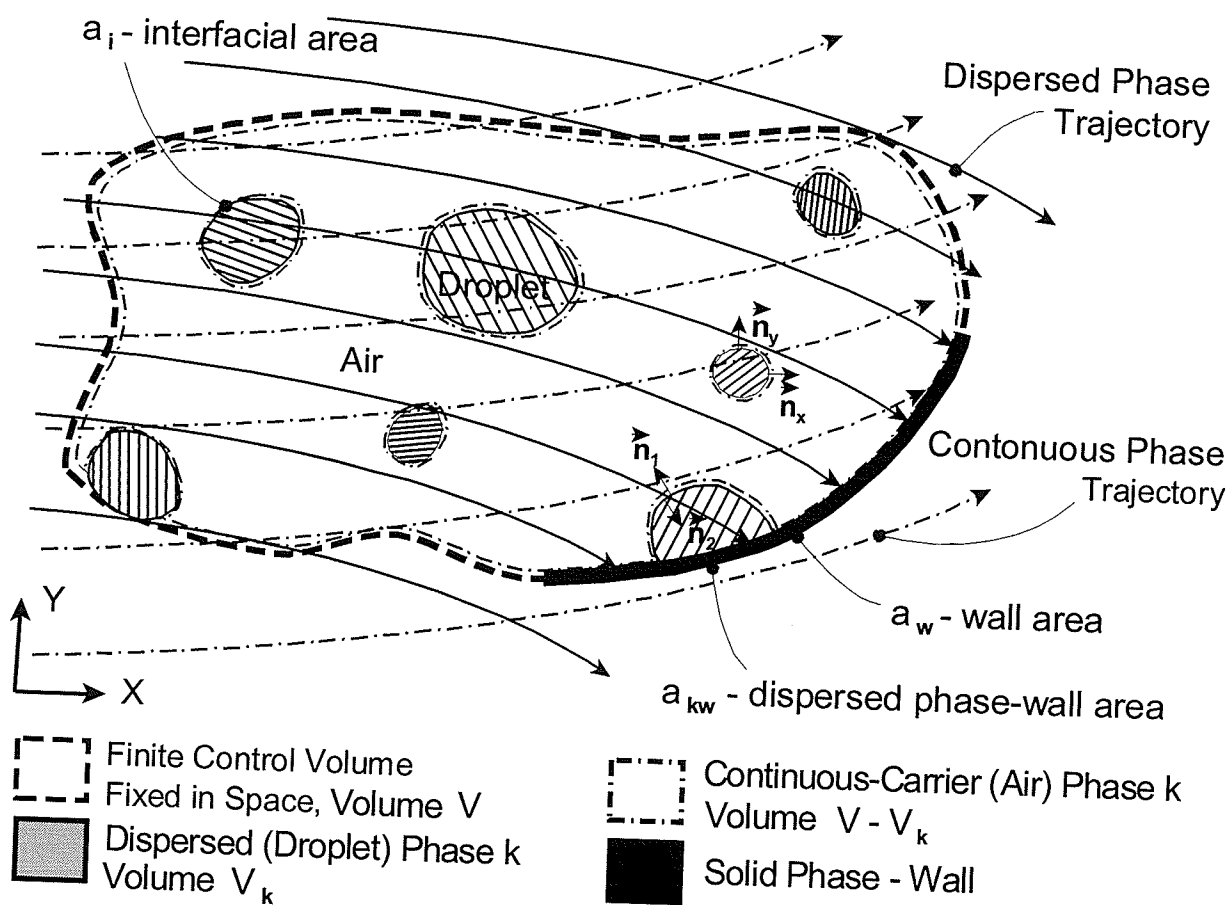


Figure 2. 2. 1: Schematic of Multiphase Control Volume

C_D	$Re_{r,max}$	Reference
$24/Re_r$	< 1 (or < 0.1)	[96]
$(24/ Re_r)[1+(3/16)Re_r]$	< 5	[8]
$(24/ Re_r)[1+(3/16)Re_r+(9/160) Re_r^2 \ln(2. Re_r)]$	$0.1 < Re_r < 2$	[103]
$(24/ Re_r)(1+0.15 Re_r^{0.687})$	$Re_r \leq 1000$	[22]
$(24/ Re_r)(1+0.15 Re_r^{0.687})+0.42/(1+4.25 \times 10^4 Re_r^{-1.16})$	$Re_r \leq 10^5$	[102]
$(24/ Re_r)+(3/ Re_r^{1/2})+0.34$	$Re_r < 1000$	[103]
$(24/ Re_r)+[6/ (1+Re_r^{1/2})]+0.40$	$Re_r < 2.10^5$	[101]
$(24/ Re_r)+(1+0.1935 Re_r^{0.6305})$	$20 < Re_r < 260$	[103]
0.42 or 0.44	$1000 < Re_r < 2.10^5$	[100]
$4[(6+Re_r^{2/3})/ Re_r]$	$1 < Re_r < 1000$	[98]
$(16/ Re_r)\{1+[(8/ Re_r)+(1/2)(1+3.315 Re_r^{-1/2})]^{-1}\}$	Large	[97]
$24/(Re_r^{0.646})$	$1 < Re_r < 400$	[103]
0.5	$400 < Re_r < 3.10^5$	[100]
$0.000366 Re_r^{0.4275}$	$3.10^5 < Re_r < 2.10^6$	[103]
0.18	$Re_r = 3.10^5$	[100]
$(24/ Re_r)+(4.73/ Re_r^{0.37}+0.00624 Re_r^{0.38})$		[99]

Table 2. 3. 1: Models of the Drag Coefficient

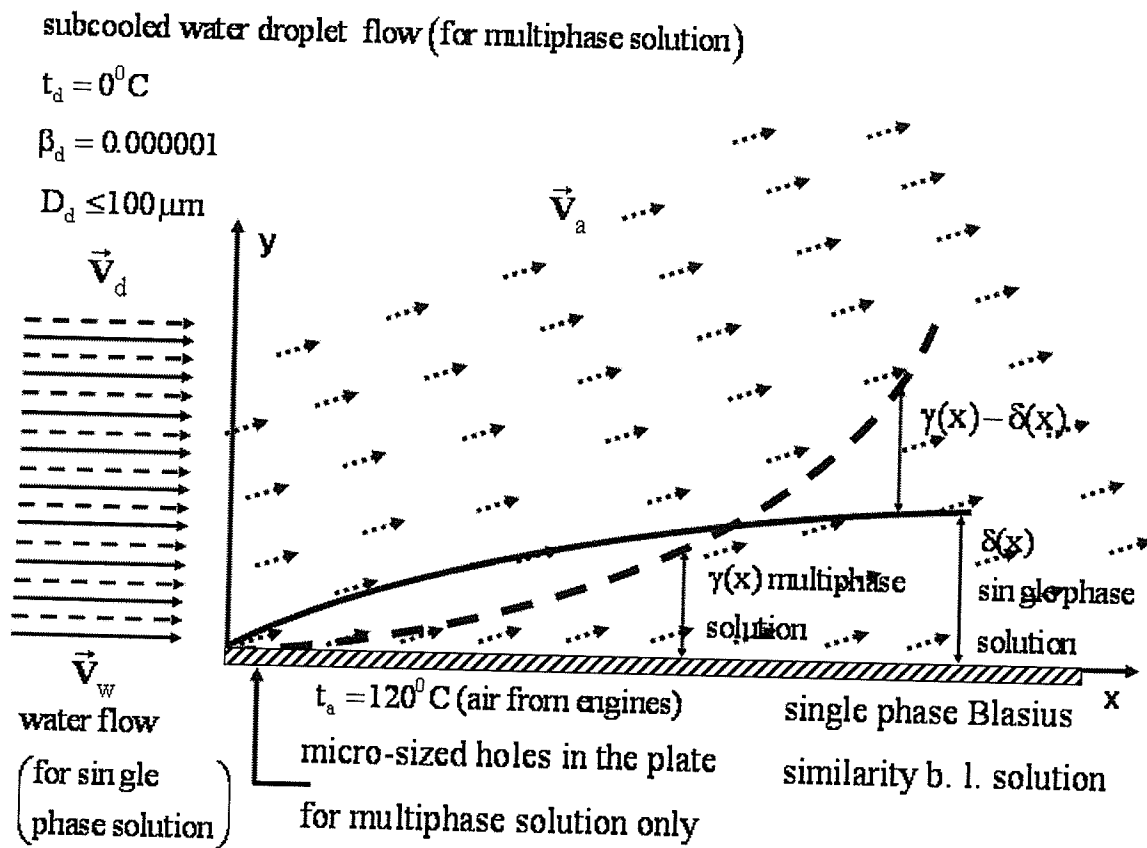


Figure 2. 4. 1: Schematic of Near-Wall Droplet Momentum Displacements (Similarity Analysis)

a) Summarized initial parameters based on scaling, sensitivity, order of magnitude and similarity analysis													
$v_{a,x}$	$v_{a,y}$	$v_{d,x}$	$v_{d,y}$	μ_a	ν_a	ρ_a	μ_d	ρ_d	D_d	β_d	γ	L	t
5	0.5	40	-4	2.26E-5	2.52E-5	0.8979	1.79E-3	999.8	E-4	10E-6	.01	.2	.005
$ \Delta v_x $	$ \Delta v_y $	Re_r	f	β_v	C	$\Gamma_{d,m}$	g_x	g_y					
35	4.5	140.076	5.4911	0.2236	223.6221	0	0	9.81					

b) Summarized terms in the droplet y-momentum equation						
TRANS.	x-CONV.	y-CONV.	MASS	PRESSURE	VISC1	VISC2
-0.7998	-0.7998	1.5997	0.0000	0.1016E+5	-1.4328E-4	3.5621E-5
DRAG	GRAV.	FAX.	SAFF.	TURB1	TURB2	
1.0061	0.0098	6.6588E-14	5.6644E-08	-1.4328E-4	3.5621E-05	

c) Summarized terms in the droplet x-momentum equation						
TRANS.	x-CONV.	y-CONV.	MASS	PRESS. TERM	VISC1	VISC2
7.9984	7.9984	-15.9968	0.0000	-0.5747	3.5820E-6	7.1242E-4
DRAG	GRAV.	FAX.	SAFF.	TURB1	TURB2	
-7.8252	0.0000	3.3294E-15	-7.2827E-9	3.5820E-6	7.1242E-04	

d) The approximated absolute percentages of terms in the droplet x-momentum equation						
TRANS.	x-CONV.	y-CONV.	MASS	PRESS.	VISC1	VISC2
50	50	100	0	0	0	0
DRAG	GRAV.	FAX.	SAFF.	TURB1	TURB2	
49	0	0	0	0	0	

Table 2. 4. 1: The Parameters for the Scaling, Sensitivity, Order of Magnitude and Similarity Analyses

Variable	Dimensional Order	Non - Dimensional Order
$v_{d,x}$	$v_{x,\infty}$	1
$v_{a,x}$	$v_{x,\infty}$	1
x	L	1
y	γ	$\xi \left(\frac{\gamma}{L} \right)$

Table 2. 4. 2: Characteristic Parameters in Order of Magnitude Analysis

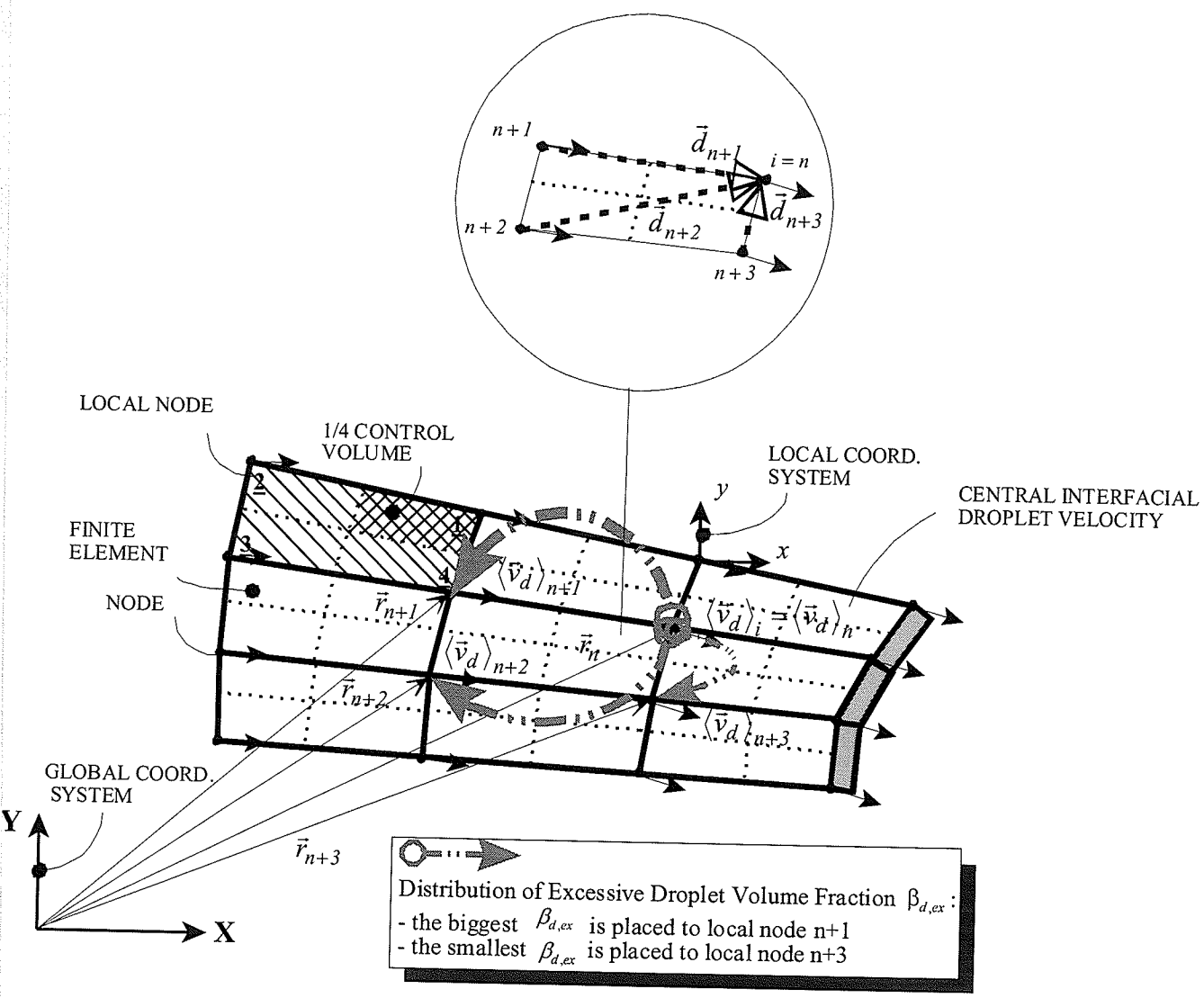


Figure 2. 5 .3: Notation for Ice Tracking Algorithm

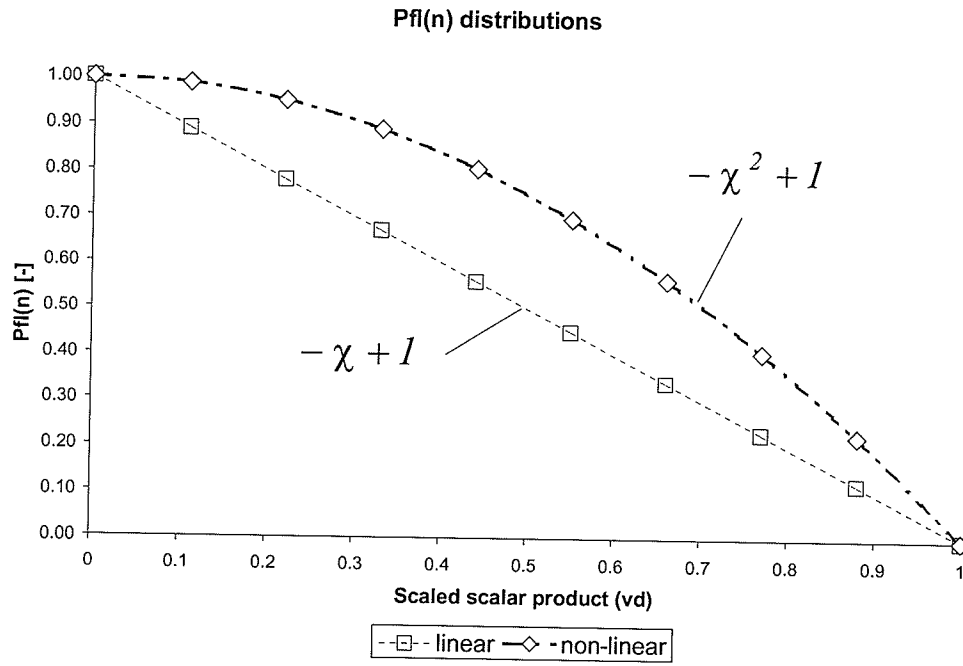


Figure 2. 5 .3 .1: Linear and Non-linear distributions for Pfl

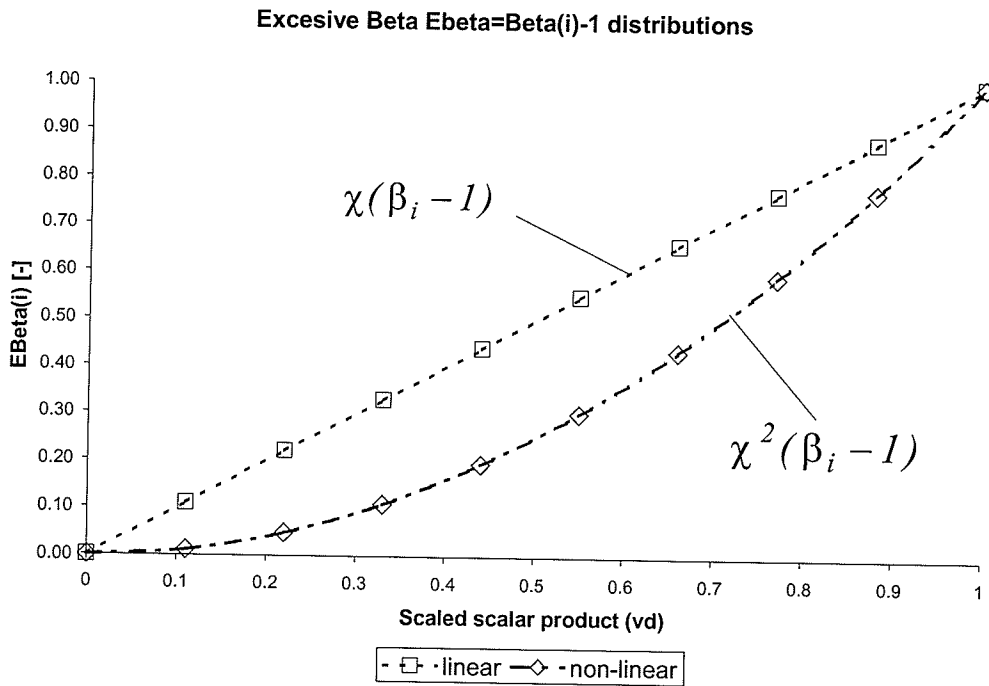


Figure 2. 5 .3 .2: Linear and Non-linear distributions for EBeta

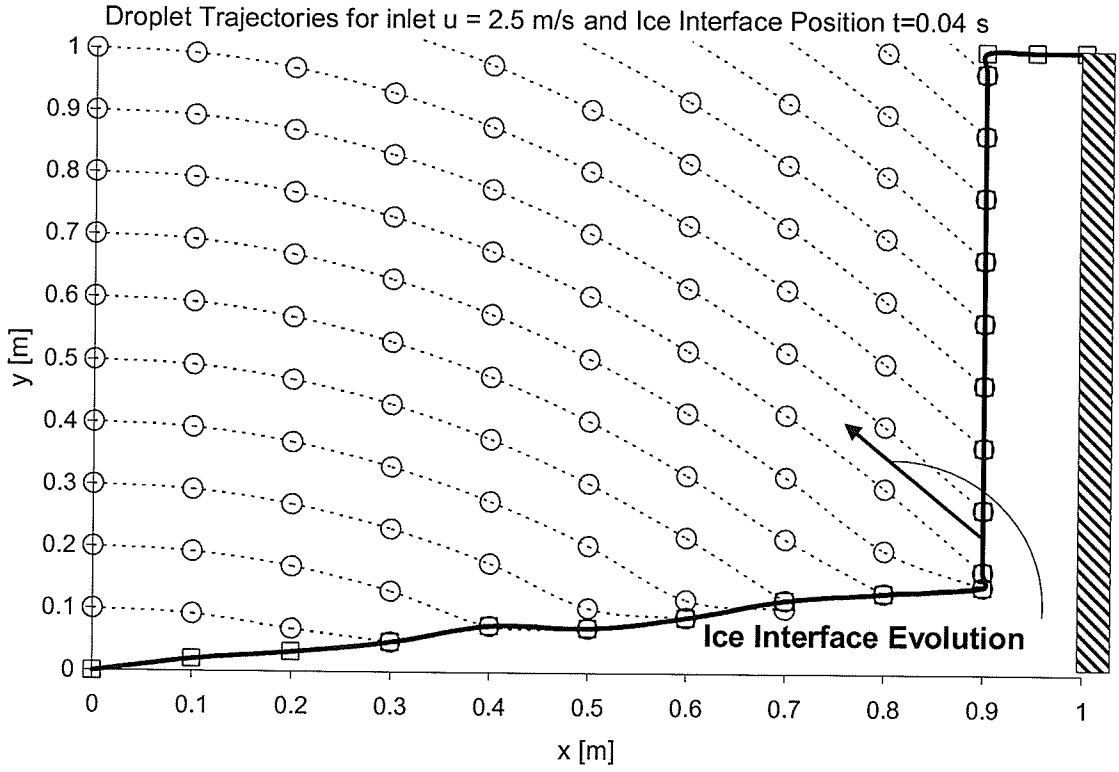


Figure 2. 5 .3 .3: Sample Case of Evolving Ice Interface Based on Analytical Droplet Trajectories

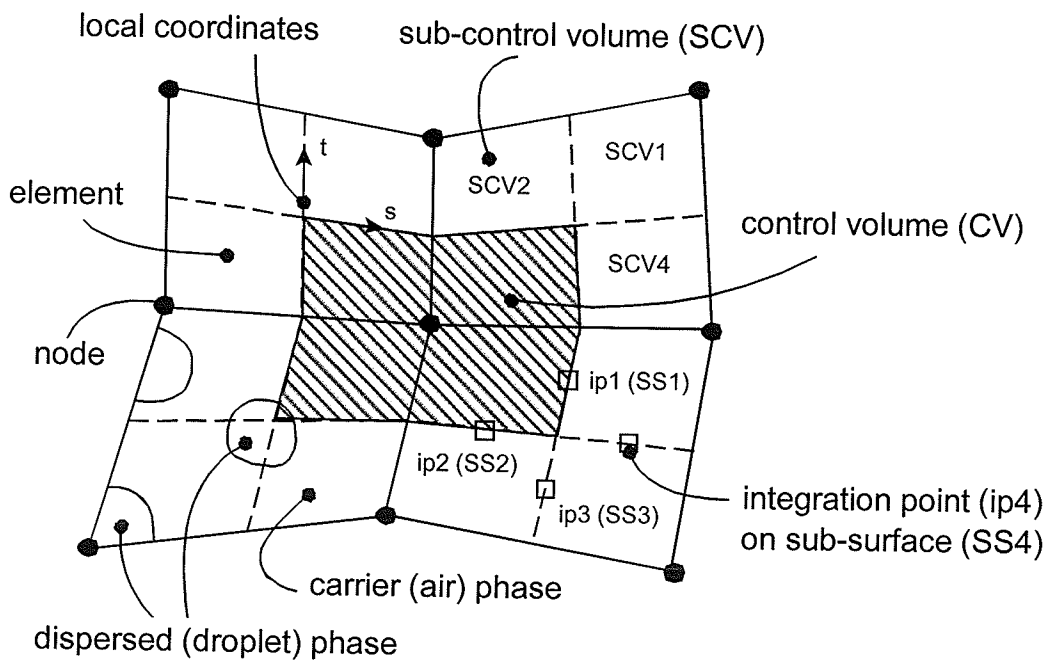


Figure 3. 1. 1: Discretization of Finite Element and Control Volume

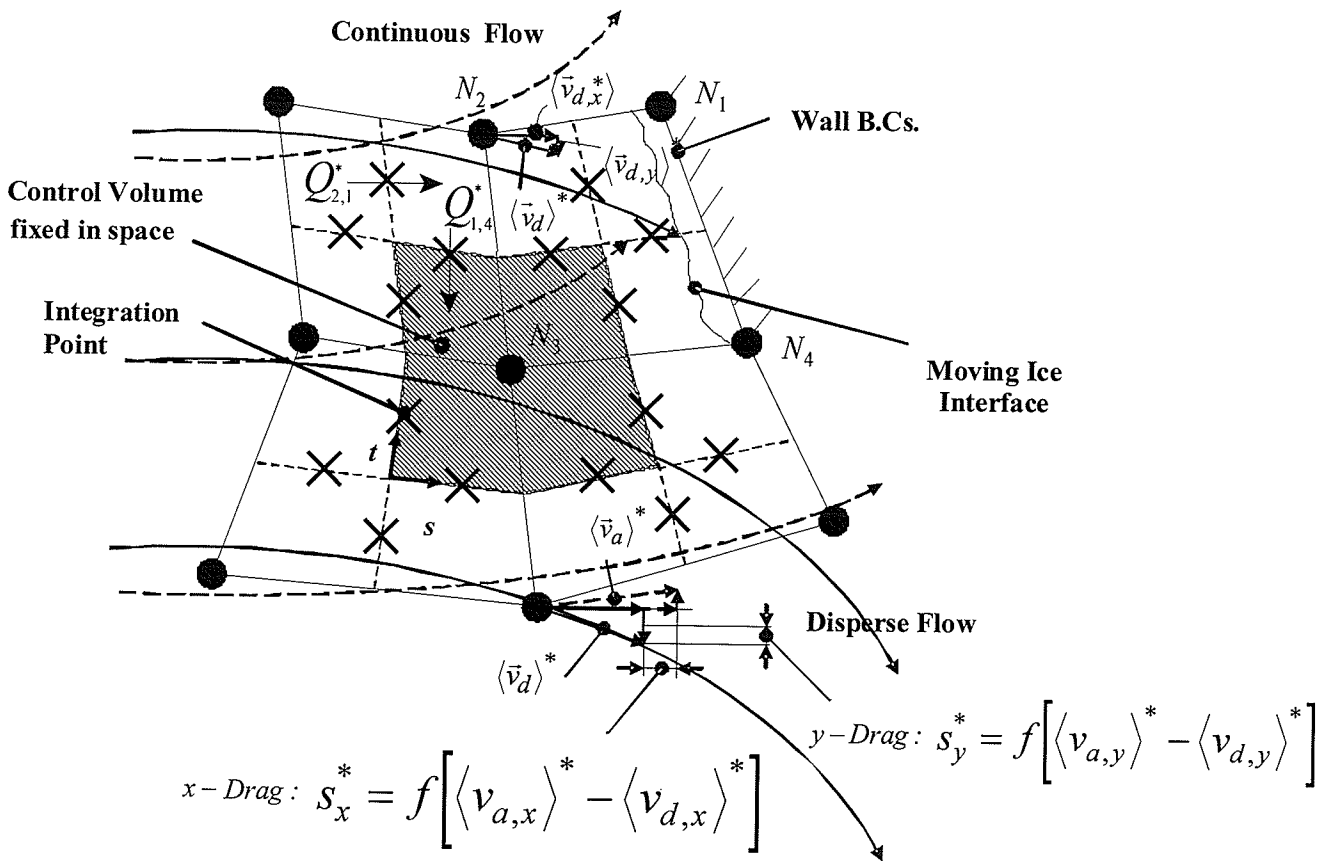


Figure 3. 3. 1. 1: Construction of the Drag term in the Dispersed Phase Momentum Equation within a Control Volume

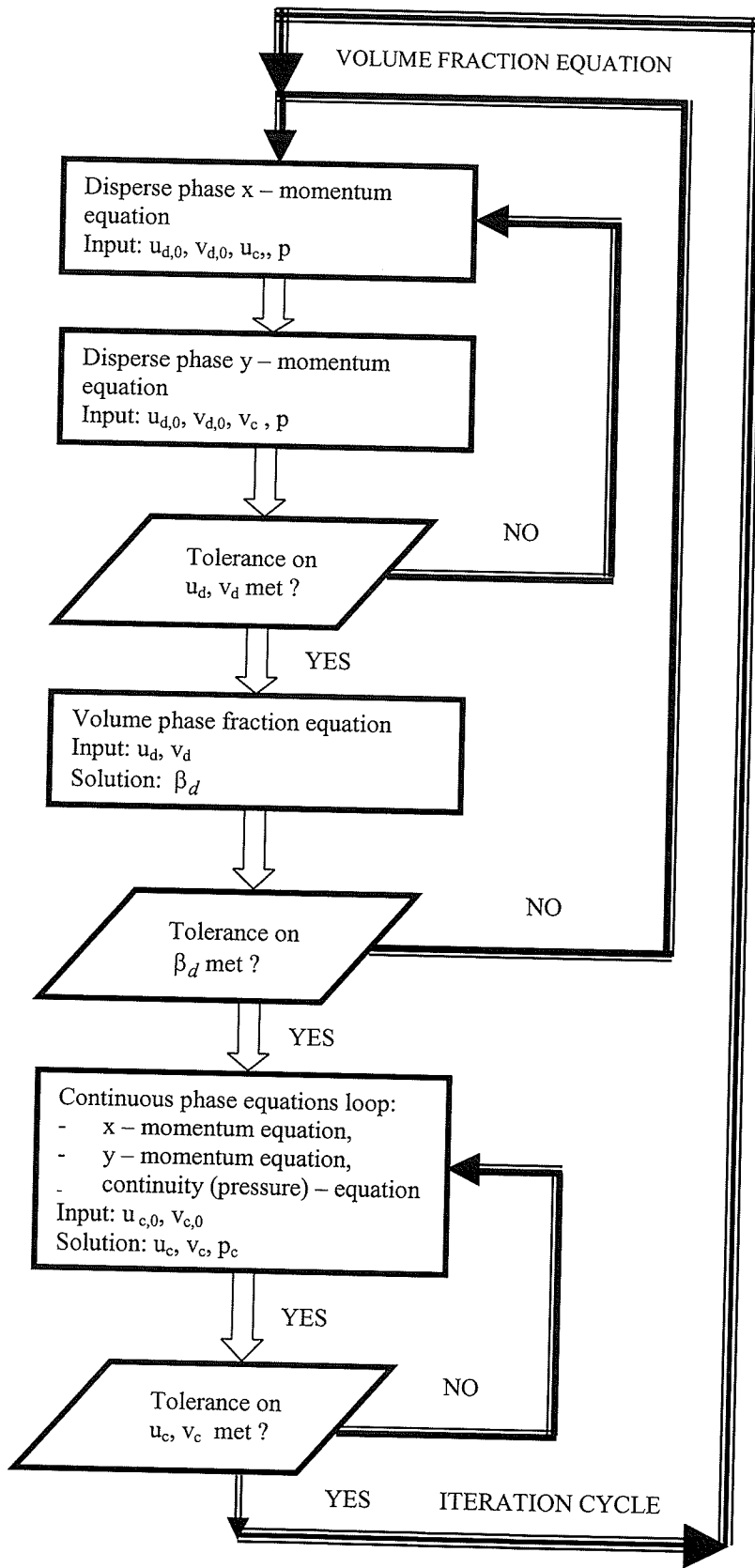


Figure 3. 6. 1: General Solution Algorithm

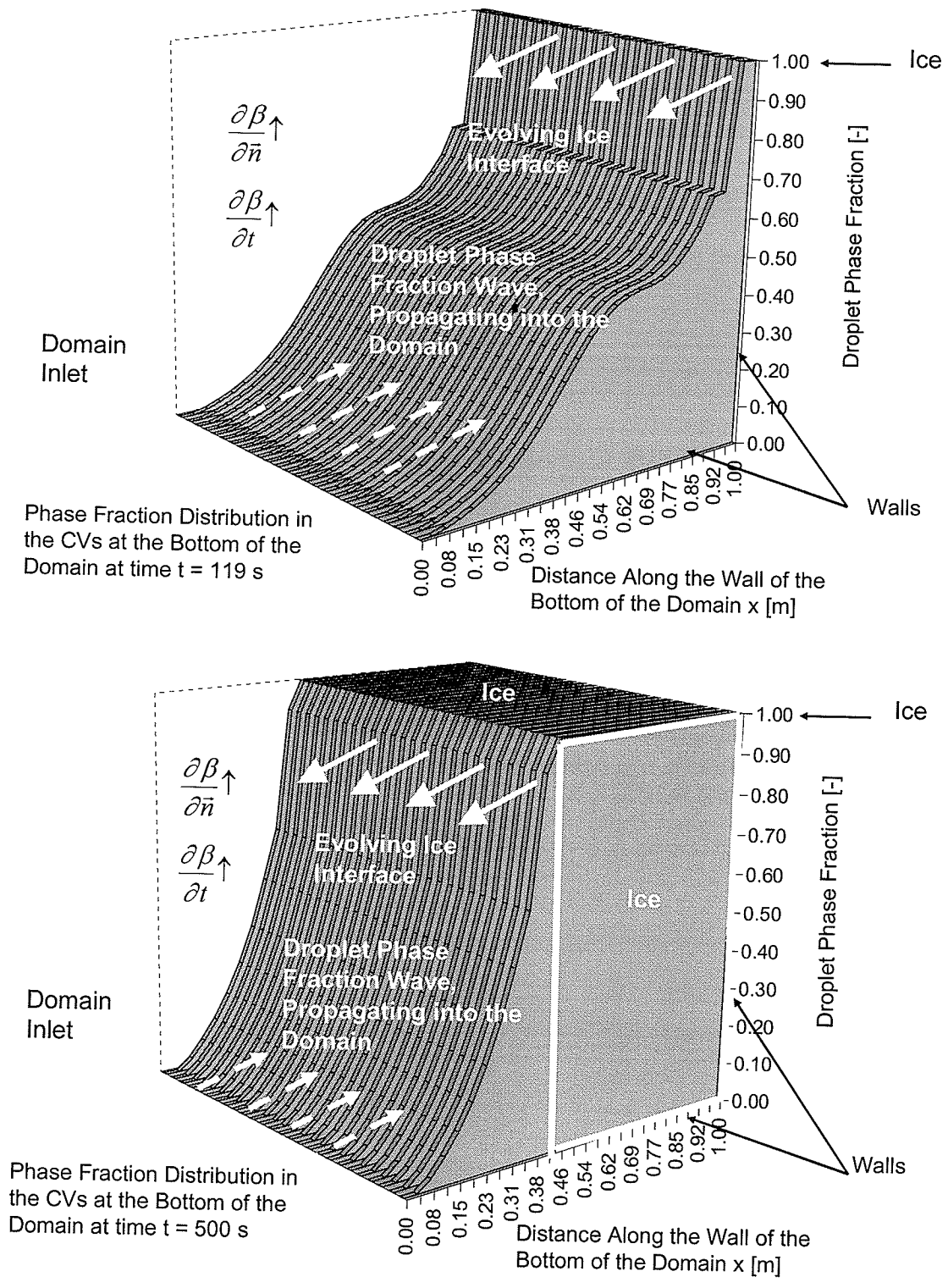


Figure 3. 6. 2. 1: Evolving Ice Interface with Accreted Ice at $t = 119.05$ s (up) and $t = 500$ s (down)

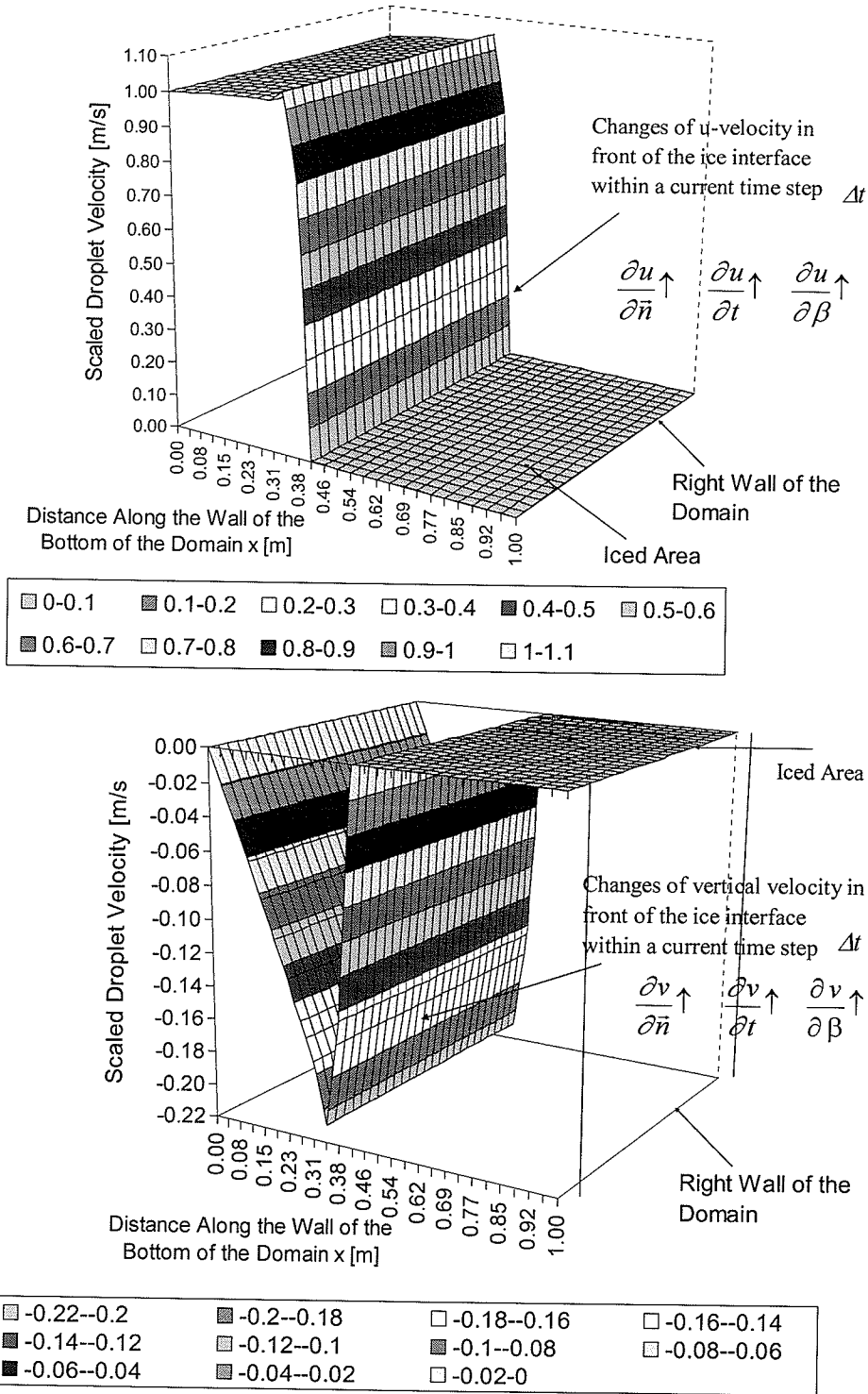


Figure 3. 6. 2. 2: Droplet x- and y- Reference Scaled ($u_r = 4$ m/s) Velocities in the Domain: Before the Ice Interface, at the Ice Interface and in the Region of Accreted Ice, $\beta_d = 1$ at $t = 500$ s

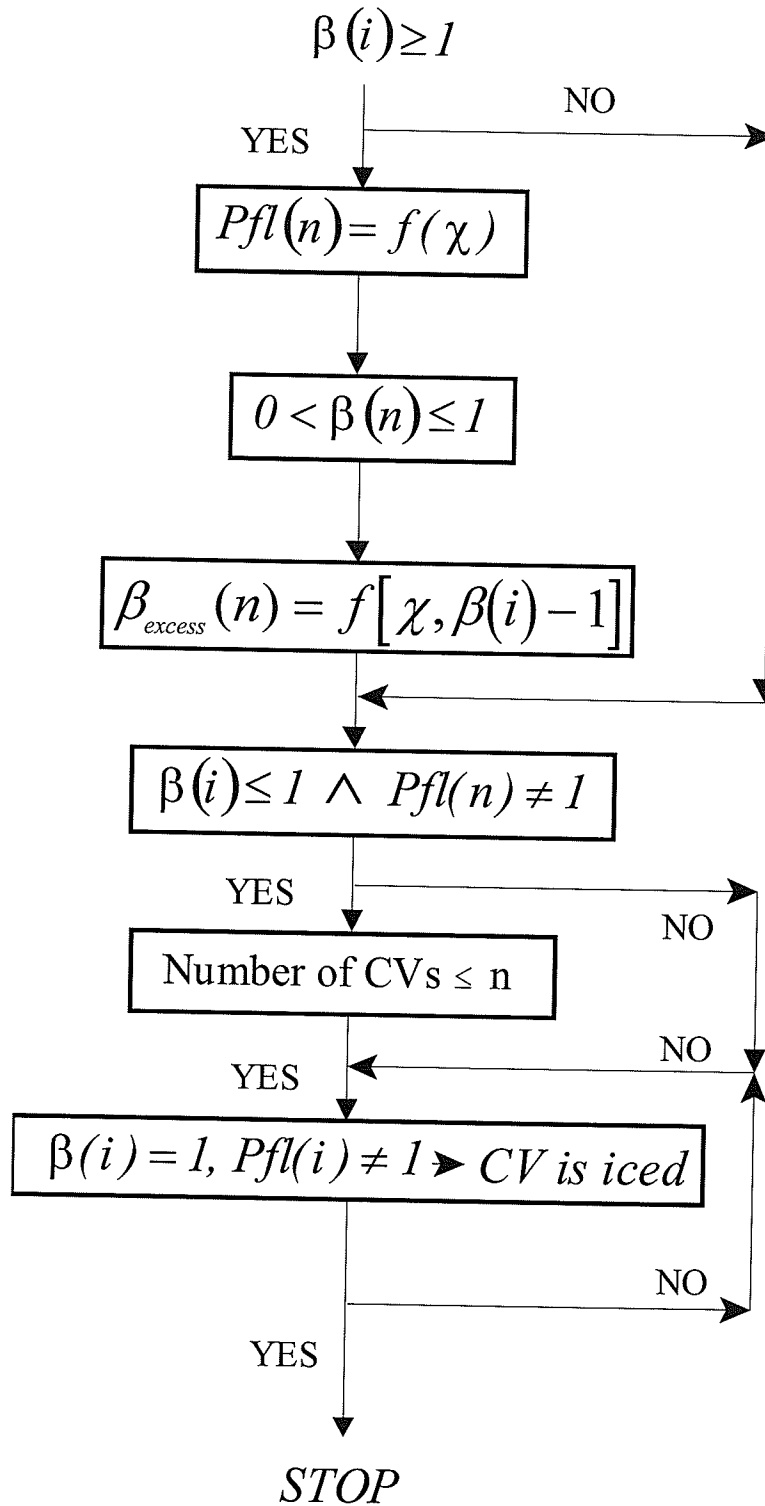


Figure 3. 6. 2. 3: Central Part of Ice Redistribution Algorithm

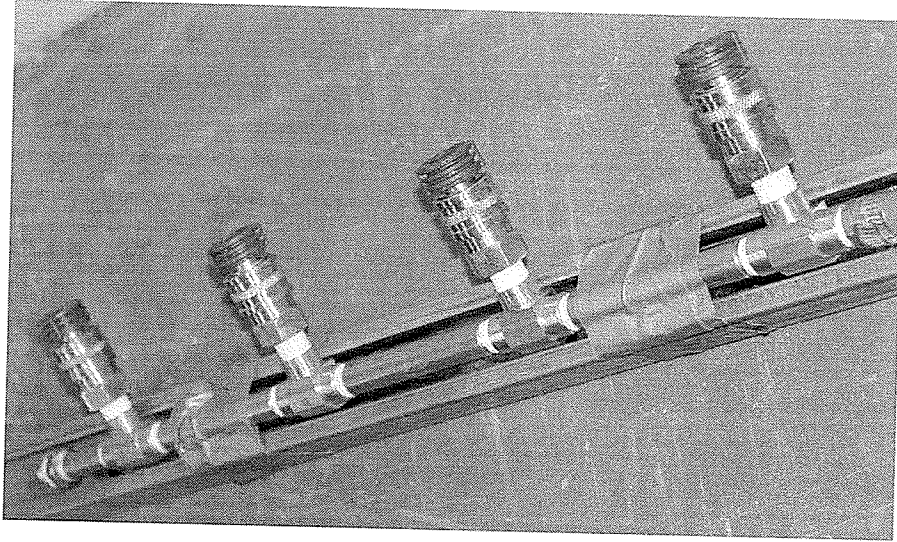


Figure 4. 1. 1. 1: Long Distance Nozzle System with Zero Degree Pressure Washer Nozzles (J. Kozub, M. Milanez)

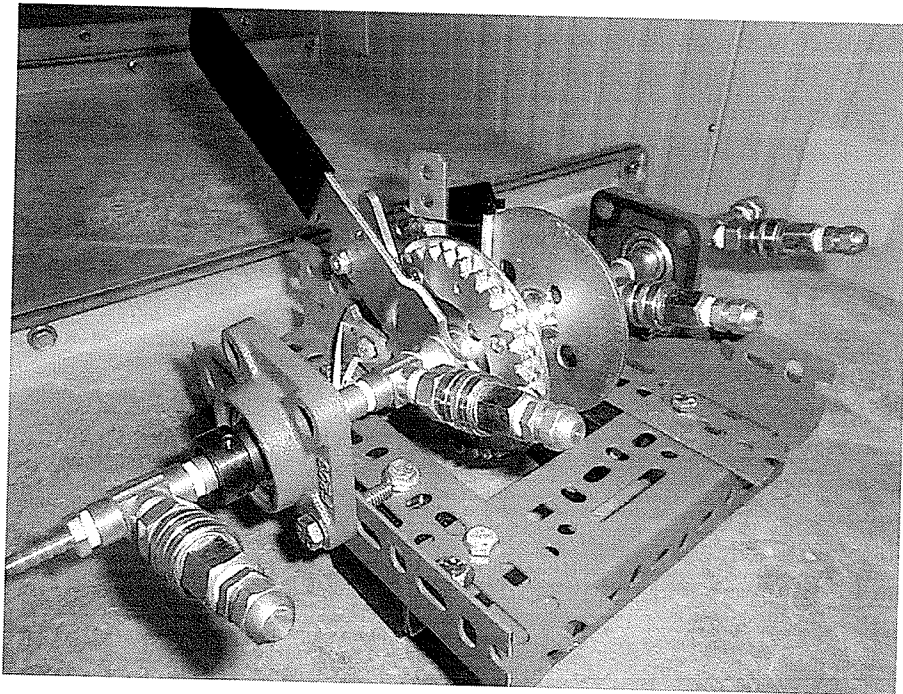


Figure 4. 1. 1. 2: Long Distance Nozzle System with Flare end Cap Nozzles (J. Kozub, M. Milanez)

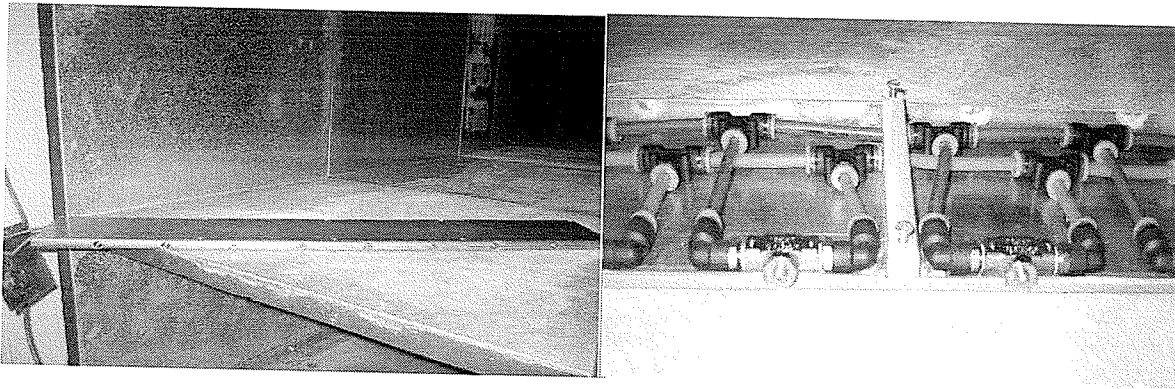


Figure 4. 1. 1. 3: Old Atomizer with the old settings (Airfoil Frame-Left, Water
Tubs and Air Tubs-Right) – J. Anderson [94]

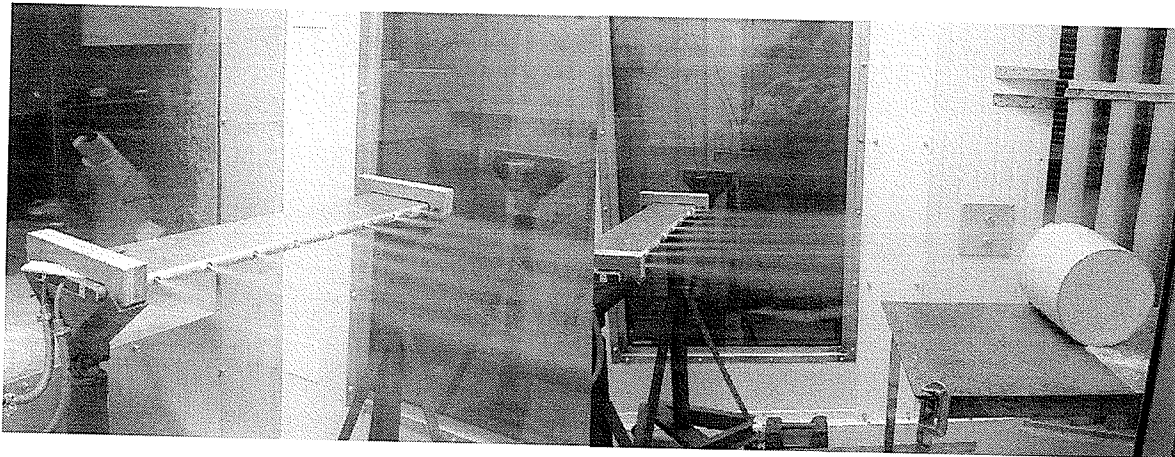


Figure 4. 1. 1. 4: Old Atomizer with Droplet-Air Flow

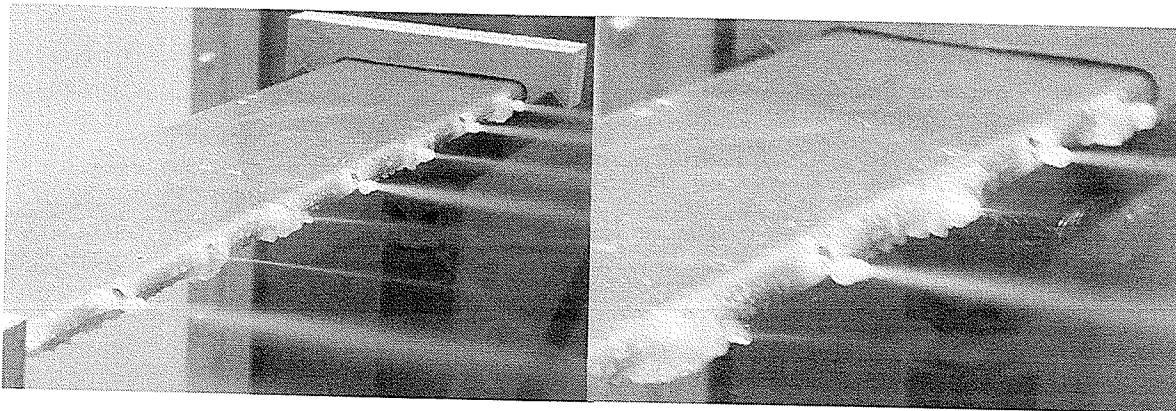


Figure 4. 1. 1. 5: Freezing Nozzles of the Old Atomizer

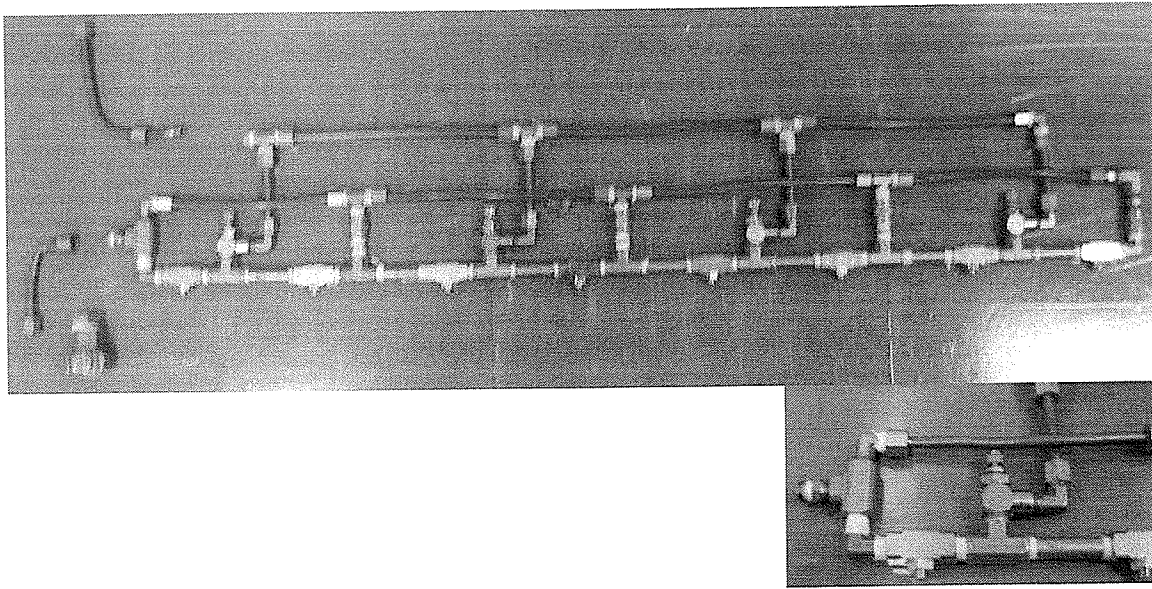


Figure 4. 1. 1. 6: Network of Tubes in the New Atomizer (M. Koupriyanov, M. Milanez)

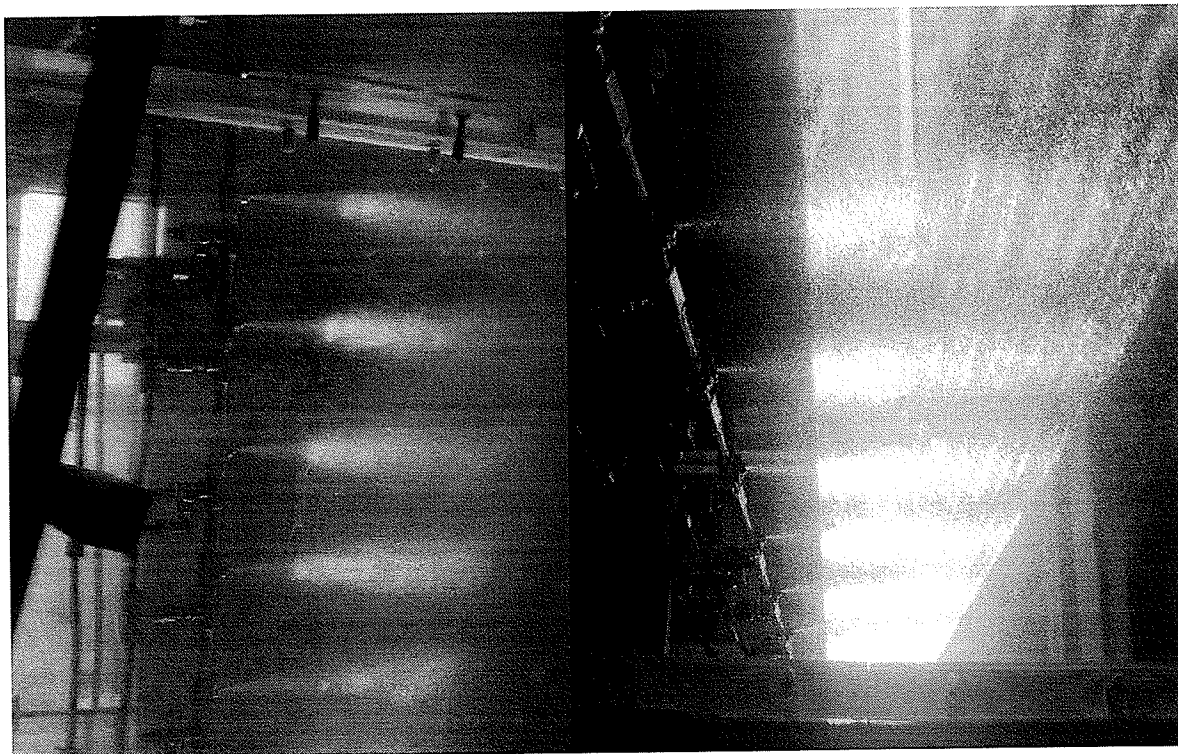


Figure 4. 1. 1. 7: Dispersed Droplet Flow Atomized by Medium (Left) and High (Right) Pressurized Air (Premixed Mist Flow in the Nozzle Mixing Chambers),

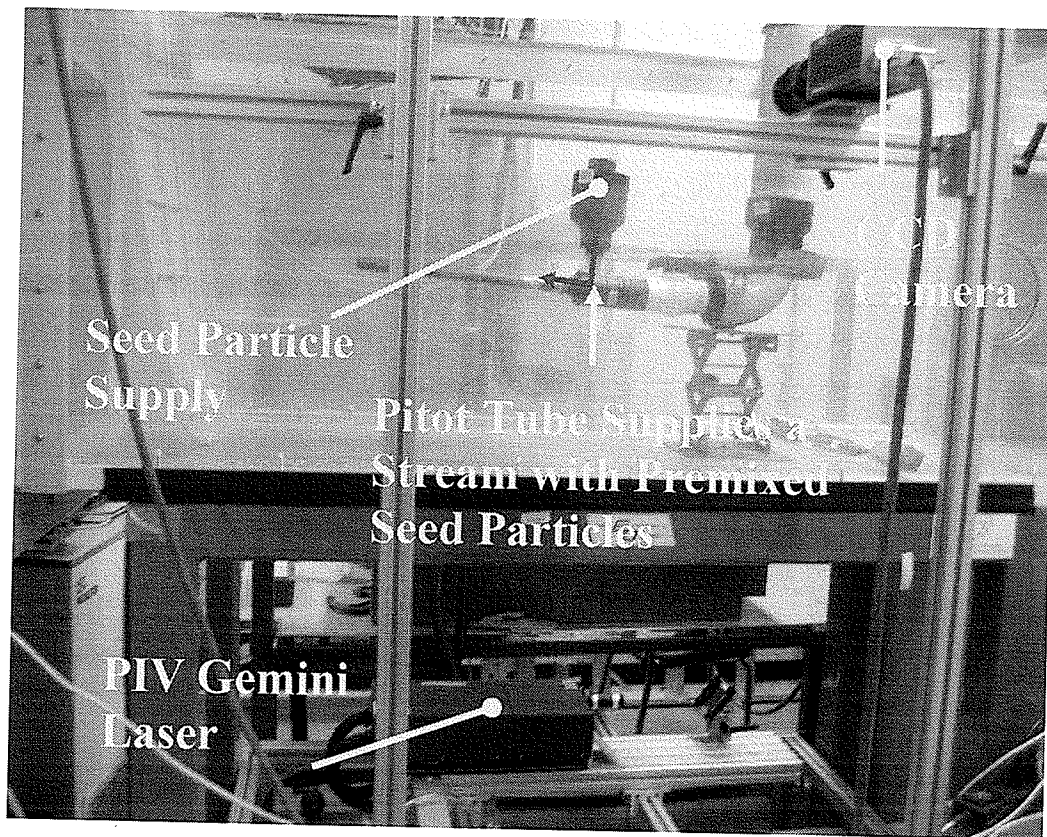


Figure 4. 1. 1. 8: Experimental Setup of Stream Flow (Up) with the Pulsed Laser (Down), (M. Milanez, M. Koupriyanov,)

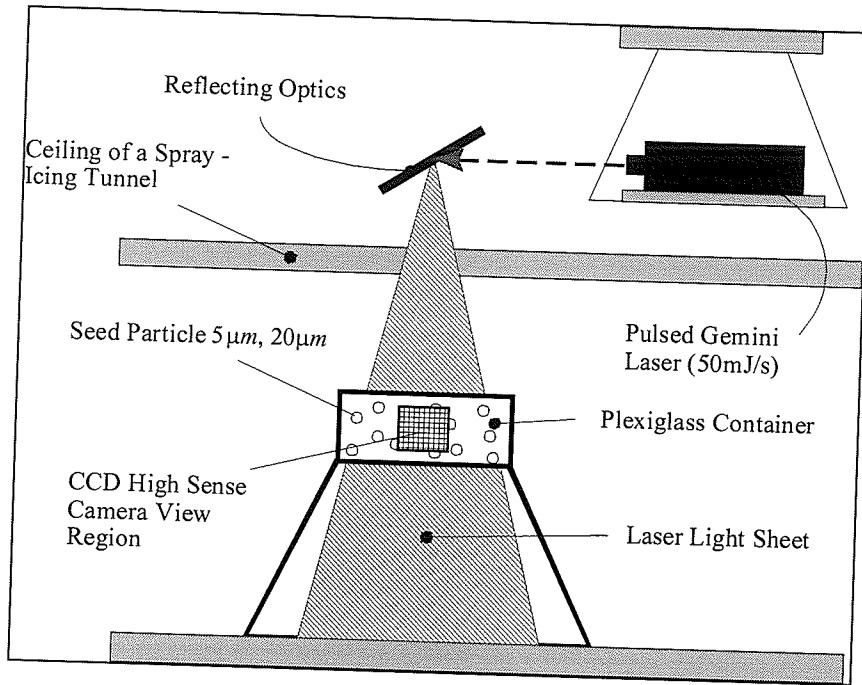


Figure 4. 1. 1. 9: Laser Measurements of Velocity Field with Internal Water Flow and Premixed Seed Particles

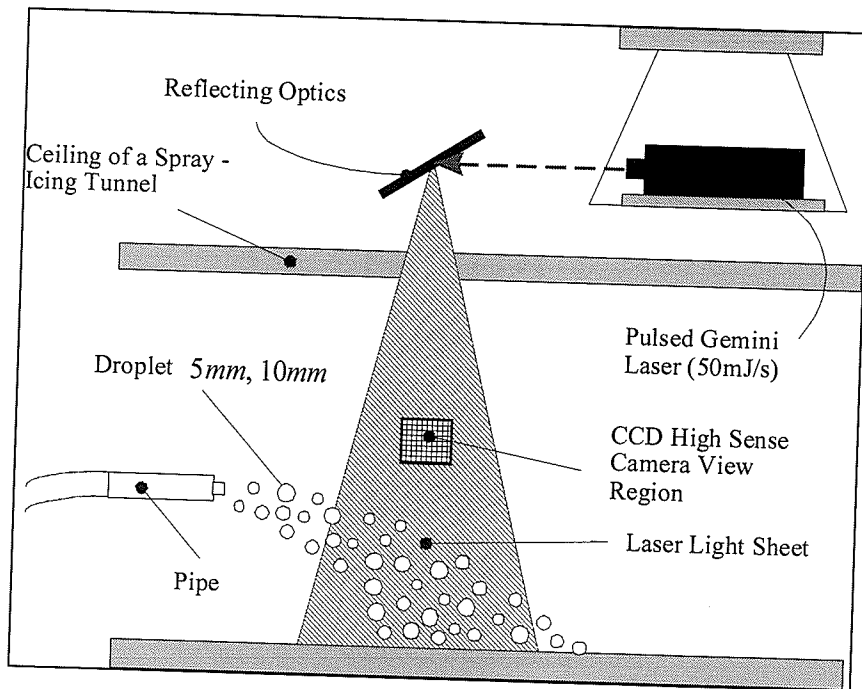


Figure 4. 1. 1. 10: Laser Measurements of Velocity Field with External Dispersed Droplet Flow (without Seed Particles)

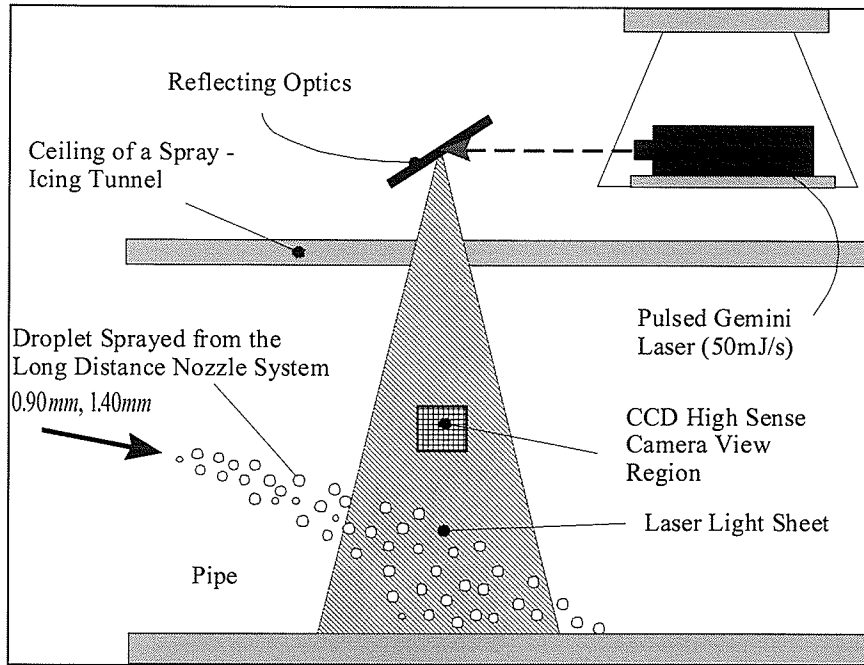


Figure 4. 1. 1. 11: Laser Measurements of Velocity Field with Dispersed Droplet Flow Sprayed from Long Distance (without Seed Particles)

INput - Image 1 Image Transfer Function (Spatial Shift) OUTput - Image 2

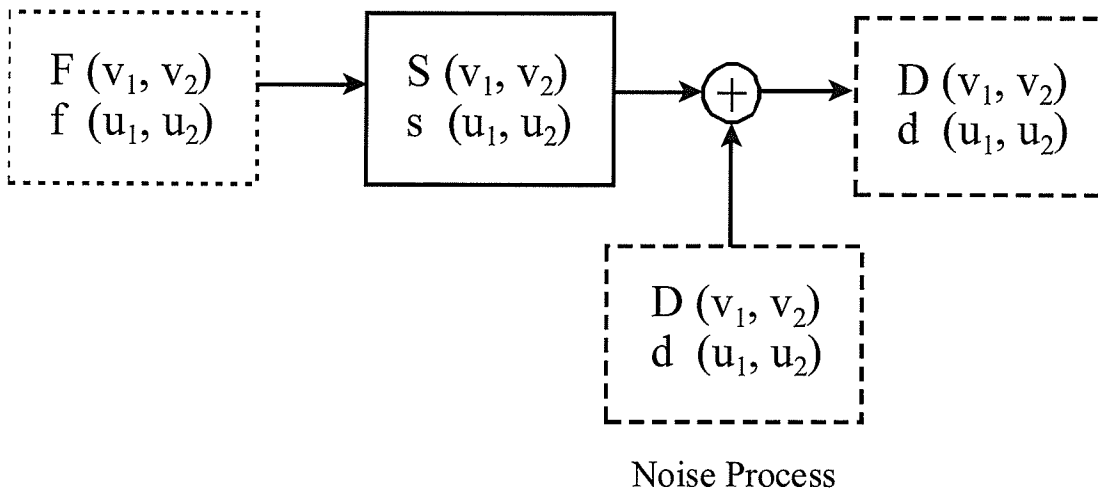
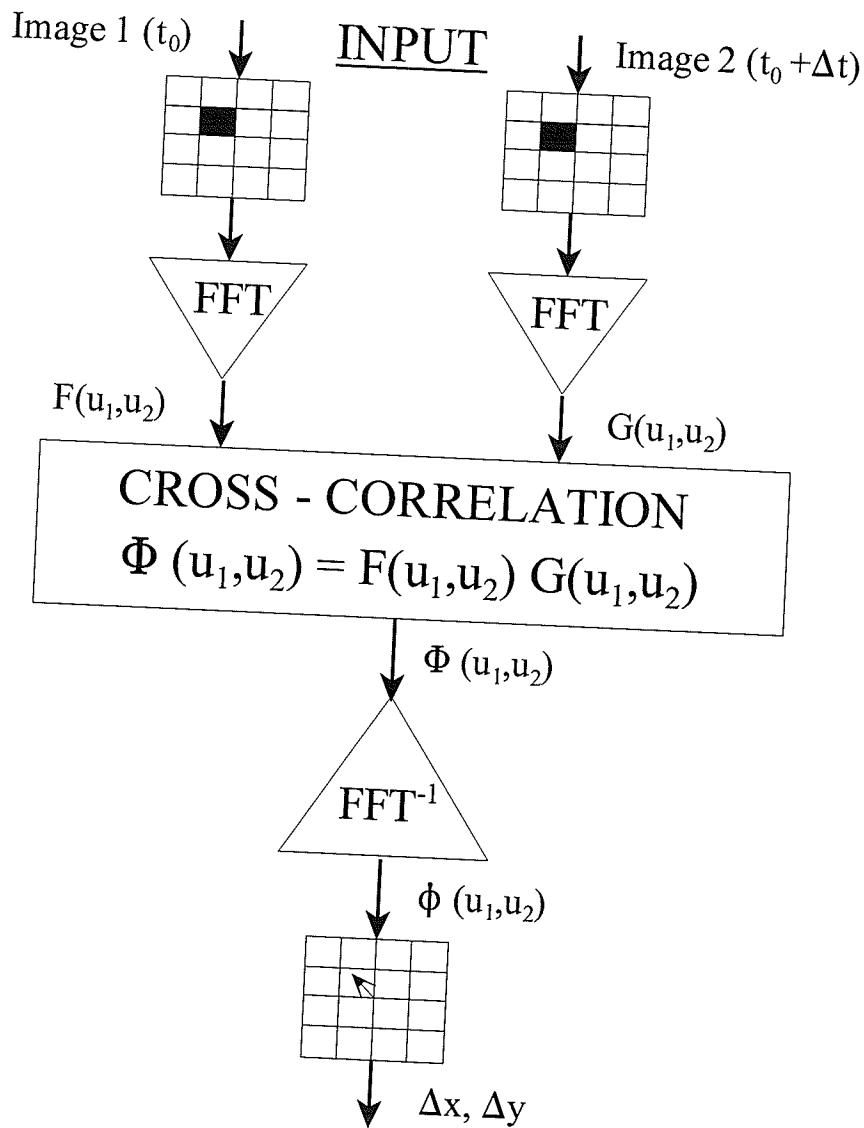


Figure 4. 2. 2. 1: Estimation of Spatial Shifting – Image Displacement Function

$$s(u_1, u_2)$$



OUTPUT: Velocity Calculation: $V_x(i,j), V_y(i,j)$

Figure 4. 2. 2. 2: *PIV* Cross – Correlation Technique within the *PIV* Evaluation Method

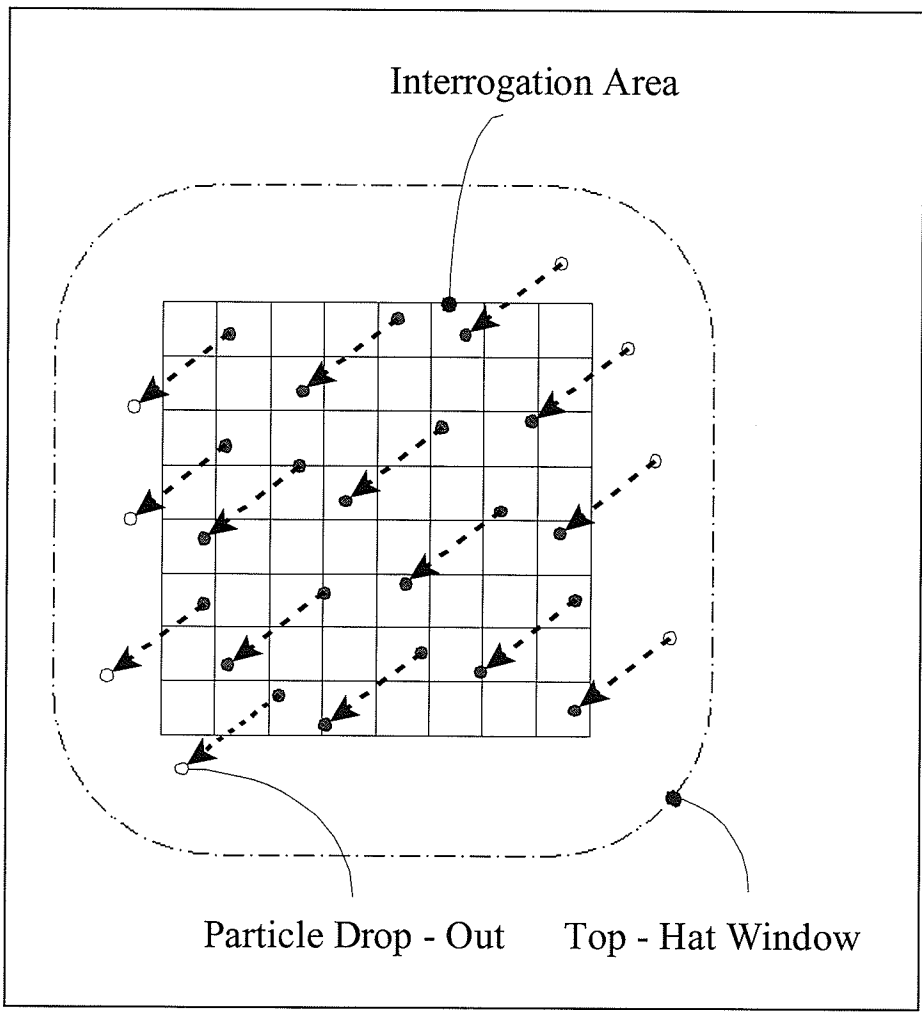


Figure 4. 2. 2. 3: Loss of Correlation Signal Due to Absence of Particles in the Interrogation Area and Enlargement of Area (Accommodation of Phantom Particles)

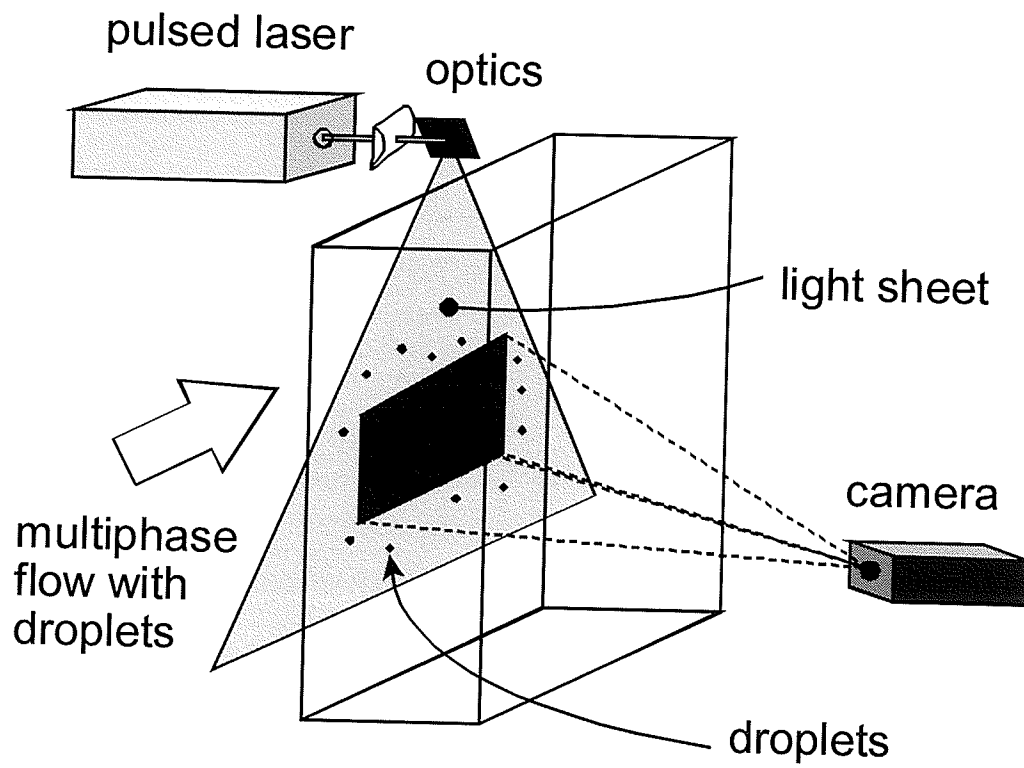


Figure 4. 2. 3. 1: Schematic of the *PIV* Laser Based Setup

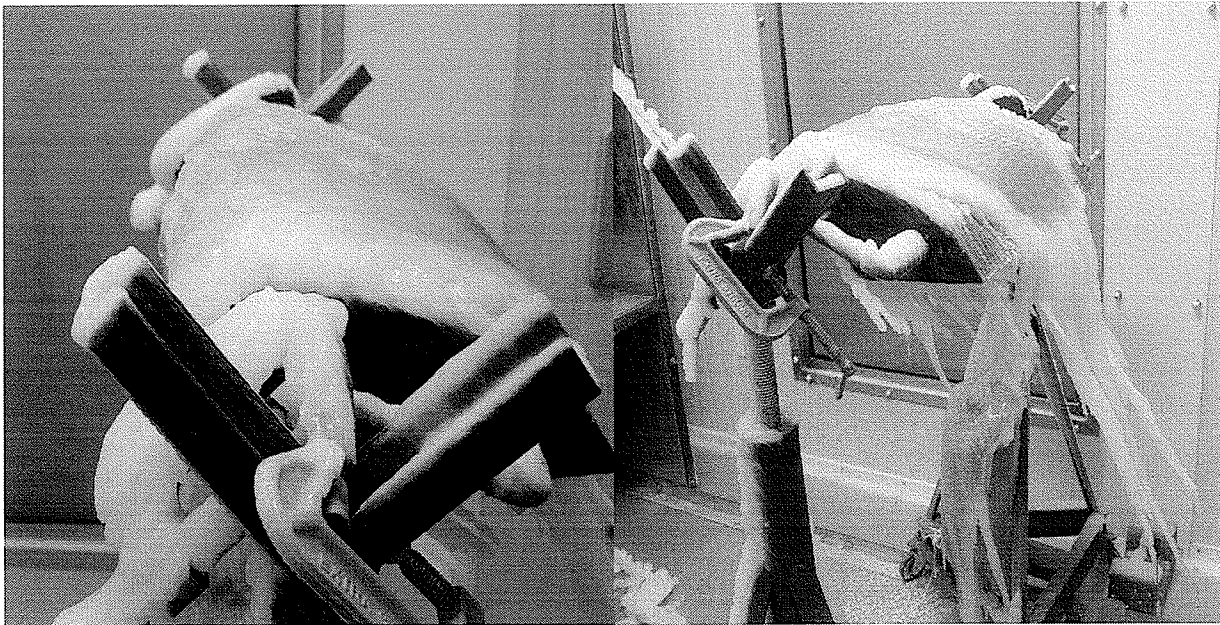


Figure 4. 4. 1: Rime Ice Buildup on Helicopter Scoop (Case 1)

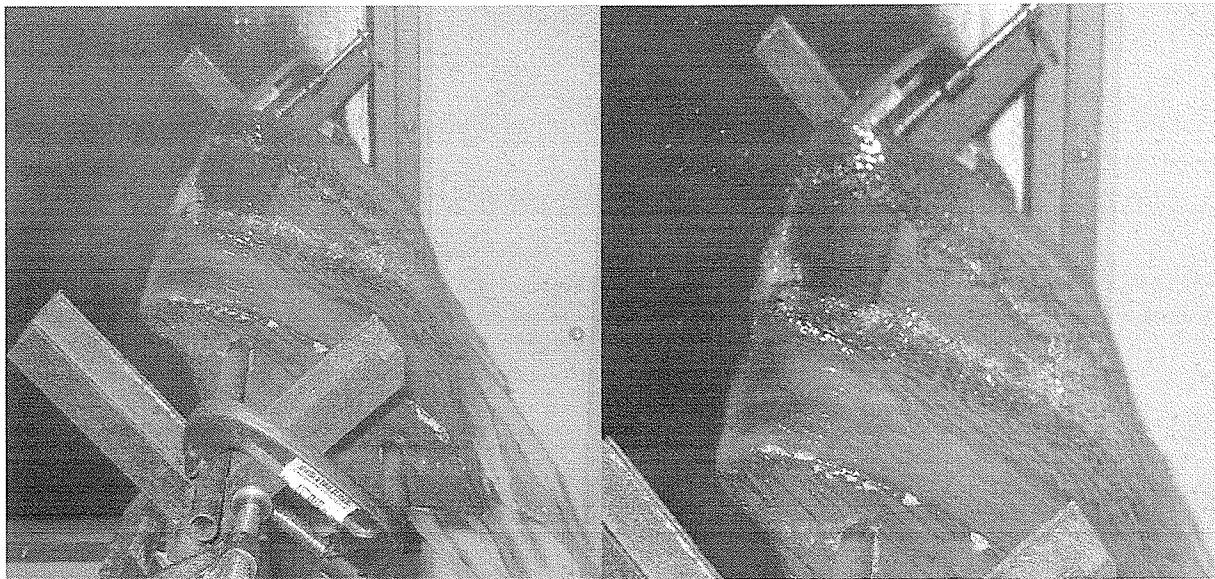


Figure 4. 4. 2: Glaze Ice Buildup on Helicopter Scoop (Case 2)

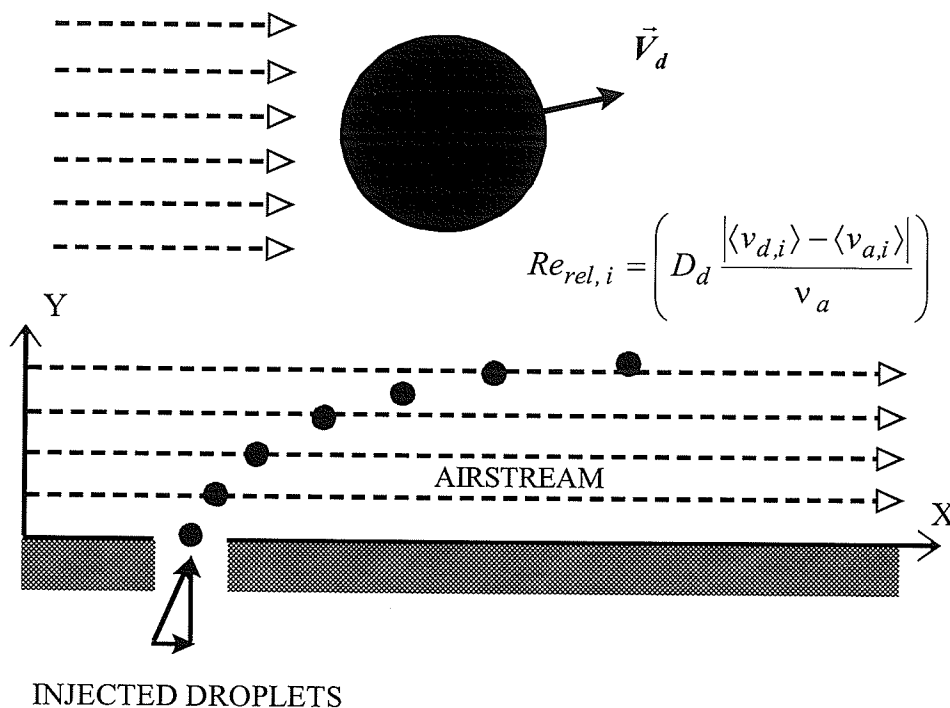


Figure 5. 1. 1: Schematic of the Injected Droplet Case

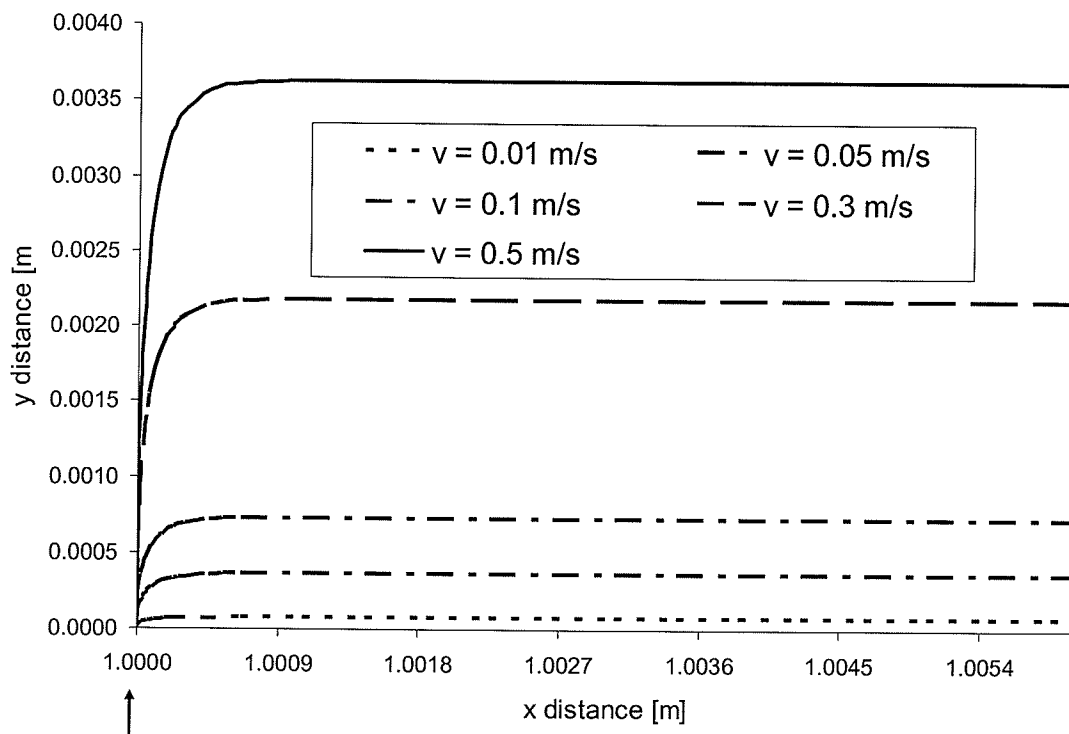


Figure 5. 1. 2: Droplet Trajectories through an Airstream [$\vec{v}_a = (0.02, 0)$] in the Low-Re Regime

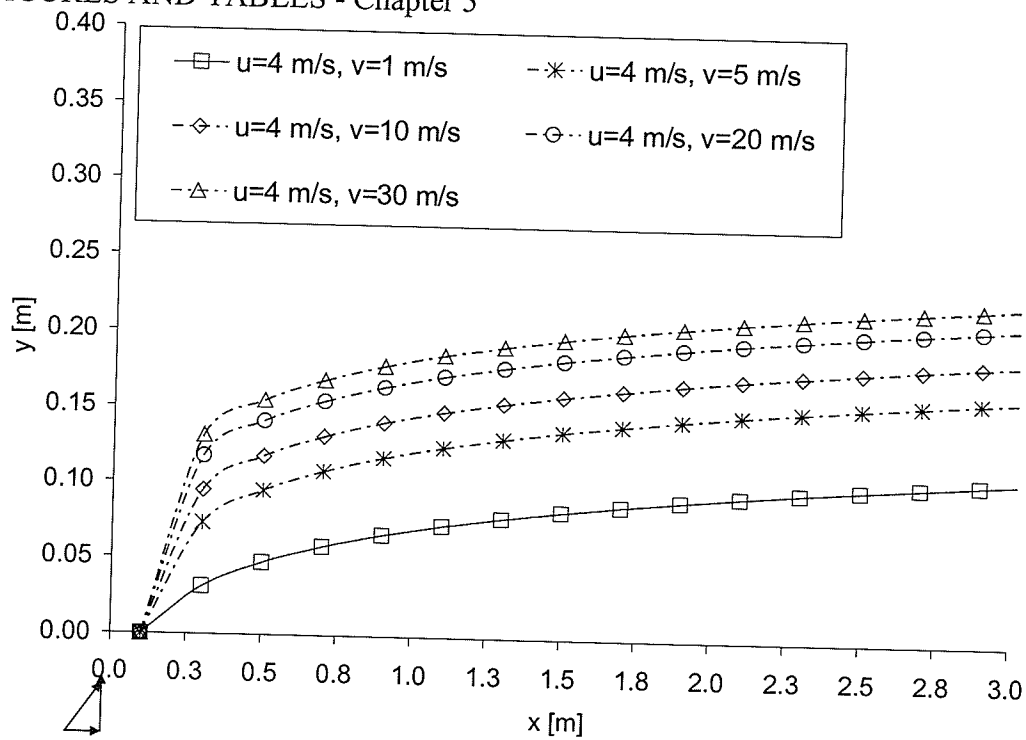


Figure 5. 1. 3: Effects of Varying Droplet Injection Velocity

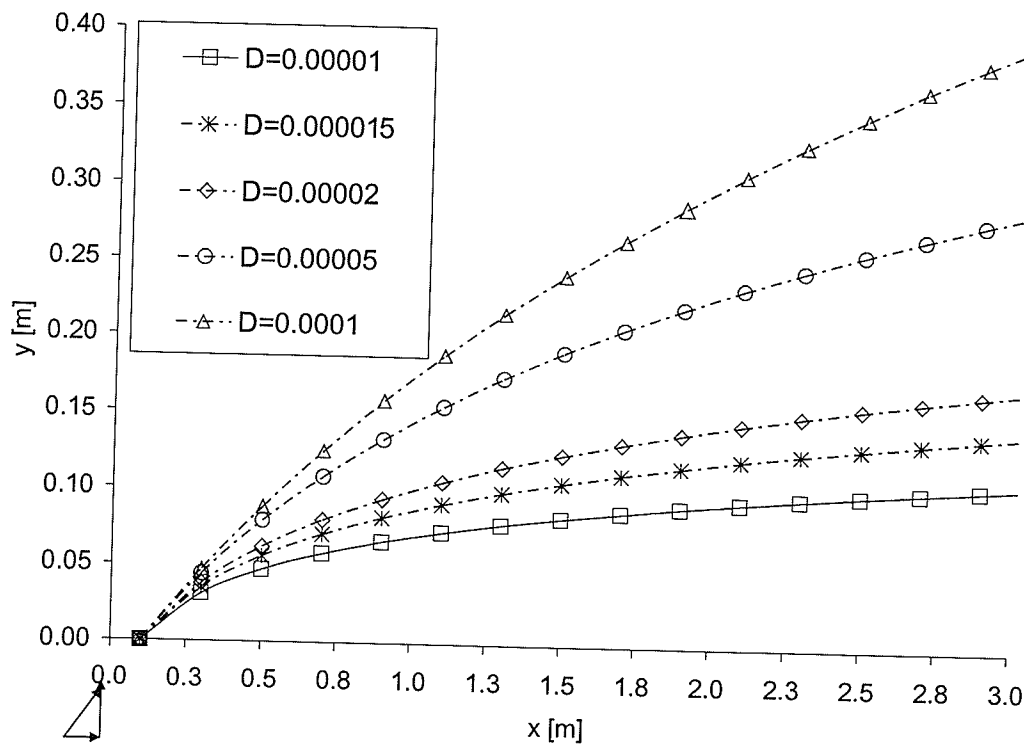


Figure 5. 1. 4: Effects of Varying Droplet Diameters D [m] on Droplet Trajectories

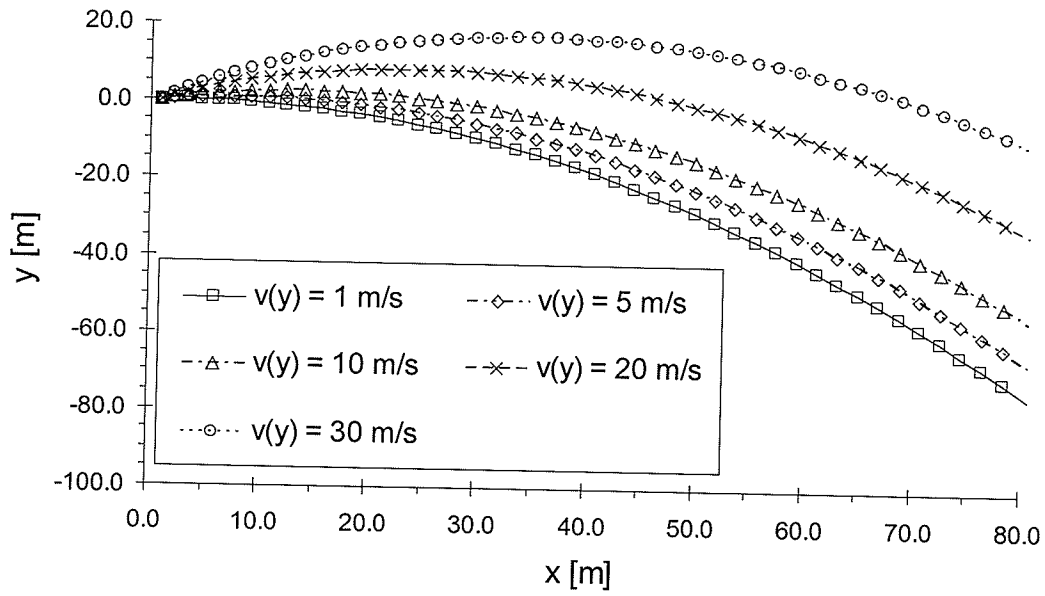


Figure 5. 1. 5: Gravitational Field Effects on Droplet Trajectories

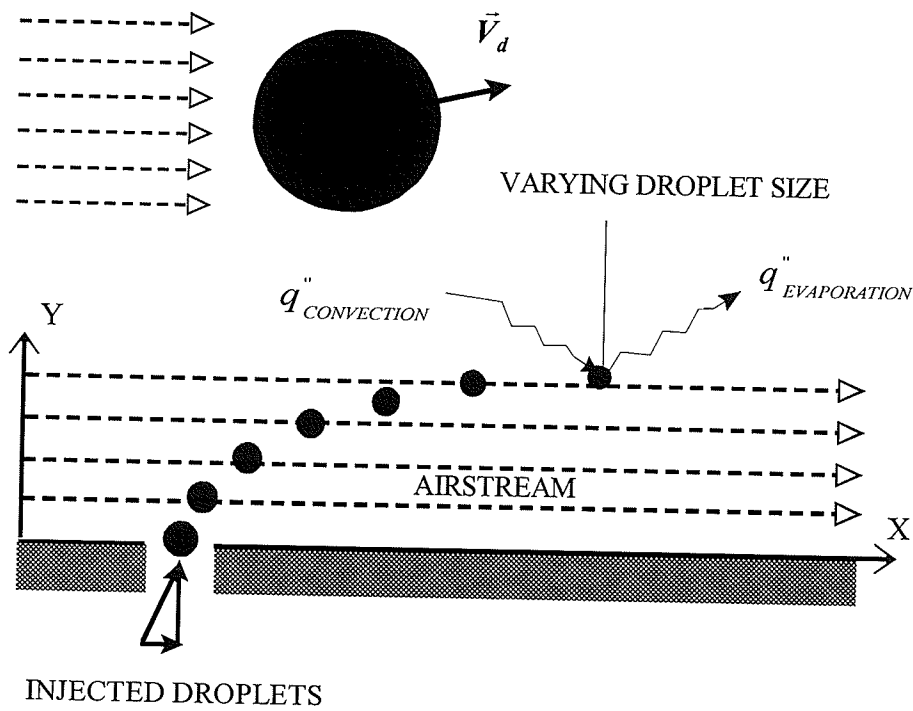


Figure 5. 1. 6: Schematic of Evaporating Droplet Problem

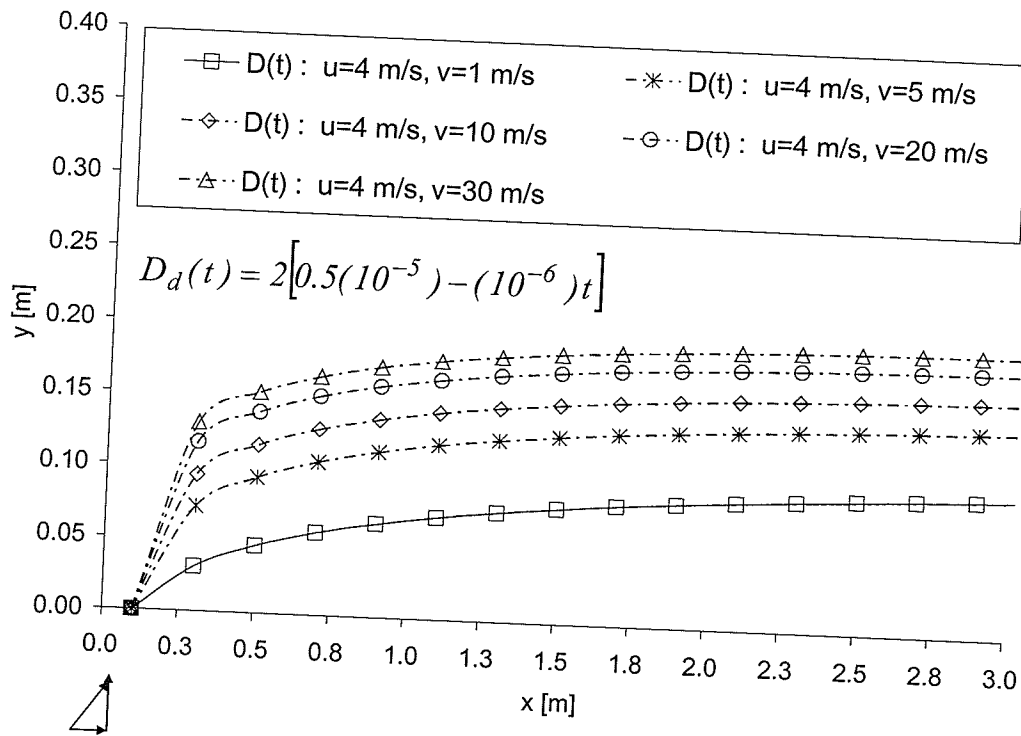


Figure 5. 1. 7: Droplet Trajectories with Time Dependent Droplet Diameter $D(t)$ due to Evaporation of the Droplet (High-Re Regime)

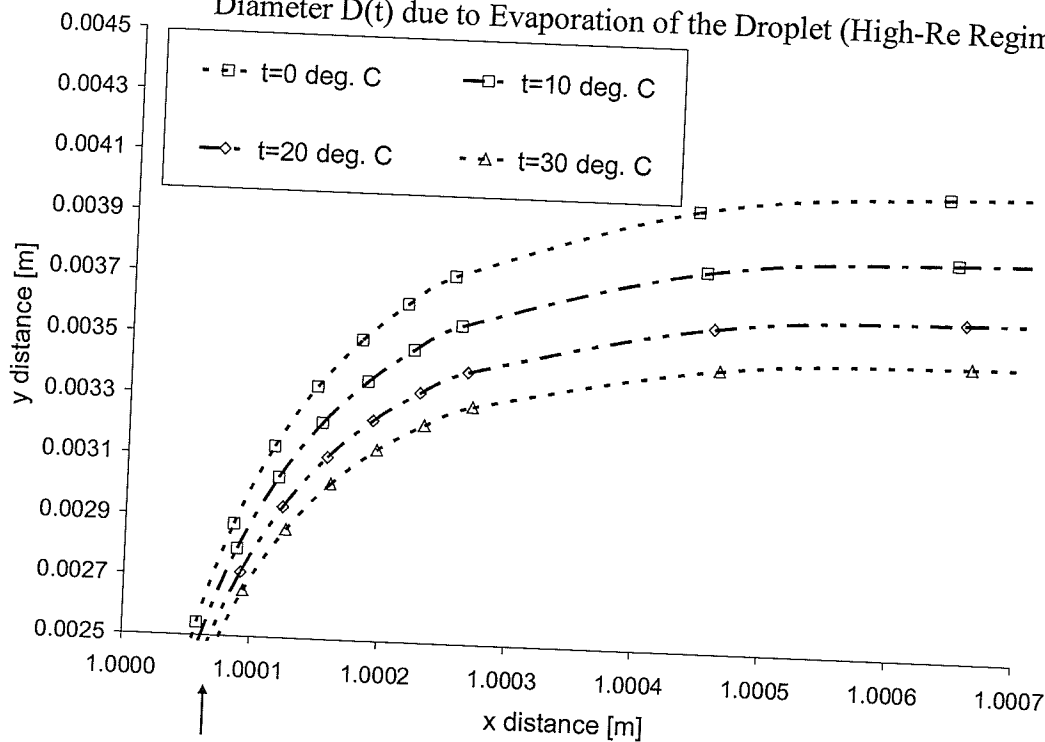


Figure 5. 1. 8: Droplet Trajectories with Temperature Dependent Thermophysical Properties and Droplet Diameter of $D = 5. 10^{-5} m$ (Low-Re Regime)

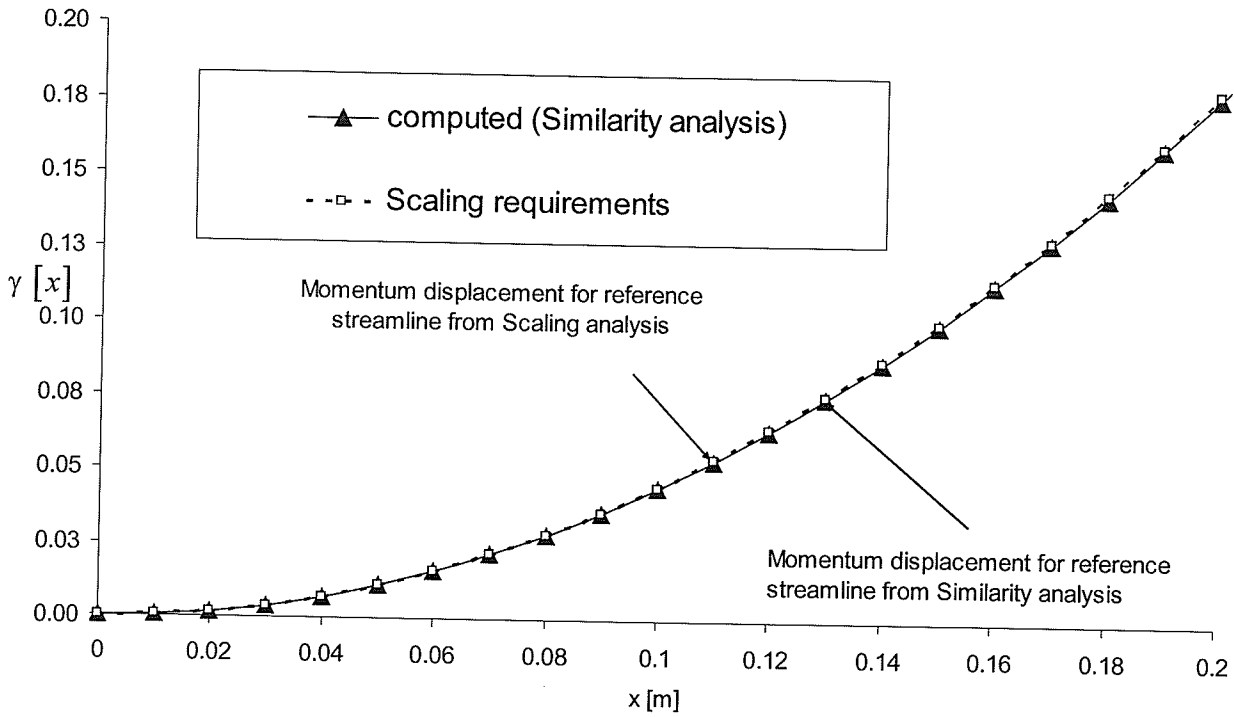


Figure 5. 2. 1: Scaling and Similarity Solution Momentum Deflection Comparison

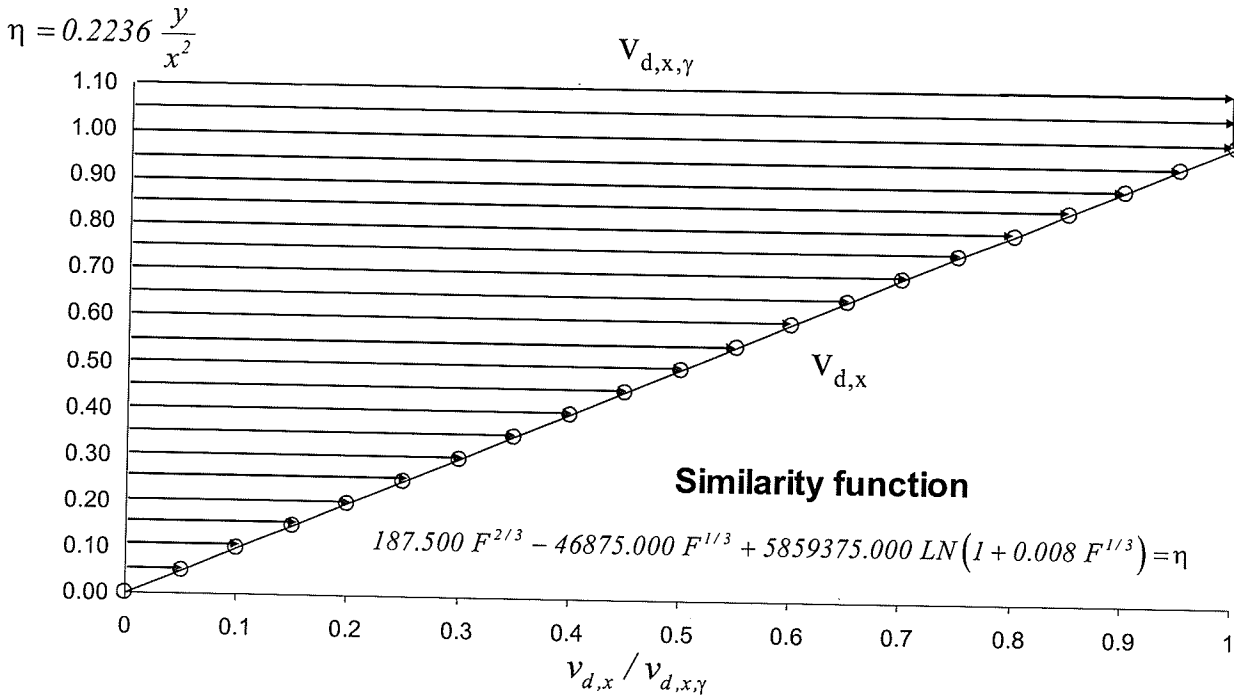


Figure 5. 2. 2: Similar Function - Solution F(h)

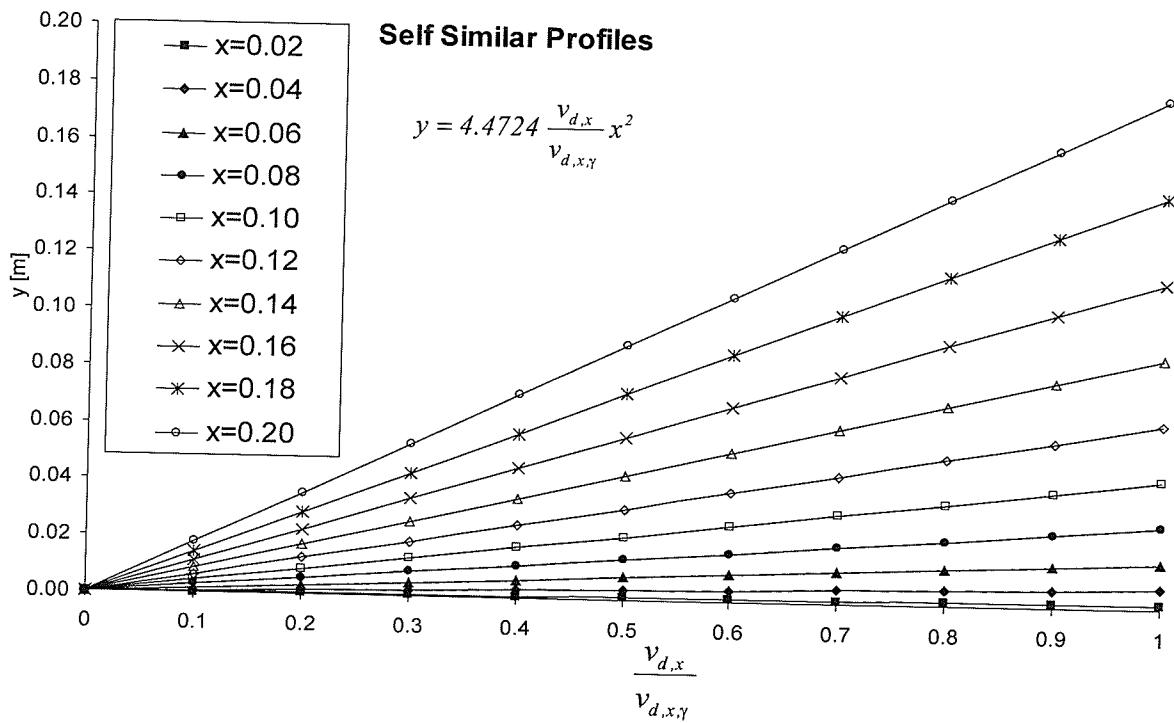


Figure 5. 2. 3: Droplet Trajectories at Different Ratios, $v_{d,x} / v_{d,x,\gamma}$ and Different x

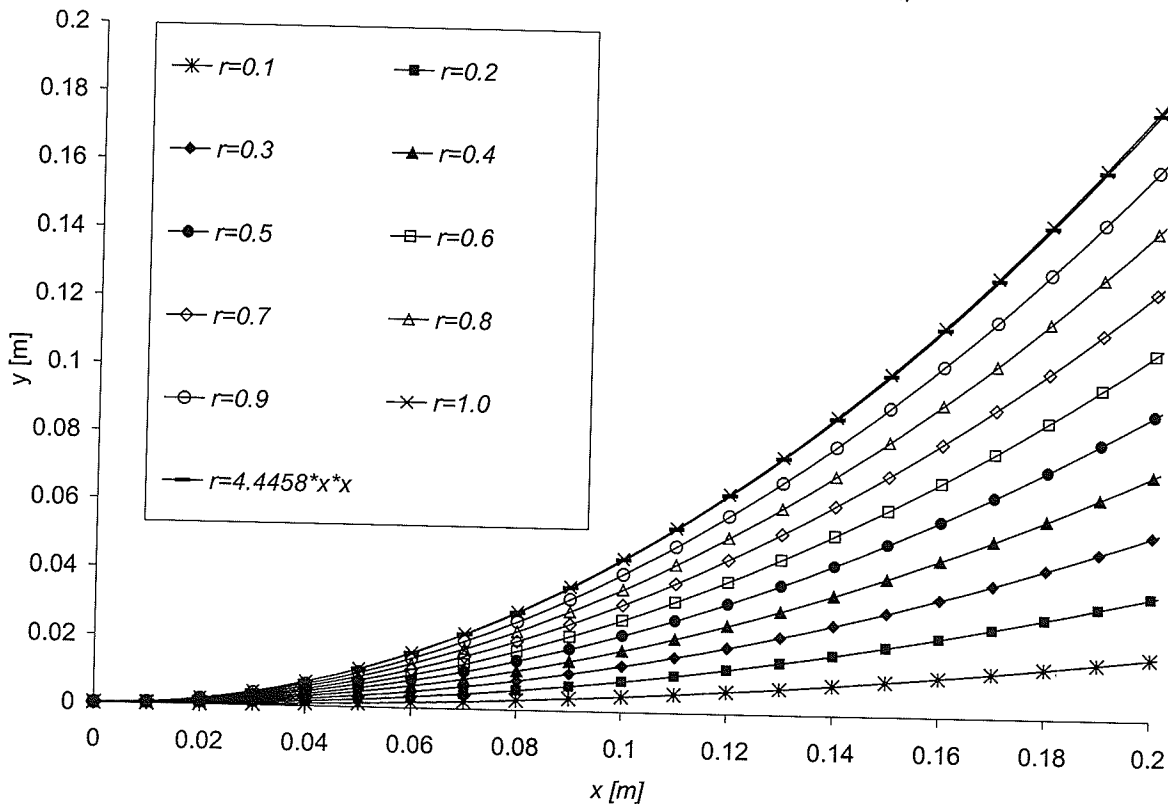


Figure 5. 2. 4: Droplet Trajectories at Different x Locations for Different Ratios of

$$r = v_{d,x} / v_{d,x,\gamma}$$

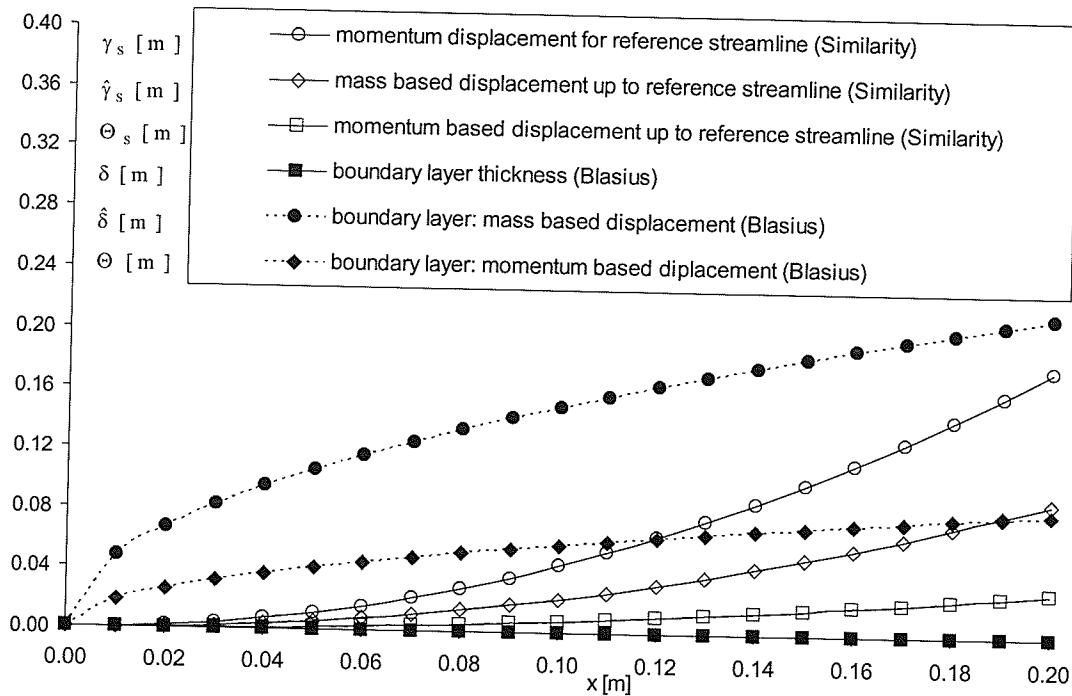


Figure 5. 2. 5: : Droplet Trajectories for Different Ratios, $r = v_{d,x} / v_{d,x,y}$, across the Physical Domain

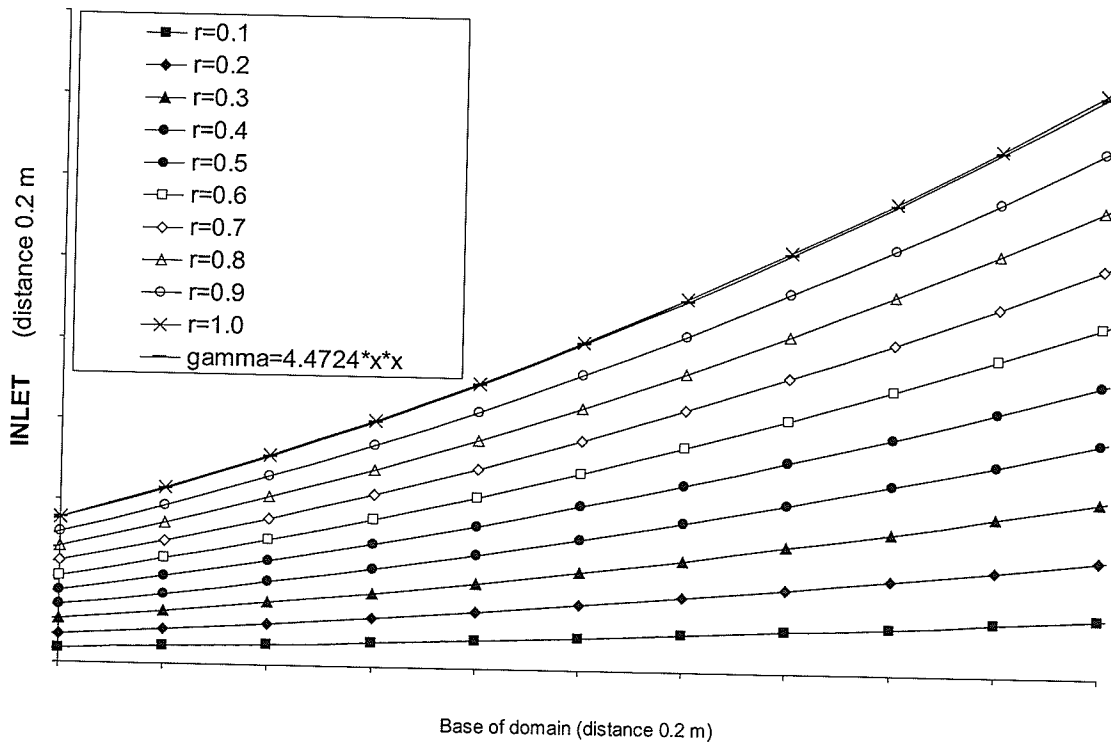


Figure 5. 2. 6: Droplet Deflections Based on Similarity Solution

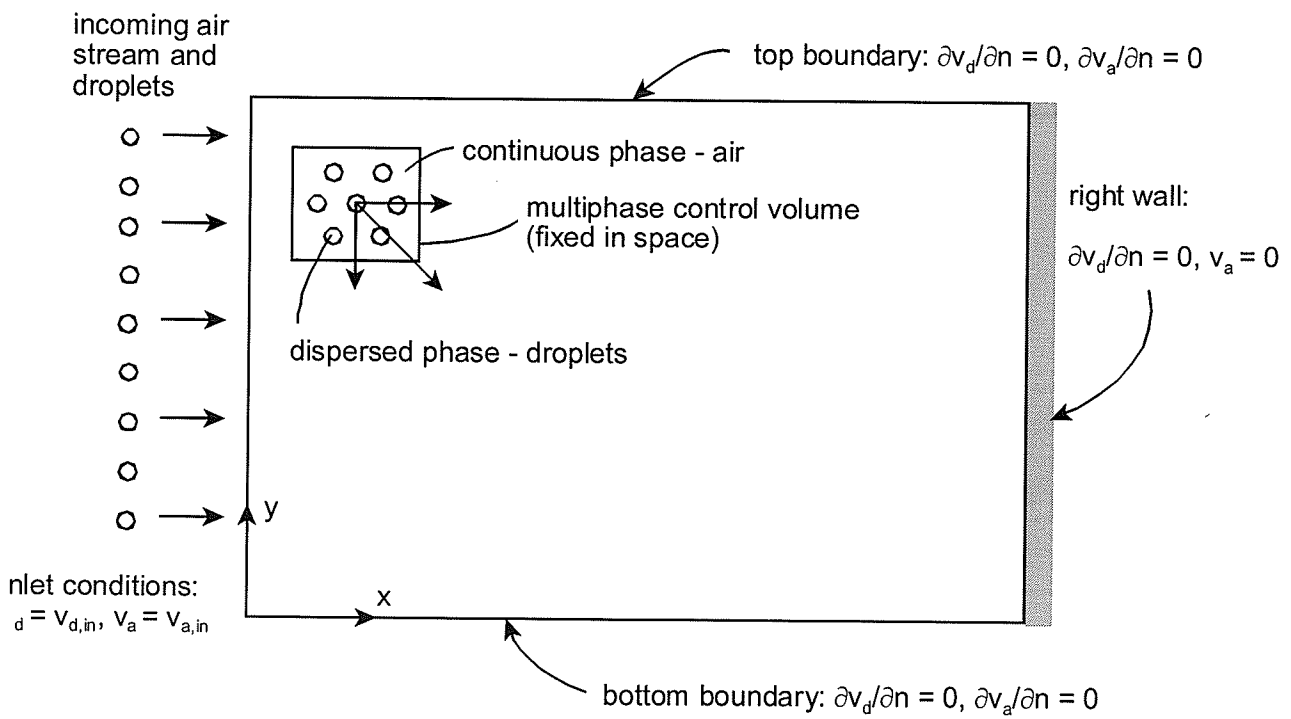


Figure 5. 3. 1: Problem Schematic (Case 1)

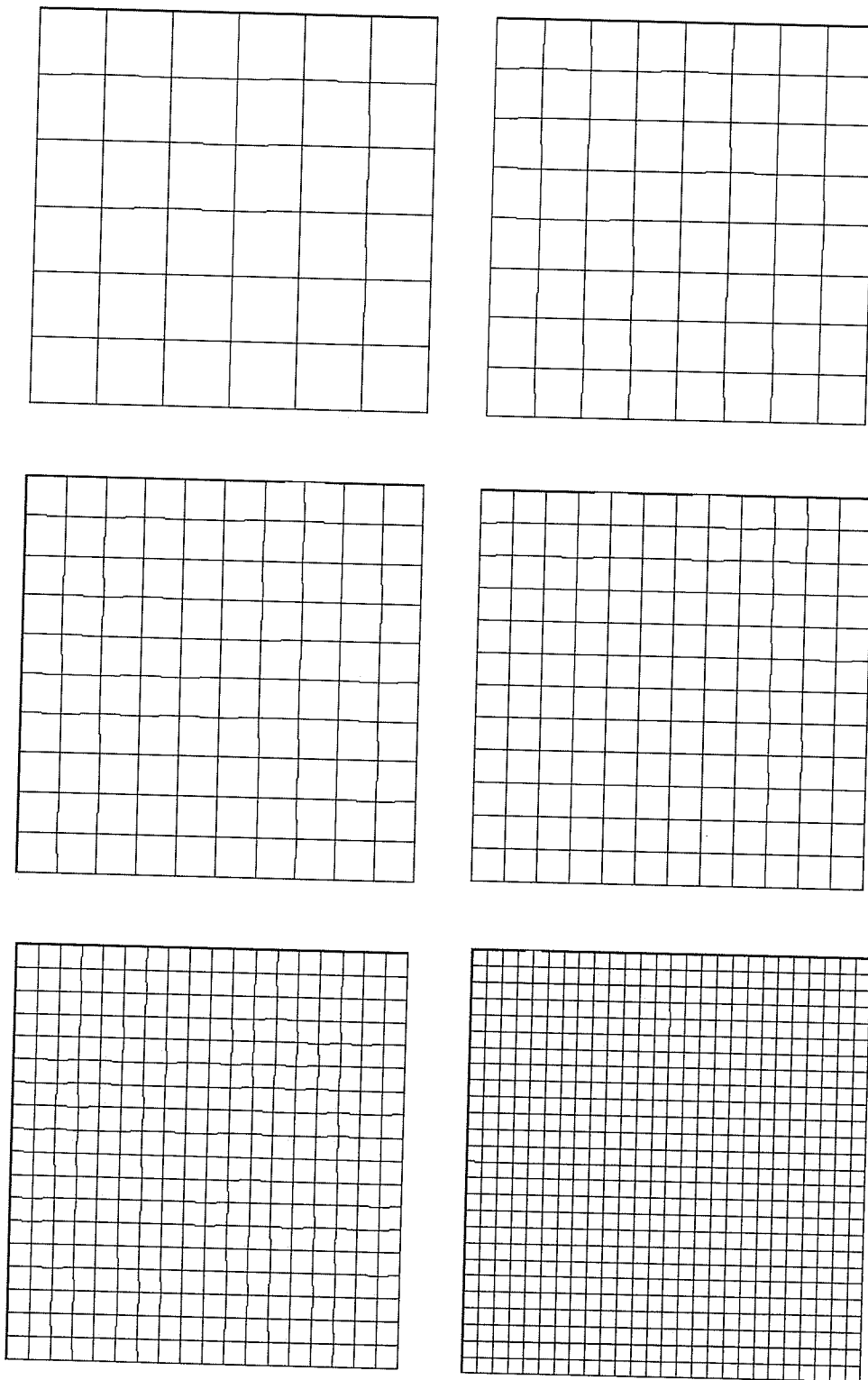


Figure 5. 3. 2: Control Volume Grids: 6×6 , 8×8 , 10×10 , 12×12 , 18×18 and 26×26 (Case1)

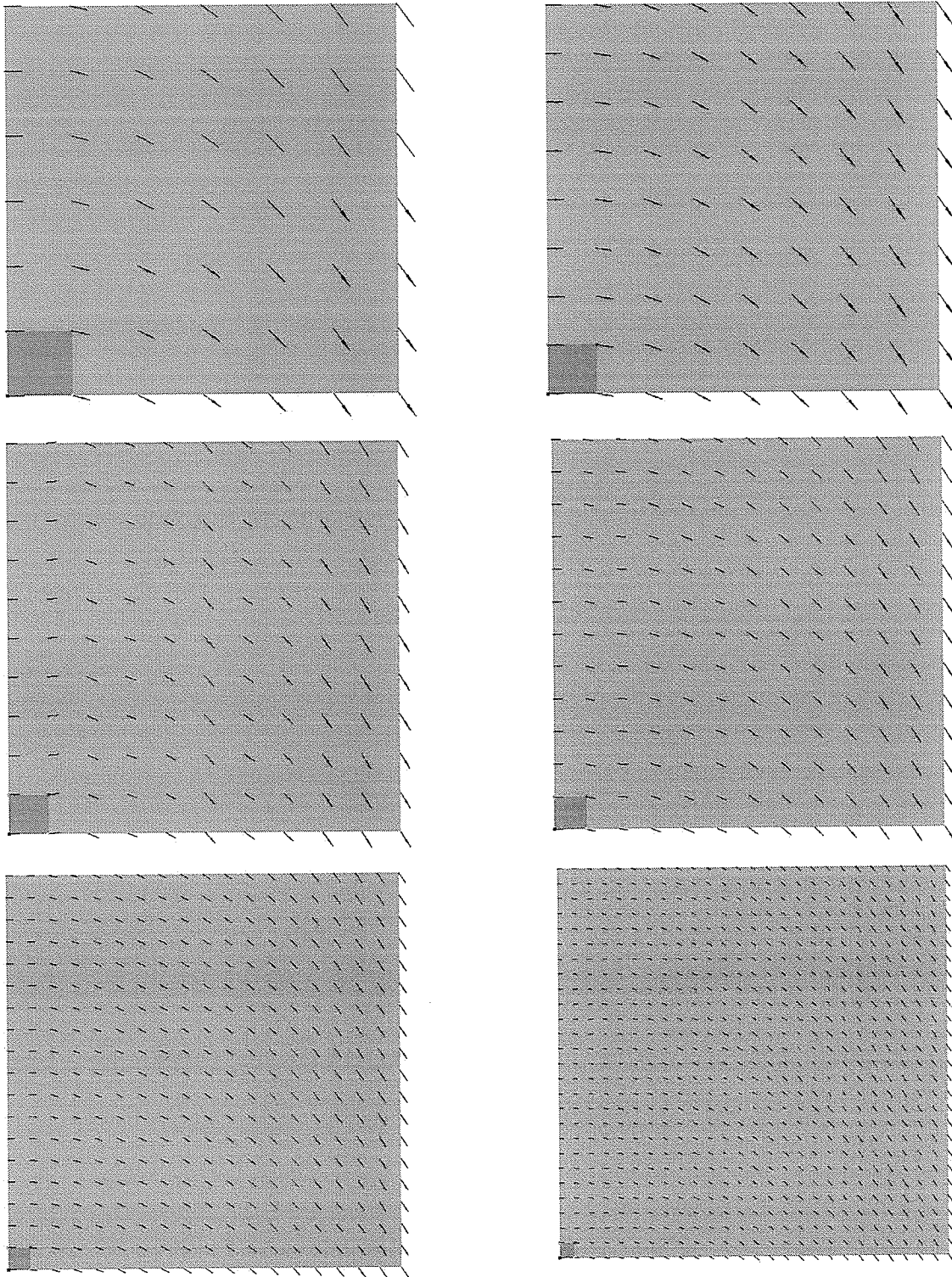


Figure 5. 3. 3: Droplet Velocity Fields for $u_{d,IN} = 2.5 m/s$ and Grids: 6×6 , 8×8 , 10×10 , 12×12 , 18×18 , 26×26 (Case 1)

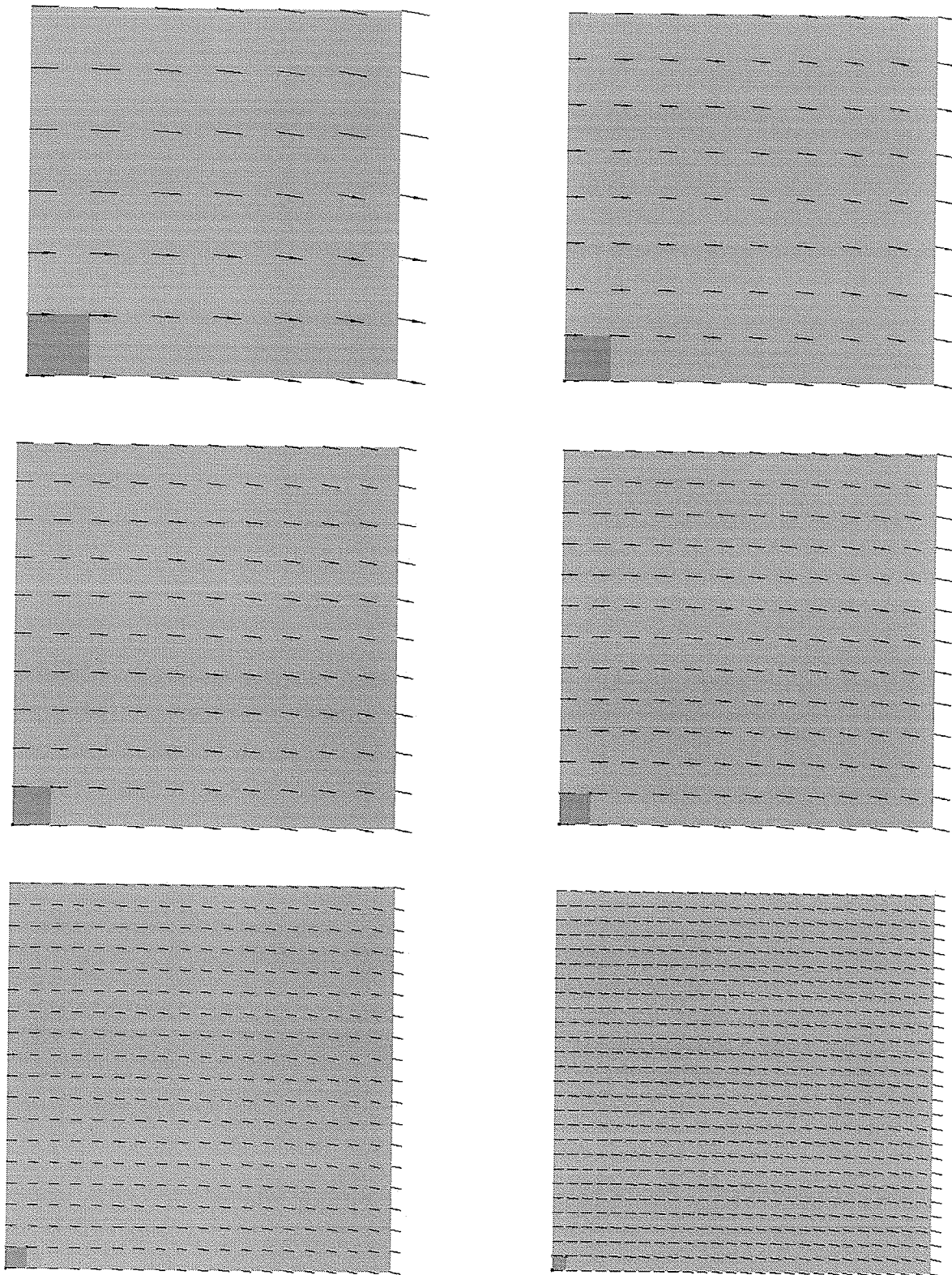


Figure 5. 3. 4: Droplet Velocity Fields for $u_{d,IN} = 7 m/s$ and Grids: 6×6 , 8×8 , 10×10 , 12×12 , 18×18 , 26×26 (Case 2)

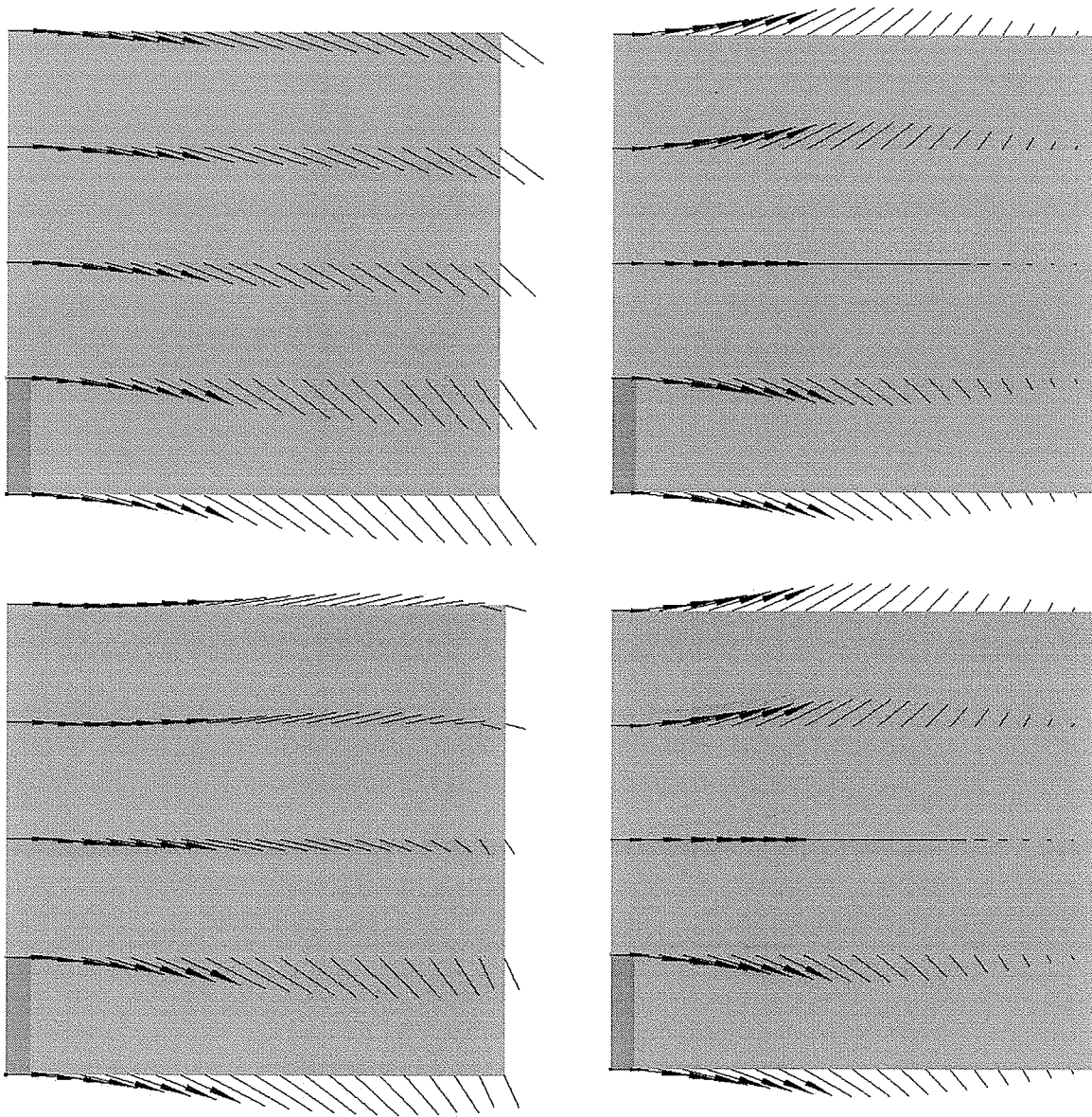


Figure 5. 3. 5: A Relative Comparison of the Droplet Velocity Fields (Left) Influenced by the Air Field (Right) for a Scaled (Reduced) Interfacial Drag of 0.001 (Up) and 0.005 (Down)

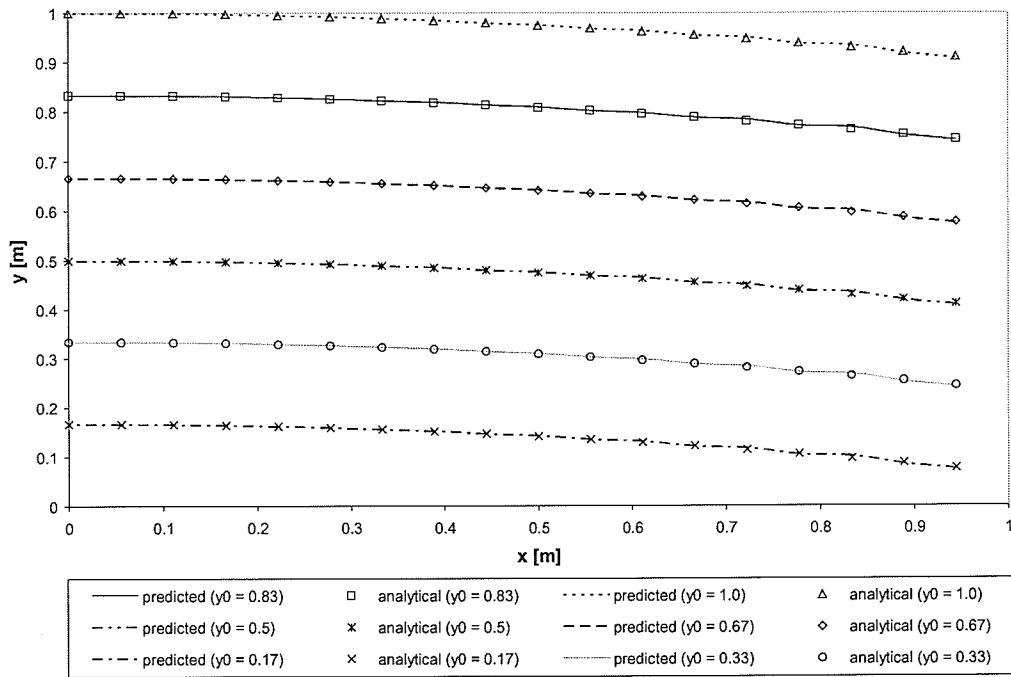


Figure 5.3.6: Droplet Trajectories (12×12 mesh; Case 1)

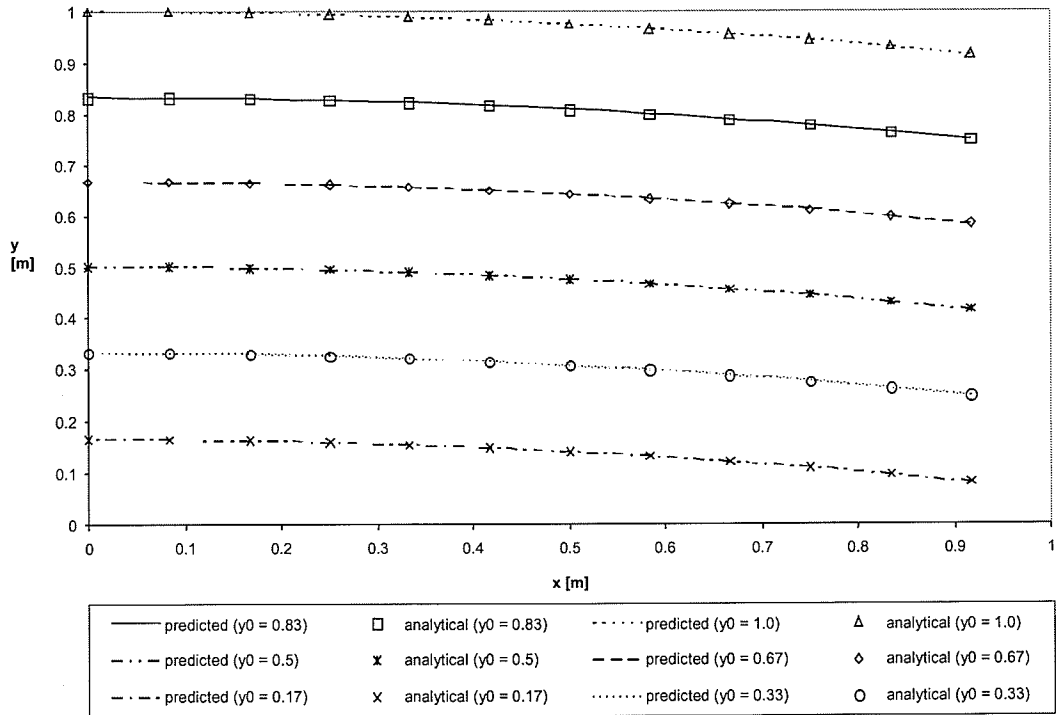


Figure 5.3.7: Droplet Trajectories (18×18 mesh; Case 1)

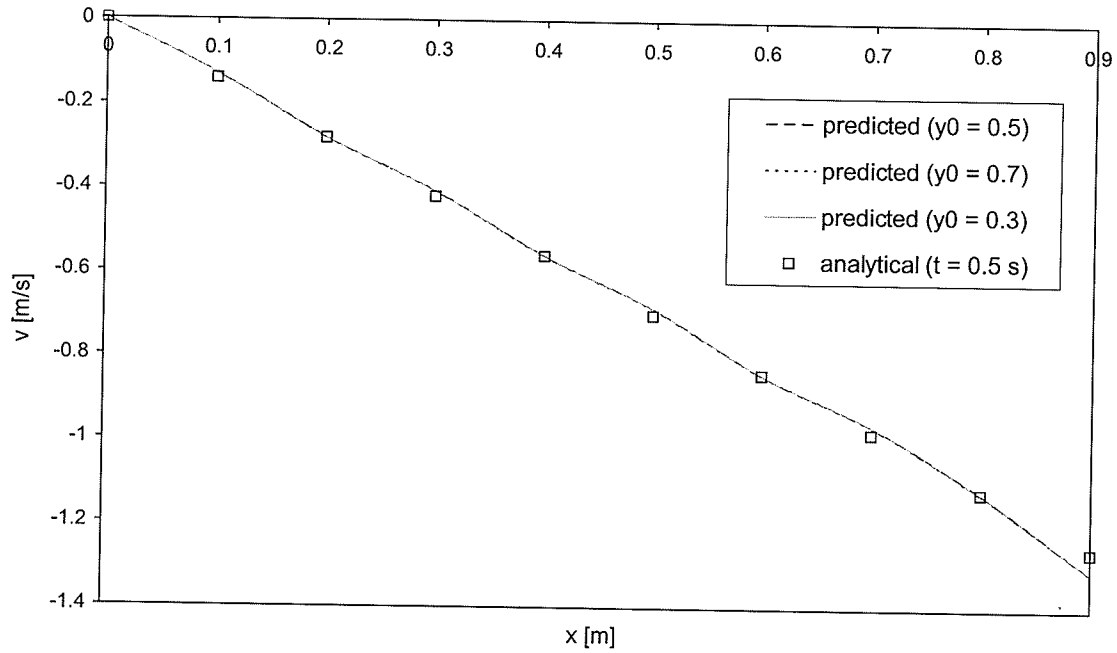


Figure 5. 3. 8: Magnitude of Droplet Velocities ($t = 0.5$ s; Case 1)

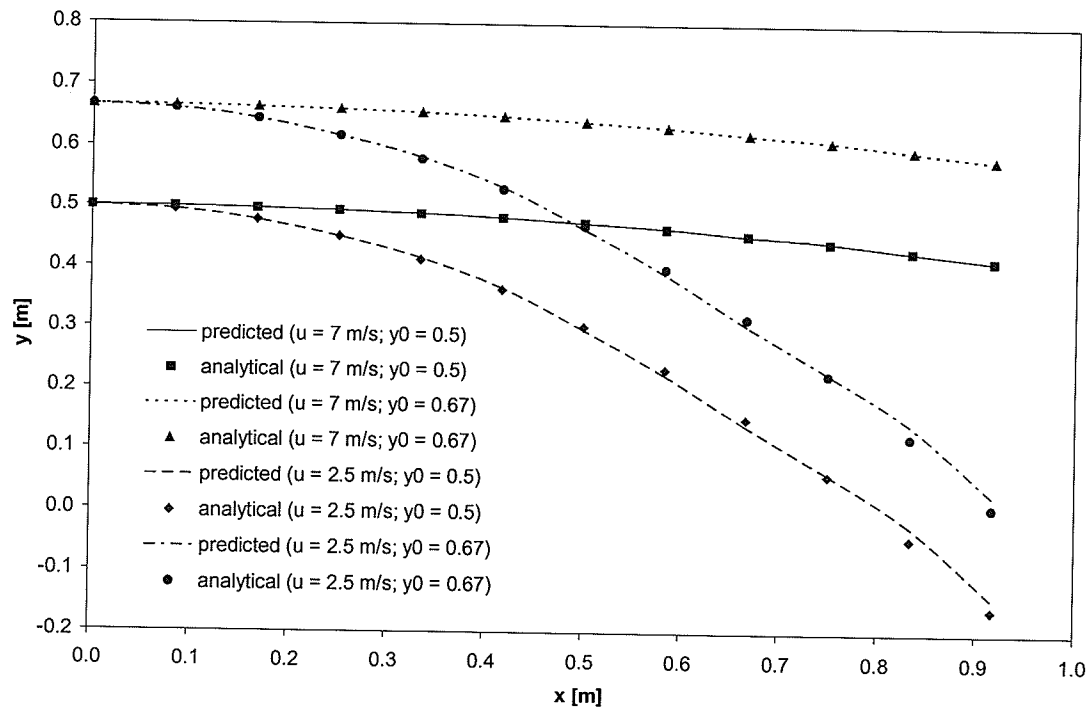


Figure 5. 3. 9: Droplet Trajectories (12×12 mesh; Case 1)

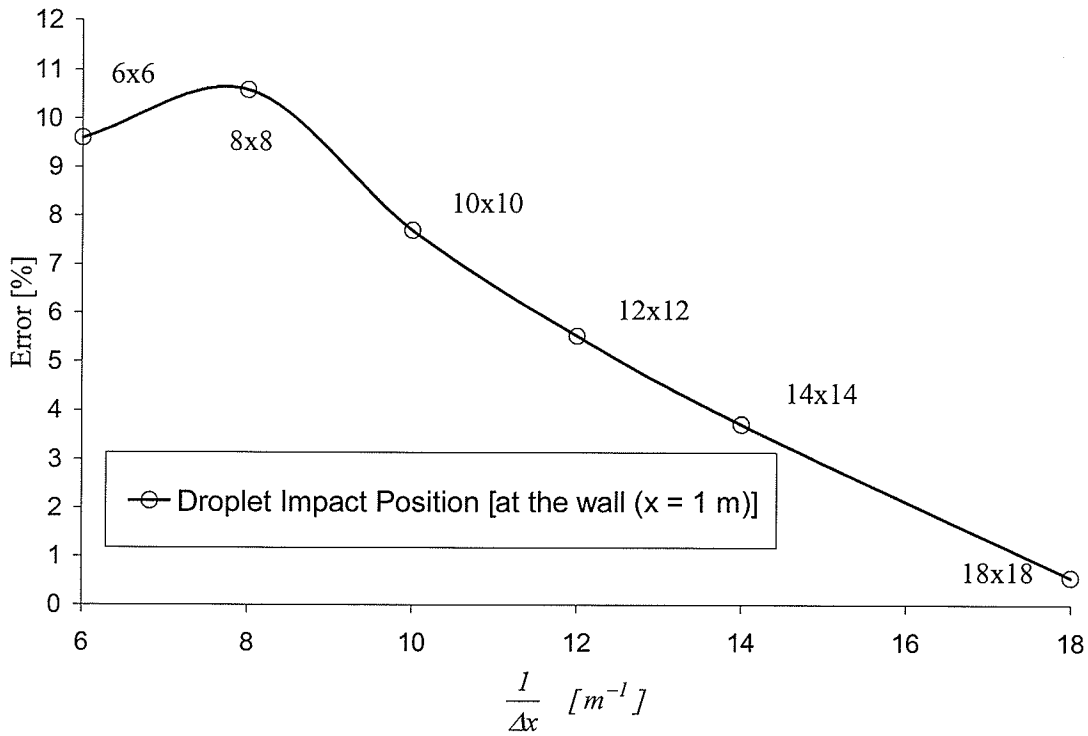


Figure 5. 3. 10: Grid Refinement Study (Case 1)

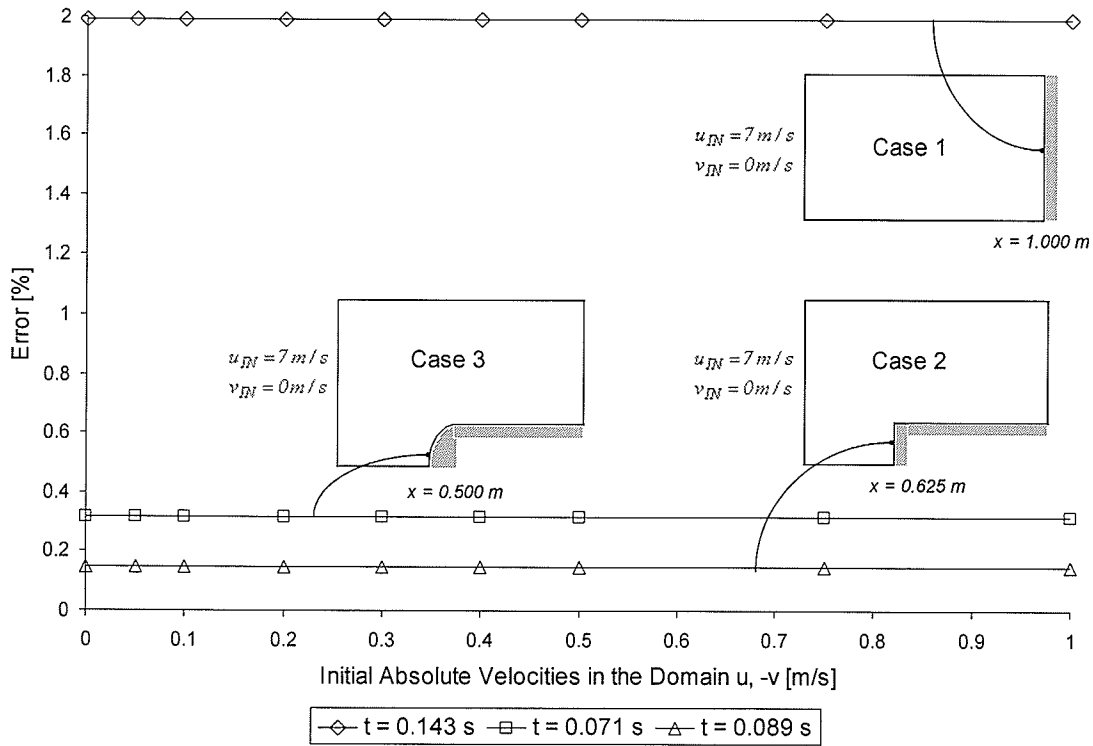


Figure 5. 3. 11: Initial Condition Independence Study (Case 1, Case 2 and Case 3)

Δt [s]	$\text{Ln} (1 / \Delta t)$ (Δt [s])	$\text{Ln} [u_d - \text{Error}]$ ($u_d - \text{Error} [\%]$)	$\text{Ln} [v_d - \text{Error}]$ ($v_d - \text{Error} [\%]$)
0.500000	0.693147	-0.861093	1.296643
0.300000	1.203973	-0.860383	1.296479
0.100000	2.302585	-0.858494	1.296370
0.050000	2.995732	-0.860856	1.296370
0.010000	4.605170	-0.858494	1.296370
0.005000	5.298317	-0.858494	1.296370

Table 5. 3. 1: Logarithms of Errors of x - and y -Velocity Distributions for Multiphase Flow with Droplets, Respectively, as Functions of the Time Step Size, Δt

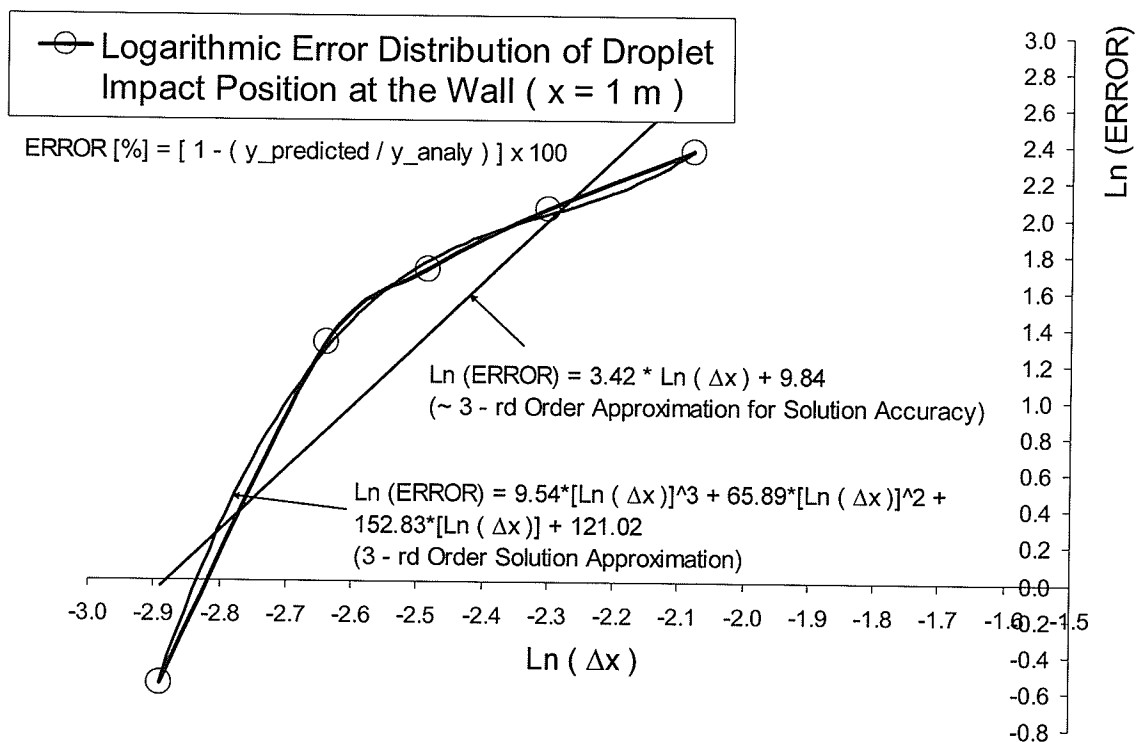


Figure 5. 3. 12: Numerical Error Distribution of Droplet Position as a Function of Grid Spacing, $\text{Ln}(\Delta x)$

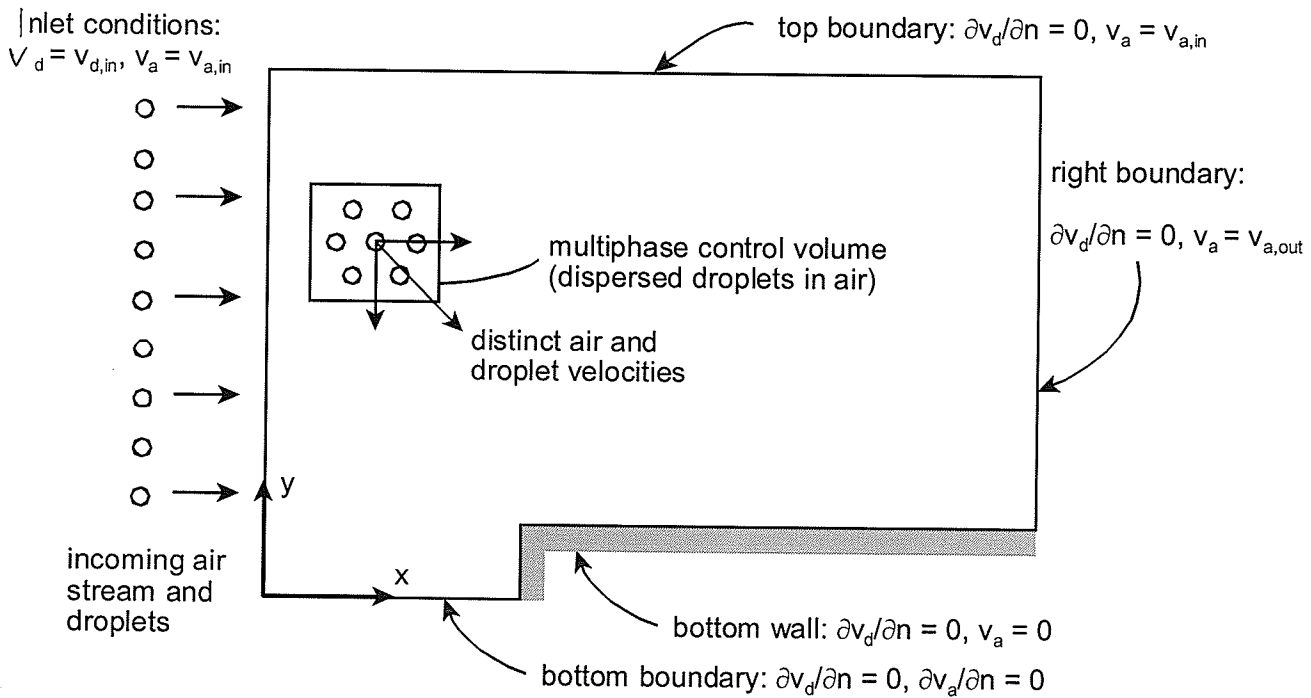


Figure 5. 3. 13: Problem Schematic (Case 2)

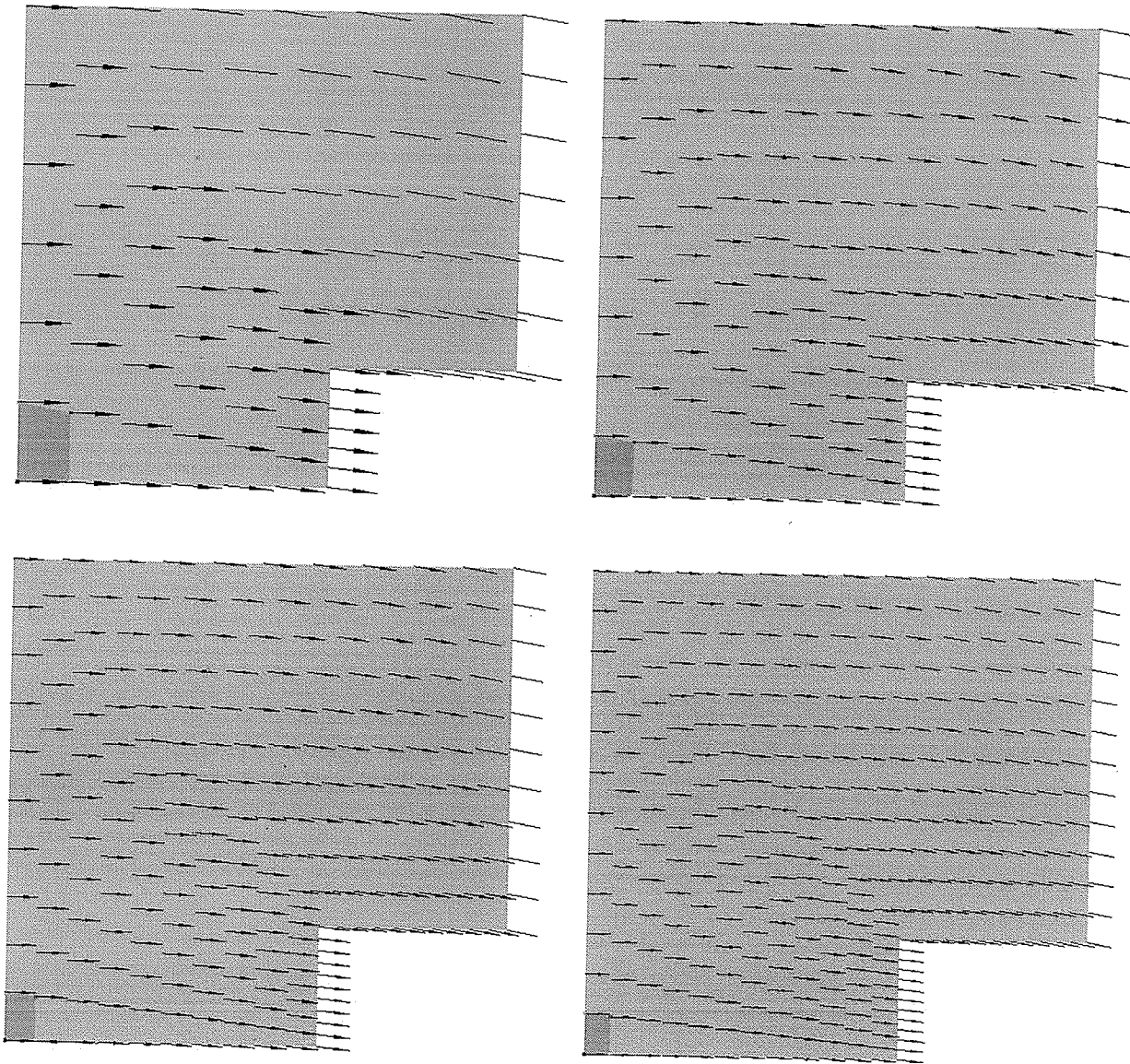


Figure 5. 3. 14: Droplet Velocity Fields for $u_{d,IN} = 7 m/s$ and Grids 12×12 , 16×16 , 20×20 and 24×24 (Case 2)

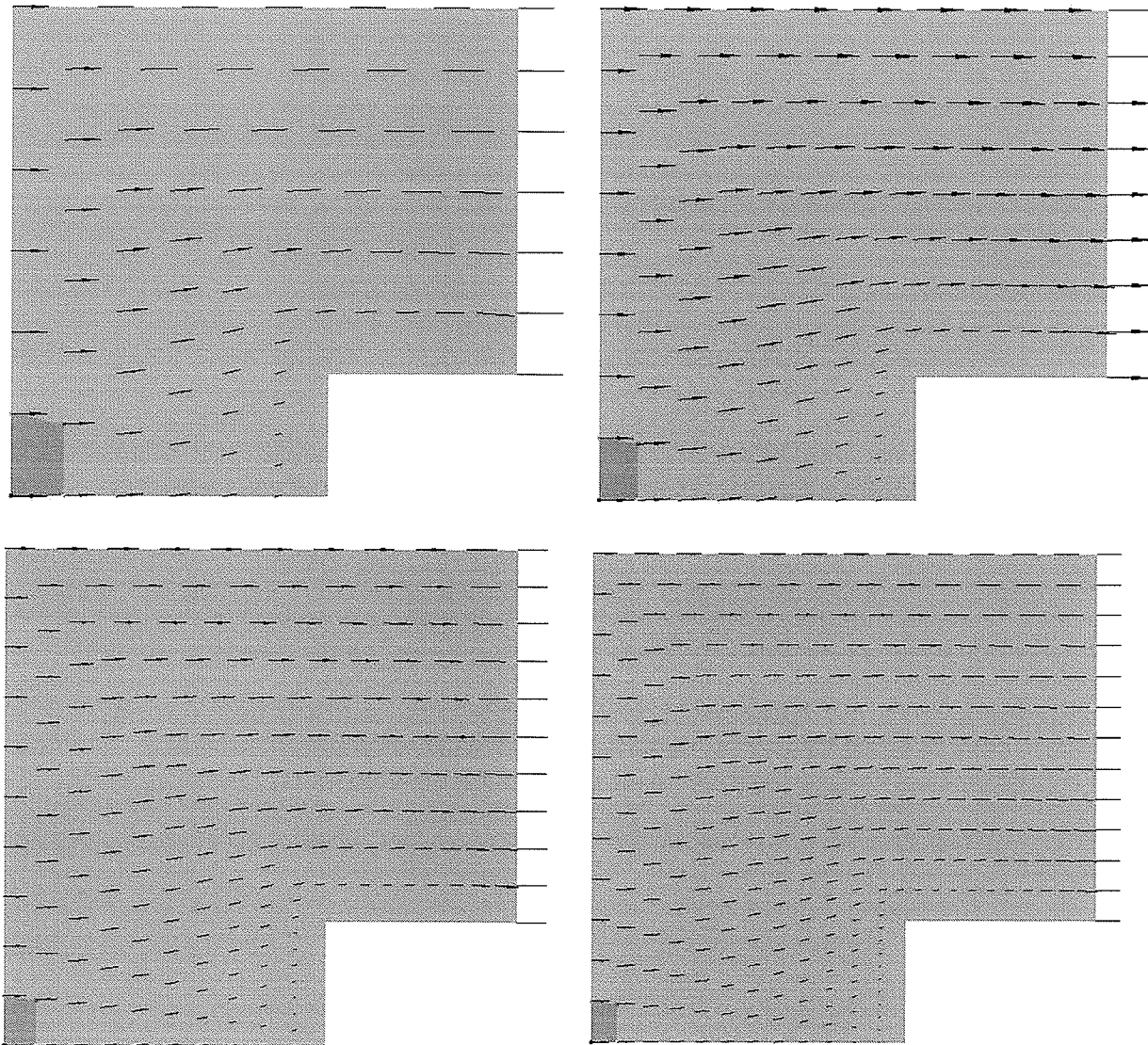


Figure 5. 3. 15: Air Velocity Fields for $u_{d,IN} = 7\text{ m/s}$ and Grids 12×12 , 16×16 , 20×20 and 24×24 (Case 2)

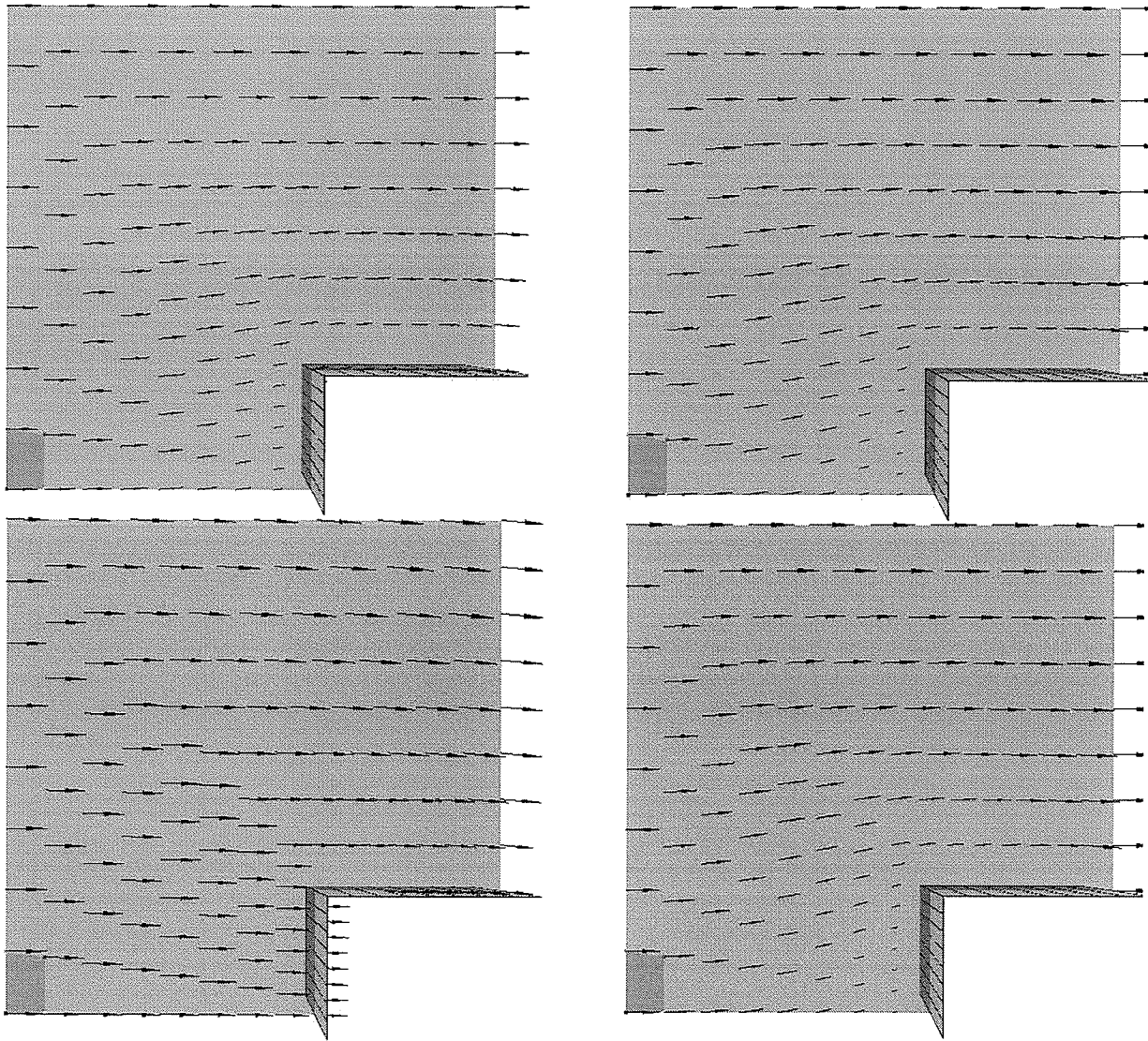


Figure 5. 3. 16: Droplet Velocity Fields (Left) Influenced by the Air Field
(Right) for Interfacial Drag with $D_d = 0.00008 m$ (Up) and
 $D_d = 0.00030 m$ (Down) - (Case 2)

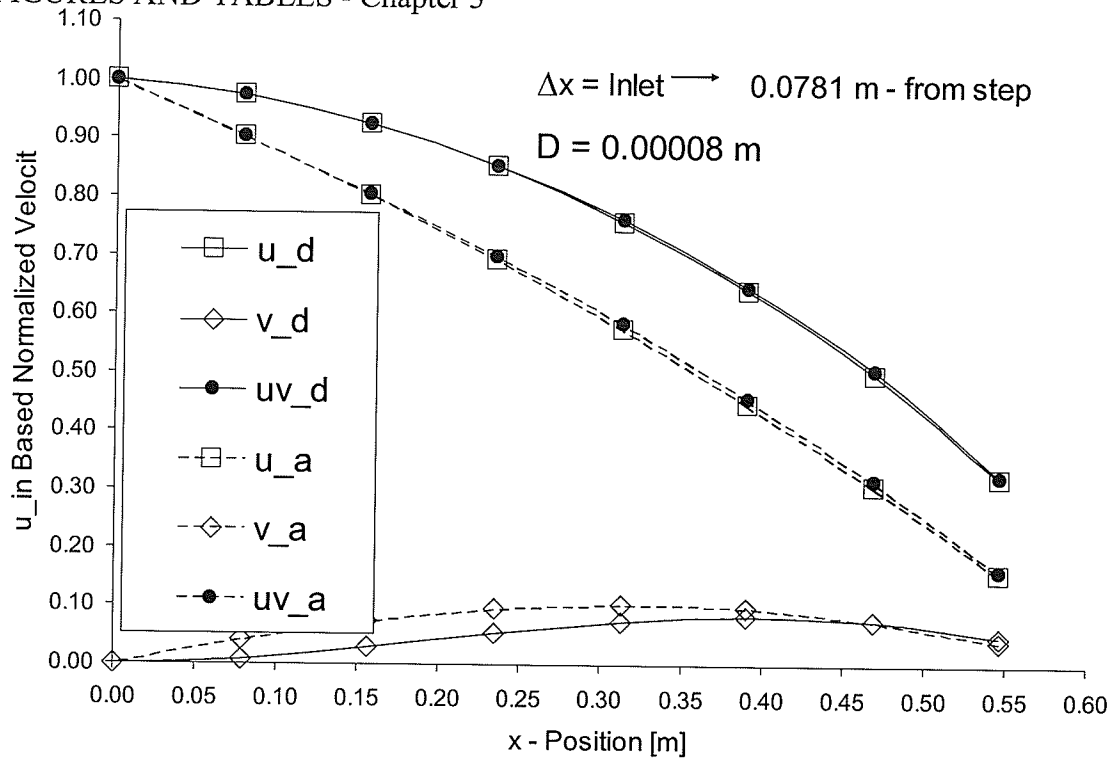


Figure 5. 3. 17: Predicted Droplet and Air Velocities based on Interfacial Drag with Droplet Diameter D (Case 2)

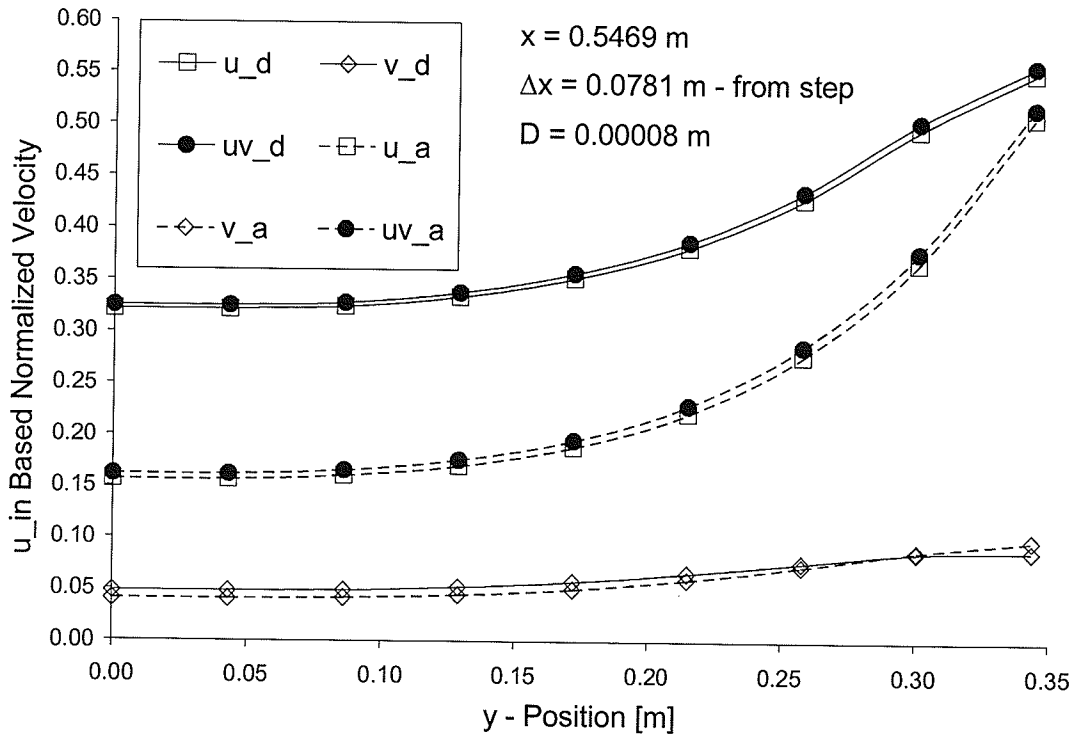


Figure 5. 3. 18: Predicted Droplet and Air Velocities based on Interfacial Drag with Droplet Diameter D (Case 2)

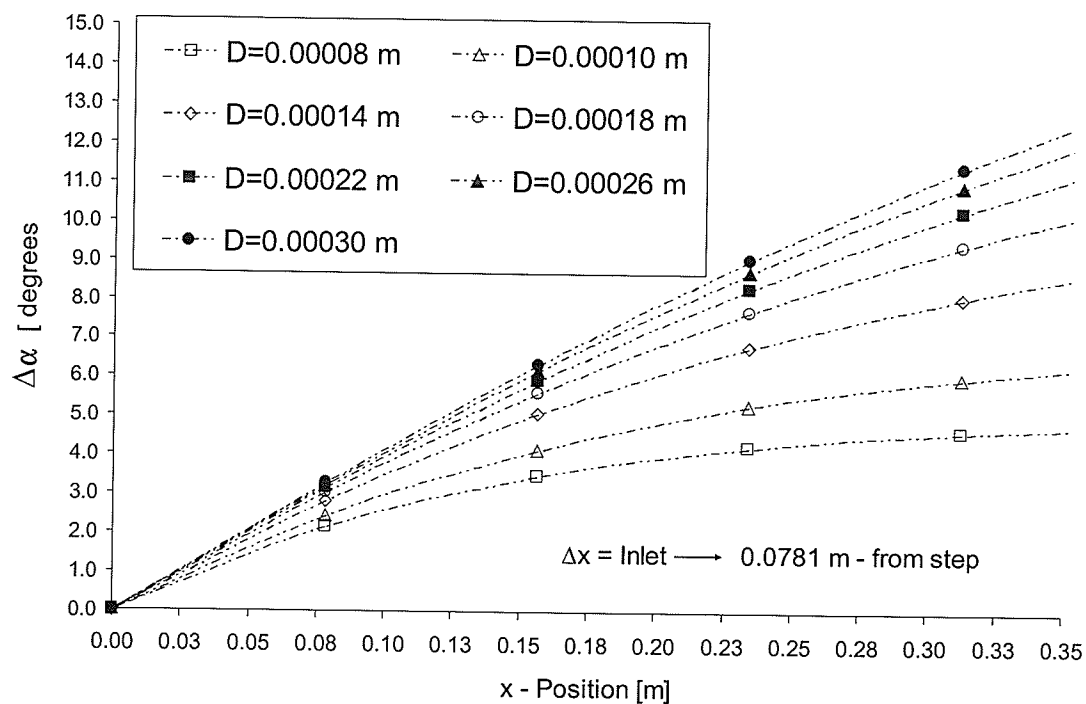


Figure 5.3.19: Effects of Droplet Diameter on the Angle Difference Between the Inlet and Step of the Domain (Case 2)

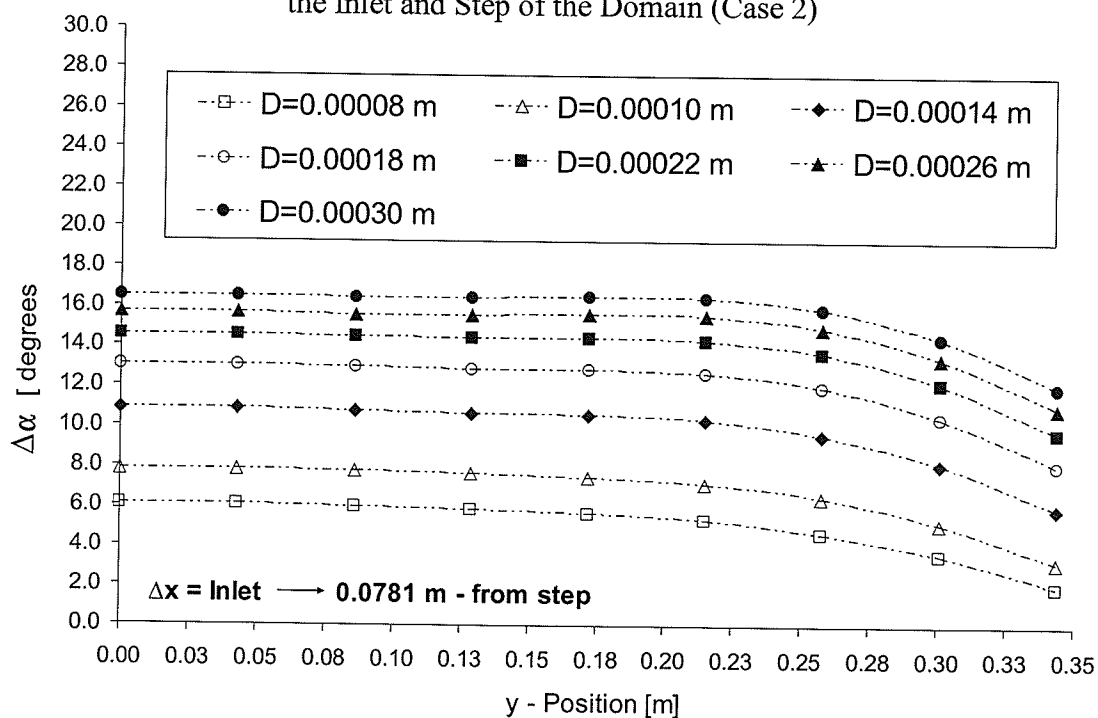


Figure 5.3.20: Effects of Droplet Diameter on the Angle Difference in the Vertical Position Along the Step of the Domain (Case 2)

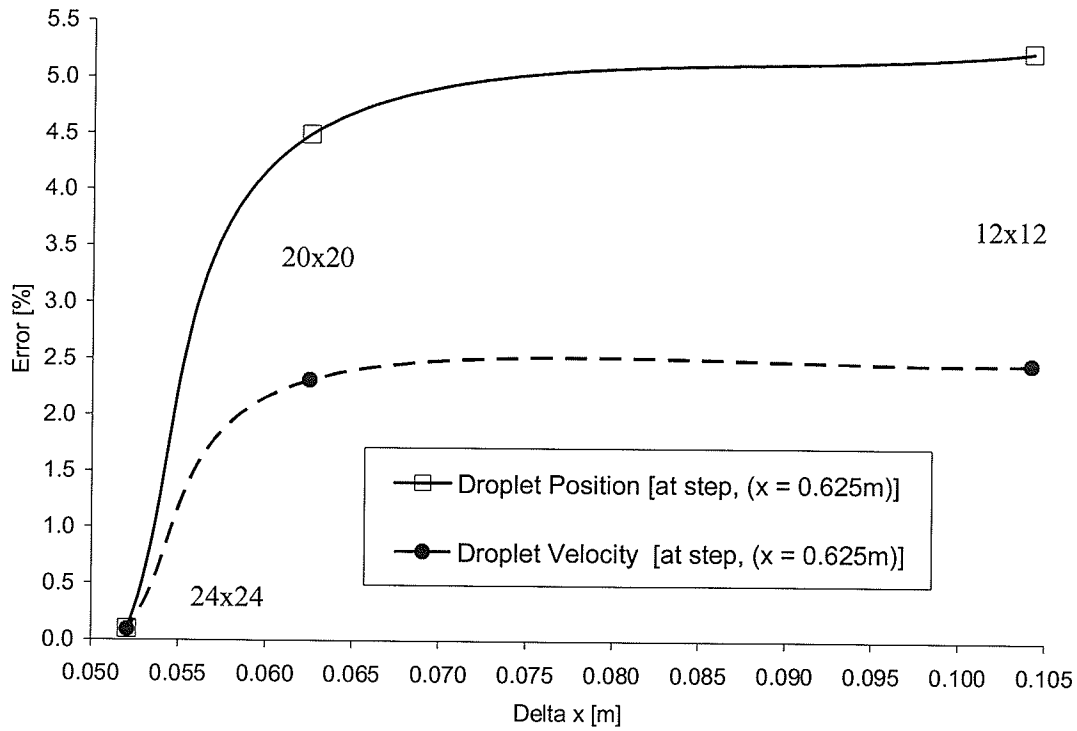


Figure 5.3.21: Grid Refinement Study (Case 2)

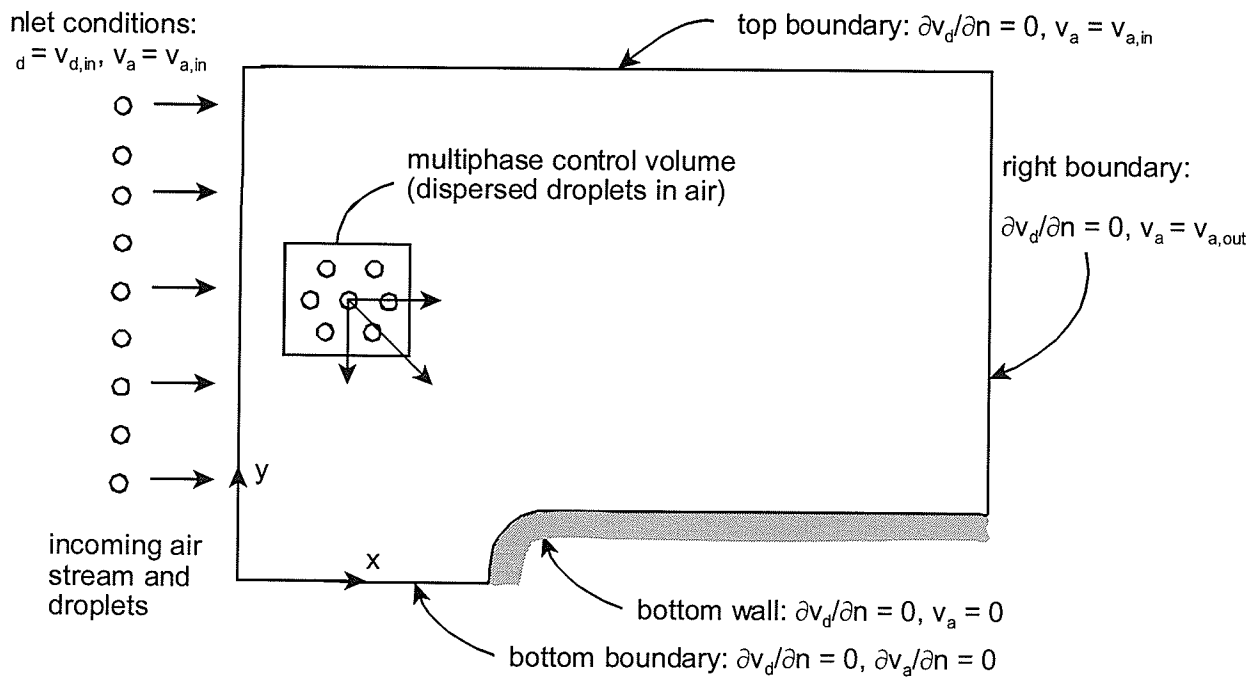


Figure 5.3.22: Problem Schematic (Case 3)

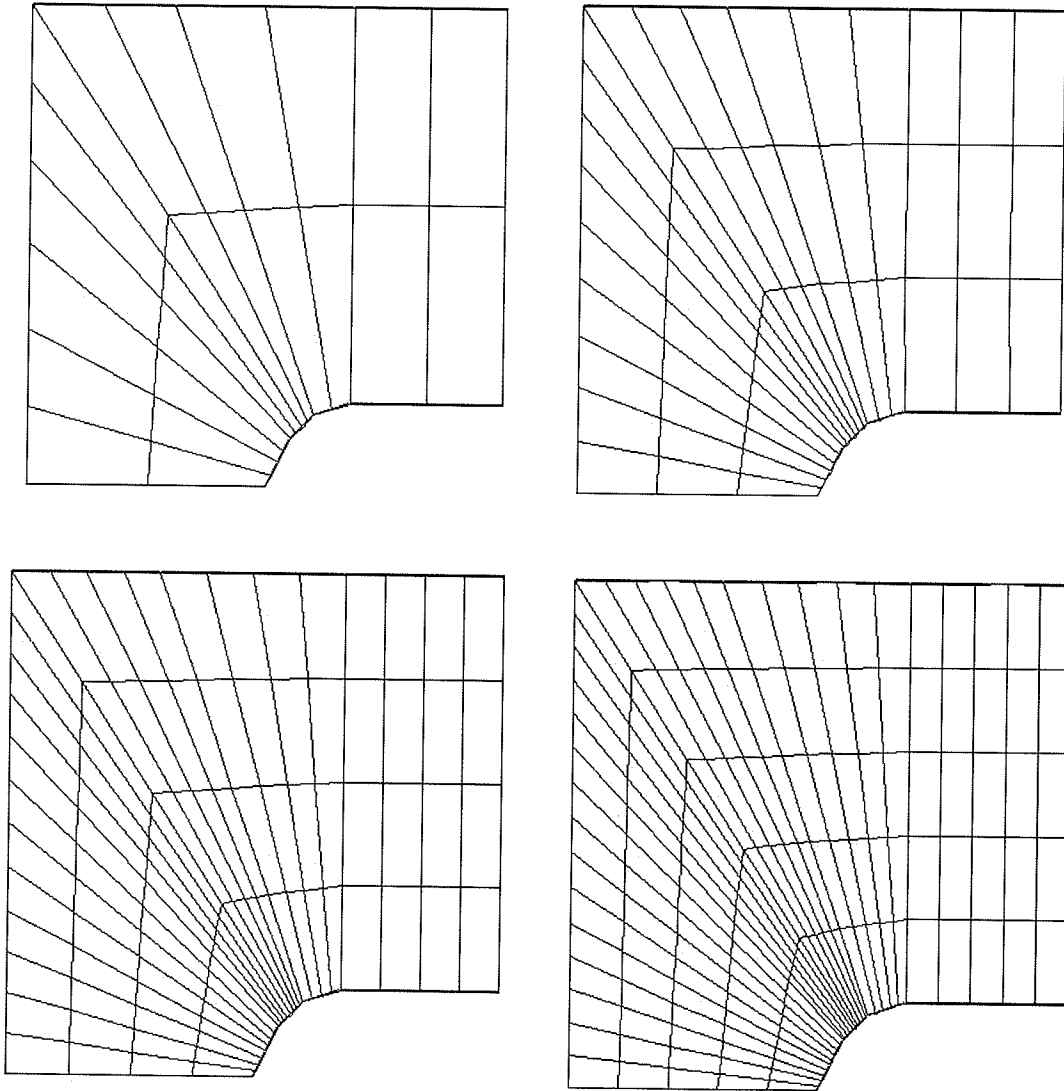


Figure 5. 3. 23: Grids of 12×12 , 27×27 , 48×48 and 75×75 (Case 3)

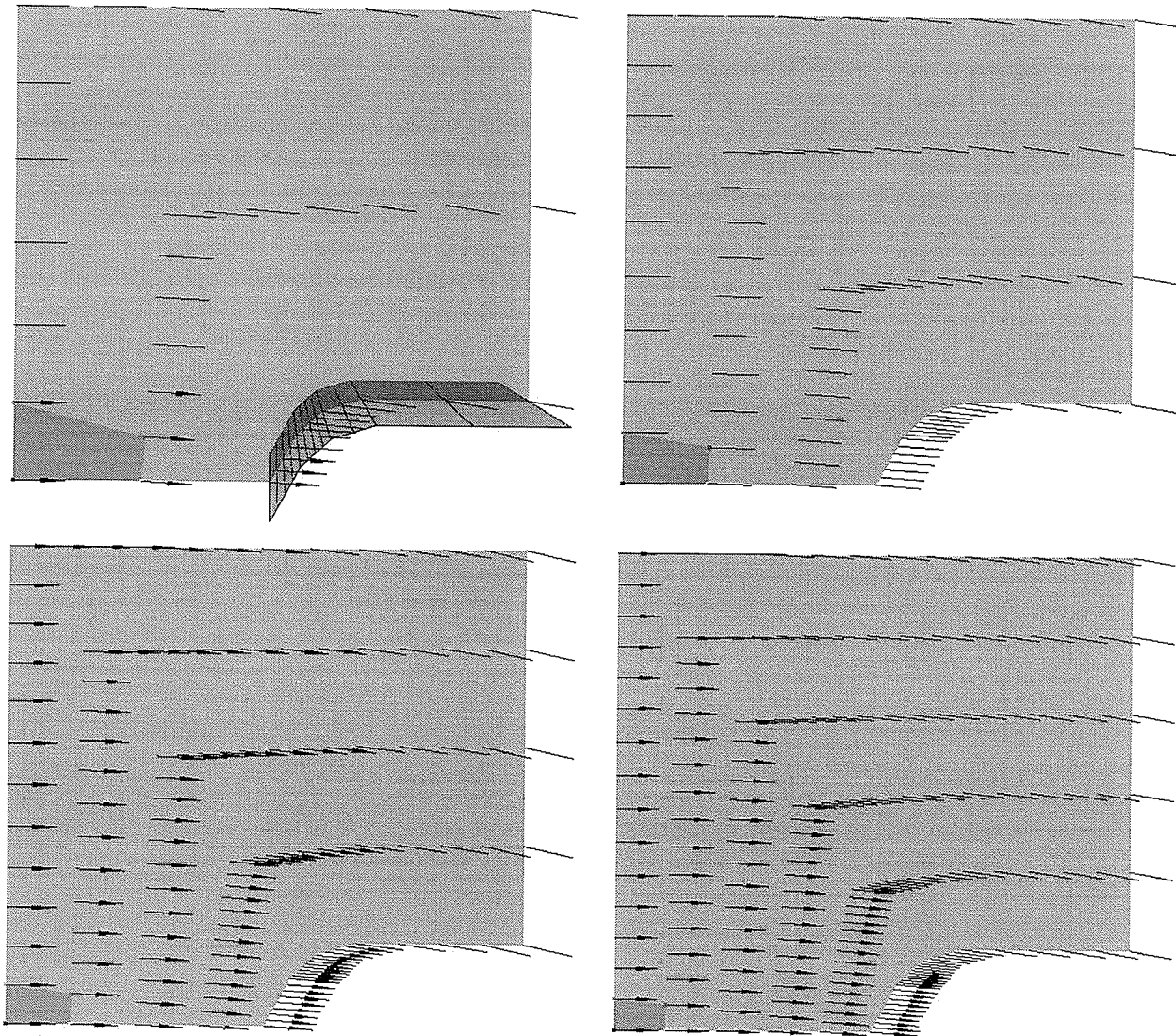


Figure 5. 3. 24: Droplet Velocity Fields for $u_{d,IN} = 7 m/s$ and Grids 12×12 ,
 27×27 , 48×48 and 75×75 (Case 3)

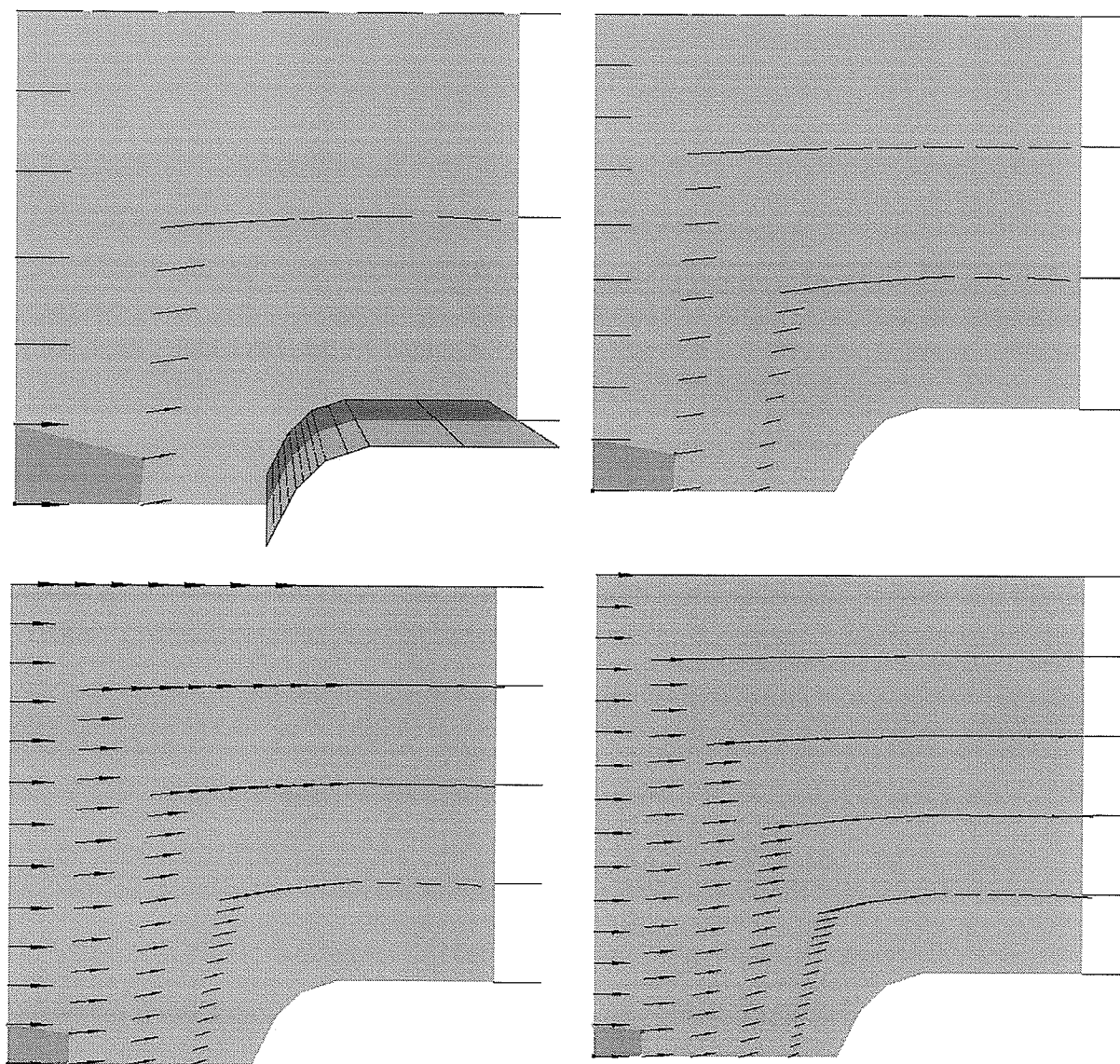


Figure 5. 3. 25: Air Velocity Fields for $u_{d,IN} = 7 m/s$ and Grids 12×12 , 27×27 , 48×48 and 75×75 (Case 3)

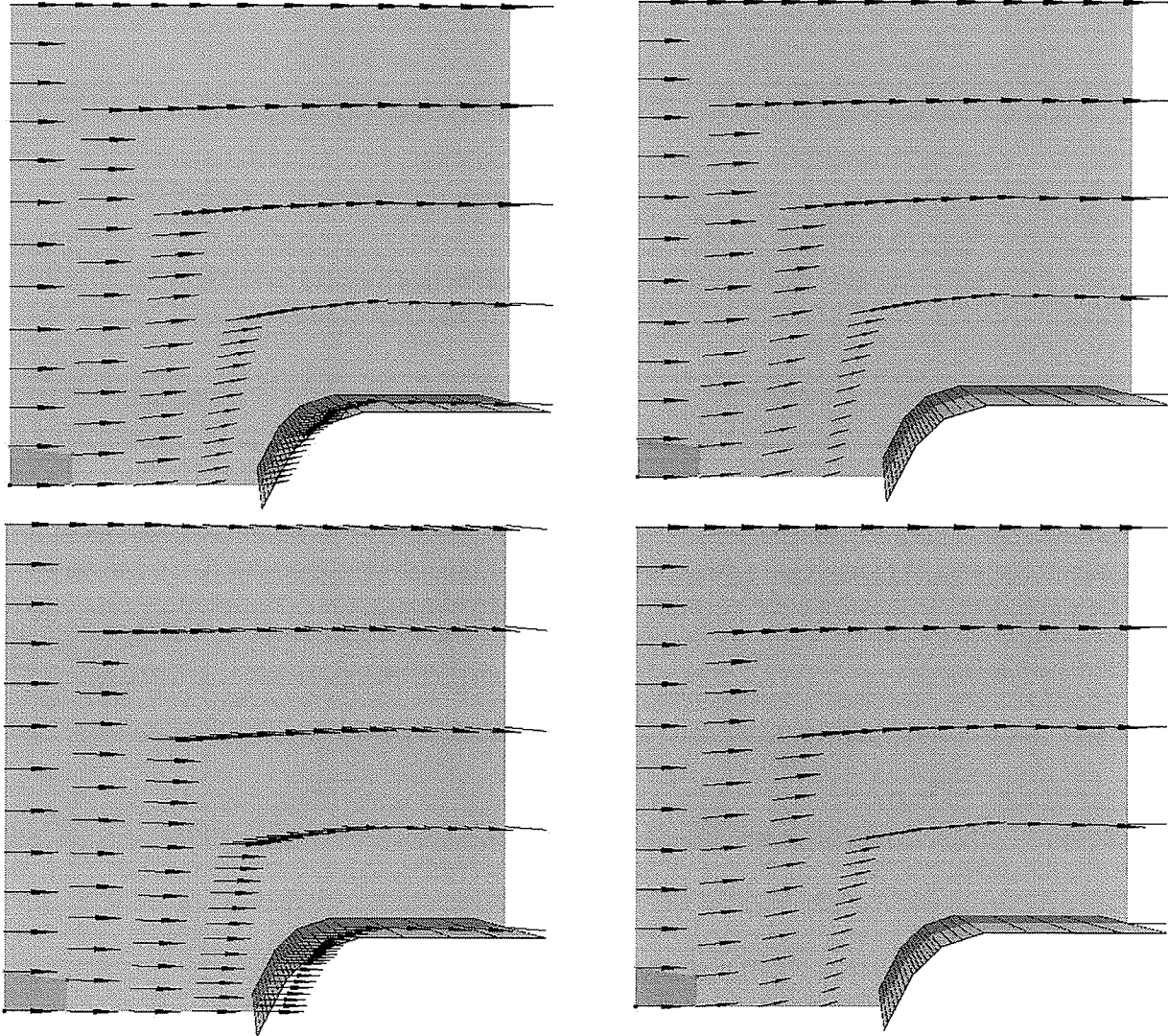


Figure 5. 3. 26: Droplet Velocity Fields (Left) Influenced by the Air Field
(Right) for Interfacial Drag with $D_d = 0.00008$ m (Up) and
 $D_d = 0.00030$ m (Down) - (Case 3)

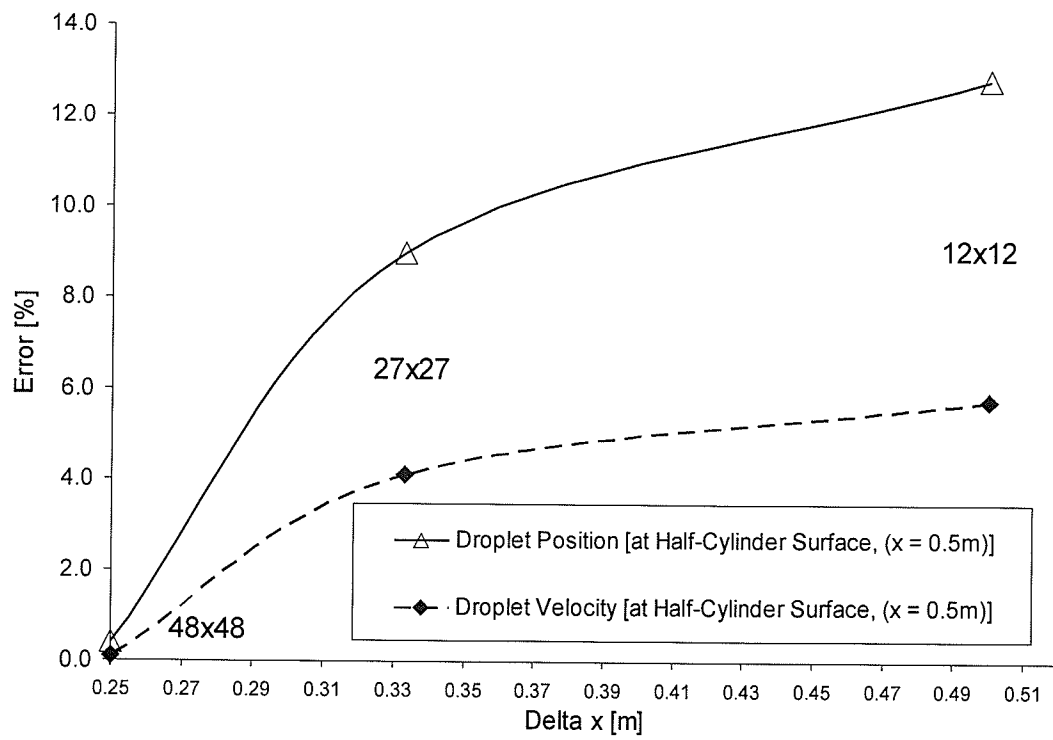


Figure 5. 3. 27: Mesh Refinement Study (Case 3)

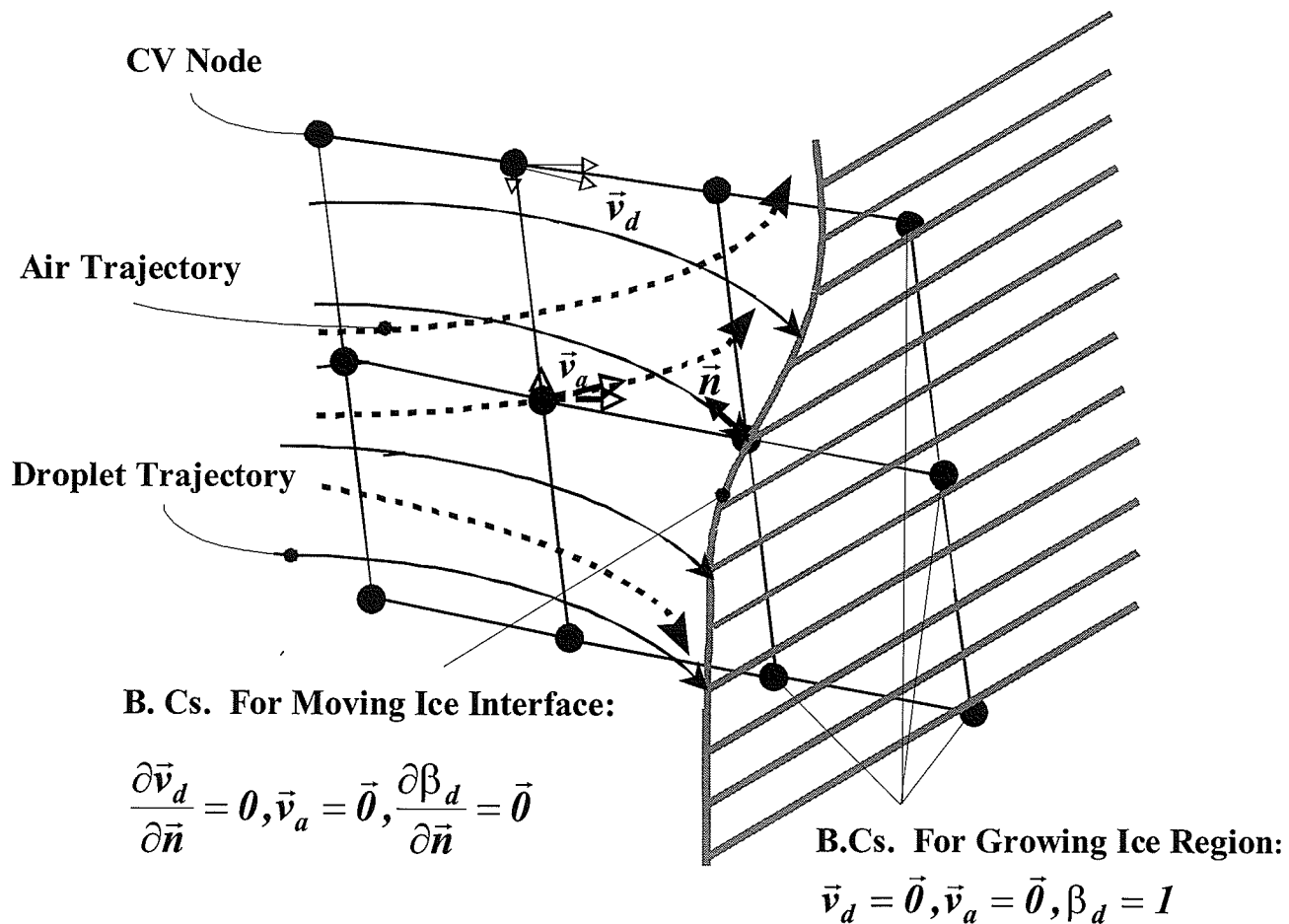


Figure 5. 4. 1: Boundary Conditions for Droplet Velocity (\vec{v}_d), Air Velocity (\vec{v}_a) and Droplet Volume Fraction (β_d) in Ice Interface Propagation

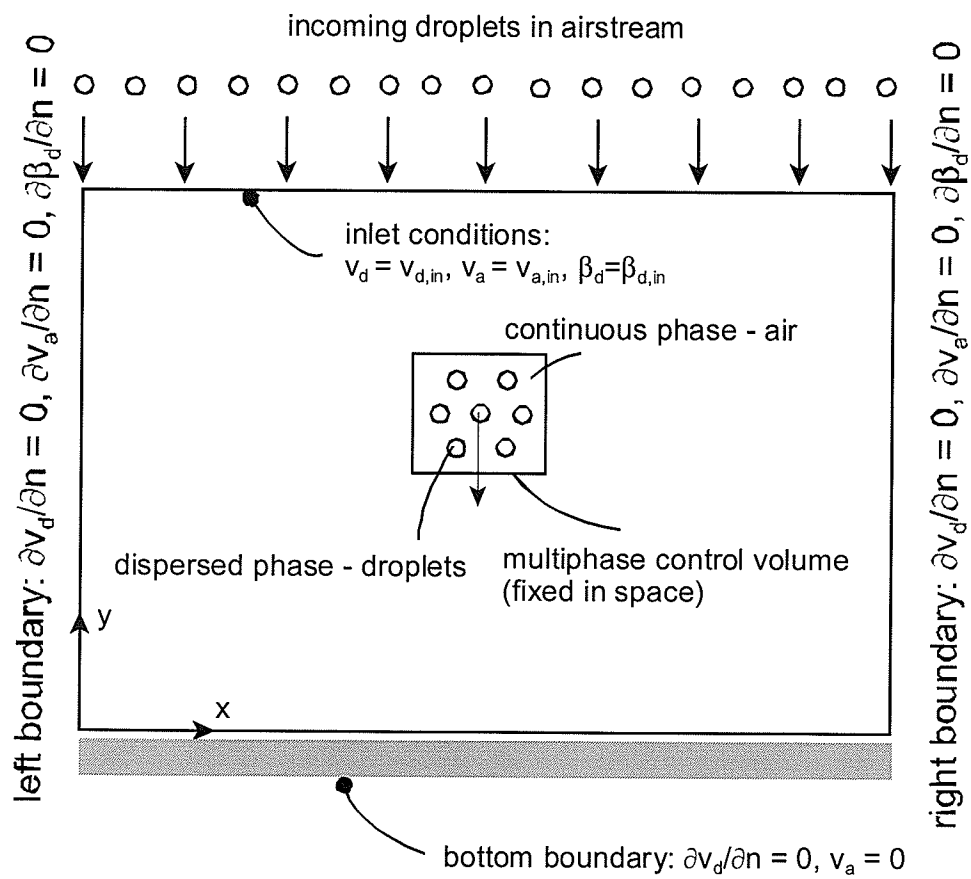


Figure 5. 4. 2: Problem Schematic (Case 1)

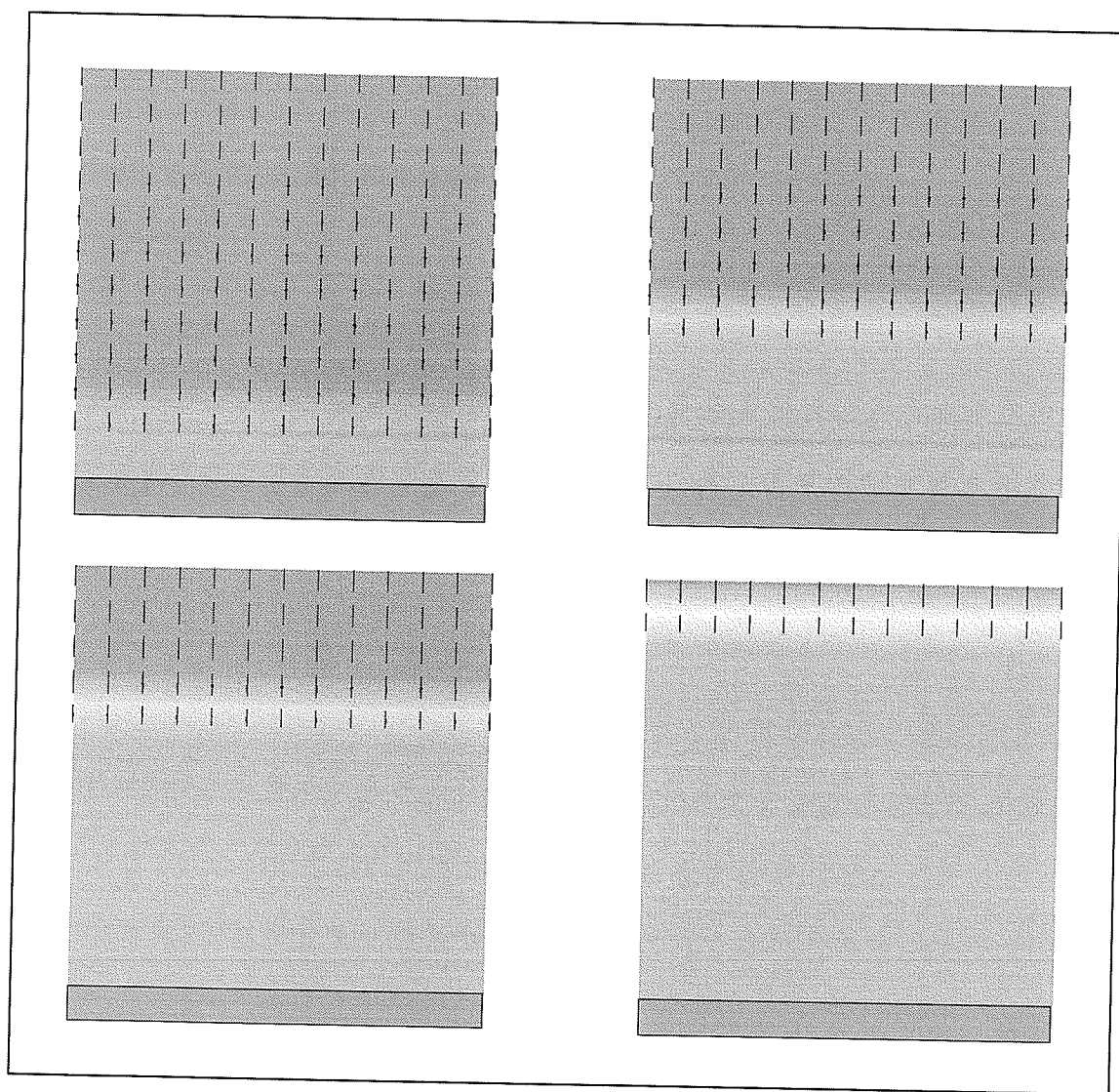


Figure 5. 4. 3: Spreading Ice with Evolving Ice Interface Position at Times: 417 s , 1042 s , 1667 s and 2292 s (Case 1)

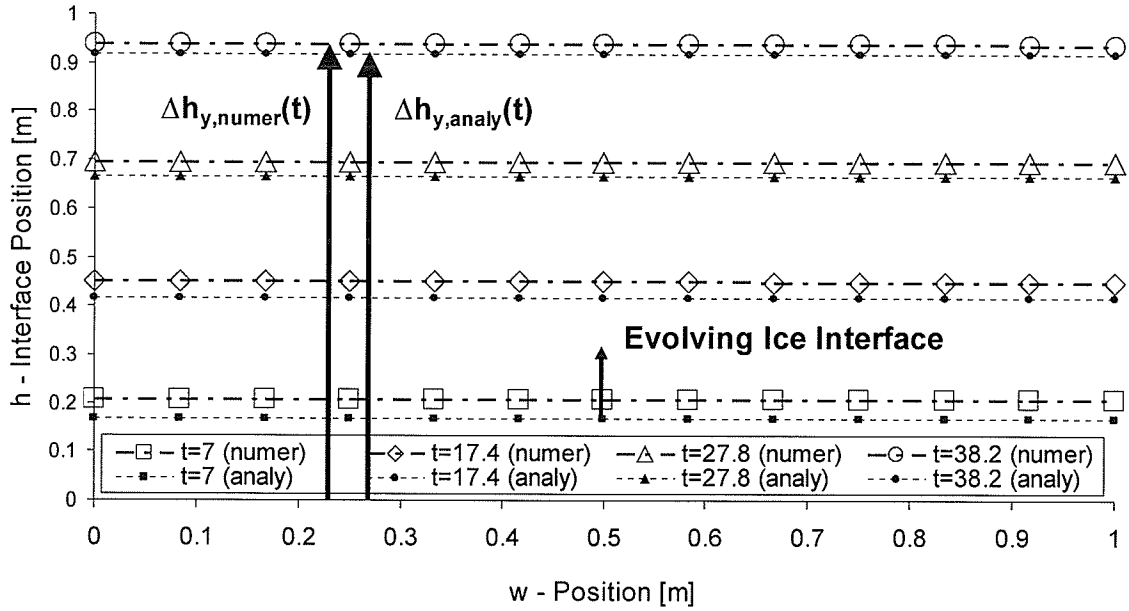


Figure 5. 4. 4: Numerical and Analytical Ice Interface Evolution at Times t [min] (Case 1)

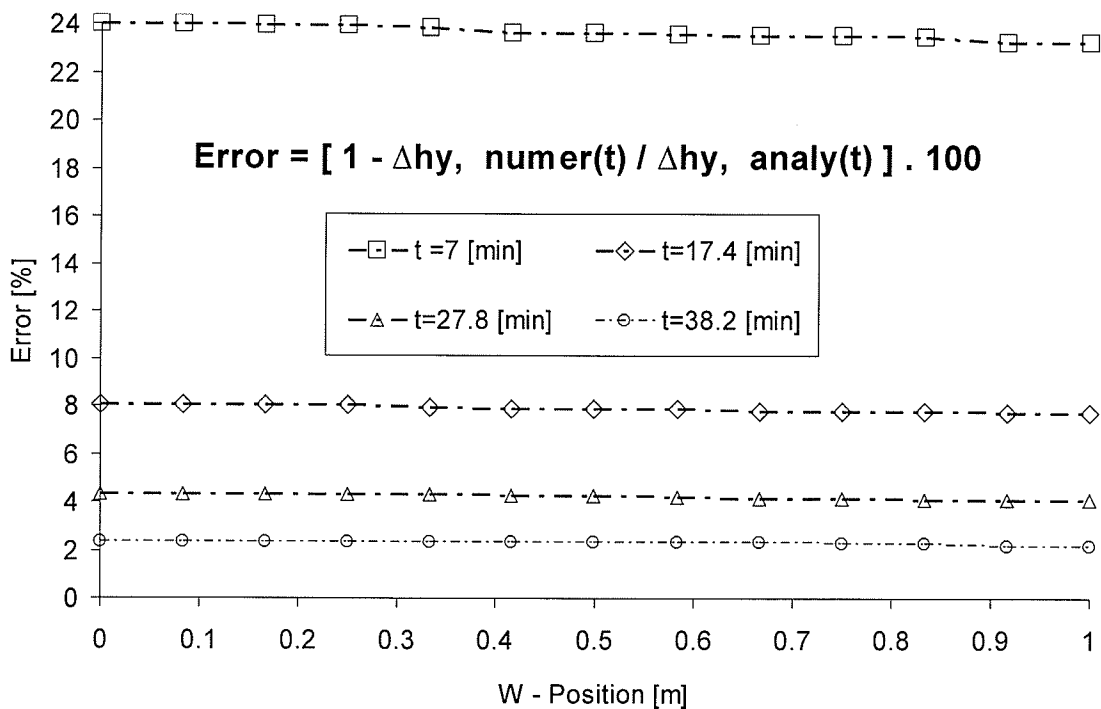


Figure 5. 4. 5: Error Distribution for Ice Interface Predictions (Numerical v. s. Analytical) at Times t [min] (Case 1)

Ice Shape Backward Evolution Across the Domain in the Air at Different Times [min]

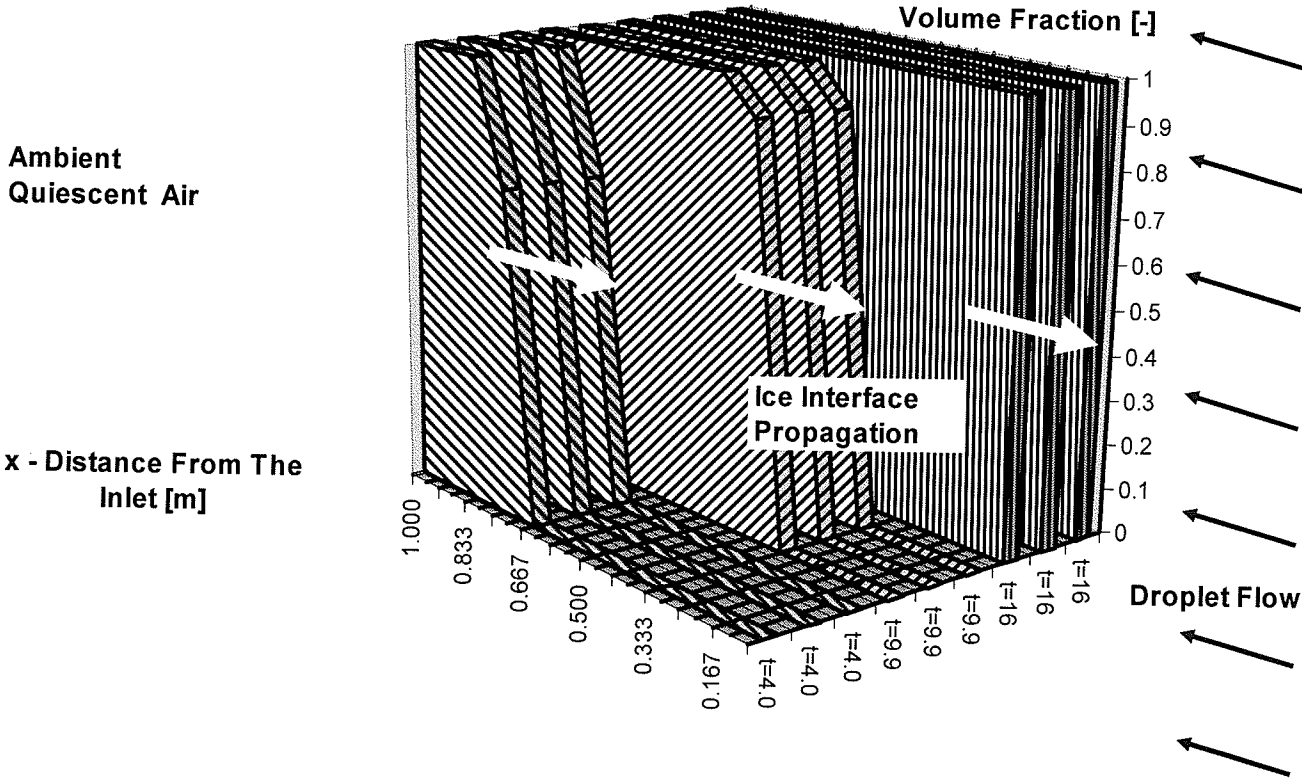


Figure 5. 4. 6: Predicted Ice Interface Propagation from the Wall Towards the Inlet at Times t [min] (Case 2)

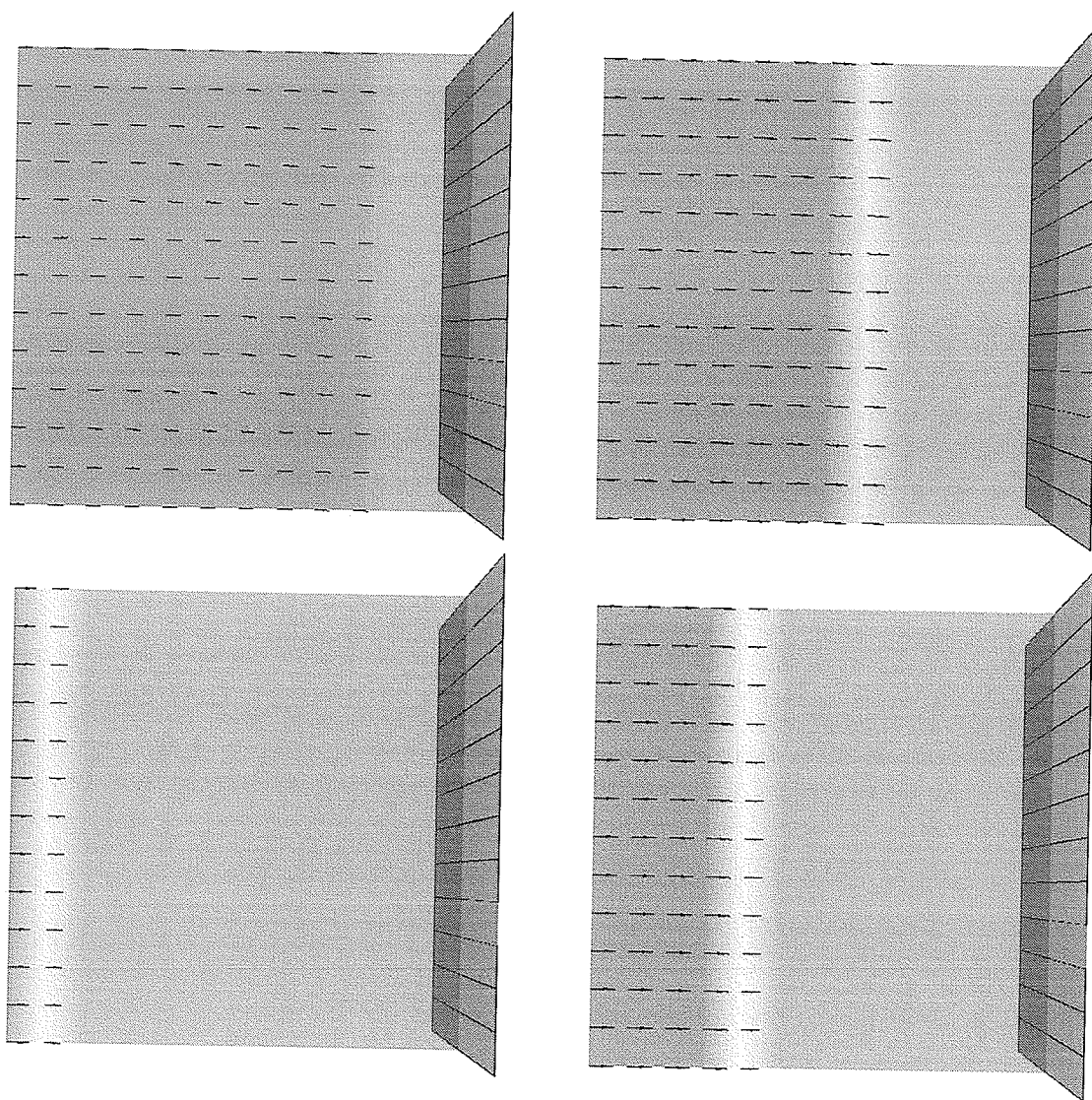


Figure 5. 4. 7: Ice Spreading with Ice Interface Evolution at Time: 400 s , 600 s , 900 s and 1200 s (Case 2)

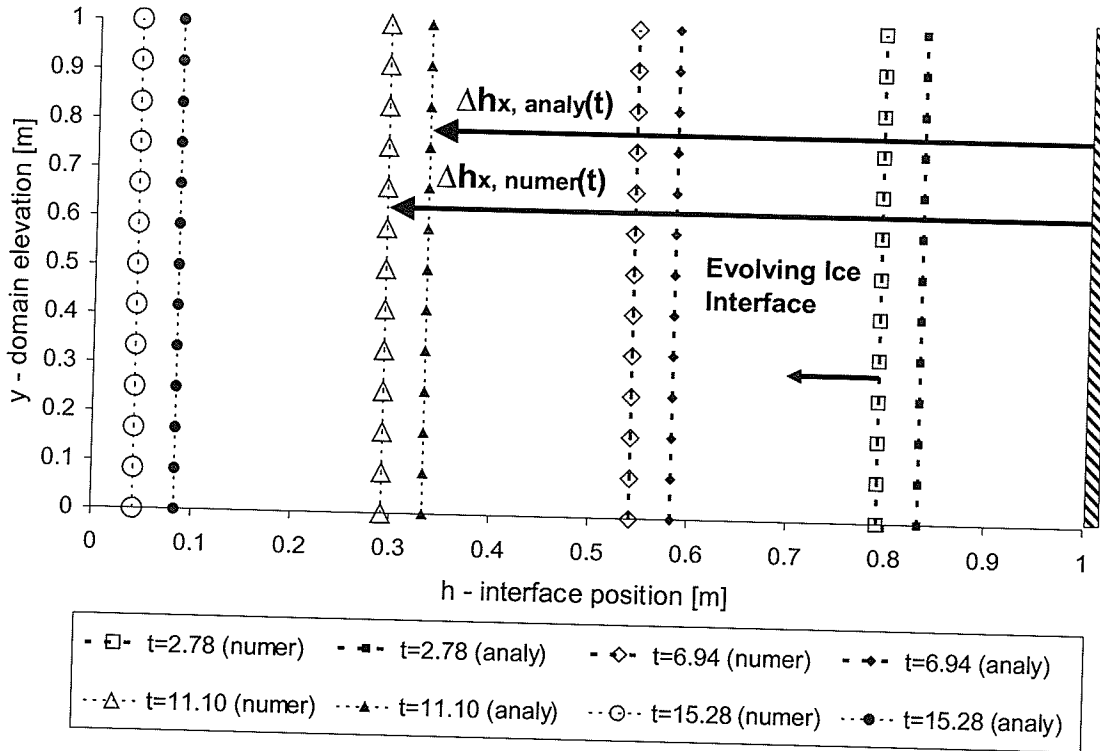


Figure 5. 4. 8: Numerical and Analytical Ice Interface Evolution at Times t [min] (Case 2)

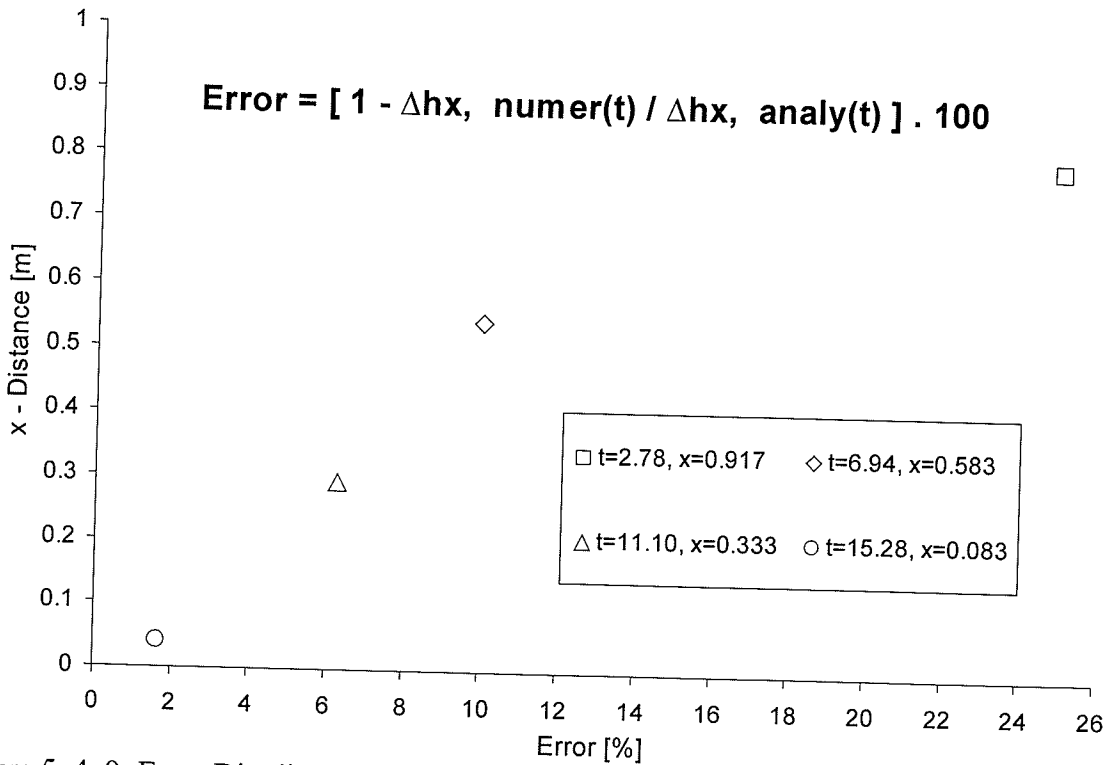


Figure 5. 4. 9: Error Distribution for Ice Interface Predictions (Numerical vs. Analytical) at Times t [min] (Case 2)

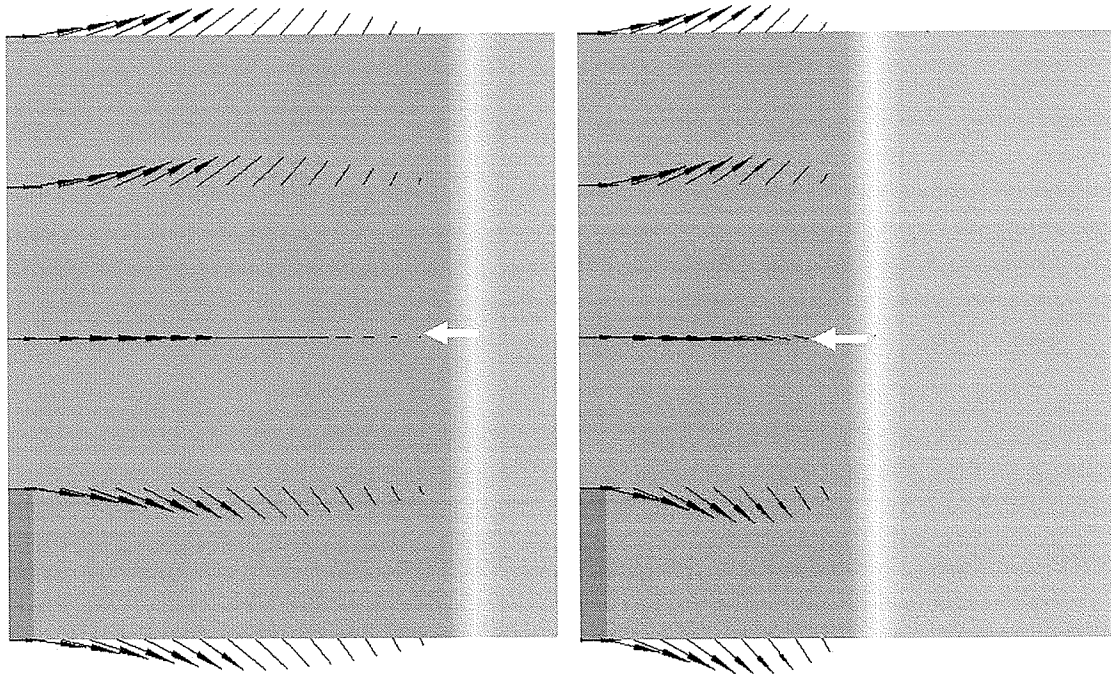


Figure 5. 4. 10: Air Flow at the Evolving Ice Interface (Case 2)

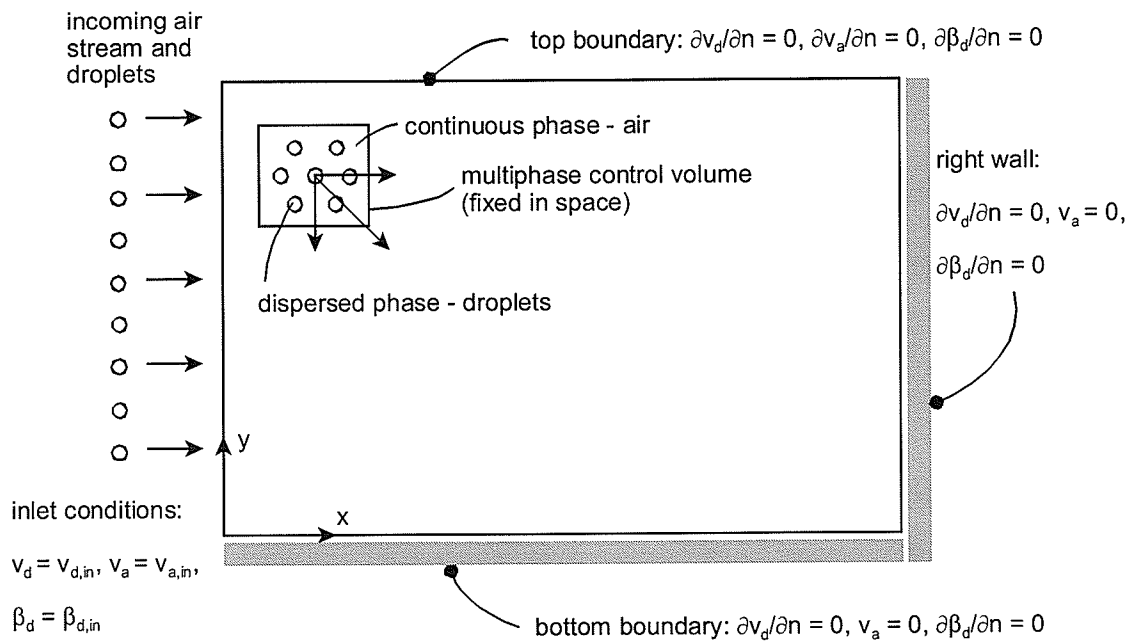


Figure 5. 4. 11: Problem Schematic for the Frontward Step Domain (Case 3)

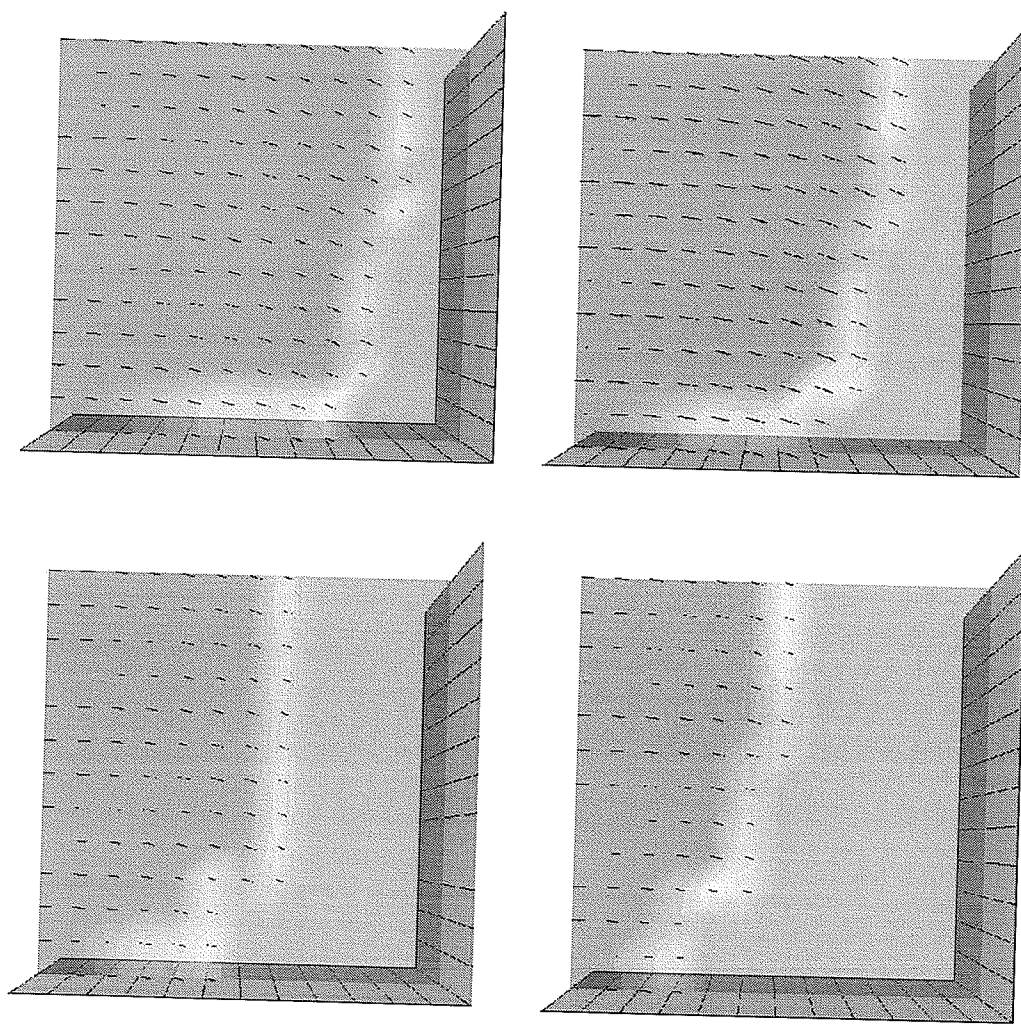


Figure 5. 4. 12: Ice Spreading with Ice Interface Evolution at Time: $400 s$, $600 s$, $900 s$ and $1200 s$ (Case 3)

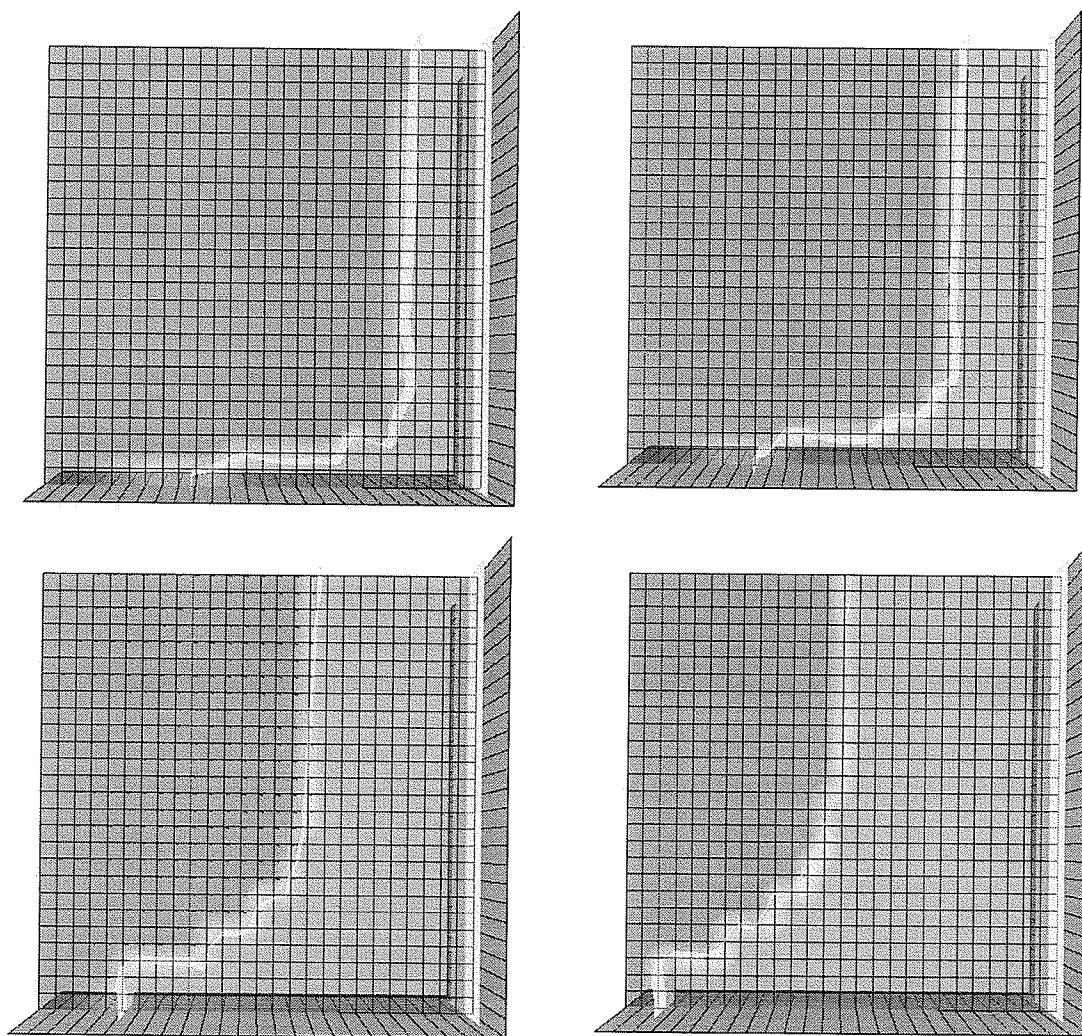


Figure 5. 4. 13: Ice Spreading with Ice Interface Evolution at Time: 400 s , 600 s , 900 s and 1200 s (Case 3)

Ice Interface Analytical Solution

$$f(x, n) = \begin{cases} \xi(x), & x_0 \leq x \leq x_I \\ \zeta(x, n), & x = x_I, n \in N \end{cases}$$

$$\xi(x) = (0.331)x + (-0.285)x^2 + (0.152)x^3 + (-0.259)x^4$$

$$\zeta(x, n) = \xi(x) + h_I(n)$$

$$h_I(n) = 0.083n$$

$$x_I = 0.800$$

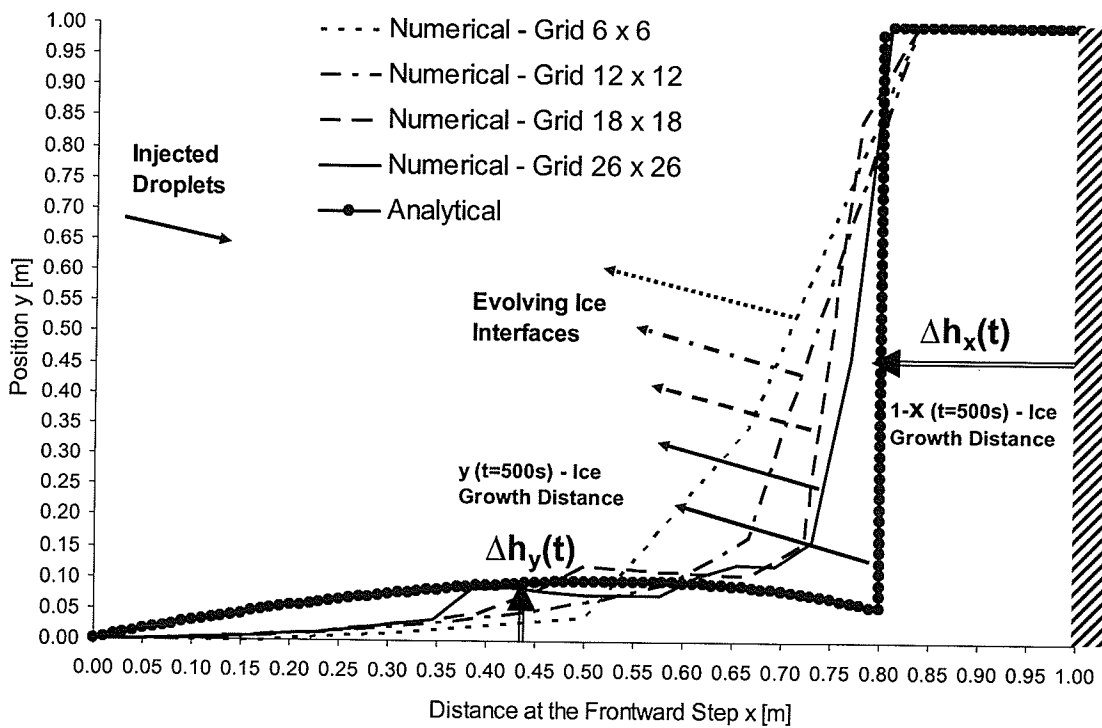


Figure 5. 4. 14: Numerical v. s. Analytical Results of Accreted Ice at Frontward Step at Time $t = 500 \text{ s}$ (Case 3)

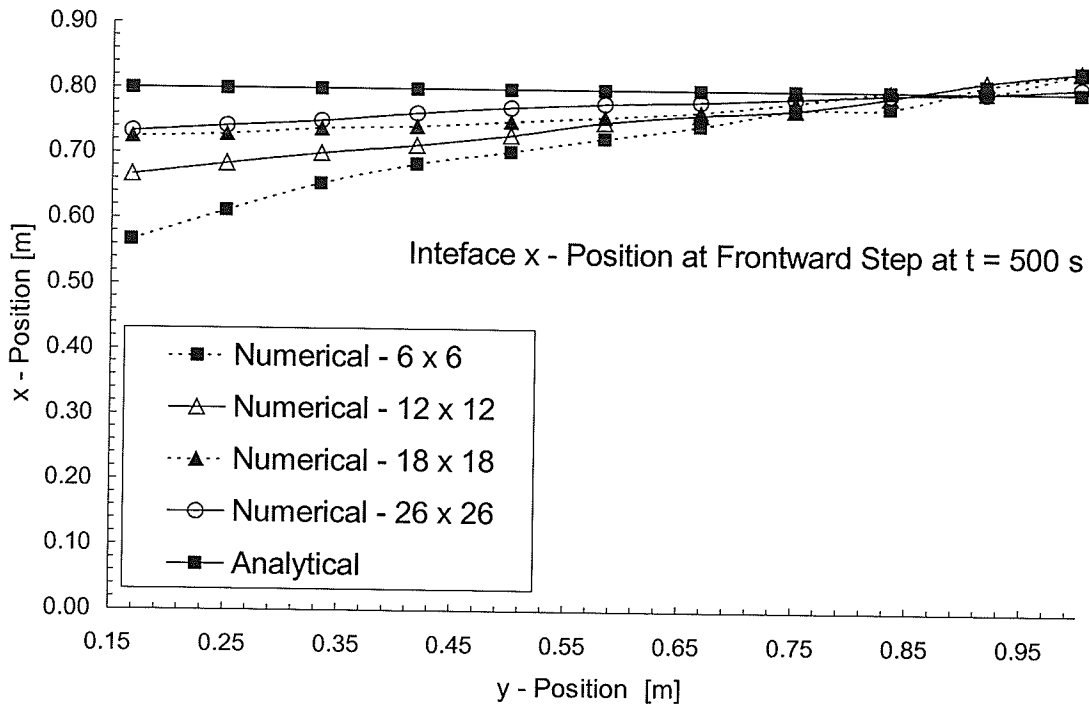


Figure 5. 4. 15: Ice Interface y-Positions at Various y-Positions from the Bottom at the Frontward Step (Case 3)

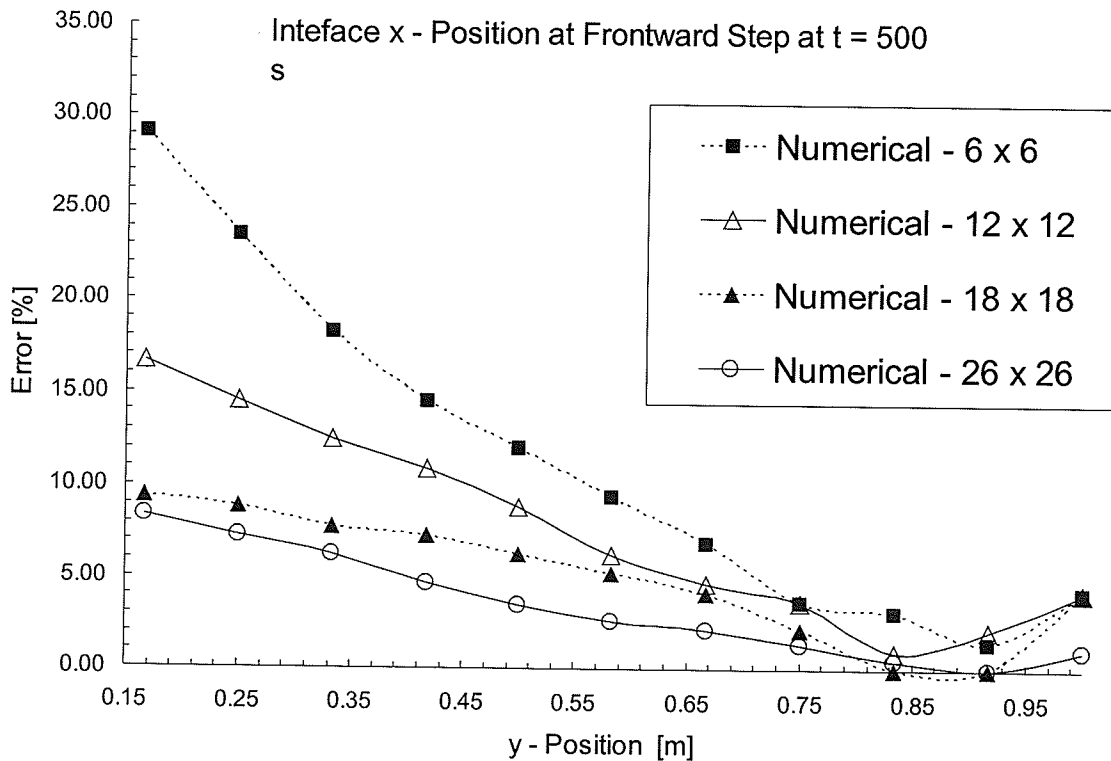


Figure 5. 4. 16: Numerical Errors at Various Y-Distances from the Bottom at the Frontward Step (Case 3)

Ice Prediction Method	Mass m_{ice} of Accreted Ice - [kg]	Error $\left 1 - \frac{m_{ice}}{m_{ice,analy}} \right \times 100$ [%]
[1] With Viscous terms --->		
[2] Viscous terms negligible --->		
[3] Difference [2] – [1] --->		
Numerical - Grid 6 x 6	[1] 318.353	[1] 17.288
	[2] 318.383	[2] 17.299
	[3] + 0.030	[3] + 0.011
Numerical - Grid 12 x 12	[1] 292.656	[1] 7.821
	[2] 292.245	[2] 7.669
	[3] - 0.411	[3] - 0.152
Numerical - Grid 18 x 18	[1] 287.113	[1] 5.779
	[2] 287.475	[2] 5.912
	[3] + 0.362	[3] + 0.133
Numerical - Grid 26 x 26	[1] 272.544	[1] 0.411
	[2] 272.828	[2] 0.516
	[3] + 0.284	[3] + 0.105
Analytical 2-D	271.428	0.000

Table 5. 4. 1: Numerical and Analytical Results of the Mass of the Ice Mass and Error Based on the Droplet Phase Formulations with/without the Viscous Terms (Case 3)

FIGURES AND TABLES – Chapter 5

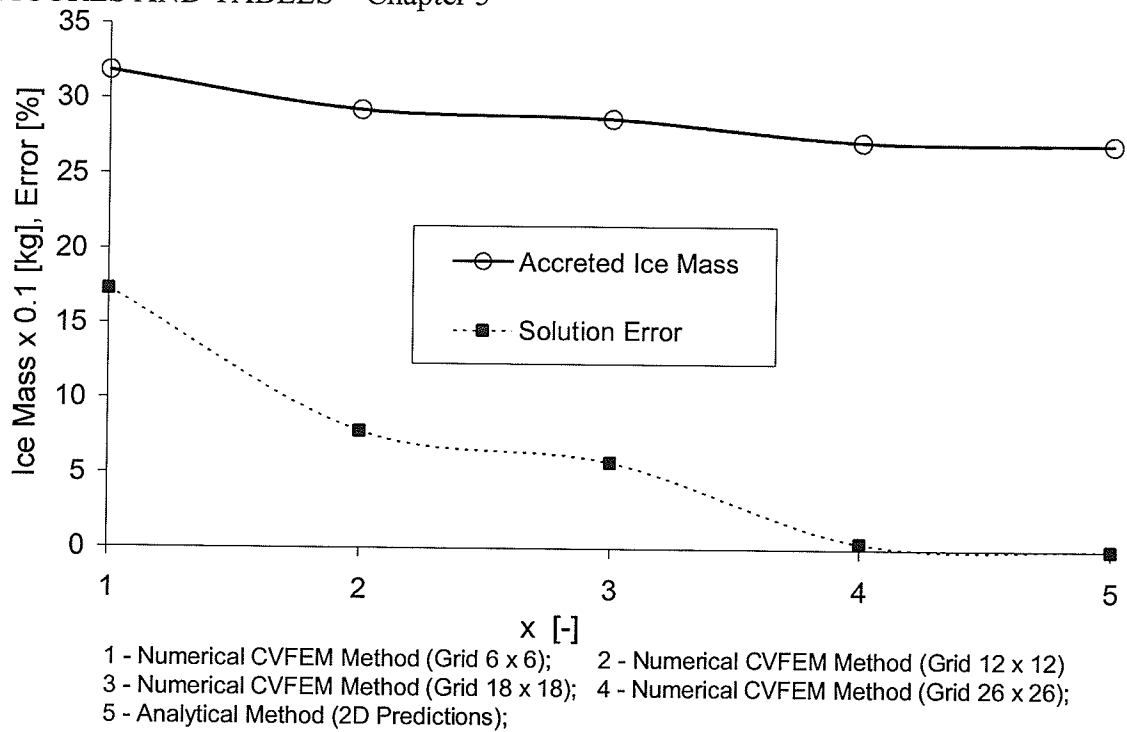


Figure 5. 4. 17: Accreted Ice Mass and Error Distributions at the Frontward Step (Case 3)

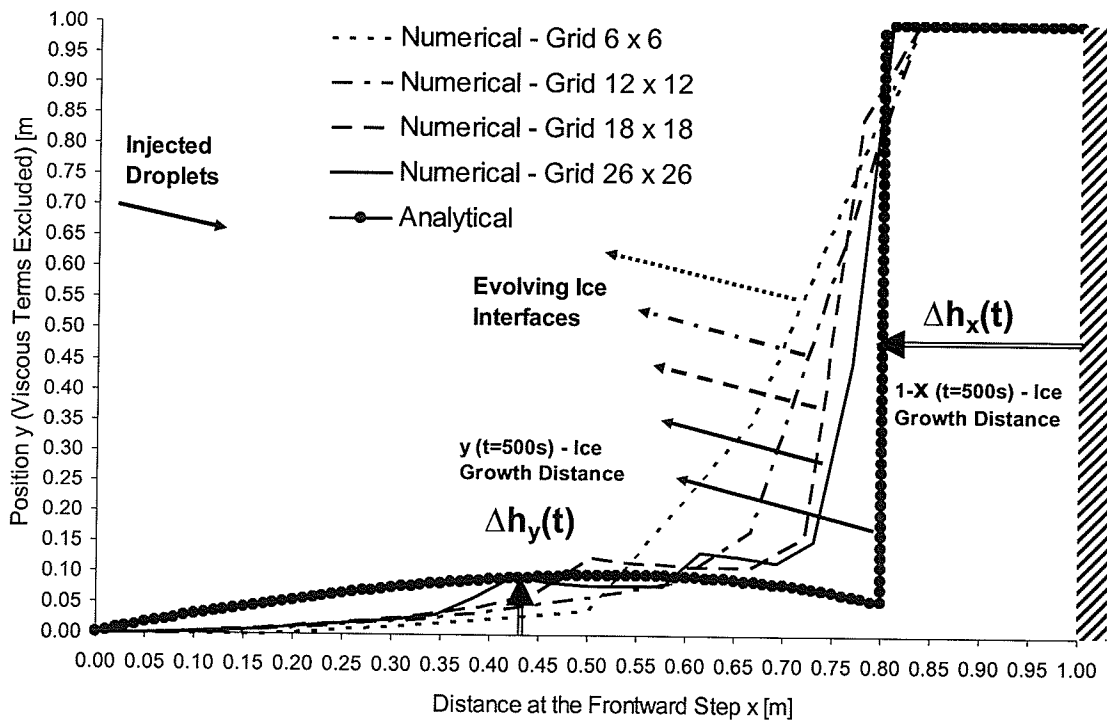


Figure 5. 4. 18: Numerical v. s. Analytical Results of Accreted Ice at Frontward Step at Time $t = 500 s$ (Case 3) – Viscous Terms are Excluded from the Droplet Flow Formulation

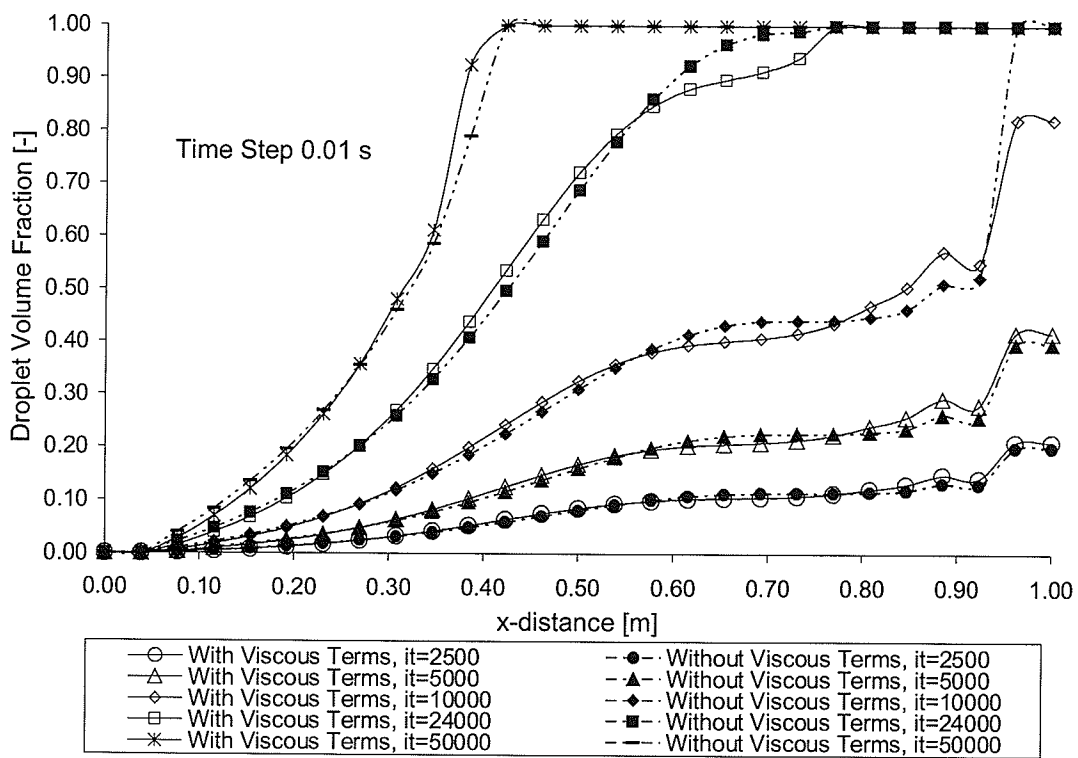


Figure 5. 4. 19: Distribution of the Droplet Volume Fraction along the bottom of the Domain at the Frontward Step at Various Times (Case 3)

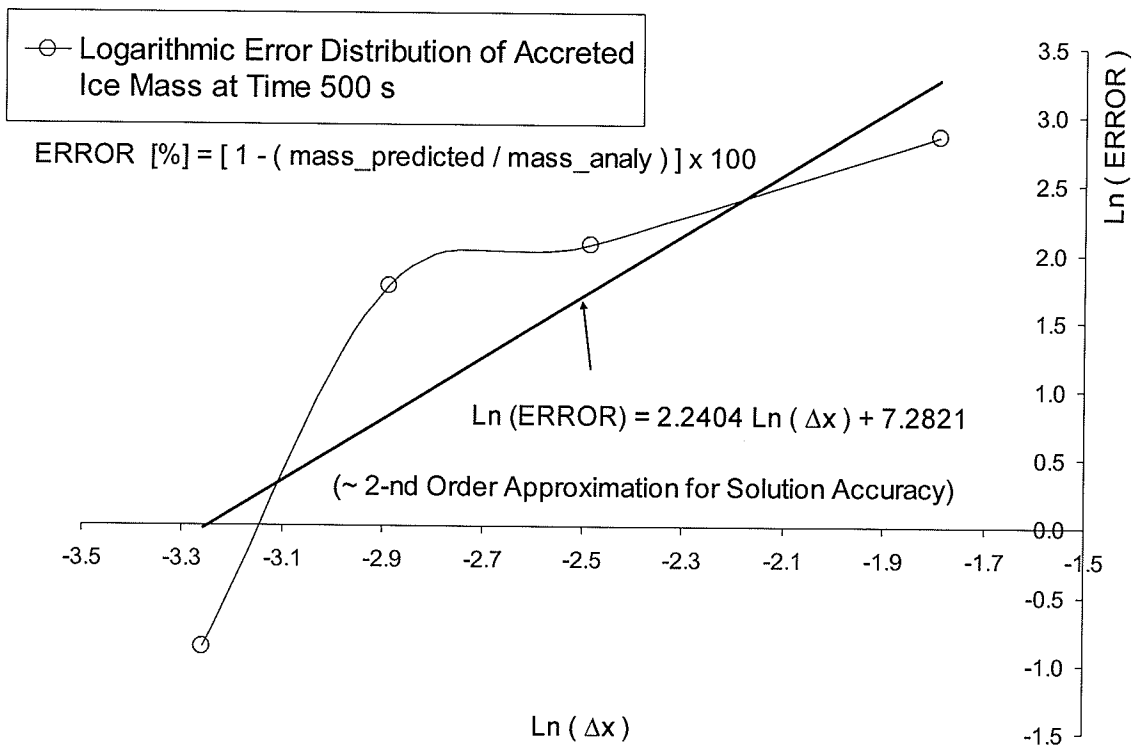


Figure 5. 4. 20: Numerical Error Distribution of Accreted Ice Mass at Time $t = 500 s$ as a Function of Grid Spacing, $Ln(\Delta x)$ (Case 3)

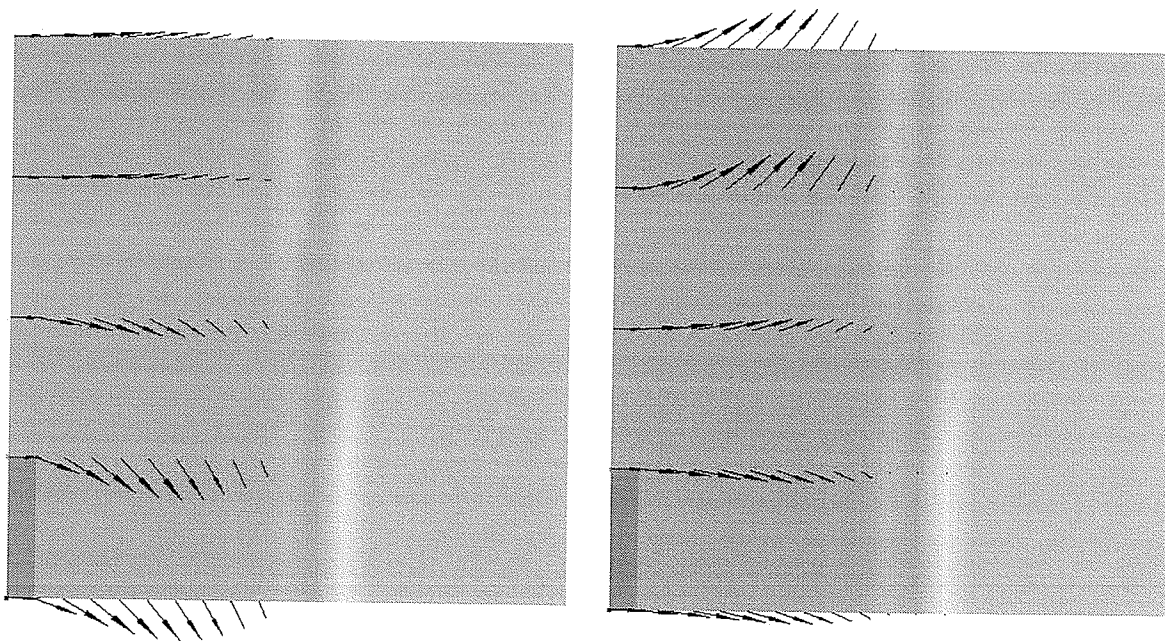


Figure 5. 4. 21: Numerical Simulation of the Droplet (Left) and Air Flows (Right) with the Scaled Interfacial Drag of 0.05 and the Evolving Ice Interface (Case 4)

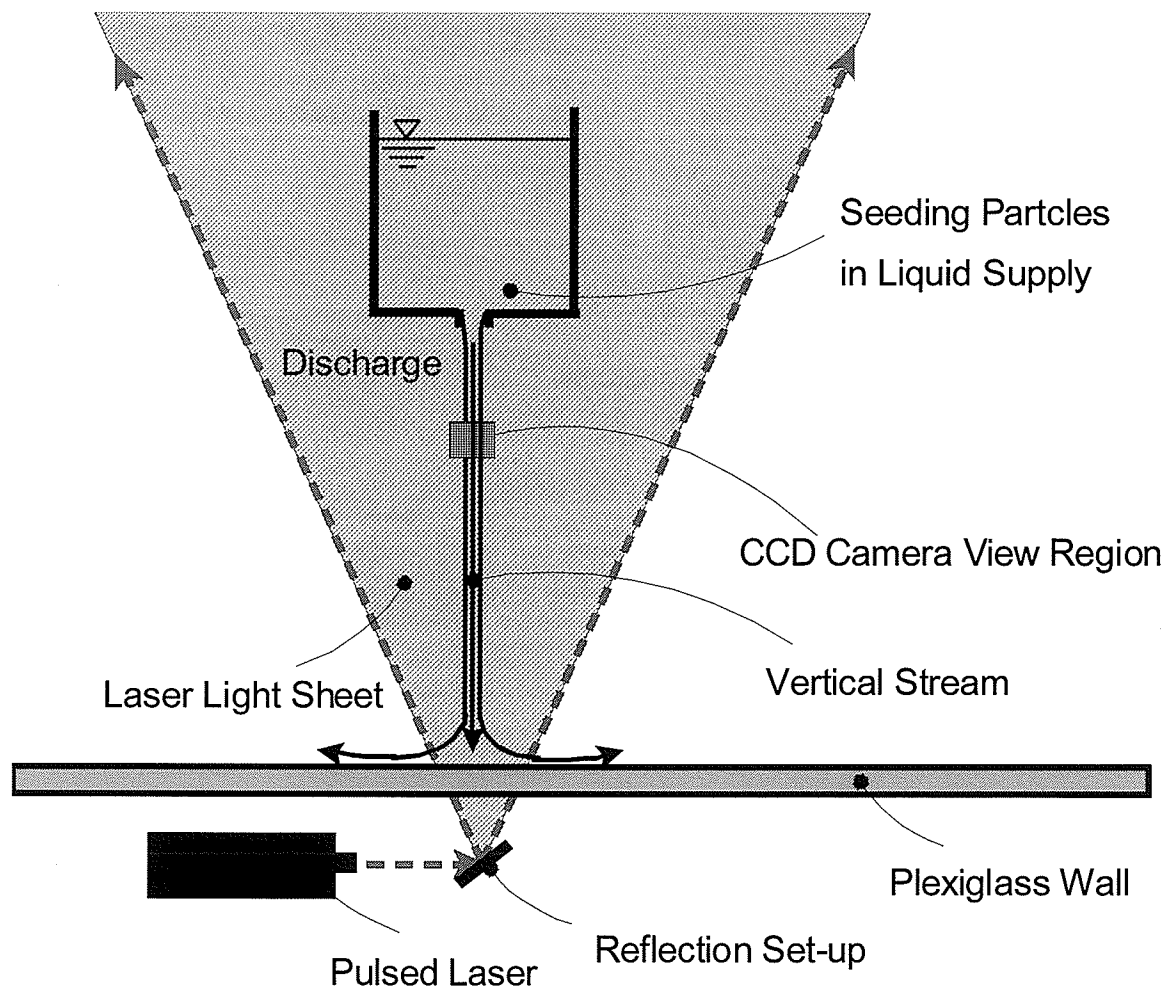


Figure 5. 5. 1: The Experimental Setup for Vertical Jet Flow (Case 1)

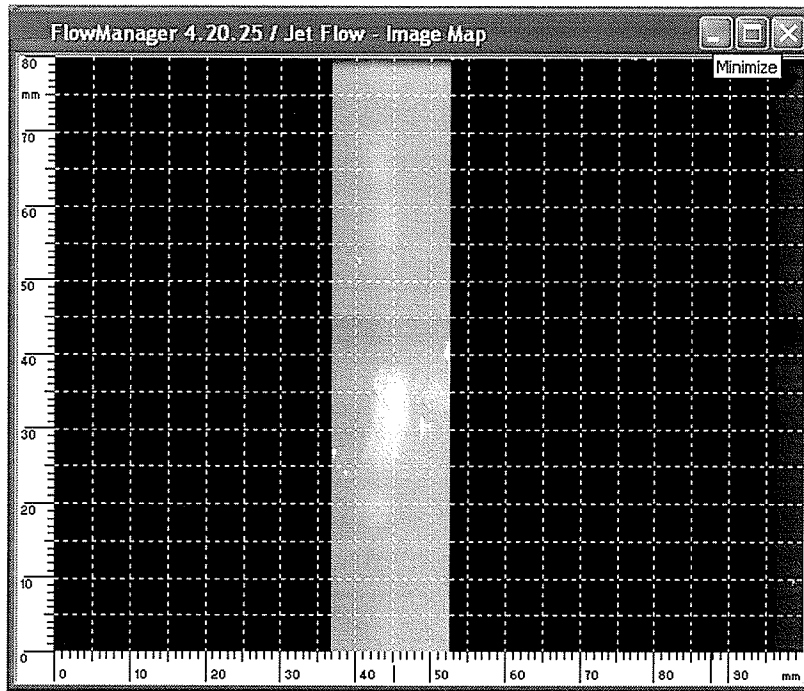


Figure 5. 5. 2: Camera Image: Vertical Jet Flow (Case 1)

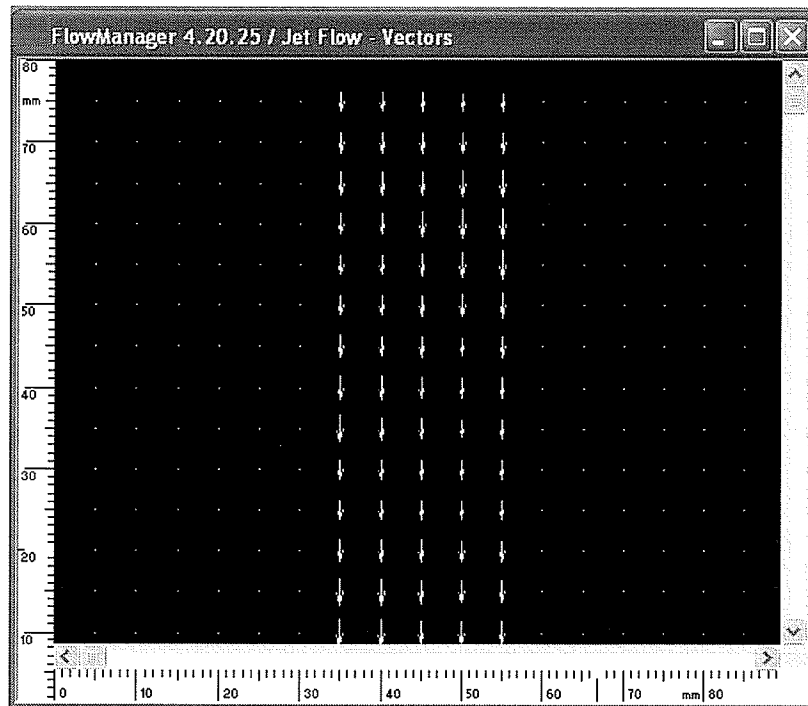


Figure 5. 5. 3: Measured Velocities for Vertical Jet Flow (Case 1). Inlet Velocity
Magnitude = 3.215 m/s



Figure 5. 5. 4: Jet Flow Trajectory (Case 2)

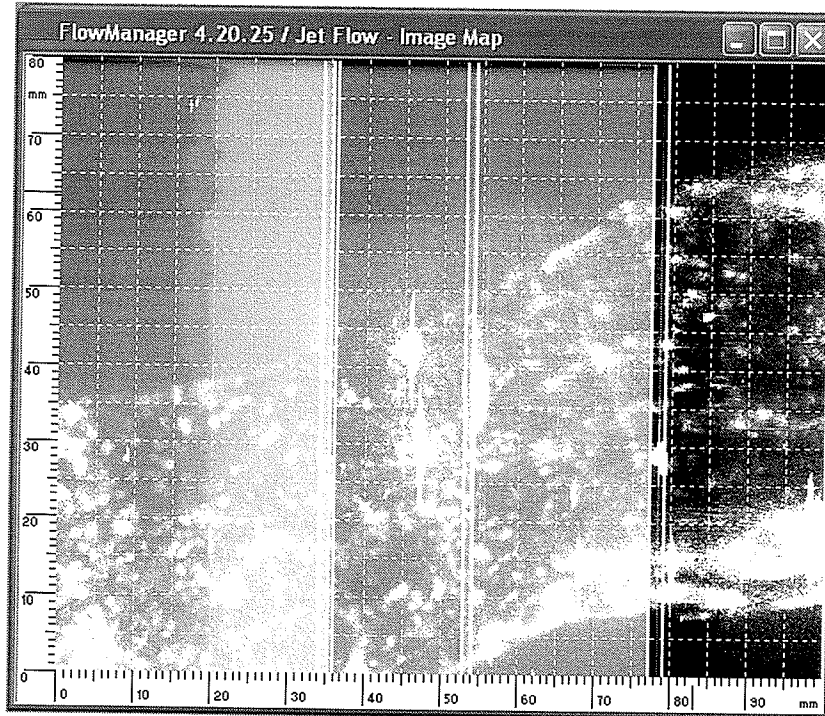


Figure 5. 5. 5: Illuminated Particles in Flow (Case 2)

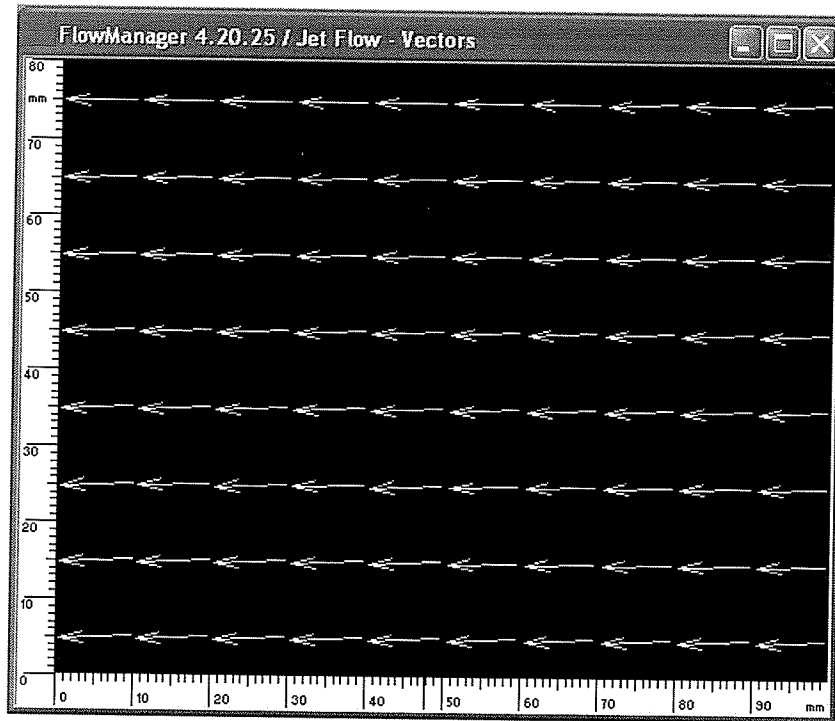


Figure 5. 5. 6: Measured Droplet Velocities (Case 2). Inlet Velocity Magnitude = 4.251 m/s

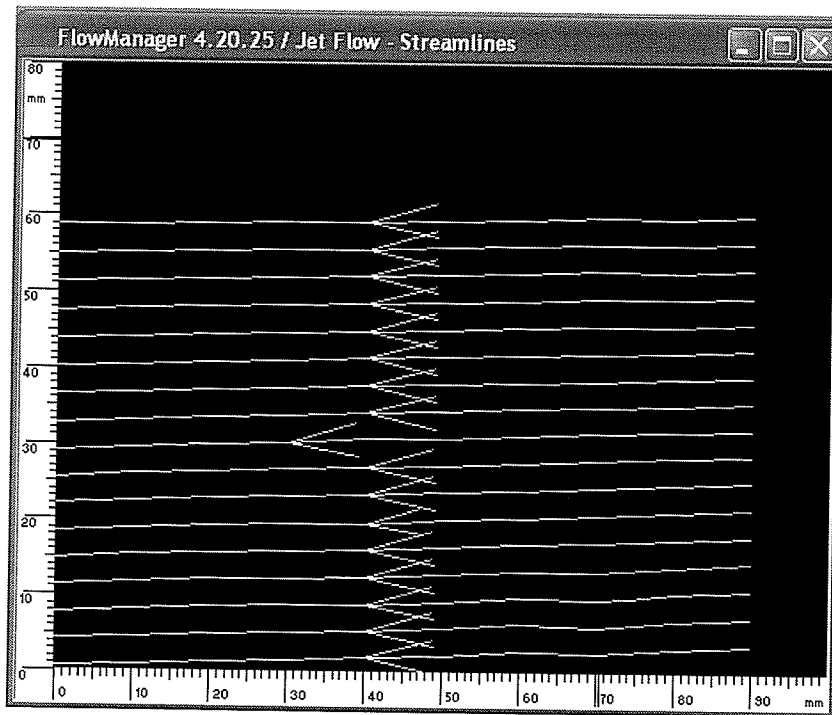


Figure 5. 5. 7: Measured Droplet Streamlines (Case 2)

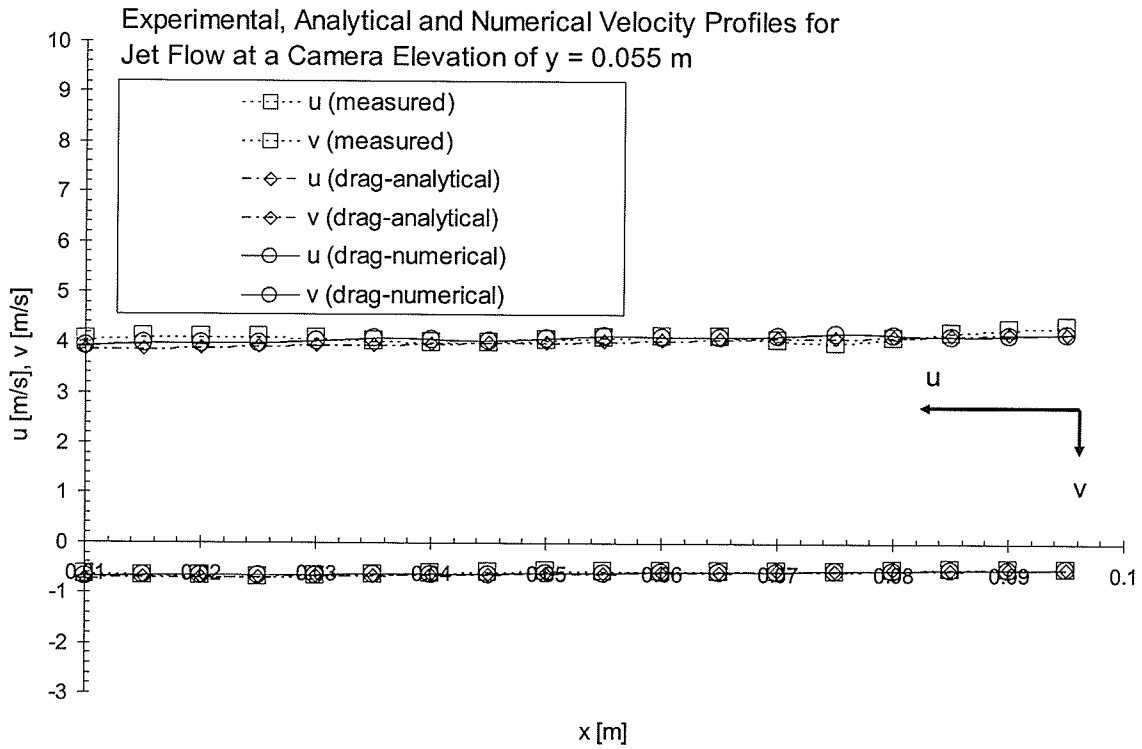


Figure 5. 5. 8: Jet Flow Velocity Components (Case 2)

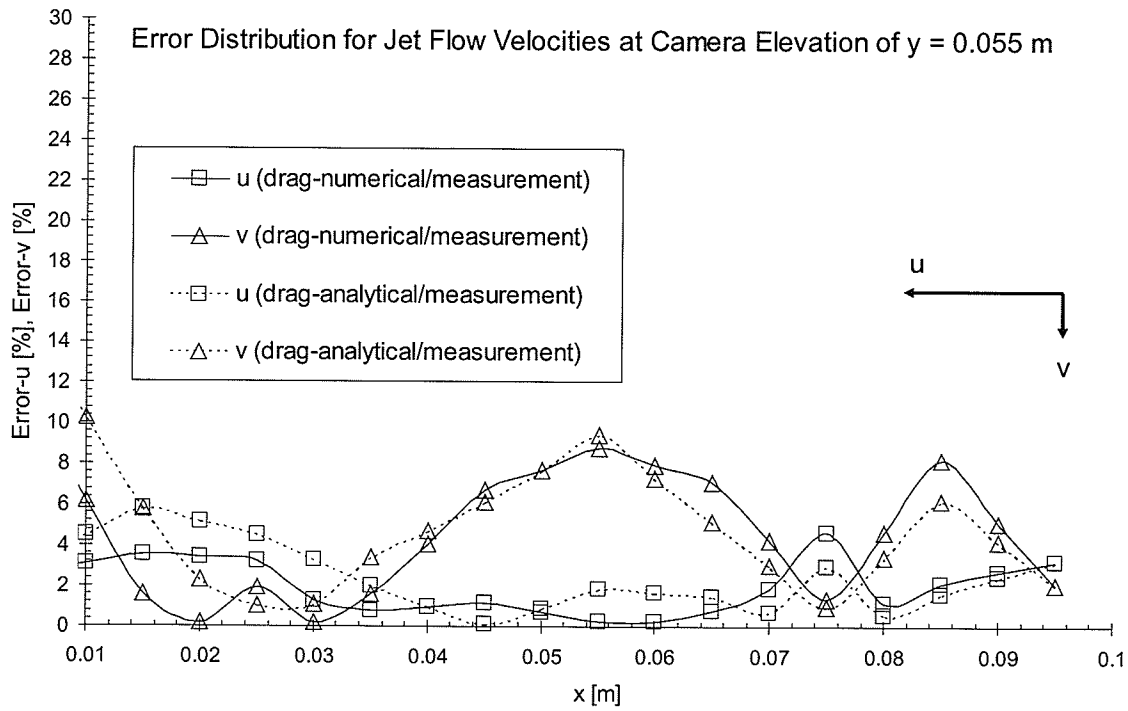


Figure 5. 5. 9: Error Distribution for Jet Flow Trajectory (Case 2)

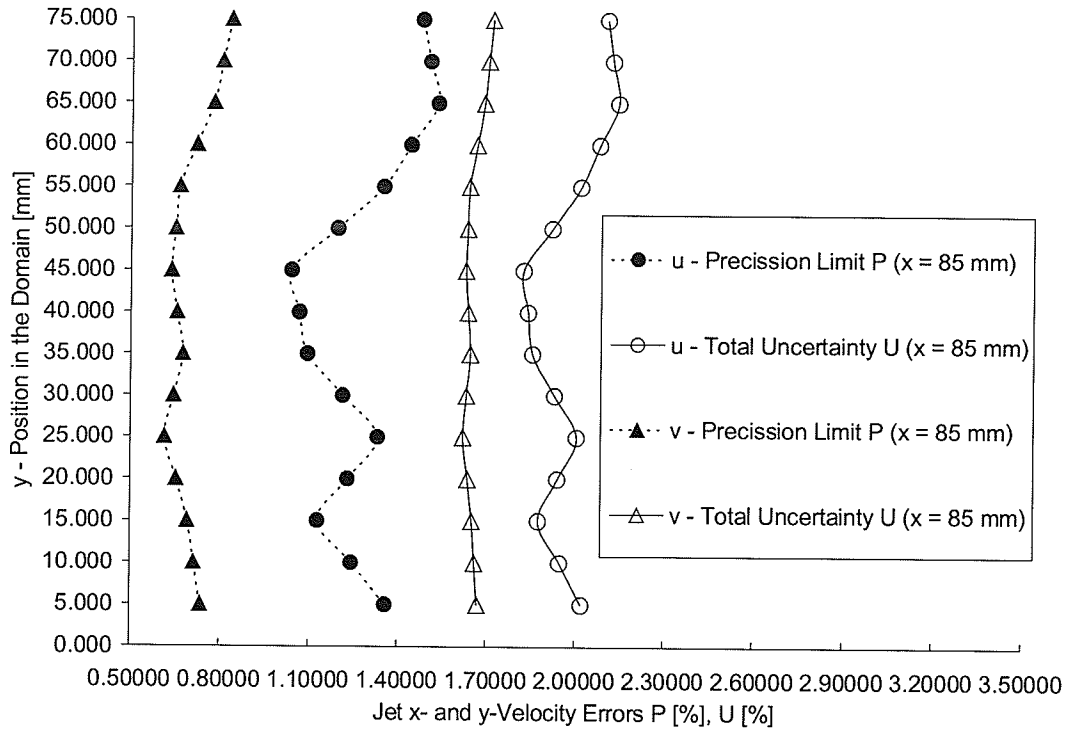


Figure 5. 5. 10: Error Distributions along the Height of the Camera Interrogation Region

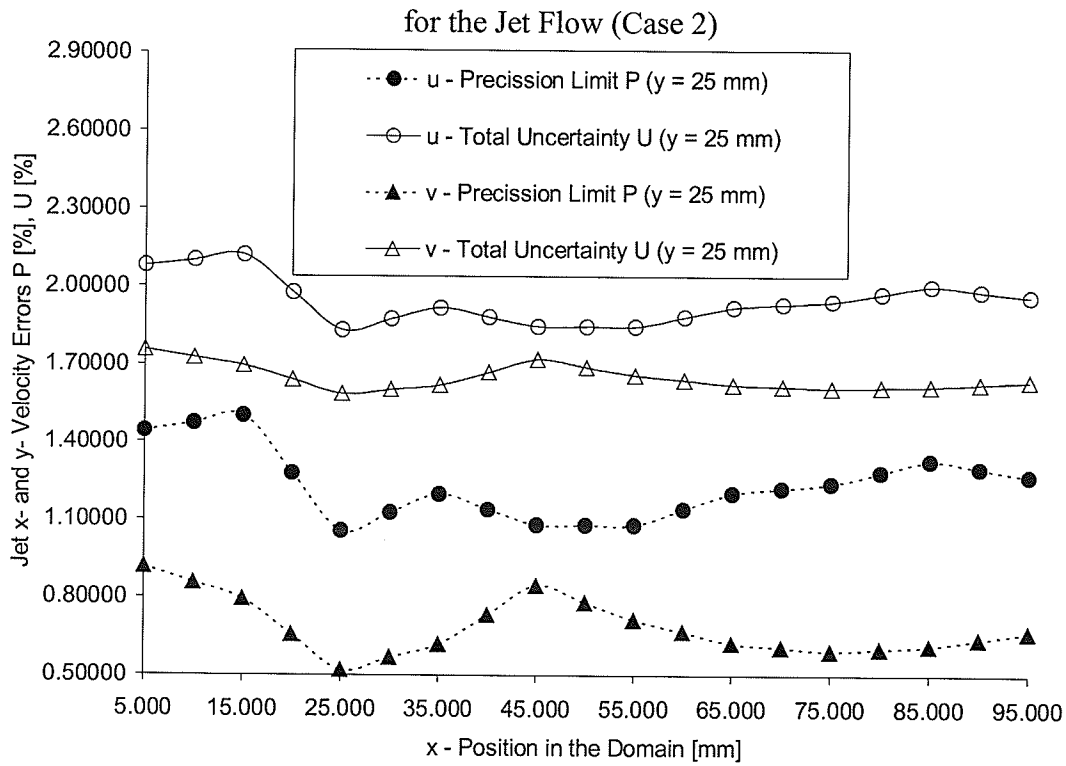


Figure 5. 5. 11: Error Distributions along the Camera Interrogation Region for the Jet Flow (Case 2)

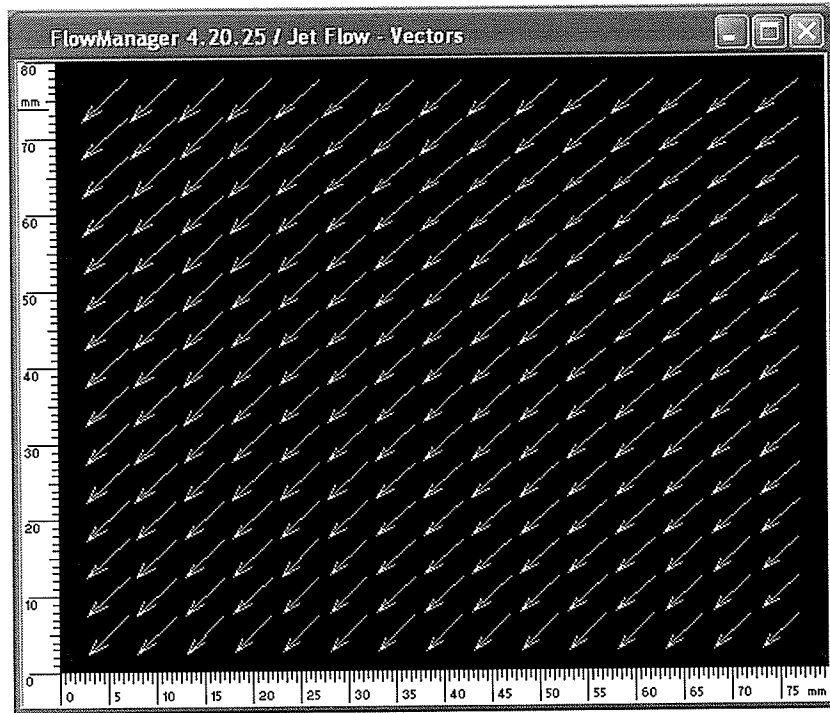


Figure 5. 5. 12: Measured Droplet Velocities (Case 3). Inlet Velocity Magnitude = 2.092 m/s

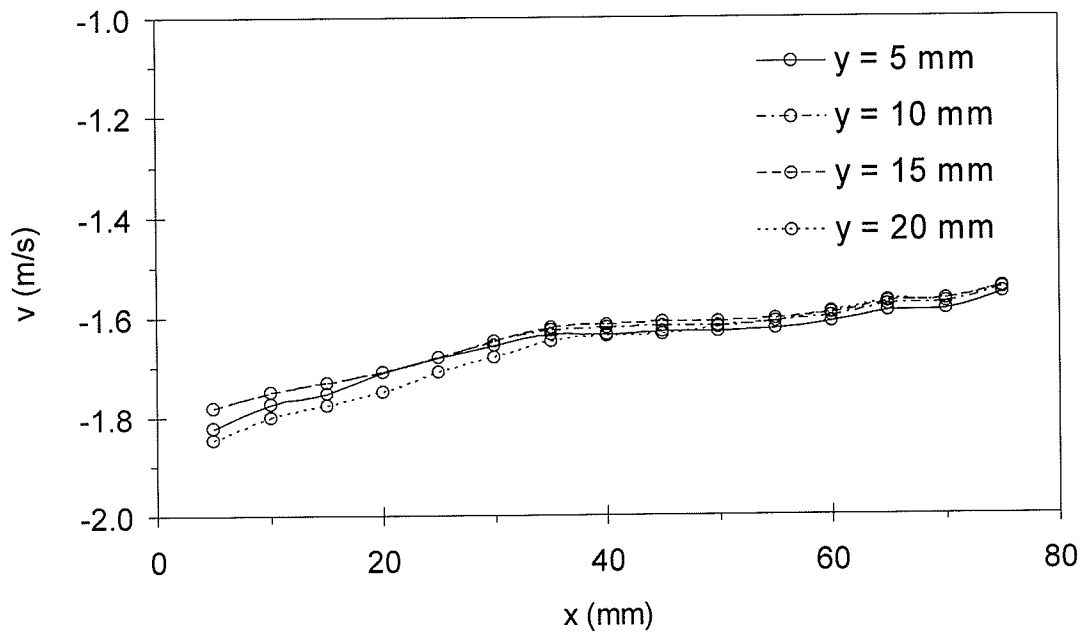


Figure 5. 5. 13: Measured Vertical Velocity Component (Case 3)

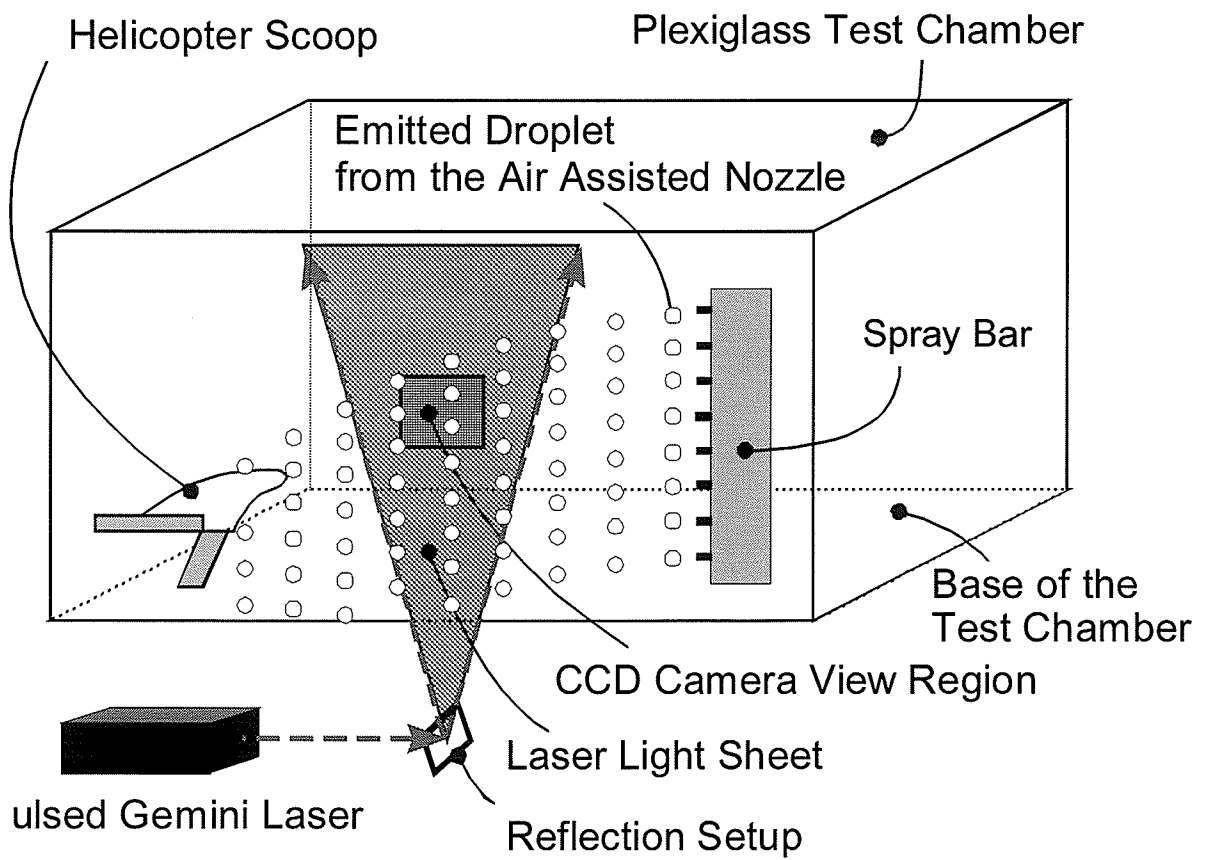


Figure 5. 5. 14: Schematic of Dispersed Droplet Flow Case

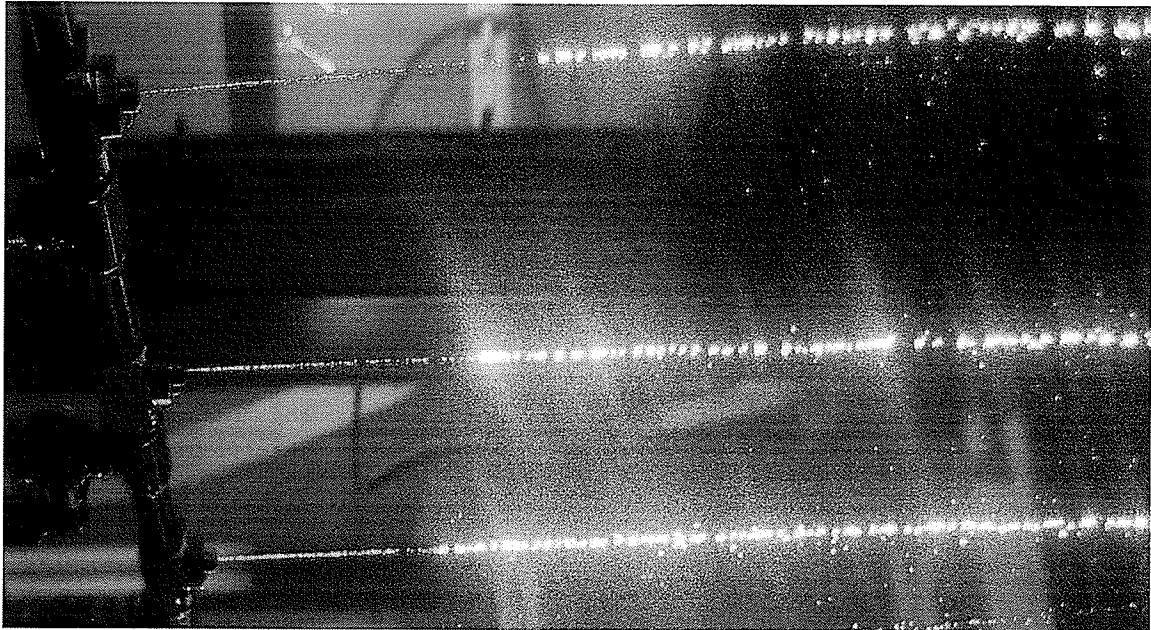


Figure 5. 5. 15: PIV Laser Based Measurements of the Droplet Velocities (Case 4)

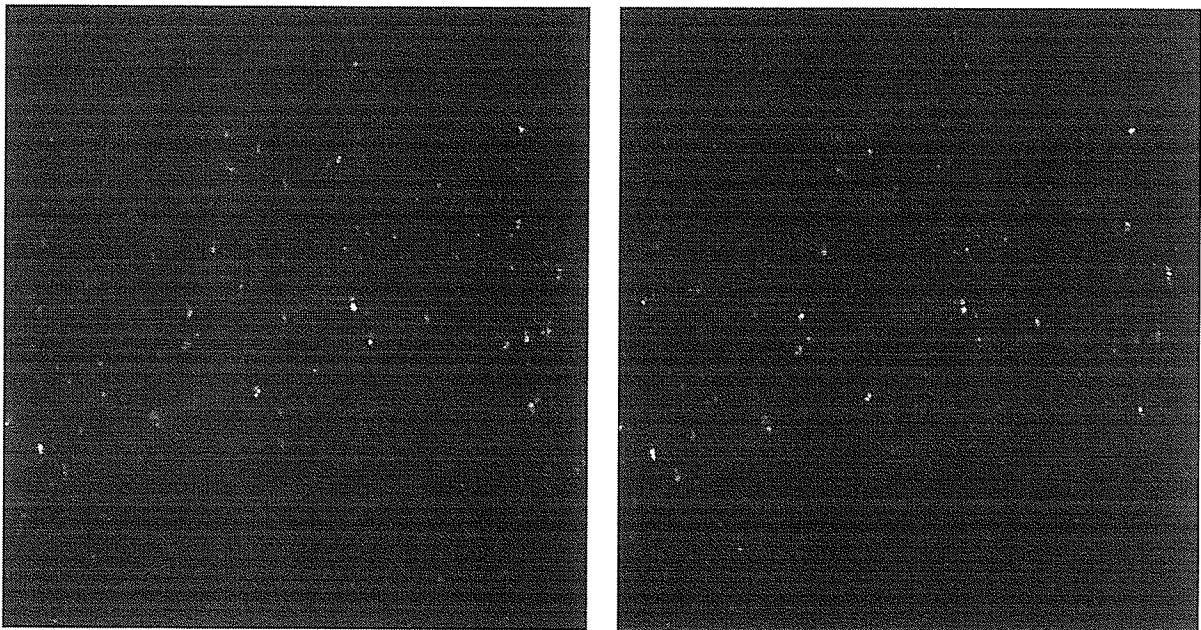


Figure 5. 5. 16: Illuminated Droplets (Case 4; Frame 1 - left and Frame 2 - right)

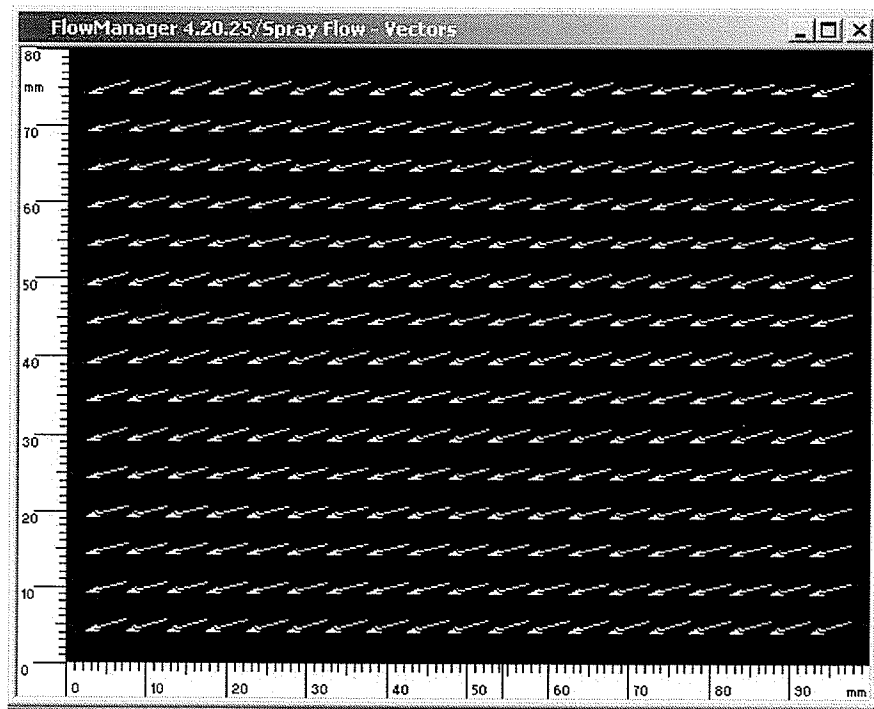


Figure 5. 5. 17 Measured Droplet Velocities (Case 4). Inlet Velocity Magnitude = 9.649 m/s

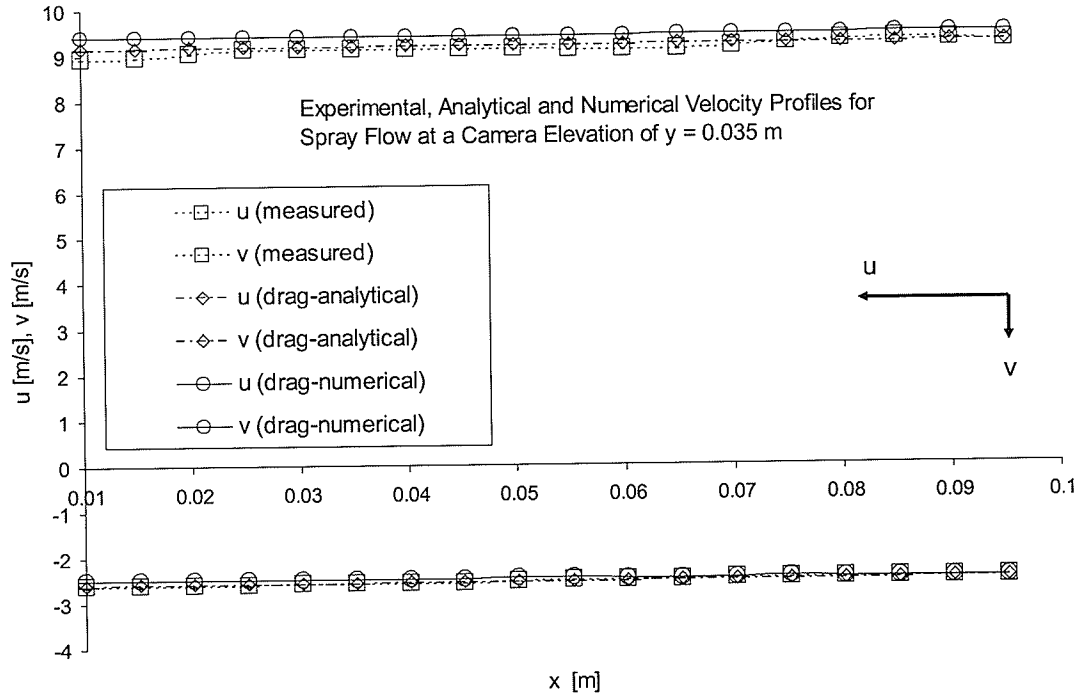


Figure 5. 5. 18: Droplet Velocity Components (Case 4)

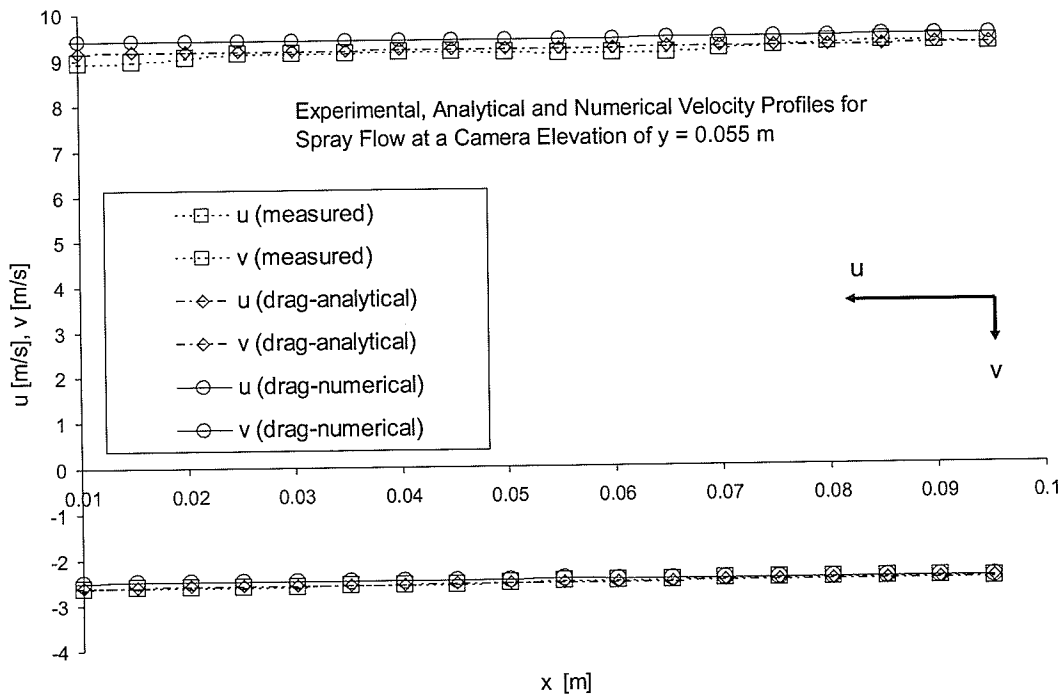


Figure 5. 5. 19: Droplet Velocity Components (Case 4)

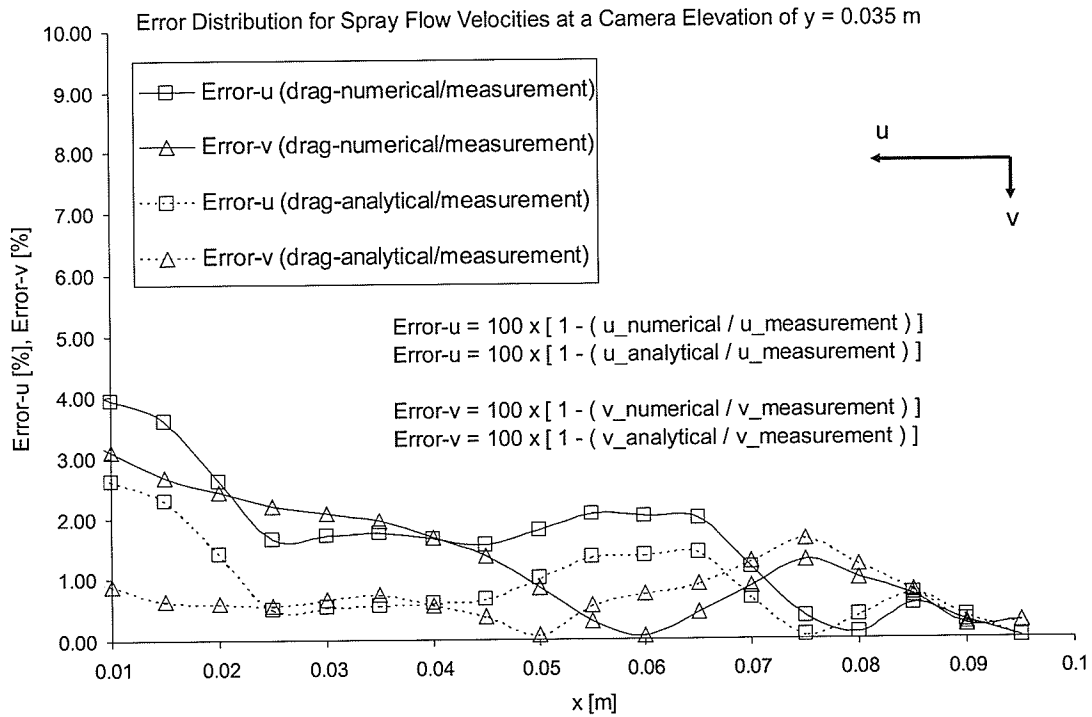


Figure 5. 5. 20: Error Distributions for Droplet Trajectories Along the Domain (Case 4)

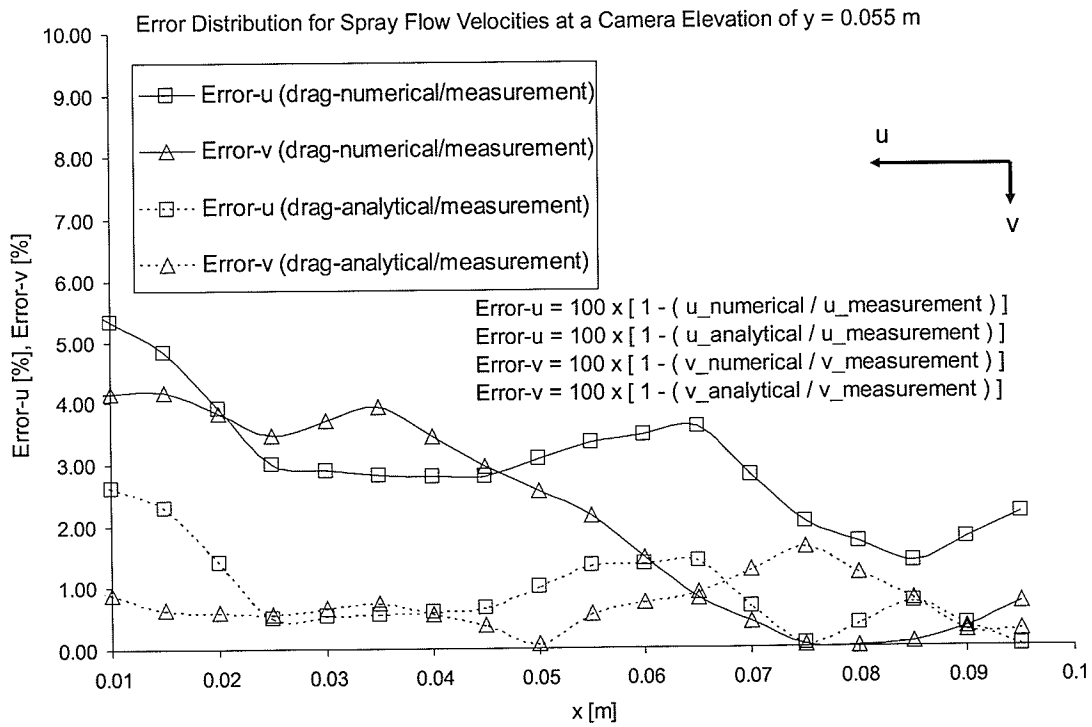


Figure 5. 5. 21: Error Distributions for Droplet Trajectories Along the Domain (Case 4)

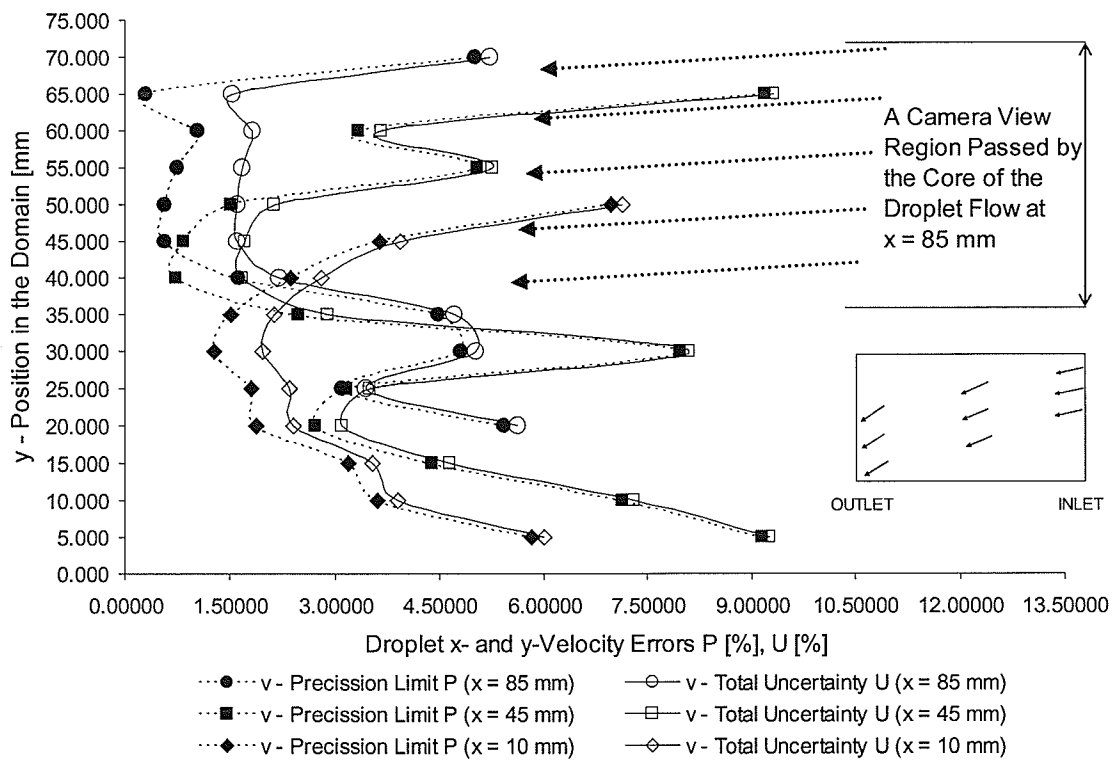


Figure 5. 5. 22: Error Distributions for the Droplet Flow Velocities Across the Width of the Camera Interrogation Region (Case 4)

Droplet Horizontal Velocity u [m / s]	x [m]	u-Precision Limit P [%]	u-Total Uncertainty U [%]
at y = 0.035 (y [m])			
	0.010	3.28292	3.60884
	0.045	3.29729	3.62191
	0.085	4.83967	5.0664
at y = 0.040 (y [m])			
	0.010	4.52032	4.76229
	0.045	1.59799	2.19082
	0.085	3.16067	3.49800

Table 5. 5. 1: Errors for Measured Droplet Velocities at Elevations y and Positions x in the Camera View Region

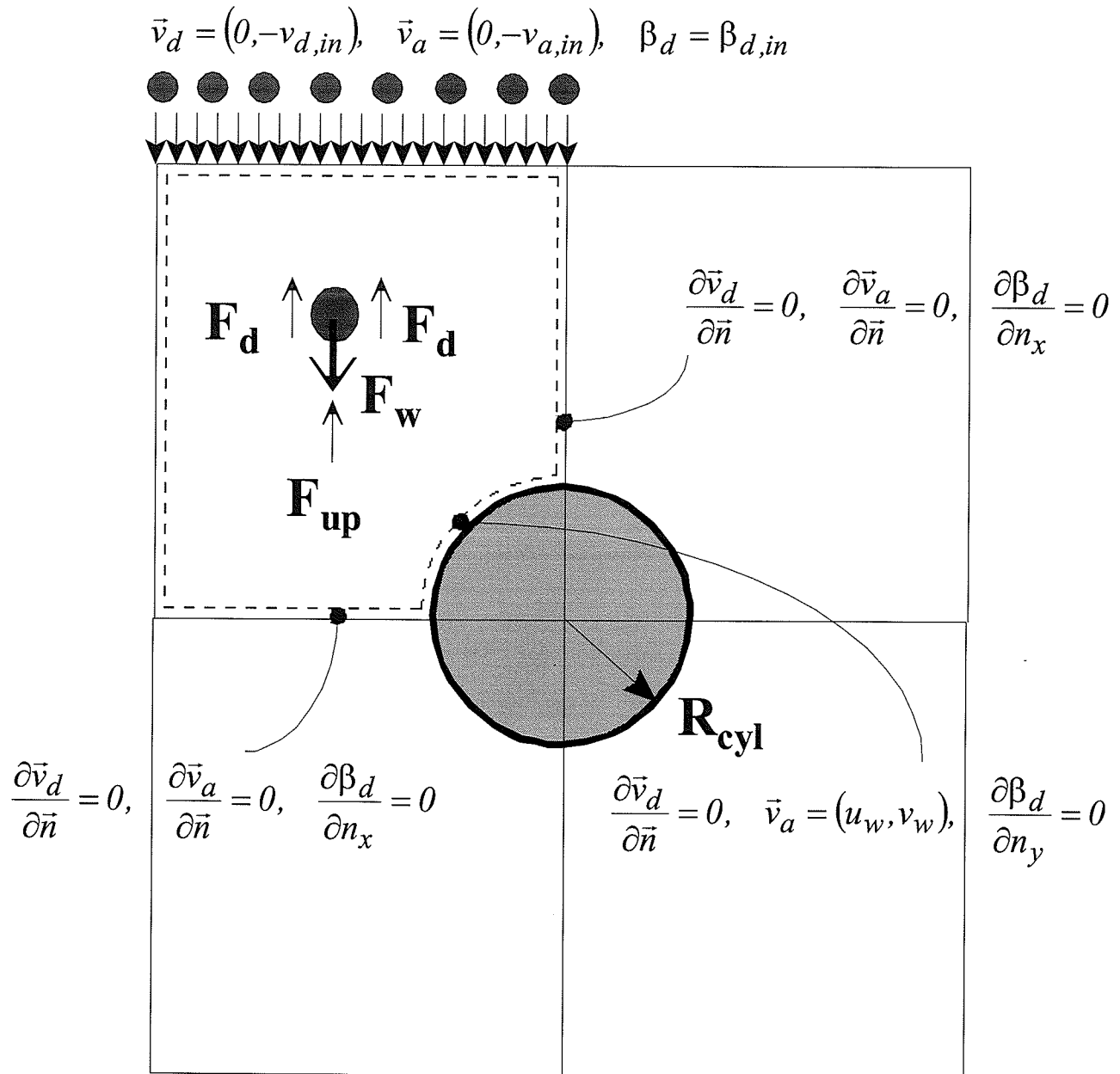


Figure 5. 5. 23: Physical and Numerical Domains for Droplet Flow Impact on the Conductor

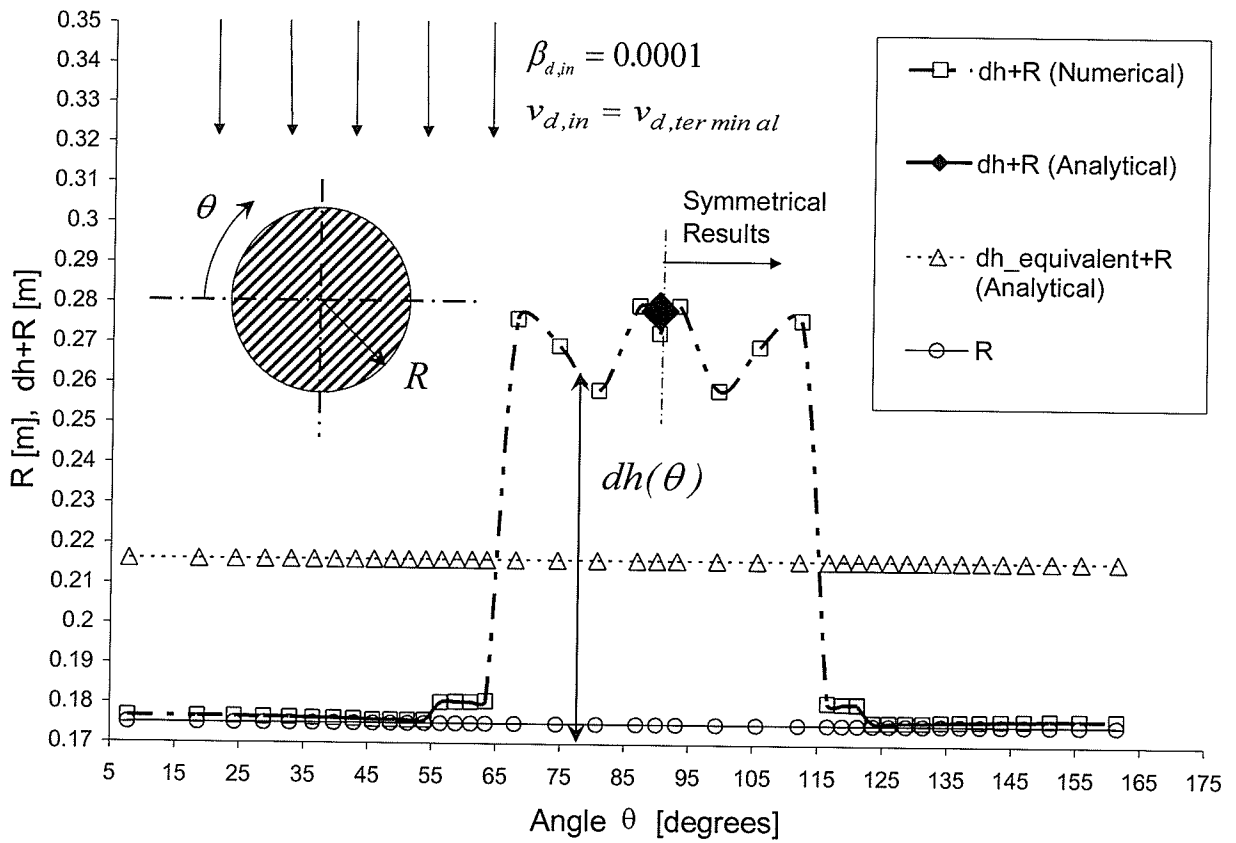


Figure 5. 5. 24: Predicted Ice Thickness Distribution, $dh = f(\theta)$, on the Conductor (in the 1st and 2nd quadrants) at Time $t = 43200$ s

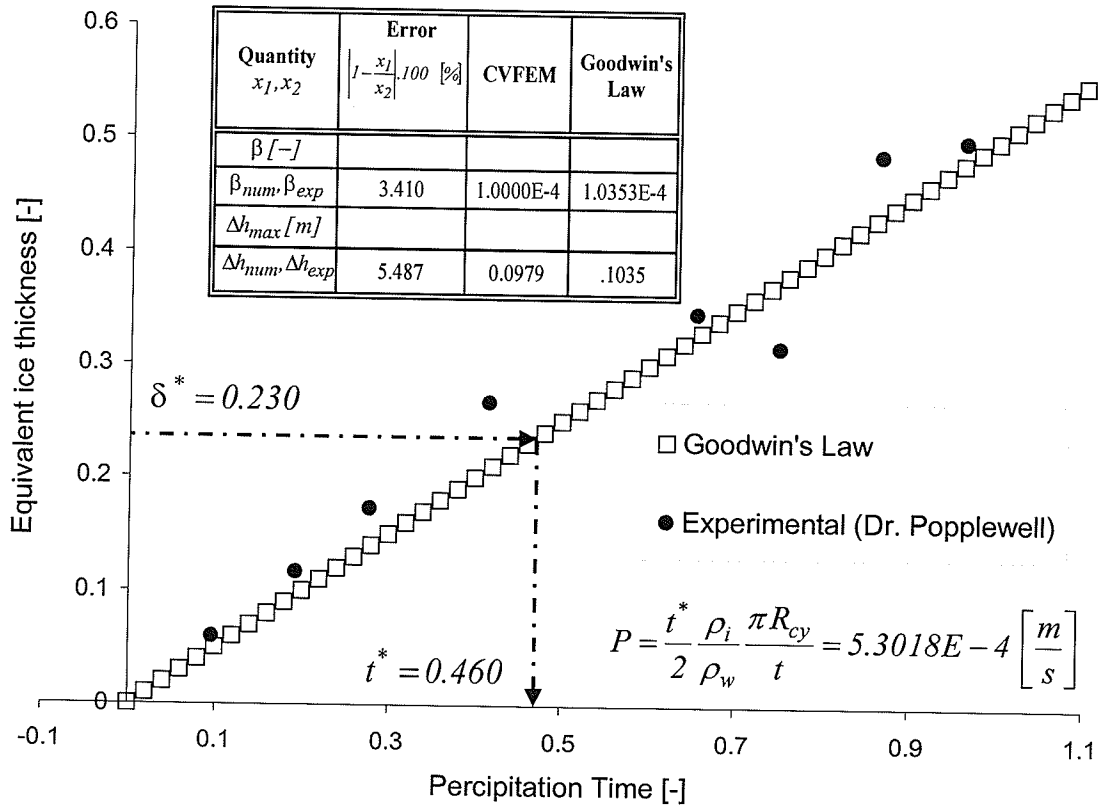


Figure 5. 5. 25: Numerical and Experimental Results of the Droplet Volume Fraction (β) and Maximum Ice Thickness (Δh_{max}) on the Conductor with a Diameter of $D_c = 0.350 m$

Physical Quantities x_1, x_2	Relative Error $\left 1 - \frac{x_1}{x_2}\right \cdot 100$ [%]	Numerical Results (CVFEM)	Experimental Results (Goodwin's Law)	Analytical Results
$\beta [-]$				
β_{num}, β_{exp}	0.034	1.0000E-4	1.0353E-4	1.0000E-4
$\beta_{num}, \beta_{analy}$	0.0000	1.0000E-4	1.0353E-4	1.0000E-4
$\beta_{analy}, \beta_{exp}$	0.034	1.0000E-4	1.0353E-4	1.0000E-4
$\Delta h_{max} [m]$				
$\Delta h_{num}, \Delta h_{exp}$	5.487	0.0979	.1035	.1000
$\Delta h_{num}, \Delta h_{analy}$	2.148	0.0979	.1035	.1000
$\Delta h_{analy}, \Delta h_{exp}$	3.412	0.0979	.1035	.1000

Table 5. 5. 2: Comparison between Results of the Droplet Volume Fraction and Ice Thickness with Different Methods for the Conductor with a Diameter of $D_c = 0.350 m$

Appendix I

ESTABLISHMENT OF SCALED PARAMETERS

A detailed procedure of the scaling analysis from section (2. 4) is presented here.

For both low-Re and high-Re flow regimes, drag factor f can be approximated by (Ref. [8])

$$f = 1 + 0.15 Re_r^{0.687} + 0.0175 Re_r \frac{1}{1 + 4.25 \cdot 10^4 Re_r^{-1.16}}. \quad (\text{A. 1. 1})$$

The relative Reynolds number in Eq. (A. 1. 1) is calculated as follows:

$$Re_r = D_d \frac{|\vec{v}_d - \vec{v}_a|}{v_a} \Rightarrow Re_r = 140.076. \quad (\text{A. 1. 2})$$

APPENDIX

The drag factor becomes

$$f = 1 + 0.15 Re_r^{0.687} + 0.0175 Re_r \frac{1}{1 + 4.25 \cdot 10^4 Re_r^{-1.16}} \Rightarrow f = 5.4911. \quad (\text{A. 1. 3})$$

The closure drag relations are required for computations of x - and y -droplet momentum equations, which yields:

$$\beta_v = \frac{\beta_d f}{\frac{D_d^2}{18\mu_a}} \Rightarrow \beta_v = 0.2236 \text{ kg}/(m^3 s). \quad (\text{A. 1. 4})$$

The droplet velocity in y -direction is derived from the droplet phase fraction equation, i.e.,

$$\frac{\partial}{\partial t}(\beta_d \rho_d) + \frac{\partial}{\partial x}(\beta_d \rho_d v_{d,x}) + \frac{\partial}{\partial y}(\beta_d \rho_d v_{d,y}) = 0. \quad (\text{A. 1. 5})$$

Individual terms are calculated below.

- The transient term yields: $\frac{\partial}{\partial t}(\beta_d \rho_d) = 0.2000 \text{ kg}/(m^3 s). \quad (\text{A. 1. 6})$

- The convective term yields:

$$\frac{\partial}{\partial x}(\beta_d \rho_d v_{d,x}) = \frac{1}{L}(\beta_d \rho_d v_{d,x}). \quad (\text{A. 1. 7})$$

$$\frac{1}{L}(\beta_d \rho_d v_{d,x}) = 0.2000 \text{ kg}/(m^3 s). \quad (\text{A. 1. 8})$$

- Finally, the droplet velocity in the y -direction can be evaluated as follows:

$$\frac{\partial}{\partial y}(\beta_d \rho_d v_{d,y}) = - \left[\frac{\partial}{\partial t}(\beta_d \rho_d) + \frac{\partial}{\partial x}(\beta_d \rho_d v_{d,x}) \right] \quad (\text{A. 1. 9})$$

APPENDIX

$$\frac{1}{\gamma}(\beta_d \rho_d v_{d,y}) = - \left[\frac{1}{t}(\beta_d \rho_d) + \frac{1}{L}(\beta_d \rho_d v_{d,x}) \right] \quad (\text{A. 1. 10})$$

$$v_{d,y} = -4.0000 \text{ m/s}. \quad (\text{A. 1. 11})$$

Droplet y -momentum equation is estimated based on the representative scaled parameters, term-by-term, as follows.

- The transient term is: $\frac{\partial}{\partial t}(\beta_d \rho_d v_{d,y}) = -0.7998 \text{ kg}/(\text{m}^2 \text{s}^2).$ (A. 1. 12)

- The x -convective term is: $\frac{\partial}{\partial x}(\beta_d \rho_d v_{d,y} v_{d,x}) = -0.7998 \text{ kg}/(\text{m}^2 \text{s}^2).$ (A. 1. 13)

- The y -convective term is: $\frac{\partial}{\partial y}(\beta_d \rho_d v_{d,y} v_{d,y}) = 1.5997 \text{ kg}/(\text{m}^2 \text{s}^2).$ (A. 1. 14)

- The mass force term is: $\Gamma_{d,m} v_{d,y} = 0.0000 \text{ kg}/(\text{m}^2 \text{s}^2).$ (A. 1. 15)

- The pressure term is: $-\beta_d \frac{\partial p_d}{\partial y} \Rightarrow -10^{-6} \frac{p_d}{0.01} = -10^{-4} p_d \text{ kg}/(\text{m}^2 \text{s}^2).$ (A. 1. 16)

- The viscous term is: $\beta_d \frac{\partial}{\partial y} \left(2\mu_d \frac{\partial v_{d,y}}{\partial y} \right) \approx -1.4328 \cdot 10^{-4} \text{ kg}/(\text{m}^2 \text{s}^2).$ (A. 1. 17)

- The viscous term is: $\beta_d \frac{\partial}{\partial x} \left[\mu_d \left(\frac{\partial v_{d,y}}{\partial x} + \frac{\partial v_{d,x}}{\partial y} \right) \right] \approx 3.5621 \cdot 10^{-5} \text{ kg}/(\text{m}^2 \text{s}^2).$ (A. 1. 18)

- The drag force term is: $\beta_v (v_{a,y} - v_{d,y}) = 1.0061 \text{ kg}/(\text{m}^2 \text{s}^2).$ (A. 1. 19)

APPENDIX

- The y -gravity term is: $\beta_d \rho_d g_y = 0.0098 \text{ kg} / (\text{m}^2 \text{s}^2)$. (A. 1. 20)

- The Faxen force is: $\bar{F}_{FAX} = \mu_a \pi \frac{D_d^3}{8} \nabla^2 \bar{v}_a$. (A. 1. 21)

The force in Eq. (A. 1. 21) accounts for the effect of a non-uniform flow field, which is expected in the boundary layer. It is usually combined with other algebraic drag forces. Its y -component expression is:

$$F_{FAX,y} = \mu_a \pi \frac{D_d^3}{8} \left(\frac{\partial^2 v_{a,x}}{\partial x \partial y} + \frac{\partial^2 v_{a,y}}{\partial y^2} \right) \quad (\text{A. 1. 22})$$

$$F_{FAX,y} \approx 6.6588 \cdot 10^{-14} \text{ (kg m)} / \text{s}^2. \quad (\text{A. 1. 23})$$

- The Saffmann lift force is:

$$\bar{F}_{SAFF} = 1.61 D_d^2 (\mu_a \rho_a)^{\frac{1}{2}} |\bar{\omega}_a|^{\frac{1}{2}} [(\bar{v}_a - \bar{v}_d) \times \bar{\omega}_a]. \quad (\text{A. 1. 24})$$

It arises due to rotation, induced by the velocity gradient between two points on the droplet surface (usually treated as top - bottom), as droplets and surrounding fluid are in contact. The y -component expression is:

$$F_{SAFF,y} = 1.61 D_d^2 (\mu_a \rho_a)^{\frac{1}{2}} \left| \frac{\partial v_{a,y}}{\partial x} - \frac{\partial v_{a,x}}{\partial y} \right|^{\frac{1}{2}} \left[(v_{a,x} - v_{d,x}) \left(\frac{\partial v_{a,y}}{\partial x} - \frac{\partial v_{a,x}}{\partial y} \right) \right] \quad (\text{A. 1. 25})$$

$$F_{SAFF,y} \approx 5.6644 \cdot 10^{-8} \text{ kg m} / \text{s}^2. \quad (\text{A. 1. 26})$$

- Another lift force (Magnus force) arises due to rotation of the particle only. It is expressed by

APPENDIX

$$\bar{F}_{MAG} = \frac{1}{2} \rho_a |\bar{v}_a - \bar{v}_d| C_{LR} A \left(\frac{(\bar{v}_a - \bar{v}_d) \times \bar{\omega}_r}{\left| \bar{\omega}_d - \frac{1}{2} \bar{\nabla} \times \bar{v}_a \right|} \right). \quad (\text{A. 1. 27})$$

where the lift coefficient and relative angle velocity are expressed as

$$C_{LR} = \frac{D_d |\bar{\omega}_d|}{|\bar{v}_a - \bar{v}_d|} \quad (\text{A. 1. 28})$$

$$\bar{\omega}_r = \bar{\omega}_d - \frac{1}{2} \bar{\nabla} \times \bar{v}_a. \quad (\text{A. 1. 29})$$

Based on scaling parameters used in this study, this force is negligible.

- The turbulent terms in the droplet momentum equations are modeled by the Boussinesq approximation. For the droplet y -momentum equation, the main turbulent stress term becomes

$$-\frac{\partial}{\partial y} (\beta_d \rho_d v'_{d,y} v'_{d,y}) = \frac{\partial}{\partial y} \left[\beta_d \mu_d \left(\frac{\partial v_{d,y}}{\partial y} + \frac{\partial v_{d,y}}{\partial y} \right) \right] \quad (\text{A. 1. 30})$$

$$\frac{\partial}{\partial y} \left[\beta_d \mu_d \left(\frac{\partial v_{d,y}}{\partial y} + \frac{\partial v_{d,y}}{\partial y} \right) \right] \approx -1.4328 \cdot 10^{-4} \text{ kg} / (\text{m}^2 \text{s}^2). \quad (\text{A. 1. 31})$$

- For y -momentum equation, the cross diffusion turbulent stress term becomes

$$-\frac{\partial}{\partial x} (\beta_d \rho_d v'_{d,y} v'_{d,x}) = \frac{\partial}{\partial x} \left[\beta_d \mu_d \left(\frac{\partial v_{d,y}}{\partial x} + \frac{\partial v_{d,x}}{\partial y} \right) \right] \quad (\text{A. 1. 32})$$

$$\frac{\partial}{\partial x} \left[\beta_d \mu_d \left(\frac{\partial v_{d,y}}{\partial x} + \frac{\partial v_{d,x}}{\partial y} \right) \right] \approx 3.5621 \cdot 10^{-5} \text{ kg} / (\text{m}^2 \text{s}^2). \quad (\text{A. 1. 33})$$

Assembling terms in the droplet y -momentum equation yields:

$$\begin{aligned}
& -0.7998 - 0.7998 + 1.5997 \approx \\
& 0.0000 - 10^{-4} p_d - 1.4328 \cdot 10^{-4} + 3.5621 \cdot 10^{-5} + 1.0061 + 0.0098 \quad (\text{A. 1. 34}) \\
& + 6.6588 \cdot 10^{-14} + 5.6644 \cdot 10^{-8} - 1.4328 \cdot 10^{-4} + 3.5621 \cdot 10^{-5}.
\end{aligned}$$

From this result, the dispersed phase pressure can be calculated as

$$p_d = 0.1016 \cdot 10^5 \text{ kg}/(m s^2). \quad (\text{A. 1. 35})$$

The pressure magnitude in Eq. (A. 1. 38) is inserted into the subsequent droplet x -momentum equation in the pressure term.

Similarly, x -momentum equation is analyzed based on the representative scale parameters, term-by-term, as follows.

- The transient term is: $\frac{\partial}{\partial t}(\beta_d \rho_d v_{d,x}) = 7.9984 \text{ kg}/(m^2 s^2).$ (A. 1. 36)

- The x -convective term is: $\frac{\partial}{\partial x}(\beta_d \rho_d v_{d,x} v_{d,x}) = 7.9984 \text{ kg}/(m^2 s^2).$ (A. 1. 37)

- The y -convective term is: $\frac{\partial}{\partial y}(\beta_d \rho_d v_{d,x} v_{d,y}) = -15.9968 \text{ kg}/(m^2 s^2).$ (A. 1. 38)

- The mass force term is: $\Gamma_{d,m} v_{d,x} = 0.0000 \text{ kg}/(m^2 s^2).$ (A. 1. 39)

- The pressure term is: $-\beta_d \frac{\partial p_d}{\partial x} = -0.0508 \text{ kg}/(m^2 s^2).$ (A. 1. 40)

- The viscous term is: $\beta_d \frac{\partial}{\partial x} \left(2\mu_d \frac{\partial v_{d,x}}{\partial x} \right) \approx 3.5820 \cdot 10^{-6} \text{ kg}/(m^2 s^2).$ (A. 1. 41)

APPENDIX

- The viscous term is: $\beta_d \frac{\partial}{\partial y} \left[\mu_d \left(\frac{\partial v_{d,x}}{\partial y} + \frac{\partial v_{d,y}}{\partial x} \right) \right] \approx 7.1242 \cdot 10^{-4} \text{ kg} / (\text{m}^2 \text{s}^2)$.

(A. 1. 42)

- The drag force term is: $\beta_v (v_{a,x} - v_{d,x}) = -7.8252 \text{ kg} / (\text{m}^2 \text{s}^2)$.

(A. 1. 43)

- The x-gravity term is: $\beta_d \rho_d g_x = 0.0000 \text{ kg} / (\text{m}^2 \text{s}^2)$.

(A. 1. 44)

- The x-component of the Faxen force yields

$$F_{FAX,x} = \mu_a \pi \frac{D_d^3}{8} \left(\frac{\partial^2 v_{a,x}}{\partial x^2} + \frac{\partial^2 v_{a,y}}{\partial x \partial y} \right) \quad (\text{A. 1. 45})$$

$$F_{FAX,x} \approx 3.3294 \cdot 10^{-15} \text{ kg m} / \text{s}^2. \quad (\text{A. 1. 46})$$

- The x-component of the Saffmann lift force is evaluated as follows.

$$F_{SAFF,x} = 1.61 D_d^2 (\mu_a \rho_a)^{1/2} \left| \frac{\partial v_{a,y}}{\partial x} - \frac{\partial v_{a,x}}{\partial y} \right|^{-1/2} \left[(v_{a,y} - v_{d,y}) \left(\frac{\partial v_{a,y}}{\partial x} - \frac{\partial v_{a,x}}{\partial y} \right) \right] \quad (\text{A. 1. 47})$$

$$F_{SAFF,x} \approx -7.2827 \cdot 10^{-9} \text{ kg m} / \text{s}^2. \quad (\text{A. 1. 48})$$

- For x-momentum equation, the main turbulent stress term becomes

$$-\frac{\partial}{\partial x} (\beta_d \rho_d v'_{d,x} v'_{d,x}) = \frac{\partial}{\partial x} \left[\beta_d \mu_d \left(\frac{\partial v_{d,x}}{\partial x} + \frac{\partial v_{d,x}}{\partial x} \right) \right] \quad (\text{A. 1. 49})$$

$$\frac{\partial}{\partial x} \left[\beta_d \mu_d \left(\frac{\partial v_{d,x}}{\partial x} + \frac{\partial v_{d,x}}{\partial x} \right) \right] = 3.5820 \cdot 10^{-6} \text{ kg} / (\text{m}^2 \text{s}^2). \quad (\text{A. 1. 50})$$

- For x-momentum equation, the cross diffusion turbulent stress term becomes

$$-\frac{\partial}{\partial y}(\beta_d \rho_d v'_{d,x} v'_{d,y}) = \frac{\partial}{\partial y} \left[\beta_d \mu_d \left(\frac{\partial v_{d,x}}{\partial y} + \frac{\partial v_{d,y}}{\partial x} \right) \right] \quad (\text{A. 1. 51})$$

$$\frac{\partial}{\partial y} \left[\beta_d \mu_d \left(\frac{\partial v_{d,x}}{\partial y} + \frac{\partial v_{d,y}}{\partial x} \right) \right] \approx 7.1242 \cdot 10^{-4} \text{ kg} / (\text{m}^2 \text{ s}^2). \quad (\text{A. 1. 52})$$

Assembling terms in droplet x -momentum equation yields:

$$\begin{aligned} &7.9984 + 7.9984 - 15.9968 \approx \\ &0.0000 - 0.0508 + 3.5820 \cdot 10^{-6} + 7.1242 \cdot 10^{-4} - 7.8252 + 0.0000 \quad (\text{A. 1. 53}) \\ &+ 3.3294 \cdot 10^{-15} - 7.2827 \cdot 10^{-9} + 3.5820 \cdot 10^{-6} + 7.1242 \cdot 10^{-4}. \end{aligned}$$

Values from first to last in Eq. (A. 1. 53) represent the following terms in the x -momentum droplet equation: transient, x -convective, y -convective, mass force, pressure, normal stress, shear stress, non-differential drag, Faxen, Saffmann and two turbulent terms. Table (2. 4. 1) represents the summarized magnitudes of the terms in the y and x droplet momentum equations. Based on the scaling analysis above, it can be concluded that only the following terms in the droplet x -momentum equation are important: *transient*, *convection* and *source drag*.

The steady-state droplet x -momentum equation (spatially averaged form) is established throughout the entire domain above a flat plate as follows:

$$\frac{\partial}{\partial x}(\beta_d \rho_d v_{d,x}^2) + \frac{\partial}{\partial y}(\beta_d \rho_d v_{d,x} v_{d,y}) = -\beta_v (v_{d,x} - v_{a,x}). \quad (\text{A. 1. 54})$$

Appendix 2

ESTABLISHMENT OF ORDER OF MAGNITUDES FOR DISPERSED- FLOW MOMENTUM EQUATIONS

In this appendix, an order of magnitude analysis is performed on important terms in final x -momentum equation. Unlike the previous scaling analysis, this analysis establishes the final relations between terms in the droplet momentum equations. It also determines the specifics of how the momentum deflection and stream function are determined, as well as their limitations. The analysis represents a unique contribution over past single phase analyses to determine the similarity parameter, η . The signs (+ or -) in the terms of the equation are retained throughout the analysis.

The droplet x -momentum equation is written in an order of magnitude form [see Eq. (A. 2. 1)]. It is assumed that all terms in the equation have the same order of magnitude. Therefore, the terms representing the momentum transport in multiphase flow with droplets can be compared on an individual basis [for additional details, see section (2. 4), (ii) Order of Magnitude Analysis]. The $v_{d,x,\gamma}$ droplet velocity represents the velocity at the edge of the momentum deflection layer.

$$\tilde{O}\left(\frac{\beta_d \rho_d v_{d,x,\gamma}^2}{x}\right) + \tilde{O}\left(\frac{\beta_d \rho_d v_{d,x,\gamma} v_{d,y,\gamma}}{\gamma}\right) = \tilde{O}\left[-\beta_V (v_{d,x,\gamma} - v_{a,x})\right]. \quad (\text{A. 2. 1})$$

- The x -momentum x -convective term and droplet part of the drag force are related by

$$\tilde{O}\left(\frac{\beta_d \rho_d v_{d,x,\gamma}^2}{x}\right) = \tilde{O}\left(-\beta_V v_{d,x,\gamma}\right). \quad (\text{A. 2. 2})$$

- The x -momentum y -convective term and air part of the drag force are related:

$$\tilde{O}\left(\frac{\beta_d \rho_d v_{d,x,\gamma} v_{d,y,\gamma}}{\gamma}\right) = \tilde{O}\left(\beta_V v_{a,x}\right). \quad (\text{A. 2. 3})$$

From Eq. (A. 2. 1), the following limited x -velocity is obtained:

$$v_{d,x,\gamma} = \tilde{O}\left(-\frac{\beta_V}{\rho_d \beta_d} x\right) \quad (\text{A. 2. 4})$$

$$v_{d,x,\gamma} = \tilde{O}(-C x). \quad (\text{A. 2. 5})$$

The parameter C is determined as

$$C = \frac{\beta_V}{\beta_d \rho_d}. \quad (\text{A. 2. 6})$$

The magnitude of the C is presented in Table (2. 4. 1). From Eq. (A. 2. 3), the momentum deflection is obtained as follows,

$$\gamma = \tilde{O} \left(\frac{\beta_d \rho_d}{\beta_V v_{a,x}} v_{d,y\gamma} v_{d,x\gamma} \right) \quad (\text{A. 2. 7})$$

$$\gamma = \tilde{O} \left[\frac{\beta_d \rho_d}{\beta_V v_{a,x}} v_{d,y\gamma} \left(-\frac{\beta_V}{\beta_d \rho_d} x \right) \right] \quad (\text{A. 2. 8})$$

$$\gamma = \tilde{O} \left(-\frac{v_{d,y\gamma}}{v_{a,x}} x \right). \quad (\text{A. 2. 9})$$

The y -droplet velocity is obtained from droplet y -momentum equation, i.e.,

$$\frac{\partial}{\partial x} (\beta_d \rho_d v_{d,y} v_{d,x}) + \frac{\partial}{\partial y} (\beta_d \rho_d v_{d,y} v_{d,y}) = -\beta_V (v_{d,y} - v_{a,y}). \quad (\text{A. 2. 10})$$

From the order of analysis on the part of droplet y -momentum equation:

$$\tilde{O} \left(\frac{\beta_d \rho_d v_{d,y} v_{d,y}}{\partial y} \right) = \tilde{O} (\beta_V v_{a,y}). \quad (\text{A. 2. 11})$$

Therefore, the droplet y -velocity component is obtained from Eq. (A. 2. 11), i.e.,

$$v_{d,y} = \pm \sqrt{\tilde{O} \left(\frac{\beta_V}{\beta_d \rho_d} v_{a,y} \gamma \right)}. \quad (\text{A. 2. 12})$$

Since the quantities under the square root are always positive, the '-' sign can be dropped. The expression in Eq. (A. 2. 12) needs to be inserted into Eq. (A. 2. 9), which yields the following equation,

$$\gamma = \tilde{O} \left\{ \frac{\sqrt{\tilde{O} \left(\frac{\beta_V}{\beta_d \rho_d} v_{a,y} \gamma \right)}}{v_{a,x}} x \right\}. \quad (\text{A. 2. 13})$$

Squaring Eq. (A. 2. 13), canceling the extra γ terms and dropping the order symbol (\tilde{O}), the equation for the y -momentum deflection yields

$$\gamma = \frac{\left(\frac{\beta_V}{\beta_d \rho_d} \right) v_{a,y}}{v_{a,x}^2} x^2 \quad (\text{A. 2. 14})$$

$$\gamma = C \left(\frac{v_{a,y}}{v_{a,x}^2} \right) x^2. \quad (\text{A. 2. 15})$$

As mentioned before, the self-similar behavior of the x -velocity profile in the y -direction along the plate is attempted to be established. In this regard, the ratio of the arbitrary droplet x -velocity and limited droplet x -velocity is used as follows:

$$\frac{v_{d,x}}{v_{d,x,\gamma}} = F\left(\frac{y}{\gamma}\right) \quad (\text{A. 2. 16})$$

$$\frac{v_{d,x}}{v_{d,x,\gamma}} = F(\eta). \quad (\text{A. 2. 17})$$

Inserting the corresponding parameters into Eq. (A. 2. 17) yields the following expressions,

$$\frac{v_{d,x}}{\frac{\beta_V}{\beta_d \rho_d} x} = F\left(y \frac{1}{C \frac{v_{a,y}}{v_{a,x}^2} x^2} \right) \quad (\text{A. 2. 18})$$

$$\frac{v_{d,x}}{\frac{\beta_V}{\beta_d \rho_d} x} = F\left(\frac{y}{x^2} \text{CONS} \right), \quad (\text{A. 2. 19})$$

where the constant is defined as

$$CONS = \frac{I}{C \frac{v_{a,y}}{v_{a,x}^2}}. \quad (\text{A. 2. 20})$$

From Eq. (A. 2. 18), the similarity parameter is recognized as follows:

$$\eta = \frac{y}{x^2} \frac{v_{a,x}^2}{C v_{ya}} \quad (\text{A. 2. 21})$$

$$\eta = \frac{y}{x^2} CONS. \quad (\text{A. 2. 22})$$

The parameter in Eq. (A. 2. 19) is a new independent variable. It represents the similarity parameter. In conclusion, self-similar velocity profiles can be derived for the velocity field in this problem.

Appendix 3

ESTABLISHMENT OF THE DISPERSED-FLOW Y-MOMENTUM EQUATION

In this appendix, spatial averaging of the y -momentum equation is presented. This averaging procedure is performed for the following four terms in Eq. (2. 2. 6) of Chapter 2 as follows: (i) second term, (ii) third term, (iii) fifth term and (iv) sixth term.

(i) Second Term

$$\bar{n}_x(\rho_k \Psi_k \bar{v}_k) = \rho_k \Psi_k (1,0,0)(v_{kx}, v_{ky}, v_{kz}) \quad (\text{A. 3. 1})$$

$$\bar{n}_x(\rho_k \Psi_k \bar{v}_k) = \rho_k \Psi_k v_{kx} \quad (\text{A. 3. 2})$$

$$\rho_k(\bar{n}_y \bar{v}_k) v_{kx} = \rho_k [(0,1,0)(v_{kx}, v_{ky}, v_{kz})] v_{kx} \quad (\text{A. 3. 3})$$

$$\rho_k(\bar{n}_y \bar{v}_k) v_{kx} = \rho_k v_{ky} v_{kx} \quad (\text{A. 3. 4})$$

The convection term includes the turbulent fluctuating component of the velocity, δv , as follows.

$$\rho_k(\bar{n}_y \bar{v}_k) v_{kx} = \rho_k (v_{ky} v_{kx} + \delta v_{ky} \delta v_{kx}) \quad (\text{A. 3. 5})$$

Furthermore,

$$\bar{n}_x \bar{j} := (1,0,0)(p_k \bar{I} - \bar{\tau}_k) \quad (\text{A. 3. 6})$$

$$\bar{n}_x \bar{j} := (p_k - \tau_{k,xx}, -\tau_{k,xy}, -\tau_{k,xz}) \quad (\text{A. 3. 7})$$

$$\begin{aligned} \bar{n}_y (p_k - \tau_{k,xx}, -\tau_{k,xy}, -\tau_{k,xz}) = \\ (0,1,0)(p_k - \tau_{k,xx}, -\tau_{k,xy}, -\tau_{k,xz}) \end{aligned} \quad (\text{A. 3. 8})$$

$$\bar{n}_y (p_k - \tau_{k,xx}, -\tau_{k,xy}, -\tau_{k,xz}) = p_k - \tau_{k,xy} \quad (\text{A. 3. 9})$$

As a result, the second term becomes

$$\begin{aligned} \bar{n}_y \frac{\partial}{\partial x} \bar{n}_x (\rho_k \Psi_k \bar{v}_k + \bar{j}_k) := \\ \frac{\partial}{\partial x} [\rho_k (v_{ky} v_{kx} + \delta v_{ky} \delta v_{kx}) - \tau_{k,xy}] \end{aligned} \quad (\text{A. 3. 10})$$

(ii) Third Term

$$\bar{n}_y(\rho_k \Psi_k \bar{v}_k) = \rho_k \Psi_k (0,1,0)(v_{kx}, v_{ky}, v_{kz}) \quad (\text{A. 3. 11})$$

$$\bar{n}_y(\rho_k \Psi_k \bar{v}_k) = \rho_k \Psi_k v_{ky} \quad (\text{A. 3. 12})$$

APPENDIX

$$\rho_k(\bar{n}_y \bar{v}_k) v_{ky} = \rho_k [(0,1,0)(v_{kx}, v_{ky}, v_{kz})] v_{ky} \quad (\text{A. 3. 13})$$

$$\rho_k(\bar{n}_y \bar{v}_k) v_{ky} = \rho_k v_{ky} v_{ky} \quad (\text{A. 3. 14})$$

Expanding the results in terms of the turbulent fluctuating component, δv , and multiplying all terms,

$$\rho_k(\bar{n}_y \bar{v}_k) v_{ky} = \rho_k (v_{ky} v_{ky} + \delta v_{ky} \delta v_{ky}) \quad (\text{A. 3. 15})$$

$$\bar{n}_y \bar{j} := (0,1,0)(p_k \bar{I} - \bar{\tau}_k) \quad (\text{A. 3. 16})$$

$$\bar{n}_y \bar{j} := (-\tau_{k,yx}, p_k - \tau_{k,yy}, -\tau_{k,yz}) \quad (\text{A. 3. 17})$$

$$\bar{n}_y (-\tau_{k,yx}, p_k - \tau_{k,yy}, -\tau_{k,yz}) = p_k - \tau_{k,yy} \quad (\text{A. 3. 18})$$

Assembling these results together in the third term of the y -momentum equation,

$$\begin{aligned} \bar{n}_y \left[\frac{\partial}{\partial y} \bar{n}_y (\rho_k \psi_k \bar{v}_k + \bar{j}_k) \right] := \\ \frac{\partial}{\partial y} [\rho_k (v_{ky} v_{ky} + \delta v_{ky} \delta v_{ky}) + p_k - \tau_{k,yy}] \end{aligned} \quad (\text{A. 3. 19})$$

(iii) Fifth Term

$$-\frac{1}{V} \int_{a_i} [\dot{m}_k \bar{v}_k + \bar{n}_k (p_k \bar{I} - \bar{\tau}_k)] dS \quad (\text{A. 3. 20})$$

Multiplying each term by \bar{n}_y yields

$$\dot{m}_k(\bar{n}_y \bar{v}_k) = \dot{m}_k(0,1,0)(v_{kx}, v_{ky}, v_{kz}) \quad (\text{A. 3. 21})$$

$$\dot{m}_k(\bar{n}_x \bar{v}_k) = \dot{m}_k(\bar{v}_{ky}) \quad (\text{A. 3. 22})$$

$$\begin{aligned}
 & - \int_{a_i} \bar{n}_k (\bar{n}_y p_k) dS = \\
 & \int_{a_i} \bar{n}_k \left[\bar{n}_y (\langle p_k \rangle + \Delta p_{ki} + \Delta p'_{ki}) \right] dS \tag{A. 3. 23}
 \end{aligned}$$

$$\begin{aligned}
 & - \int_{a_i} \bar{n}_k (\bar{n}_y p_k) dS = - \left[\langle p_k \rangle + \Delta p_{ki} \right] \frac{\partial \beta_k}{\partial y} + \frac{1}{V} \int_{a_i} \bar{n}_k (\bar{n}_y \Delta p'_{ki}) dS \tag{A. 3. 24}
 \end{aligned}$$

Furthermore,

$$\frac{1}{V} \int_{a_i} \bar{n}_y \bar{n}_k \bar{\tau}_k dS = \frac{1}{V} \int_{a_i} \bar{n}_k \bar{\tau}_{ky} dS \tag{A. 3. 25}$$

$$\frac{1}{V} \int_{a_i} \bar{n}_y \bar{n}_k \bar{\tau}_k dS = \langle \bar{n}_k \bar{\tau}_{ky} \rangle_i \tag{A. 3. 26}$$

Assembling the fifth term in the y -momentum equation yields,

$$\begin{aligned}
 & - \frac{1}{V} \int_{a_i} \bar{n}_y \left[\dot{m}_k \bar{v}_k + \bar{n}_k (p_k \bar{I} - \bar{\tau}_k) \right] dS = - \langle \dot{m}_k v_{ky} \rangle_i + \\
 & - \left[\langle p_k \rangle + \Delta p_{ki} \right] \frac{\partial \beta_k}{\partial y} - \langle \Delta p'_{ki} \rangle_i + \langle \bar{n}_k \bar{\tau}_{ky} \rangle_i \tag{A. 3. 27}
 \end{aligned}$$

(iv) Sixth Term

$$- \frac{1}{V} \int_{a_{kw}} \bar{n}_{kw} \bar{j}_k dS := - \frac{1}{V} \int_{a_{kw}} \bar{n}_{kw} (p_k \bar{I} - \bar{\tau}_k) dS \tag{A. 3. 28}$$

$$\bar{n}_{kw} \bar{n}_y p_k = 0 \tag{A. 3. 29}$$

$$- \frac{1}{V} \int_{a_{kw}} \bar{n}_y (\bar{n}_{kw} \bar{\tau}_k) dS = \langle \bar{n}_{kw} \bar{\tau}_{ky} \rangle_w \tag{A. 3. 30}$$

The final form of these terms is used in the governing equations for the multiphase flow with droplets.